UNIVERSIDAD COMPLUTENSE DE MADRID

FACULTAD DE CIENCIAS QUÍMICAS
DEPARTAMENTO DE QUÍMICA INORGÁNICA I

TESIS DOCTORAL

SÍNTESIS - ASISTIDA POR MICROONDAS - Y CARACTERIZACIÓN DE MATERIALES INORGÁNICOS

(MICROWAVE - ASSISTED SYNTHESIS AND CHARACTERIZATION OF INORGANIC MATERIALS)

MEMORIA PARA OPTAR AL GRADO DE DOCTOR

PRESENTADA POR

Jesús de la Paz Prado Gonjal

Directores

Emilio Morán Miguélez
Rainer Schmidt

Madrid, 2014

Dpto. Química Inorgánica I Facultad de CC. Químicas
Universidad Complutense de Madrid

Tesis Doctoral

SÍNTESIS - ASISTIDA POR MICROONDAS - Y CARACTERIZACIÓN DE MATERIALES INORGÁNICOS

(MICROWAVE - ASSISTED SYNTHESIS AND CHARACTERIZATION OF INORGANIC MATERIALS)

Jesús de la Paz Prado Gonjal

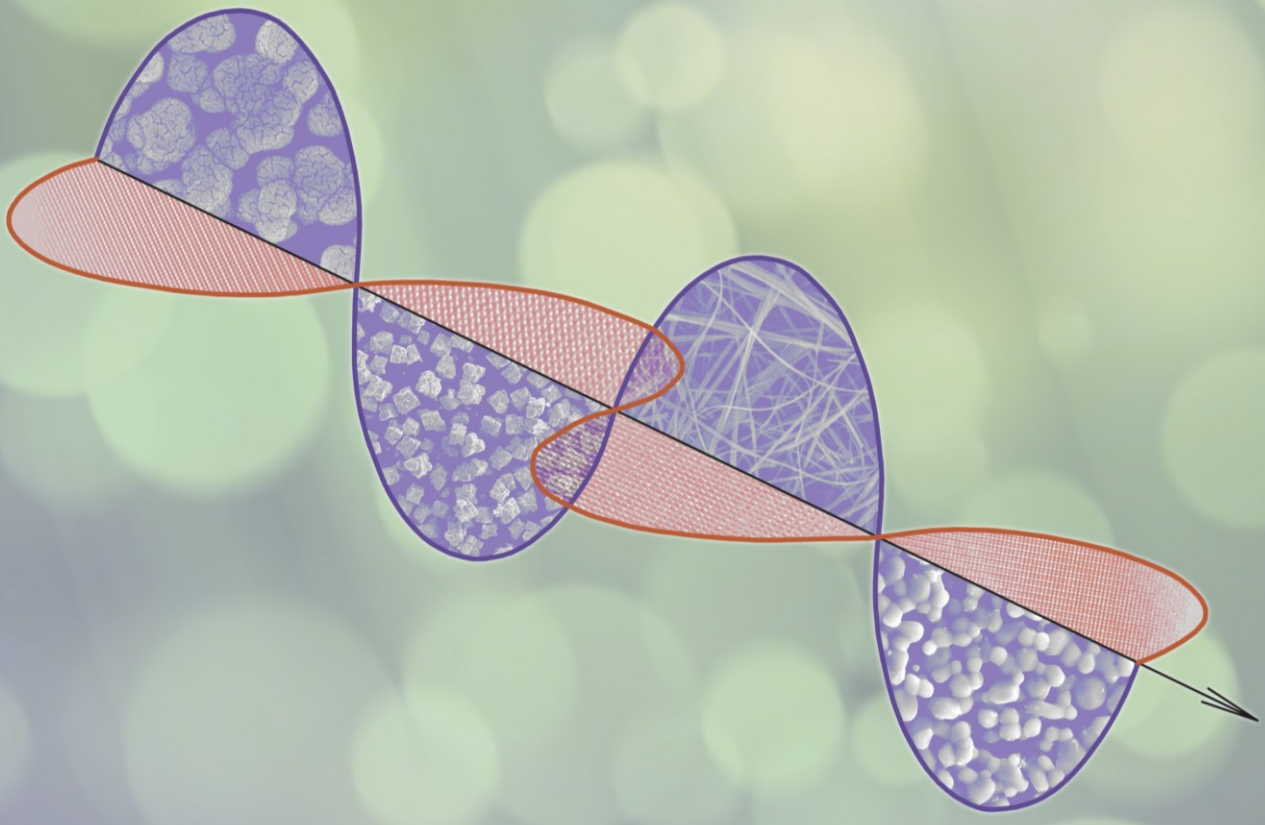

Directores: Dr. Emilio Morán / Dr. Rainer Schmidt

Madrid, 2014

UNIVERSIDAD COMPLUTENSE
MADRID

Dpto. Química Inorgánica I
Facultad de CC. Químicas

Síntesis - asistida por microondas - y caracterización de materiales inorgánicos

(Microwave - assisted synthesis and characterization of inorganic materials)

Memoria de la Tesis Doctoral presentada por:

Jesús de la Paz Prado Gonjal

Para optar al grado de:

Doctor en CC. Químicas con mención Europea

Dirigida por:

Prof. Emilio Morán Miguélez

Dr. Rainer Schmidt

Madrid, 2014

—No esperaba yo menos de la gran magnificencia vuestra, señor mío —respondió Don Quijote, y así os digo que el don que os he pedido y de vuestra liberalidad me ha sido otorgado es que mañana en aquel día me habéis de armar caballero, y esta noche en la capilla deste vuestro castillo velaré las armas, y mañana, como tengo dicho, se cumplirá lo que tanto deseo, para poder como se debe ir por todas las cuatro partes del mundo buscando las aventuras, en pro de los menesterosos, como está a cargo de la caballería y de los caballeros andantes, como yo soy, cuyo deseo a semejantes fazañas es inclinado.

Capítulo III: Donde se cuenta la graciosa manera que tuvo Don Quijote en armarse Caballero.

El Ingenioso Hidalgo Don Quijote de la Mancha, Miguel de Cervantes y Saavedra (1547 – 1616)

Esta tesis se ha realizado en el Dpto. de Química Inorgánica I de la Universidad Complutense de Madrid gracias a la concesión de una beca del "programa de becas predoctorales UCM" (convocatoria 2010), y con la financiación aportada por la Comunidad de Madrid (proyecto Materyener, S2009PPQ-1626) y el Ministerio de Economía y Competitividad (proyecto MAT2010-19460). El proyecto SOPRANO, FP7-PEOPLE-2007-1-1-ITN–Seventh Framework Programme, concedido por la Unión Europea, ha permitido la realización de una estancia predoctoral en CRISMAT – CNRS (Caen – Francia).

Agradecimientos

Me gustaría que estas líneas sirvieran para expresar mi más profundo y sincero agradecimiento a todas aquellas personas que con su ayuda han colaborado en la realización del presente trabajo.

En primer lugar debo agradecer de manera especial y sincera a mi director de tesis, el Profesor Emilio Morán y a mi codirector, el Dr. Rainer Schmidt, por su seguimiento, supervisión y su capacidad para guiarme, algo imprescindible no sólo en el desarrollo de esta tesis, sino también en mi formación como investigador. La motivación, la confianza, el apoyo recibido y también su complicidad y cariño a lo largo de estos años han sido pilares fundamentales cada día de trabajo.

Quiero destacar a la Dra. Mª Elena Villafuerte (UNAM México), una de las principales "culpables" de que me decidiese a realizar el doctorado. El año que compartimos mientras yo aun era estudiante de licenciatura fue memorable. Además juntos descubrimos "el poder de las microondas". Espero poder seguir contando con su amistad, simpatía y visitas anuales durante mucho tiempo.

No puedo olvidarme de la Dra. Susana García (UCM) y del Profesor Flaviano García (San Pablo CEU), por haber confiado en mí desde el principio. Al Dr. David Ávila (UCM) por habernos ayudado a solucionar con sus conocimientos de microscopía electrónica muchos de los problemas cristalográficos a los que nos enfrentábamos y, al Dr. Ángel Arévalo (The University of Edinburgh) por su ayuda y por los días que estuvimos midiendo algunas muestras en el sincrotrón.

Quisiera hacer extensiva mi gratitud al resto de profesores del Dpto. de Química Inorgánica I de la UCM. Al grupo de Estado Sólido, capitaneado por el Profesor Miguel Ángel Alario, a la Dra. Mª José Torralvo, al Prof. Regino Sáez, al Prof. Carlos Otero, al Dr. Khalid Boulahya, al Dr. José Manuel Gallardo y al Dr. Antonio Dos Santos. Mención especial a la Dra. Carmen Parada, por ser una de las pioneras en España en la utilización de energía microondas para preparar sólidos inorgánicos.

Tampoco me puedo olvidar de los profesores y compañeros del Dpto. de Química de la Universidad San Pablo CEU con los que he colaborado de una forma muy activa: Dr. Alois Kuhn, Dr. Ulises Amador, Dra. Maite Azcondo, Dr. Juan Carlos Pérez, Dra. Elena Gonzalo (actualmente en CICenergigune), Dra. Mar López y Dra. Zuriñe Maupoey.

A los investigadores de CRISMAT – CNRS en Caen (Francia) por su gran acogida durante los meses de mi estancia predoctoral. En especial a la Dra. Sylvie Hébert, al Dr. Denis Pelloquin, al Dr. Sylvain Marinel y al Dr. Antoine Maignan, así como a mis compañeros: Dr. Alex Badev, Romain Heuguet, Marine Beaumale e Hidefumi Takahashi.

Un saludo afectuoso al Dr. Luis Fuentes (CIMAV – México) por sus consejos y colaboración cada vez que le reclamo y, sobre todo, por su simpatía y amistad.

También al Prof. Kenneth Poeppelmeier (Northwestern University), siempre dispuesto a ayudarme.

Agradezco a todas las personas que me han aportado alguna medida o imagen, tanto en el "CAI de medidas físicas" como en el "CAI de difracción de rayos X" y en el Centro Nacional de Microscopía Electrónica (CNME): Dr. Julio Romero, Dr. Julián Velázquez, Dr. Emilio Matesanz, Dr. Esteban Urones, Dr. Adrián Gómez, Eugenio Baldonedo, Ana Vicente, Alfonso Rodríguez. Tampoco me olvido de los responsables y científicos de línea española BM25A del sincrotrón ESRF de Grenoble, por el tiempo de medida concedido y la ayuda con la preparación y medida de las muestras.

A mis compañeros, con los que he compartido tantos momentos durante estos años: Ivan, Sourav Marik, Tedy, Dani, Subakti, Rafa, Paola, César, Sourav Laha, Tamil, Elena Solana, Rebeca, Mahmoud, Juliana, Álvaro, Elena Mesa y Lucía. He tenido la suerte de poder interaccionar en un ambiente intercultural, lo que me ha ayudado a enriquecerme tanto profesionalmente como personalmente. Espero seguir contando con la amistad de todos vosotros durante muchos años

Agradecimientos para mi gran equipo de "síntesis por microondas", y no me refiero al MILESTONE Ethos One (¡que también!) sino a los estudiantes de máster, licenciatura o grado con los que he trabajado codo con codo. Ha sido un orgullo compartir lo poco que sé con ellos y además, poder aprender muchas cosas gracias a ellos (p.ej. como evitar explosiones en el reactor de teflón, ¿verdad Bea?): Beatriz Molero (The University of Calgary), Alex Gómez (San Pablo CEU), Irene Herrero (UCM), Julia Gutiérrez (UCM), Jesús Espíndola (UNAM), Julian Truchot (Marseille Université), Jorge Val (UCM), Pablo Salcedo (UCM), Raquel Villamor (UCM).

A mis amigos, por "la química" especial que siempre nos ha unido, en especial a Mariana, Ángel, Maider, Sara, Isa, Isa Guti y Bea.

A mis abuelos y tíos, por ser mis Ángeles de la Guarda. Siempre os sentiré conmigo y tendré en cuenta vuestras enseñanzas. En cada logro u objetivo que vaya cumpliendo brindaré por vosotros, por supuesto, en "copa grande".

A Ana, no sólo por apoyarme incondicionalmente en todo. No sólo por su amor, comprensión, paciencia, por estar siempre cerca de mí. No se conforma con hacerme sonreír cada día, también tiene que aportar su granito de arena cada vez que puede, ya sea en el diseño de la portada de mi tesis, en el cartel de las Paces o en cualquier cosa. No podría encontrar palabras para agradecerte todo lo que haces por mí, simplemente, eres la mejor.

Por último, a mi familia. A mi hermana Rosa Mª y a mis padres. Por estar siempre ahí. Por haberme enseñado que para conseguir lo que uno desea hay que esforzarse. Por su ejemplo de superación ante cualquier adversidad. Por todos los valores que me habéis transmitido. Por haber creído siempre en mí. Por ser esa primera chispa que enciende cada día mi Operación 2000.

Index

Resumen

Introducción

La utilización de la radiación microondas como fuente de calentamiento es una alternativa prometedora en la síntesis de materiales inorgánicos. Al emplear este tipo de síntesis se produce una reducción considerable de la temperatura de reacción y del tiempo de procesado, lo que provoca un "efecto secundario" positivo ya que, generalmente, se reduce de manera eficiente el crecimiento de las partículas durante la reacción y el tamaño de dichas partículas. Esto no sólo es interesante en aplicaciones potenciales de materiales nanométricos debido a sus nuevas funcionalidades, sino que también facilita el estudio de los aspectos fundamentales de la física de la materia condensada en la nano-escala. Por lo general no se encuentran desventajas cualitativas significativas en los materiales sintetizados por microondas, en términos de cristalinidad y propiedades físicas. En algunos casos incluso se producen mejoras cuantitativas en las propiedades de los materiales e interesantes morfologías de las partículas.

La síntesis asistida por microondas puede considerarse un método de "Fast Chemistry" ("Química rápida"). Por otra parte, teniendo en cuenta los requisitos de bajo consumo de energía, la técnica es compatible con la mayoría de los principios de la "Green Chemistry" o "Química Verde":[1] utiliza reactivos y disolventes que no son tóxicos ni peligrosos, proporciona una alta eficiencia en términos de consumo de energía frente al rendimiento del proceso, y se puede llevar a cabo una monitorización fácil del proceso para prevenir la contaminación.

La preparación de óxidos mediante síntesis asistida por microondas en el estado sólido está normalmente limitada a la obtención de composiciones "simples" (hasta óxidos ternarios), pero la posibilidad de combinar las microondas con otros métodos tales como la síntesis hidrotermal , el método sol- gel, o la combustión permite un mejor control estequiométrico de fases más

complejas. En particular, la combinación del calentamiento por microondas con la síntesis solvotermal puede dar lugar a fases metaestables y nuevas morfologías. La síntesis de microondas – monomodal empleando una cavidad TE_{10p} permite la separación de las componentes magnética y eléctrica de la onda y proporciona un control preciso de la temperatura, necesitando tiempos de procesado mucho más cortos (minutos).

Aportaciones de la tesis

En esta tesis se analiza la interacción de las microondas con diferentes tipos de materia sólida, incluyendo reactivos, disolventes y productos, proporcionando una visión global sobre la naturaleza del calentamiento por microondas y estableciendo las diferencias existentes con respecto a la calefacción convencional.

Se ha demostrado que es posible preparar una amplia gama de materiales mediante técnicas de microondas (síntesis asistida por microondas en estado sólido, microondas monomodal con una cavidad TE_{10p} y microondas - hidrotermal). Los óxidos preparados se engloban en materiales ferromagnéticos, ferroeléctricos, dieléctricos o multiferroicos, con una gran diversidad estructural: perovskitas, pirocloros, holanditas, fluoritas y estructuras unidimensionales.

Síntesis asistida por microondas en estado sólido

La síntesis asistida por microondas en estado sólido es un método eficaz para la producción de perovskitas y pirocloros. Mediante este método se han preparado $LaMO_3$ (M = metal de transición), con estructura perovskita. Estos materiales pueden ser utilizados en diferentes aplicaciones tecnológicas: componentes de pilas de combustible de óxido sólido (SOFC), membranas de separación, materiales magneto-ópticos o magneto-resistentes, o como sustratos para películas delgadas. [2, 3] Dentro de esta familia de materiales, el $LaCoO_3$ se considera una "cobaltita modelo" en cuanto a la existencia de una transición de estados de spin [4] inducidos térmicamente. En este trabajo, se propone que hay

una transición de spines que puede ocurrir gradualmente (bajo spin → spin intermedio → alto spin). La competencia entre los diferentes estados de spin será responsable de las propiedades eléctricas y magnéticas del $LaCoO_3$. Se han comparado las propiedades magnéticas y dieléctricas de la muestra preparada por microondas con una muestra preparada por el método cerámico, de esta manera se puede estudiar el efecto de los defectos por vacantes de oxígeno, que va a estar relacionado con el tipo de síntesis empleada. La síntesis por el método cerámico tiene lugar en condiciones de equilibrio térmico por difusión, mientras que empleando radiación microondas se está lejos de este equilibrio.

Por otra parte, se han sintetizado perovskitas $(RE)CrO_3$ (RE = Tierra Rara) empleando este método de síntesis asistida por microondas en estado sólido. Actualmente, las cromitas son objeto de intensa investigación, existe un interés particular en las especies con tierras raras donde es posible que haya un acoplamiento magneto – eléctrico.[5] Se ha llegado a afirmar que algunas cromitas de tierras raras podrían pertenecer a una nueva familia de materiales multiferroicos (ferroeléctricos y antiferromagnéticos).[6] Sin embargo, en este trabajo no se ha encontrado ninguna evidencia de grupo espacial no centrosimétrico ni ferroelectricidad asociada a estos materiales (requisitos fundamentales). Se puede decir que las cromitas de tierras raras sintetizadas por microondas no pueden ser clasificadas como materiales magneto- eléctricos o multiferroicos.

El tercer grupo de materiales producidos por esta vía han sido los pirocloros de tierras raras $(RE)_2Ti_2O_7$ (RE = Gd , Ho), materiales que pueden poseer una amplia gama propiedades funcionales tales como la conductividad iónica, propiedades magnéticas exóticas y multiferroicidad.[7] Con el fin de estudiar la presencia de defectos catiónicos "anti-site" y su influencia con la temperatura, se han realizado experimentos de difracción de rayos X en sincrotrón.[8] La concentración de defectos encontrada fue de 3.6 % para el $Gd_2Ti_2O_7$ y de 2.4 % para el $Ho_2Ti_2O_7$, ambos a 1100 ^oC. Se observa una disminución de la concentración de defectos "anti-site" con el aumento de la

temperatura. En los pirocloros, la interacción antiferromagnética puede conducir a una fuerte frustración magnética. En ambas muestras estudiadas se observó una débil componente ferromagnética a la temperatura de 1.7 K. Mediante espectroscopia de impedancia se ha observado que la muestra de $Gd_2Ti_2O_7$ presenta una conductividad iónica mucho mayor que en el caso de la muestra de $Ho_2Ti_2O_7$.

Síntesis empleando un microondas monomodal

Se ha sintetizado la holandita $Ba_{1.2}Mn_8O_{16}$ empleando la componente magnética de la microondas en un equipo monomodal y se han estudiado sus propiedades termoeléctricas y magnéticas. Es bien conocido que los materiales que contienen valencia mixta Mn^{3+}/Mn^{4+} exhiben propiedades físicas de interés relacionadas con el hecho de que los diferentes estados de oxidación de Mn poseen diferente momento magnético.[9-11] El material sintetizado presenta un comportamiento semiconductor, en consonancia con la presencia de un intervalo de "hopping" hasta ≈ 400 K. Por encima de esta temperatura, las muestras presentan una transición estructural (monoclínica – monoclínica) y el transporte de carga sigue una conductividad linear tipo Arrhenius. El coeficiente de Seebeck es negativo y se vuelve prácticamente constante por encima de la temperatura de la transición.

Síntesis hidrotermal asistida por microondas

En los últimos años, las soluciones sólidas basadas en la ceria dopada con tierras raras $Ce_{1-x}RE_xO_{2-\delta}$ han sido consideradas candidatos prometedores para servir como electrolitos en pilas de combustible de óxido sólido de temperatura intermedia (IT – SOFC), ya que su conductividad de iones de oxígeno en el rango de temperatura intermedia (500 - 800 ^oC) es más elevada que la de la circonia estabilizada con itrio (YSZ).[12] Un problema importante para poder aplicar estos materiales como electrolitos SOFC es la resistencia de la frontera de grano en la cerámica (GB), que es por lo general mayor o está en el mismo rango de resistencia que el grano. Esto implica que las fronteras de grano

constituyen barreras para el transporte de la carga iónica y de hecho, a menudo actúan como barreras Schottky.[13, 14] Por lo tanto, la reducción de la resistividad de la barrera, es decir, la reducción de la resistencia GB, es de vital importancia para que estos electrolitos policristalinos se puedan aplicar en IT - SOFCs. Mediante la síntesis de microondas - hidrotermal se han preparado: $Ce_{0.85}RE_{0.15}O_{1.925}$ (RE = Gd, Sm), $Ce_{0.8}(Gd_{0.1}Sm_{0.1})O_{1.9}$, $Ce_{0.8}Sm_{0.18}Ca_{0.02}O_{1.9-\delta}$ y $CeO_{2-\delta}$. La deconvolución de la conductividad iónica de la frontera de grano y del grano en cerámicas sinterizadas, revela que la muestra de ceria dopada con Sm - Ca ($Ce_{0.8}Sm_{0.18}Ca_{0.02}O_{1.9-\delta}$) exhibe la mayor conductividad iónica de la frontera de grano y también la más alta conductividad iónica en el grano. Dicha muestra se ha sinterizado empleando el equipo de microondas-monomodal. Los valores de resistividad obtenidos para la muestra sinterizada por microondas durante 5 minutos (1450 ^{o}C) son similares a los valores de la muestra sinterizada por el método convencional (8h, 1450 ^{o}C).

El $BiFeO_3$ es un material multiferroico magnetoeléctrico que presenta un gran interés en el campo de la espintrónica, ya que sus condiciones de ferroeléctrico y antiferromagnético tienen lugar simultáneamente a temperatura ambiente.[15, 16] En este trabajo se presenta la caracterización estructural y microestructural de una muestra de $BiFeO_3$ obtenida por microondas-hidrotermal. El material, de elevada pureza y cristalinidad, presenta el grupo espacial R3c. Las propiedades magnéticas de la muestra son similares a las descritas en la literatura para $BiFeO_3$ obtenidos por métodos convencionales. Se ha observado un ferromagnetismo débil debido a un posible canteo de los espines. Mediante espectroscopia de impedancia se aprecia que la resistividad del grano es muy elevada, lo que confirma la naturaleza aislante del material.

Los óxidos de vanadio, con nanoestructuras unidimensionales (1D) despiertan un gran interés debido a sus diversas propiedades físico-químicas. Estos óxidos pueden encontrarse en un gran número de estructuras diferentes y presentan una amplia gama de estados de oxidación (de +2 a +5). Son excelentes materiales como electrodos en baterías de litio recargables debido a

su gran capacidad específica, buena ciclabilidad y bajo coste. El $H_2V_3O_8$ es uno de los más atractivos debido a sus interesantes propiedades electroquímicas. En este trabajo se ha sintetizado este material en forma de nanocintas y se ha resuelto su estructura cristalina mediante experimentos de difracción de rayos X en sincrotrón y de HRTEM. Dicha estructura se caracteriza por un entramado en dos dimensiones (capas V_3O_8) formado por 3 tipos de poliedros: dos octaedros VO_6 y una pirámide de base cuadrada distorsionada VO_5. Los primeros trabajos acerca de este material muestran la inserción de hasta 2.5 unidades de Li/fórmula en un intervalo de 4 – 1.5 V, proporcionando una capacidad específica de 240 mAh g^{-1}. Respecto a la muestra preparada por microondas-hidrotermal, en las condiciones de medida C/20, se obtiene una capacidad inicial de ≈ 400 $mAhg^{-1}$ en el intervalo de 3.75 – 1.5 V. Hay una pérdida significativa de capacidad en el primer ciclo, pero después se mantiene constante en 300 $mAhg^{-1}$. Además, se ha mostrado la reducción completa a V^{3+} en la descarga de la batería bajando hasta 1 V por primera vez; se consigue así un aumento significativo de la capacidad (498 mAh g^{-1}). Todos estos valores obtenidos en el material sintetizado por microondas son mucho más altos que los valores que aparecen en la literatura. Es un claro ejemplo de la mejora de una propiedad de un nanomaterial sintetizado mediante radiación de microondas.

Conclusiones

Se han sintetizado numerosos materiales inorgánicos mediante el uso de las diferentes técnicas de microondas, dichos materiales abarcan un amplio rango en cuanto a su composición, estructuras o propiedades. Además, la extensa variedad de posibles combinaciones de técnicas de microondas abre nuevas oportunidades para la preparación de nanopartículas inorgánicas y nanoestructuras. Este hecho va a permitir el ajuste de las propiedades físicas y químicas de los materiales a un nivel nanométrico, a través de la variación del tamaño de partícula y de su morfología.

Referencias

1. Ryan, M. A.; Tinnesand, M., *Introduction to Green Chemistry*. ACS: Washington DC, 2002; p 68.

2. Backhaus-Ricoult, M., SOFC - A playground for solid state chemistry. *Solid State Sciences* **2008,** 10, (6), 670-688.

3. Petrovic, S.; Terlecki-Baricevic, A.; Karanovic, L.; Kirilov-Stefanov, P.; Zdujic, M.; Dondur, V.; Paneva, D.; Mitov, I.; Rakic, V., $LaMO_3$ (M = Mg, Ti, Fe) perovskite type oxides: Preparation, characterization and catalytic properties in methane deep oxidation. *Applied Catalysis B: Environmental* **2008,** 79, (2), 186-198.

4. Goodenough, J. B., An interpretation of the magnetic properties of the perovskite-type mixed crystals $La_{1-x}Sr_xCoO_3$. *Journal of Physics and Chemistry of Solids* **1958,** 6, (2-3), 287-297.

5. Sardar, K.; Lees, M. R.; Kashtiban, R. J.; Sloan, J.; Walton, R. I., Direct Hydrothermal Synthesis and Physical Properties of Rare-Earth and Yttrium Orthochromite Perovskites. *Chemistry of Materials* **2011,** 23, (1), 48-56.

6. Sahu, J. R.; Serrao, C. R.; Ray, N.; Waghmare, U. V.; Rao, C. N. R., Rare earth chromites: a new family of multiferroics. *Journal of Materials Chemistry* **2007,** 17, (1), 42-44.

7. Greedan, J. E., Geometrically Frustrated Magnetic Materials. In *Functional Oxides*, Bruce, D. W.; O'Hare, D.; Walton, R. I., Eds. Wiley: 2011; pp 41-117.

8. Shlyakhtina, A. V.; Karyagina, O. K.; Shcherbakova, L. G., Order-Disorder Transformations in $Ln_2Ti_2O_7$(Ln = Lu, Yb, Tm, Gd). *Inorganic Materials* **2004,** 40, (1), 59-65.

9. Kuwabara, T.; Isobe, M.; Gotou, H.; Yagi, T.; Nishio-Hamane, D.; Ueda, Y., Synthesis, Structure, and Electromagnetic Properties of Manganese Hollandite, $K_xMn_8O_{16}$. *Journal of the Physical Society of Japan* **2012,** 81, 104701

10. Lan, C.; Gong, J.; Liu, S.; Yang, S., Synthesis and magnetic properties of single-crystalline $Na_{2-x}Mn_8O_{16}$ nanorods. *Nano Express* **2011,** 6, 133.

11. Ishiwata, S.; Bos, J. W. G.; Huang, Q.; Cava, R. J., Structure and magnetic properties of hollandite $Ba_{1.2}Mn_8O_{16}$. *Journal of Physics: Condensed Matter* **2006,** 18, (15), 3745.

12. Brett, D. J. L.; Atkinson, A.; Brandon, N. P.; Skinner, S. J., Intermediate temperature solid oxide fuel cells. *Chemical Society Reviews* **2008,** 37, (8), 1568-1578.

13. Guo, X.; Waser, R., Electrical properties of the grain boundaries of oxygen ion conductors: Acceptor-doped zirconia and ceria. *Progress in Materials Science* **2006,** 51, (2), 151-210.

14. Mahato, N.; Gupta, A.; Balani, K., Doped zirconia and ceria-based electrolytes for solid oxide fuel cells: a review. *Nanomaterials and Energy* **2012,** 1, (1), 27-45.

15. Fuentes-Cobas, L. E.; Matutes-Aquino, J. A.; Fuentes-Montero, M. E.; Buschow, K. H. J., Magnetoelectricity. In *Handbook of Magnetic Materials*, Elsevier: 2011; Vol. 19, pp 129-229.

16. Khomskii, D., Trend: Classifying multiferroics: Mechanisms and effects. *Physics* **2009,** 2, (20).

Abstract

Introduction

The use of microwave irradiation is a promising alternative heat source for the synthesis of inorganic materials. The considerable reduction in reaction temperature and time involved with this recent innovative synthesis technique has the interesting effect that the particle growth during reaction and the resulting particle size of the synthesized products are usually reduced efficiently. This is not only interesting for potential new applications of nano-sized materials due to novel functionalities, but also facilitates studying fundamental aspects of the physics of condensed matter at the nano-scale. Significant qualitative drawbacks in microwave synthesized materials in terms of crystal quality and physical properties are usually not encountered. In some cases even quantitative improvements, novel crystal arrangements and interesting particle shapes can be achieved.

The technique can be regarded a "Fast Chemistry" method. Furthermore, taking into account the low energy requirements, the technique is also consistent with most of the "Green Chemistry" principles:[1] use of non-hazardous reactants and solvents, high efficiency in terms of energy consumption vs. yield, and easy monitoring to prevent pollution.

In order to further minimize the heat exposure and particle growth during synthesis, the microwave method can be combined with other techniques such as hydrothermal, sol-gel or combustion synthesis. Furthermore, single-mode microwave synthesis (using a TE_{10p} cavity) is an interesting field of study, because it allows separating the magnetic and electric components of the microwave and provides an accurate control of the temperature together with much shorter reaction and processing times.

Contributions of this thesis

In this thesis the interaction of microwaves with different types of solid matter including reactants, solvents and final product materials is discussed, providing a comprehensive overview over the nature of microwave heating and the differences to conventional heating.

The synthesis of a wide range of oxide materials is shown to be feasible by various microwave techniques: solid-state microwave synthesis, single-mode microwave using a TE_{10p} cavity and microwave-hydrothermal synthesis. The materials synthesized include ferromagnetic, ferroelectric, dielectric and multiferroic systems, but also a plethora of structure-types: perovskite, pyrochlore, hollandite, fluorite and one-dimensional structures.

Solid – state microwave synthesis

It is well-known that solid state - microwave assisted synthesis is an effective method for the production of perovskites and pyrochlores. $LaMO_3$ (M= transition metal) perovskite can be easily prepared by this method. These materials can be used in different technological applications such as components for solid oxide fuel cells (SOFCs), separation membranes, magneto-optical or magnetoresistance materials and substrates for thin films.[2, 3] Among the $LaMO_3$ family, $LaCoO_3$ may be particularly interesting, because it is a model compound for many cobaltites in terms of the thermally induced spin-state transition.[4] In this work it has been argued that there is a spin transition that may occur gradually, involving spin – state coexistence (low spin → intermediate spin → high spin). This leads to a competition between the different spin – states that will be responsible for the electrical and magnetic properties of $LaCoO_3$ materials. The magnetic and dielectric properties were compared to conventionally synthesized $LaCoO_3$, which allows studying the effect of oxygen vacancy defects. The oxygen vacancy defect concentration is naturally different in different types of synthesis, where conventional synthesis occurs in thermal equilibrium by diffusion and in microwaves it occurs far from equilibrium conditions.

Furthermore, $(RE)CrO_3$ (RE = Rare Earth) materials have been synthesized by the solid-state microwave method. Chromites in general are under intense investigation nowadays, where the particular interest into the RE species is debited to potential magneto-electric coupling.[5] Initial studies had claimed that certain rare-earth chromites belong to a new family of ferroelectric and antiferromagnetic multiferroics.[6] However, no indications for a non-centrosymmetric space-group and associated ferroelectricity were detected from XRD pattern, Raman spectroscopy and temperature dependent dielectric permittivity data. Microwave synthesized $(RE)CrO_3$ chromites may therefore not be classified as magneto-electric or multiferroic materials.

$(RE)_2Ti_2O_7$ pyrochlore oxide compounds are materials that can possess a wide range functional properties such as ionic conductivity, exotic magnetic properties and multiferroic behaviour.[7] $(RE)_2Ti_2O_7$ (RE = Gd, Ho) were prepared by solid-state microwave synthesis. Synchrotron X-ray diffraction experiments were carried out in order to study cation anti-site defects in pyrochlore $(RE)_2Ti_2O_7$ (RE = Gd, Ho) and the temperature influence of this effect.[8] An antisite defect concentration of 3.6 % for $Gd_2Ti_2O_7$ and 2.4 % for $Ho_2Ti_2O_7$ at 1100 ^oC were obtained, where the antisite defect concentration decreases with the increase of temperature. In pyrochlores, antiferromagnetic interaction can lead to a strong magnetic frustration. In both studied samples, a weak ferromagnetic component was observed at 1.7 K. Impedance spectroscopy reveals that $Gd_2Ti_2O_7$ shows higher ionic conductivity as compared to $Ho_2Ti_2O_7$.

Single - mode microwave synthesis

$Ba_{1.2}Mn_8O_{16}$ hollandite rods have been directly prepared in a few minutes by using the magnetic component of the microwave in a novel single-mode microwave set-up. Thermoelectric and magnetic properties of this material have been studied in this work. It is well-known that mixed-valence Mn^{3+}/Mn^{4+} materials exhibit interesting physical properties related to the fact that different oxidation states of Mn possess different magnetic moments.[9-11]

The single-mode microwave synthesized $Ba_{1.2}Mn_8O_{16}$ hollandite presents semiconducting behaviour and resistance vs temperature trends consistent with one-dimensional variable-range hopping up to ≈ 400 K. Above this temperature, samples undergo a structural transition (monoclinic – monoclinic) and charge transport is now by linear Arrhenius activated conduction. The Seebeck coefficient is negative and has a plateau above the transition temperature.

Microwave - hydrothermal synthesis

Ceria-based solid solutions have been regarded promising candidates to serve as electrolytes in intermediate temperature SOFCs (IT – SOFC) since their oxygen ion conductivities are higher than that of yttria stabilized zirconia YSZ in the intermediate temperature range (500 – 800 ^oC).[12] One major problem for the application of polycrystalline oxygen ionic conductors as SOFC electrolytes is the ceramic grain boundary (GB) resistance, which is usually larger than or in the same range as the bulk resistance although GB areas are expected to be thin. This implies that GBs constitute barriers for ionic charge transport and they indeed often act as Schottky barriers.[13, 14] Therefore, the reduction of the barrier height, i.e. the reduction of the GB resistance, is of uppermost importance to facilitate application of polycrystalline electrolytes. Microwave-hydrothermal synthesis of $Ce_{0.85}RE_{0.15}O_{1.925}$ (RE = Gd, Sm), $Ce_{0.8}(Gd_{0.1}Sm_{0.1})O_{1.9}$, $Ce_{0.8}Sm_{0.18}Ca_{0.02}O_{1.9-\delta}$ and $CeO_{2-\delta}$ nanopowders was performed. Deconvolution of GB and intrinsic bulk ionic conductivity in sintered ceramics revealed that the Sm - Ca doped ceria $Ce_{0.8}Sm_{0.18}Ca_{0.02}O_{1.9-\delta}$ exhibits the highest GB ionic conductivity. The highest intrinsic bulk ionic conductivity was detected for the $Ce_{0.8}Sm_{0.18}Ca_{0.02}O_{1.9-\delta}$ ceramic as well. Single mode microwave sintering was performed for $Ce_{0.8}Sm_{0.18}Ca_{0.02}O_{1.9-\delta}$ and the obtained results for 5 minutes microwave sintered sample reveals similar resistivity values as the conventionally sintered samples.

$BiFeO_3$ is an interesting magnetoelectric multiferroic because its ferroelectric and antiferromagnetic orderings take place concurrently at room

temperature.[15, 16] The structural and microstructural characterization of hydrothermal – microwave synthesized $BiFeO_3$ is presented. The sample showed phase purity and crystallizes in the expected *R3c* space group. Magnetic properties of the sample are similar to reports in the literature for samples obtained by conventional methods, including the occurrence of a weak ferromagnetism possibly due to the spin - canting. Impedance spectroscopy demonstrates that the bulk resistance of the sample is high confirming insulating nature of the material.

Vanadium oxides, with one-dimensional (1D) nanostructures have attracted great attention due to their diverse physicochemical properties. These oxides present a large number of different structures and exist in a range of single and mixed vanadium oxidation states (from +2 to +5). They are excellent electrode materials for rechargeable lithium batteries, due to their large specific capacity, good cyclability and low cost. $H_2V_3O_8$ is one of the most attractive vanadium oxide hidrates due to its interesting electrochemical properties. Early works reported the insertion of up to 2.5 Li/formula unit in the 4 - 1.5 V range corresponding to a specific capacity of 240 mAh g^{-1}. Nanobelts $H_2V_3O_8$ have been obtained by the microwave-hydrothermal method. The crystallographic structure of the phase, obtained in this work by synchrotron X-ray diffraction experiments and HRTEM, is characterized as a nearly two-dimensional framework (V_3O_8 layers) comprised of 3 kinds of polyhedra: 2 VO_6 octahedra and a VO_5 distorted square based pyramid.At C/20 rate an initial capacity of ≈ 400 mAh g^{-1} is developed in the 3.75 - 1.5 V range. After a significant capacity loss in the first cycle, a capacity of ≈ 300 mAh g^{-1} is maintained upon cycling. Full reduction to V^{3+} has been observed for the first time by discharging Li cells down to 1 V with $H_2V_3O_8$ serving as a cathode material; a significant increase of reversible capacity to 498 mAh g^{-1} is thereby obtained. All these obtained values for microwave synthesized nanobelts are much higher that the literature values. This is a clear example of an improved property after synthesizing a material using microwave irradiation.

Conclusions

The preparation of inorganic oxide materials by using the different microwave techniques is promising, from the compositional, structural or physical aspect. Furthermore, the broad variety of possible combinations of microwave techniques opens up new opportunities for the preparation of inorganic nanoparticles and nanostructures. This allows the possibility to tune the physical and chemical properties of nanoscale materials through varying the crystal sizes and shapes by varying the microwave synthesis conditions.

References

1. Ryan, M. A.; Tinnesand, M., *Introduction to Green Chemistry*. ACS: Washington DC, 2002; p 68.

2. Backhaus-Ricoult, M., SOFC - A playground for solid state chemistry. *Solid State Sciences* **2008,** 10, (6), 670-688.

3. Petrovic, S.; Terlecki-Baricevic, A.; Karanovic, L.; Kirilov-Stefanov, P.; Zdujic, M.; Dondur, V.; Paneva, D.; Mitov, I.; Rakic, V., $LaMO_3$ (M = Mg, Ti, Fe) perovskite type oxides: Preparation, characterization and catalytic properties in methane deep oxidation. *Applied Catalysis B: Environmental* **2008,** 79, (2), 186-198.

4. Goodenough, J. B., An interpretation of the magnetic properties of the perovskite-type mixed crystals $La_{1-x}Sr_xCoO_3$. *Journal of Physics and Chemistry of Solids* **1958,** 6, (2-3), 287-297.

5. Sardar, K.; Lees, M. R.; Kashtiban, R. J.; Sloan, J.; Walton, R. I., Direct Hydrothermal Synthesis and Physical Properties of Rare-Earth and Yttrium Orthochromite Perovskites. *Chemistry of Materials* **2011,** 23, (1), 48-56.

6. Sahu, J. R.; Serrao, C. R.; Ray, N.; Waghmare, U. V.; Rao, C. N. R., Rare earth chromites: a new family of multiferroics. *Journal of Materials Chemistry* **2007,** 17, (1), 42-44.

7. Greedan, J. E., Geometrically Frustrated Magnetic Materials. In *Functional Oxides*, Bruce, D. W.; O'Hare, D.; Walton, R. I., Eds. Wiley: 2011; pp 41-117.

8. Shlyakhtina, A. V.; Karyagina, O. K.; Shcherbakova, L. G., Order-Disorder Transformations in $Ln_2Ti_2O_7$(Ln = Lu, Yb, Tm, Gd). *Inorganic Materials* **2004,** 40, (1), 59-65.

9. Kuwabara, T.; Isobe, M.; Gotou, H.; Yagi, T.; Nishio-Hamane, D.; Ueda, Y., Synthesis, Structure, and Electromagnetic Properties of Manganese Hollandite, $K_xMn_8O_{16}$. *Journal of the Physical Society of Japan* **2012,** 81, 104701

10. Lan, C.; Gong, J.; Liu, S.; Yang, S., Synthesis and magnetic properties of single-crystalline $Na_{2-x}Mn_8O_{16}$ nanorods. *Nano Express* **2011,** 6, 133.

11. Ishiwata, S.; Bos, J. W. G.; Huang, Q.; Cava, R. J., Structure and magnetic properties of hollandite $Ba_{1.2}Mn_8O_{16}$. *Journal of Physics: Condensed Matter* **2006,** 18, (15), 3745.

12. Brett, D. J. L.; Atkinson, A.; Brandon, N. P.; Skinner, S. J., Intermediate temperature solid oxide fuel cells. *Chemical Society Reviews* **2008,** 37, (8), 1568-1578.

13. Guo, X.; Waser, R., Electrical properties of the grain boundaries of oxygen ion conductors: Acceptor-doped zirconia and ceria. *Progress in Materials Science* **2006,** 51, (2), 151-210.

14. Mahato, N.; Gupta, A.; Balani, K., Doped zirconia and ceria-based electrolytes for solid oxide fuel cells: a review. *Nanomaterials and Energy* **2012,** 1, (1), 27-45.

15. Fuentes-Cobas, L. E.; Matutes-Aquino, J. A.; Fuentes-Montero, M. E.; Buschow, K. H. J., Magnetoelectricity. In *Handbook of Magnetic Materials*, Elsevier: 2011; Vol. 19, pp 129-229.

16. Khomskii, D., Trend: Classifying multiferroics: Mechanisms and effects. *Physics* **2009,** 2, (20).

1. *INTRODUCTION*

1.1. General Aspects.

The well-established "ceramic method" is the usual procedure for the preparation of most non molecular inorganic materials. The method is especially well-suited for oxides since reactions are carried out in air at ambient pressure. The procedure consists in the homogeneous mixing of the stoichiometric amounts of solid reactants followed by heating them in an appropriate atmosphere at elevated temperatures for long periods of time (often from 1000 ^{o}C to 1600 ^{o}C and several hours or days). This process needs to be repeated as many times as needed in order to get a pure phase. There is no doubt about the usefulness and easiness of this universal method of synthesis which works in thermodynamic equilibrium conditions, but there are some intrinsic drawbacks such as the need for high temperatures to accelerate diffusion -which prevents metastable phases to appear-, the volatility of some reactants, the need of regrinding several times and the high energy and time consumptions.[1,2]

On these grounds, there is a permanent stimulus for searching alternative routes such as the so-called "Soft Chemistry" methods, pioneered by Rouxel and Livage in the 70's, where the reactions are performed at moderate temperature, preferably at room temperature but always below 500 ^{o}C.[3] The term "Soft Chemistry" has historically been used to describe several types of low-temperature solid-solid transformations such as intercalation/ deintercalation, ion exchange, hydrolysis and redox reactions. A common

feature of soft chemical reactions is the possibility to produce metastable compounds. [4,5]

Another class of alternative synthesis methods for inorganic solids are the so-called "Fast Chemistry" techniques, which enhance the diffusion rate of the ceramic precursors by several orders of magnitude, reaction time is shortened –and often lower reaction temperatures are feasible. Such techniques include combustion synthesis, sonochemistry, spark plasma sintering and the procedures that are the object of this thesis: microwave-assisted methods of synthesis. It will be shown that with the latter techniques combined with the hydrothermal synthesis technique it is possible to induce interesting changes in particle morphology and sizes.

Some of the "Fast Chemistry" processes, mainly microwave-assisted techniques, are understood to be more environmentally friendly, i.e. requiring less energy than conventional processes. Taking into account the energy requirements of the process and finding ways to minimize the energy are important considerations in "Green chemistry" or "sustainable chemistry". This is considered a new philosophy of chemical research and engineering that encourages the utilization of a set of principles that reduces or eliminates the use or generation of hazardous substances in the design, manufacture, and application of chemical products.[6, 7, 8] In 2002, The American Chemical Society monograph on Green Chemistry recommended to "use methods that minimize the energy required for a reaction to take place. For example, some reactions can be accelerated by using catalysts or microwave radiation and concomitantly much less energy is needed in the overall process".[9]

From a more general aspect, green chemistry offers an opportunity to improve public perception of nanoscience, as this approach is relatively easy to explain and can be used to convey a responsible attitude toward the development of this new technology. Therefore, green chemistry can play a prominent role in guiding the development of nanotechnology to provide the maximum benefit for society and the environment.[10]

1.2. History: Electromagnetic Radiation and Microwaves.

Although the first thorough scientific discussion of electricity and magnetism by William Gilbert (1544-1603) dates back to the year 1600, the connection between the two was developed only much later in the comprehensive theory of electromagnetism by Scottish physicist James Clerk Maxwell (1831-1879).[11, 12] This theory paved the way for the discovery of radio-waves (frequencies from 300 GHz to as low as 3 kHz) and micro-waves (frequencies between 300 MHz - 300 GHz).

During the 1860s James Clerk Maxwell devoted several years to the problem of electromagnetism, and published his results in their complete form in 1873.[13] At the time few physicists could understand Maxwell's work, but in the following years scientists around the world recognized that Maxwell had written down the essential laws of electrodynamics and the principles of how the electromagnetic force operates.[12] Today Maxwell's discovery is usually expressed in four short equations called Maxwell's Equations. These equations permit the existence of invisible electromagnetic waves of any wavelength. In a series of experiments beginning in 1886, the German physicist Heinrich Hertz (1857-1894) succeeded to create electromagnetic waves with an electric spark, transmitted to the other end of his laboratory, and made them produce another smaller spark at a receiver.[14] In the following, throughout the 1920-30s, scientists and engineers began experiments with what they called "ultra-short waves" or "micro-waves."

The first simple magnetron was developed in 1920 by Albert Hull at General Electric's Research Laboratories (Schenectady, New York) during his working on the magnetic control of vacuum tubes.[15] In 1924, Czech physicist August Žáček (1886–1961) and German physicist Erich Habann (1892–1968) independently discovered that the magnetron could generate waves of 100 megahertz to 1 gigahertz.[16, 17] Since there were no commercial applications of these waves, they were used mostly in the laboratory until the beginning of World War II (1939-1945). The 'resonant' cavity magnetron variant of the earlier

magnetron tube was invented by John Randall and Harry Boot in 1940 at the University of Birmingham, England. The high power of pulses from the cavity magnetron made centimeter-band radar practical, with shorter wavelength radars allowing detection of smaller objects.[18] The compact cavity magnetron tube drastically reduced the size of radar sets so that they could be installed in anti-submarine aircraft and escort ships.

Six years later, Percy LeBaron Spencer, an American engineer working on magnetrons for the Raytheon Company, accidentally discovered the rapid effect of microwaves on heating a chocolate bar and after some proofs being made with other kinds of food it was realized that microwave cooking was feasible and the path for a new kind of domestic furnaces (Figure 1.1), nowadays of general use, was opened.[19]

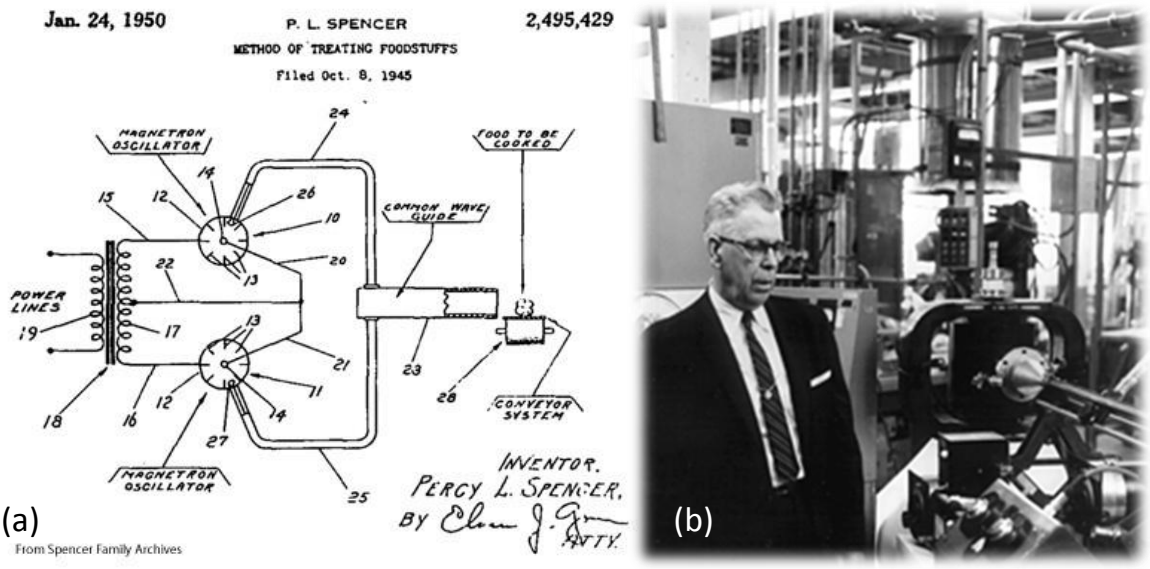

Figure 1.1. a) Original Microwave Oven Patent, b) Spencer in front of early microwave equipment. (Pictures taken from http://www.smecc.org/microwave_oven.htm, the material available through this site may be freely used for attributed noncommercial educational purposes only)

Investigation into the industrial applications for microwave energy began in the 1950s and has continued to the present. It was not until 1975 that the heating effect of microwaves on ceramic materials was observed, described and studied.[20] The effects on microwave irradiation in organic synthesis were not explored until the mid of 1980s, the two first papers were published in 1986

and many organic chemist have since discovered the benefits of using microwave energy to drive synthetic reactions.[21, 22] Microwave-assisted synthesis flourished firstly in organic and pharmaceutics industry but in solid state chemistry and materials science it is still in its beginnings; there are many questions to be solved, yet, such as mechanisms and kinetic aspects of the reactions involved which turns the method into a trial and error one at the current state of knowledge.[23, 24]

1.3. Initial objectives of the work presented.

Objective 1. To discuss the interaction of microwaves with different types of solid matter including reactants, solvents and final product materials, providing a comprehensive overview over the nature of microwave heating and the differences to conventional heating. This summarizes the materials, tools and knowledge necessary to effectively apply microwave energy to the synthetic routes presented later for a large range of different materials.

Objective 2. To study and evaluate different types of microwave-assisted techniques for the synthesis of solids: solid-state, single-mode and solvothermal routes. For each method it is necessary to use a different set up and procedure.

Objective 3. To demonstrate that microwave assisted synthesis is a fast and efficient method to produce solids, in some cases in the nanometric scale, with potential application in different areas: energy materials (components for solid oxide fuel cells SOFC's, lithium batteries), magnetic, ferroelectric or multiferroic materials. It is demonstrated that such materials synthesized by microwaves possess the typical structural and physical properties, in some cases the physical properties are shown to be superior as compared to materials synthesized conventionally.

1.4. Outline.

This thesis is structured in 7 chapters. Chapter 1 and 2 give an introduction to the field. Chapter 3 describes the different experimental techniques that have been employed. The most relevant results are discussed in Chapter 4, 5 and 6, and Chapter 7 constitutes the general conclusions. In each chapter an introduction and conclusion specific to the chapter's topic is presented.

Chapter 1. A brief introduction of general aspects and some comments about the historical evolution of the field studied have been presented above. Furthermore, the motivation of this work was discussed.

Chapter 2. This chapter concerns the fundamentals of microwave irradiation, taking into account the microwave – material interactions and the difference between microwave and conventional heating. Furthermore, it describes the different experimental set-ups that have been employed for the synthesis of materials of potential technological importance.

Chapter 3. The different experimental techniques employed for structural and microstructural characterization of microwave-synthesized materials are described briefly (X-ray diffraction, scanning and transmission electron diffraction techniques). Furthermore, magnetic property measurements, impedance spectroscopy, charge transport and thermal property measurements are described.

Chapter 4. The solid state – microwave synthesis of different Rare Earth perovskites and pyrochlores using a domestic microwave oven is presented. The characterization of structural and physical properties of each one material is presented and discussed.

Chapter 5. The single-mode microwave synthesis of a $Ba_{1.2}Mn_8O_{16}$ hollandite phase by using the magnetic part of the microwave is described, as well as the main results obtained from the characterization of magnetic and transport properties for thermoelectric applications.

Chapter 6. The microwave-hydrothermal synthesis and characterization of three different groups of materials is presented: Rare Earth doped ceria for SOFCs electrolyte, the multiferroic $BiFeO_3$ and the intercalation chemistry of $H_2V_3O_8$ for lithium batteries.

Chapter 7. This chapter contains the general conclusions of this thesis.

1.5. References.

1. Rao, C. N. R.; Gopalakrishnan, J., *New Directions in Solid State Chemistry*. 2nd ed.; Cambridge University Press: 1986; p 568.

2. Smart, L.; Moore, E. A., *Solid State Chemistry: An Introduction*. CRC Press: 2005.

3. Rouxel, J.; Tournoux, M., Chimie douce with solid precursors, past and present. *Solid State Ionics* **1996,** 84, (3-4), 141-149.

4. Schleich, D. M., Chimie douce: Low temperature techniques for synthesizing useful compounds. *Solid State Ionics* **1994,** 70-71, 407-411.

5. Gopalakrishnan, J., Chimie Douce Approaches to the Synthesis of Metastable Oxide Materials. *Chemistry of Materials* **1995,** 7, (7), 1265-1275.

6. Ritter, S. K., Green Chemistry. *Chemical & Engineering News Archive* **2001,** 79, (29), 27-34.

7. Sheldon, R. A.; Arends, I.; Hanefeld, U., *Green Chemistry and Catalysis*. Wiley: 2007.

8. Cavani, F.; Centi, G.; Perathoner, S.; Trifirò, F., *Sustainable Industrial Chemistry*. Wiley: 2009; p 599.

9. Ryan, M. A.; Tinnesand, M., *Introduction to Green Chemistry*. ACS: Washington DC, 2002; p 68.

10. Dahl, J. A.; Maddux, B. L. S.; Hutchison, J. E., Toward Greener Nanosynthesis. *Chemical Reviews* **2007,** 107, (6), 2228-2269.

11. Maxwell, J. C., A Dynamical Theory of the Electromagnetic Field. *Philosophical Transactions of the Royal Society of London* **1865,** 155, 459–512.

12. Forfar, D., *Celebrating the Achievements and Legacy of James Clerk Maxwell: Tuesday 25 Novemeber 2008 at the Royal Society of Edinburgh*. Royal Society of Edinburgh: 2008.

13. Maxwell, J. C., *A Treatise on Electricity and Magnetism*. Cambridge University Press: 1873.

14. Hertz, H., *Über sehr schnelle elektrische Schwingungen: vier Arbeiten (1887-1889)*. Deutsch Harri GmbH: 1971; p 122.

15. Hull, A. H., The effect of a uniform magnetic field on the motion of electrons between coaxial cylinders. *Physical Review* **1921,** 18, (1), 31-57.

16. Fürth, R. H., Obituary: "Prof. August Žáček. *Nature* **1962,** 193, (4816), 625.

17. Habann, E., Eine neue Generatorröhre. *Zeitschrift für Hochfrequenztechnik* **1924,** 24, 115-120.

18. Willshaw, W. E.; Rushforth, L.; Stainsby, A. G.; Latham, R.; Balls, A. W.; King, A. H., The high-power pulsed magnetron: development and design for radar applications. *The Journal of the Institution of Electrical Engineers - Part IIIA: Radiolocation* **1946,** 93, (5), 985.

19. Spencer, P. L. Method of treating foodstuffs. Patent 2,495,429. 1950.

20. Sutton, W. H.; Brooks, M. H.; Chabinsky, I. I., *Microwave processing of materials*. 1988; p 399.

21. Gedye, R.; Smith, F.; Westaway, K.; Ali, H.; Baldisera, L.; Laberge, L.; Rousell, J., The use of microwave ovens for rapid organic synthesis. *Tetrahedron Letters* **1986,** 27, (3), 279-282.

22. Giguere, R. J.; Bray, T. L.; Duncan, S. M.; Majetich, G., Application of commercial microwave ovens to organic synthesis. *Tetrahedron Letters* **1986,** 27, (41), 4945-4948.

23. Hayes, B. L., *Microwave synthesis: chemistry at the speed of light*. CEM Pub.: 2002; p 295.

24. Adam, D., Microwave chemistry: Out of the kitchen. *Nature* **2003,** 421, 571-572.

2. *MICROWAVE & MATTER*

2.1. Microwaves in the electromagnetic spectrum.

Electromagnetic radiation is a kind of pure energy radiated in the form of a wave travelling at the speed of light. An electromagnetic wave is formed by both electric and magnetic fields that oscillate at right angles to each other in the direction of propagation (Figure 2.1).[1]

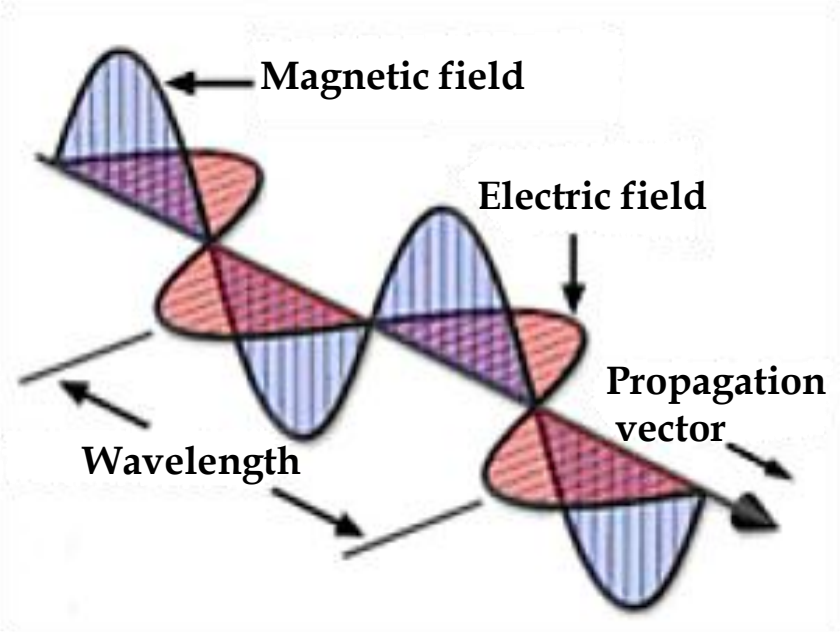

Figure 2.1. Schematic representation of an electromagnetic wave.

The energy in an electromagnetic wave is tied up in the electric and magnetic fields. In general, the energy per unit volume in an alternating electric field (U_{elec}) propagating in vacuum is given by:

$$U_{elec} = \frac{1}{2} \cdot \varepsilon_o \cdot E^2 \qquad [2.1]$$

Where ε_o corresponds to the dielectric permittivity of vacuum and E is the amplitude of the alternating electric field.

In an alternating magnetic field in vacuum, the energy per unit volume is:

$$U_{mag} = \frac{1}{2 \cdot \mu_0} \cdot B^2 \qquad [2.2]$$

μ_o is the magnetic permittivity in vacuum and B is the amplitude of the alternating magnetic field.[2]

For an electromagnetic wave, the energy associated with the electric field is equal to the energy associated with the magnetic field, so the energy density can be written in terms of just one or the other:

$$U = \frac{1}{2} \cdot \varepsilon_o \cdot E^2 = \frac{1}{2 \cdot \mu_0} \cdot B^2 \qquad [2.3]$$

This also implies that the E and B fields are proportional. Rearranging, it is possible to obtain equation 2.4.

$$E = \frac{1}{\sqrt{\varepsilon_0 \mu_0}} \cdot B \qquad [2.4]$$

The constant factor $\frac{1}{\sqrt{\varepsilon_o \mu_o}}$ corresponds to the speed of light in vacuum (c), hence:

$$E = c \cdot B \qquad [2.5]$$

A more common way to handle the energy is to look at how much energy is carried by the wave from one place to another. A good measure of this is the intensity of the wave (S), which is the power that passes perpendicularly through an area divided by the size of this area. The intensity, S, and the energy density are related by a factor of c:

$$S = c \cdot U = c \cdot \left(\frac{1}{2} \cdot \varepsilon_o \cdot E^2 + \frac{1}{2 \cdot \mu_o} \cdot B^2 \right) \qquad [2.6]$$

In the electromagnetic spectrum, the microwave region is located between infrared and radiowave radiation (Figure 2.2). Microwaves have wavelength of 1 m – 1 mm, corresponding to wave frequencies between 0.3 and 300 GHz respectively.

Telecommunication and microwave radar equipment occupy many of the band frequencies in this region. The wavelength at which industrial and domestic microwave apparati operate is standardized to 12.25 cm (2.45 GHz), but other frequency allocations do exist.

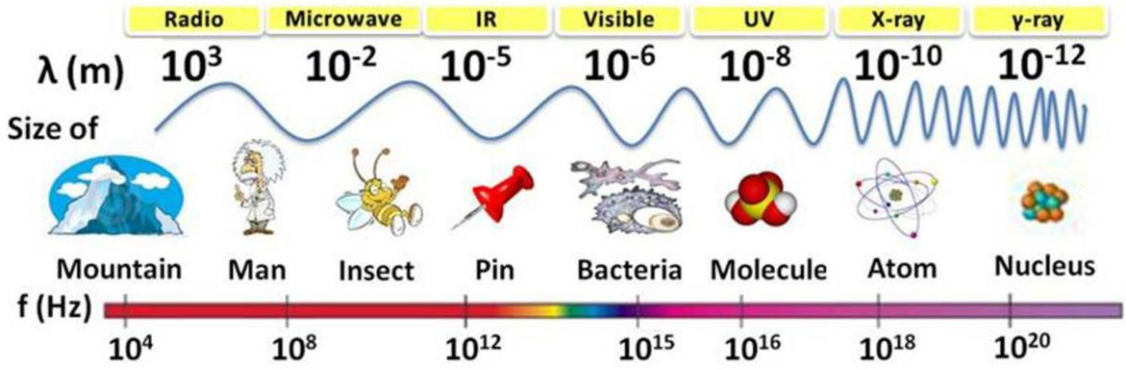

Figure 2.2. Electromagnetic spectrum. Microwave frequencies range between 0.3 and 300 GHz.

The choice of this particular frequency is motivated by several requirements. First of all, any interference with telecommunication, wireless networks or cellular phones has to be avoided. Second, 2.45 GHz is adequate for kitchen microwaves because the associated 12.25 cm wavelength is smaller than the cooking chamber.[3] However, this frequency is not optimized for the heating of water, because liquid water has a higher resonance frequency of 18 GHz, and therefore the most effective conversion of microwave energy into thermal energy in water containing food products would occur at 18 GHz.[3, 4]

The difference between microwave energy and others forms of radiation, for example X-ray or γ-ray, is that microwave energy is non-ionizing - it does not carry enough energy per quantum to ionize atoms or molecules, that is, to completely remove an electron from an atom or molecule, and therefore it provides only thermal activation.[5] At a first glance, microwave heating effects

are quite surprising since radiation ranges in the low-energy zone of the electromagnetic spectrum. As it is shown in Table 2.1, a microwave frequency of 2.45 GHz is equivalent to 0.00001 eV, which is far below the energy corresponding to a weak bond energy such as the hydrogen bonding of 0.21 eV (Table 2.2.).[6]

The microwave heating effect can have up to five different contributions, as described in more detail in *section* 2.2, where the most important contribution may be the dipoles in the material following the alternate electromagnetic field associated to the microwave, i. e. dipolar molecules such as water do rotate, the very fast changing electric field occurs 2.4 x 10^9 times per second and the resistance to that movement generates a considerable amount of heat.[7]

Table 2.1. Energy of common radiation.[6]

	Typical frequency (MHz)	**Quantum energy (eV)**
γ rays	3.0 x 10^{14}	1.24 x 10^6
X-rays	3.0 x 10^{13}	1.24 x 10^5
UV	1.0 x 10^9	4.1
Visible	6.0 x 10^8	2.5
IR	3.0 x 10^6	1.2 x 10^{-2}
Microwaves	2450	1.0 x 10^{-5}
Radio	1	4 x 10^{-9}

Table 2.2. Energy of common chemical bonds.[6]

	Chemical bond energy (eV)
H - OH	5.2
H – CH_3	4.5
H – $NHCH_3$	4.0
H_3C – CH_3	3.8
$PhCH_2$ - COOH	2.4
Hydrogen bonding	0.21

In order to understand the mechanism underlying the microwave heating process, it is necessary to comprehend the different mechanisms of interaction between microwaves and matter.[8-10]

2.2. Condensed Matter Interacting With Microwaves.

There are at least five different contributions that can be part of the heating effect by interactions between microwave and matter:

- Dielectric Polarization
- Dielectric losses (conduction currents)
- Magnetic heating
- Magnetic losses (induction currents)
- Second Order effects

The existence of 5 possible contributions may explain the great efficiency of microwave heating, when in fact several effects may contribute to the heating at the same time. On the other hand, it makes controlled reactions difficult, because it is usually not straight forward to identify to which extent each mechanism contributes to the heating.

2.2.1 Dielectric Polarization Mechanism.

The microwave heating process of polar materials critically depends on both the dielectric permittivity and the dielectric losses. The dielectric permittivity describes the "polarizability" of the material, which reflects the magnitude of the electric dipoles which can rotate with the applied electric field. The overall polarization is termed (α_1), which includes several accumulative components (equation 2.7.): electronic polarization (α_e), atomic polarization (α_a), dipolar polarization (α_p), ionic polarization (α_{ion}) and interfacial polarization (α_{if}):

$$\alpha_1 = \alpha_e + \alpha_a + \alpha_p + \alpha_{ion} + \alpha_{if} \quad [2.7]$$

- Electronic polarization α_e: when the atom is subjected to an external electric field, redistribution of the charges occurs and the atomic electron cloud shifts away from the equilibrium position with respect to the positive nucleus resulting in an induced dipole moment. This effect occurs in all solid matter containing localized electrons.
- Atomic polarization α_a: This is equivalent to the electronic polarization, except that it accounts for the shift of the positively charged atomic cores as a response to the applied electric field. It is usually small as compared to α_e.
- Dipolar polarization α_p: In thermal equilibrium, electric dipoles in the material will be randomly oriented and thus carry no net polarization. An external field can align these dipoles to some extent and thus induces a net polarization to the material. This contribution only exists in polar materials such as dielectrics or polar liquids with a strong ionic character of the chemical bonds.
- Ionic polarization (or ionic displacement) α_{ion}: This occurs due to relative displacements of positive and negative ions from their equilibrium lattice sites. The positively and negatively charged ions in the crystals are displaced spontaneously and the centers of negative and positive charge within one unit cell do not coincide. This constitutes a net dipole moment, which can be switched by high applied electric fields. This effect only occurs in piezo- and ferroelectrics.
- Interfacial polarization α_{if}: Surfaces, grain boundaries, interphase boundaries (including the surface of precipitates) may be polarized, i.e. they contain dipoles which may become oriented to some degree in an external field and thus contribute to the total polarization of the material. Such effects can occur in all kind of condensed matter, but the quantitative contribution to the total polarization is usually small due to the generally small volume fraction of interfaces in bulk material.

Polarization of dielectric materials highly depends on the frequency of the applied electric field as illustrated in Figure 2.3. At low frequencies all dipoles can follow the applied field, but with increasing frequency the different contributions to the overall polarization consecutively "relax out", which involves that the respective dipoles cannot follow the alternating applied electric field anymore and do not polarize. This is reflected in a consecutive reduction of the dielectric permittivity ε'. Atomic and electronic contributions show a double-peak structure in the dielectric permittivity, which occurs when the frequency of the applied field matches the resonance frequency of the switching dipoles. [1, 11-13]

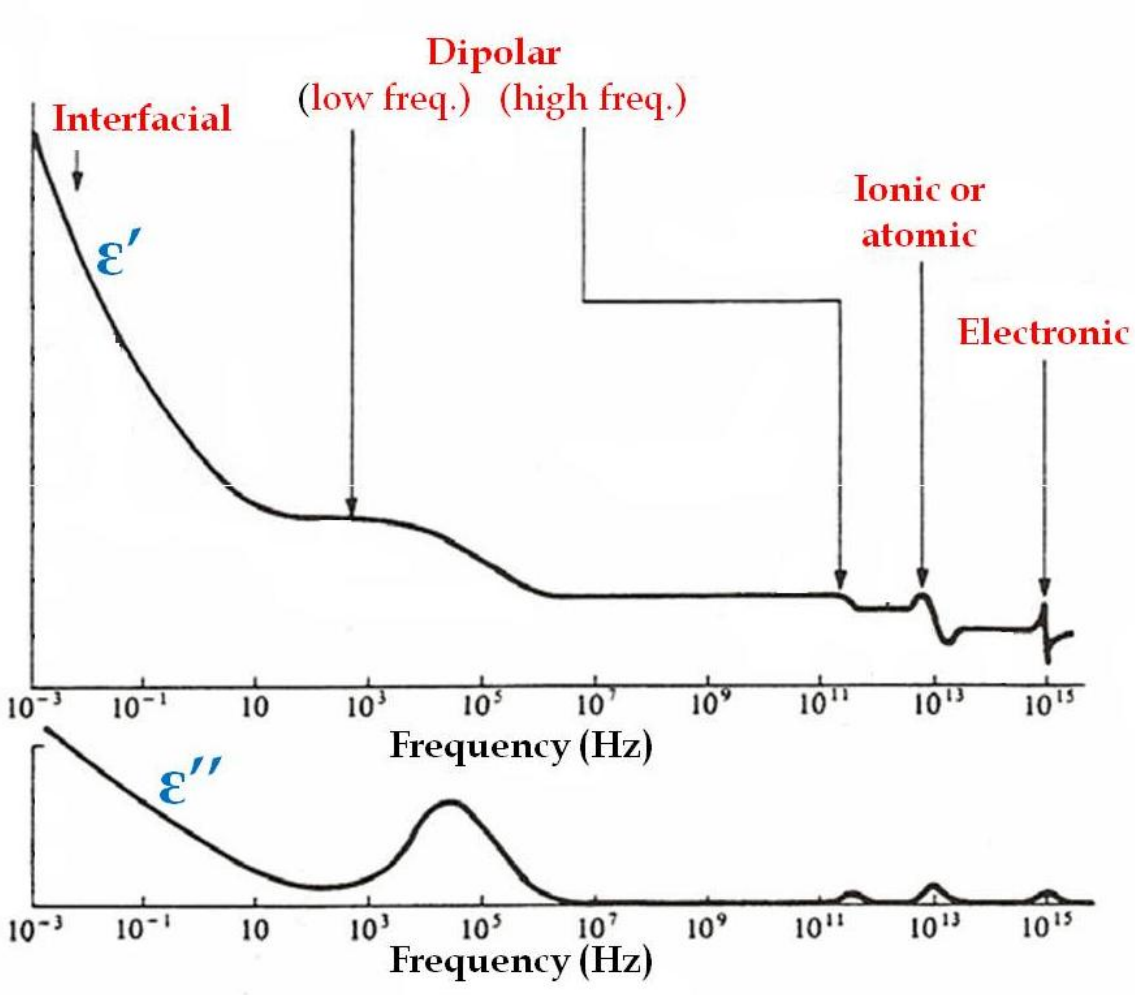

Figure 2.3. Frequency dependence of the polarization mechanisms for dielectrics at room temperature.[1]

If a substance possesses a dipole moment, heat can be generated by irradiation with microwaves, as is the case in the water molecule.[3] Under low frequency irradiation, the molecule will rotate in phase with the oscillating electric field. The molecule gains some energy by this rotation, but the overall heating effect is small due to the low frequency. Alternatively, under the influence of high frequency, the dipoles do not have enough time to respond to the oscillating field and do not rotate and therefore no heating occurs.

If the oscillating field is in the microwave radiation region, a situation between these two extremes occurs. The frequency is low enough so the dipoles can follow the alternating electric field and therefore rotate. At the same time, the frequency is high enough to create a considerable amount of heat by relatively quick dipole rotations (245 M rotations per second at 2.45 GHz). It should be noted though that the dipole rotations do not always follow the field precisely but a phase difference between the orientation of the field and that of the dipole can emerge (Figure 2.4). This phase difference causes energy to be lost from the dipole molecular friction and collisions. [14, 15]

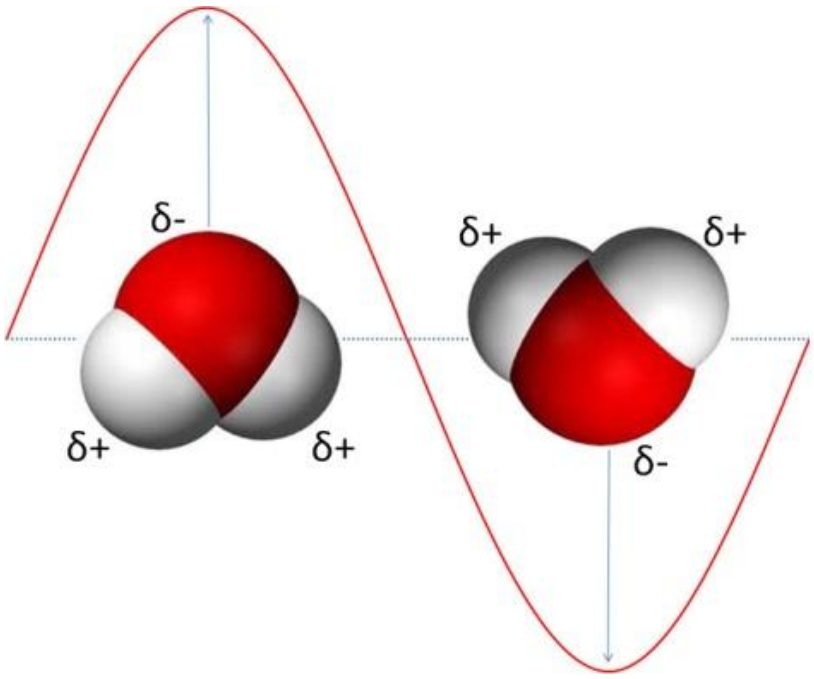

Figure 2.4. Water dipolar molecule trying to align with an oscillating electric field.

2.2.2. Dielectric losses: Conduction Mechanism.

Conduction is a mechanism normally referred to as long-range movement of free charge carriers as a response to an applied electric field. When an AC electric field is applied, the charge carriers will perform an oscillating movement (Figure 2.5). Usually the charge carriers are electrons, but in some cases the ions are mobile as well (Ionic conduction).[6, 10, 16]

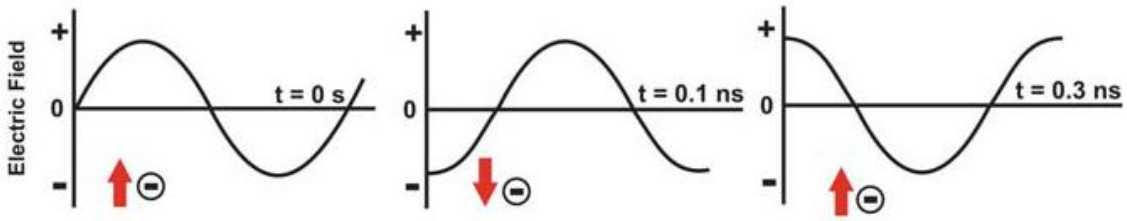

Figure 2.5. Conduction mechanism. Irradiation of a sample with microwaves results in oscillating movements of the charge carriers in the electric field.[3]

Such conduction mechanism of the free charge carriers as a response to an applied alternating electric field is usually referred to as the dielectric loss (ε"), which is shown as a function of temperature for sintered alumina in figure 2.6.[17]

The dielectric loss heating effect is by heat dissipation due to Joule heating of the loss currents and depends strongly on the electrical resistance of the material. At room temperature the effect of heat dissipation by conduction is considerable only at lower frequencies. However as temperature increases, the effect of heat conduction increases rapidly in semiconducting materials and eventually becomes as important as dielectric polarization.[12]

In metals, a large amount of free and mobile electrons are available, whereas in semiconductors only a small amount of electrons get thermally activated from the valence into the conduction band. Therefore, at high temperatures the electrons get activated into the conduction band, the materials conductivity increases and concomitantly the contribution of dielectric losses to the microwave heating effect increases.[17,18]

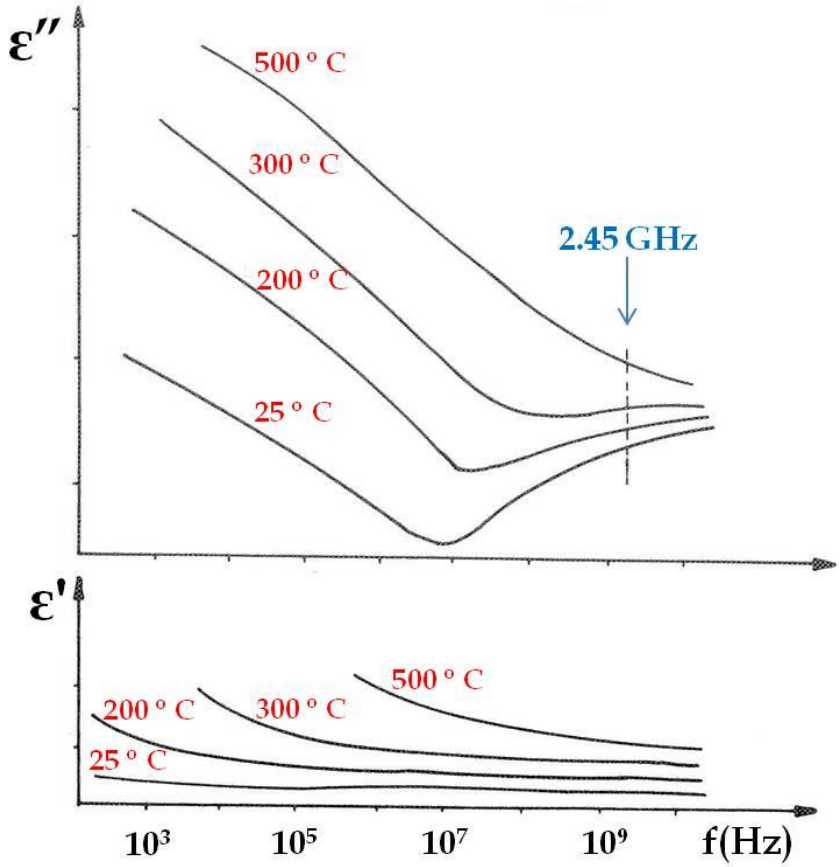

Figure 2.6.Dielectric properties of sintered alumina as a function of frequency and temperature[17]

The effect of conduction heating can be demonstrated easily by heating a beaker of distilled water and a beaker containing a water solution of sodium chloride in a domestic microwave oven. In distilled water, heating mainly arises through dipolar polarization; the heating rate is significantly lower than that observed when the same volume of a dilute salt solution is heated. In the latter case, there is an additional contribution to the heating from the conduction of Na^+ and Cl^- ions in the salt solution.[19]

The power density per unit volume (P) of absorbed microwaves in W/m^3 by a sample due to dielectric losses may be expressed as shown in equation 2.8. It should be noted though that P describes only the microwave energy absorbed

by the material, which is related to but not exactly the same as the thermal energy created within the material.

The average power (P) due to dielectric losses is given by:

$$P = \sigma \cdot E_{rms}^2 = \omega \varepsilon_o \varepsilon'' E_{rms}^2 = 2 \pi f \varepsilon_o \varepsilon'' E_{rms}^2 \quad [2.8]$$

Where σ is the conductivity of the material, E_{rms} is the internal electrical field of the microwave, ω= 2πf is the angular frequency of the microwave, ε_o corresponds to the dielectric permittivity of vacuum and ε" represents the relative dielectric losses in the material.

Polar materials with losses $\varepsilon'' < 10^{-2}$ are quite difficult to be heated up, while for those with ε" > 5 the surface is heated rather than the bulk. Materials with intermediate values, $10^{-2} < \varepsilon'' < 5$, are best candidates for microwave heating. [20, 21]

The depth to which the microwaves will penetrate into the material is determined by the real and imaginary parts of the dielectric permittivity (ε' and ε") as shown in equation 2.9. The penetration depth (D) into the material is defined as the depth at which the power density of microwave irradiation is reduced to 37% of its initial value at the surface for a specific incident wavelength (λ_0). For materials with a loss tangent ($\tan\delta = \tan(\varepsilon''/\varepsilon')$) lower than unit, the penetration depth is given by:[22]

$$D = \frac{\lambda_0}{2\pi} \frac{\sqrt{\varepsilon'}}{\varepsilon''} \quad [2.9]$$

Materials with relatively high values of ε" are characterized by low values of the penetration depth.

The depth of penetration is important since it will determine the uniformity of heating throughout the material. Small values of ε' and large values of ε" will result in surface heating, while large values of ε' and small values of ε" will result in more volumetric heating but with reduced efficiency.[10]

One of the limitations in using microwave energy in a controlled way to process materials is the current lack of dielectric data for the respective materials in the microwave frequency range as a function of temperature.

2.2.3. Magnetic losses: Induction mechanism

The magnetic induction heating of materials originates from magnetic losses. The total power loss is composed fundamentally of eddy current losses.[23-26]

Eddy currents are basically induction currents, where the changing magnetic field of the microwave induces such currents in the material. The heating effect is based on Joule heating due to the Eddy currents and hence depends much on the electrical resistivity of the material, equivalent to dielectric loss heating.

Magnetic induction occurs in all kinds of materials. Eddy current Joule heating may be regarded as a similar effect as the dielectric losses and their corresponding electrical current Joule heating.

In a similar way as far for the electric losses, the power that is absorbed per unit volume of a sample is given by,

$$P = \omega \mu_o \mu'' H_{rms}^2 = 2 \pi f \mu_o \mu'' H_{rms}^2 \qquad [2.10]$$

Where μ_o is the magnetic permeability in vacuum, μ'' the relative magnetic losses of the material and H_{rms} the internal magnetic field of the microwave.[1]

Moulson *et al*.[27] claimed that for ferrite materials the magnetic losses can be expressed in terms of three main contributions:

$$\mu''_{\mu} = \mu''_{h} + \mu''_{e} + \mu''_{r} \qquad [2.11]$$

In which μ''_h, μ''_e, μ''_r are the hysteresis, eddy current and 'residual' losses respectively. The processes that contribute to the residual losses include the resonance losses and at high frequencies these will often dominate.[27, 28]

Furthermore, it is important to remark that induction heating is well-known for domestic applications.

2.2.4. Magnetic heating

In theory, magnetic materials may be directly heated by microwaves coupling to the magnetic moments. The magnetic moments may follow the magnetic field of the electromagnetic wave, as is the case for example in electron paramagnetic resonance spectroscopy. However, such movements have never been clearly identified to create any considerable heating and the overall amount of heat created may be small as compared to the heating mechanism described before. In the literature, several reports [27, 28,29] exist though which suggest that certain magnetic materials can be heated more efficiently with the magnetic part of the electromagnetic wave. This indicates that magnetic resonance could contribute under certain circumstances, but the role of this mechanism for microwave heating and the exact role of dielectric loss currents and Eddy currents in the examples reported [29] are unclear.

2.2.5. Non Thermal Effects

Many research groups are currently studying a number of anomalies involved with microwave heating that have been broadly termed "non-thermal effects", which include any differences of the microwave method as compared to conventional methods which cannot be explained by differences in the temperature and the temperature profile.[30] Today's debate focuses on anomalous effects between the electric field and the interfaces of the particles which possibly involves the formation of a plasma and the solid diffusion may be increased due to such second-order effects.[31, 32] These effects may in fact be important to explain the great efficiency of microwave synthesis technique.

The effects of dielectric polarization and dielectric/magnetic loss currents are much better understood as compared to more exotic effects like magnetic resonance and non-thermal effects. Therefore, most of the discussion in the literature focuses on the more established mechanisms.

2.3. Classification of materials

An electromagnetic microwave may be mainly reflected, transmitted or absorbed by condensed matter depending on the nature of such matter. For non-magnetic condensed matter interacting with microwaves three different classes of materials are commonly defined (Figure 2.8a). This classification is related to the penetration depth of the microwave according to eq. 2.9 and to the absorption due to dielectric polarization and losses: [33, 34]

- Reflecting materials do not allow deeper penetration by the electromagnetic wave, the penetration depth is low and a large part of the intensity of the microwave is reflected. Materials with free electrons such as certain metals behave in this way. Metals possess high electrical conductivity which corresponds to high losses.

- Transparent materials allow the wave to propagate all the way through with low attenuation, such as Teflon and silica glass. Generally speaking, insulators or materials with low dielectric permittivity and low losses are concerned here. The penetration depth is high and the absorption of microwave energy due to dielectric polarization is low.

- Absorbing materials transform the electromagnetic energy efficiently into heat. This is the case for dipolar liquids such as water and dielectric or polar materials such as ferroelectrics with high dielectric permittivity. Intermediate values of dielectric losses favor the absorption of the microwave energy by the material.[35] The penetration depth is intermediate and the absorption of microwave energy due to dielectric polarization is high.

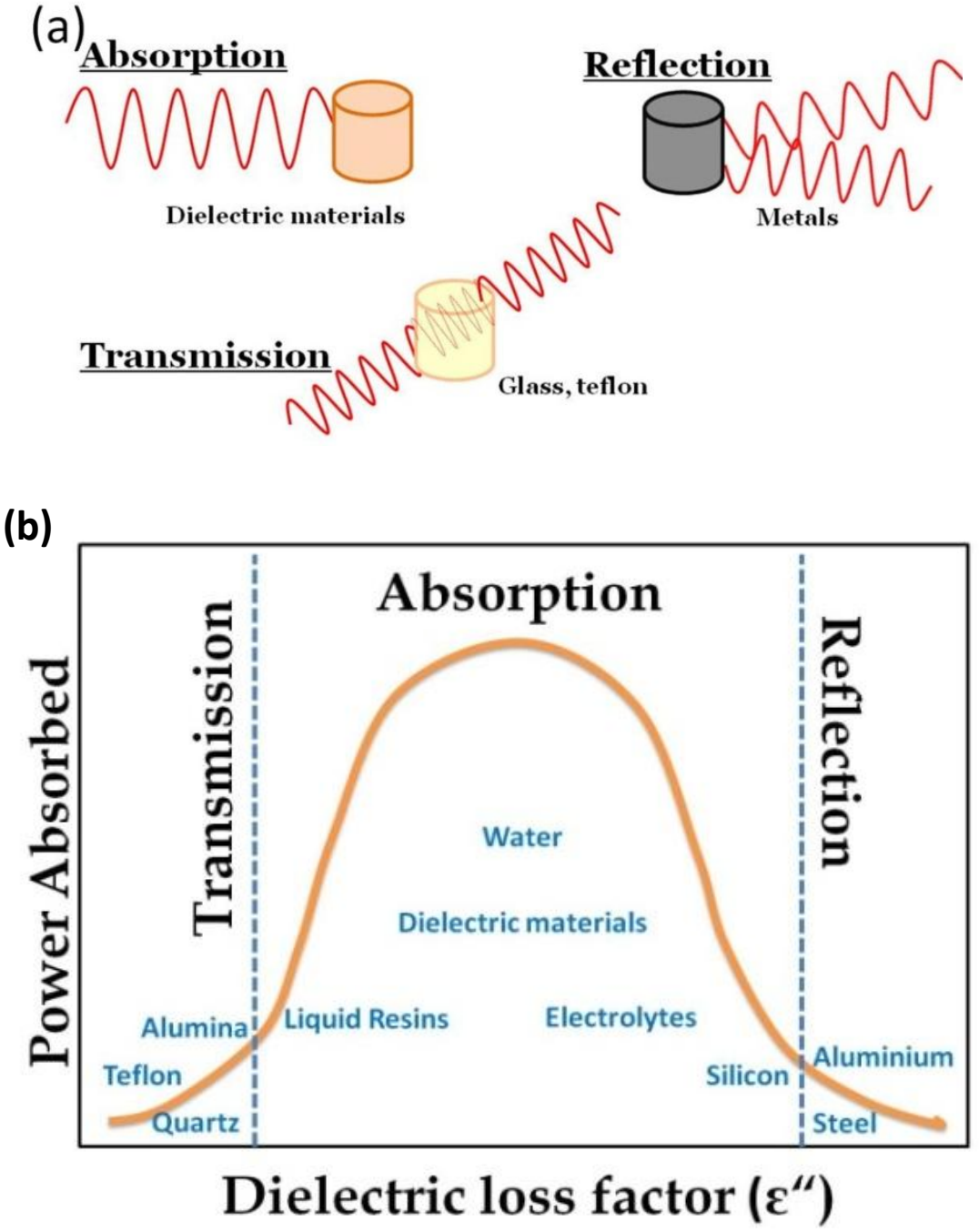

Figure 2.7. a) Interaction of the electromagnetic field with different materials. b) Relationship between the dielectric loss factor and ability to absorb microwave power for some common solid and liquid substances. Reproduced from Thostenson *et al.*[36]

Materials with low dielectric losses have a large penetration depth. As a result, little of the energy is absorbed in the material, and the material is transparent to microwave energy. Because of this behaviour, microwaves

transfer energy most effectively to materials that have dielectric losses corresponding to the middle of the conductivity range (Figure 2.7b). In contrast, conventional heating transfers heat most efficiently to materials with high thermal conductivity.[36]

As mentioned before, in magnetic materials the magnetic component of the electromagnetic wave can contribute to the heating effect as well (Figure 2.8).[1, 37, 38]

A recent article [39] on ferrite materials, namely $BaFe_{12}O_{19}$, $SrFe_{12}O_{19}$, $CuFe_2O_4$, $CuZnFe_4O_4$, and $NiZnFe_4O_4$, shows that the classification mentioned before should be unaffected though by the calculated magnetic losses, at 2.45 GHz. It is found though that magnetic losses are up to approximately four times greater than dielectric losses in the microwave heating of these ferrites.

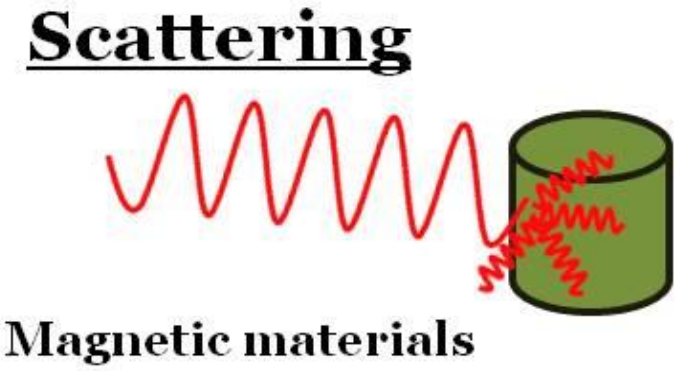

Figure 2.8. Interaction of the electromagnetic field with a magnetic material.

It is clear that different materials will have greatly different heating behaviours in the electric (E) and magnetic (H) microwave fields, as it is explained in *section 2.6.2: Solid State – Single Mode Microwave*. As commented, above, these recent results have re-opened the discussion on the interaction between microwaves and materials by incorporating considerations of the magnetic field component of the microwave.

2.4. Microwave Heating.

The main features which distinguish microwave heating from conventional methods are: Faster energy transfer rate, rapid heating and selective heating of materials. This leads to a different temperature distribution of the material when heated in a microwave furnace.

2.4.1. Energy Transfer.

In conventional heat treatments energy is transferred to the material through heat conduction and convection creating thermal gradients. In the case of microwave heating, energy is directly transferred to the material through the interaction of the electromagnetic wave and the material at the molecular level (Figure 2.9) [40, 41] as discussed in *section 2.2.*

It has been argued that the way of energy transfer is in fact crucial in the synthesis of materials. The ability of microwaves to penetrate and heat the material from within provides the possibility of rapid and volumetric heating without overheating the surfaces.[42] Bulky material can be heated more uniformly by microwaves due to the greater depth of penetration and a shortening of the process time, thus improving the product quality and consistency.[1]

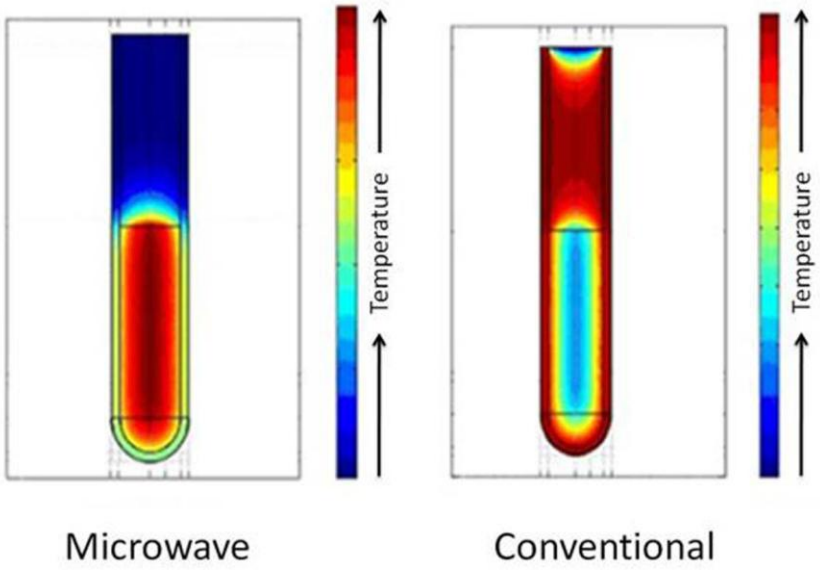

Figure 2.9. Differences in the temperature distribution in microwave and conventional processes.[40]

2.4.2. Fast Heating.

For the purpose of chemical synthesis, microwaves massively reduce the processing time as compared to conventional synthesis but significant qualitative changes in the resulting material in terms of crystal structure and physical properties are usually not encountered. In some cases even quantitative improvements can be achieved.[43-46] Some authors claim that chemical reactions, when microwave-assisted, are accelerated between 10 - 1000 times compared with conventional methods. [47, 48]

2.4.3. Selective Heating.

A problem with such fast heating is the possible formation of "hot spots", which is a thermal effect that arises as a consequence of non-homogeneous or selective heating, resulting in the temperature in certain zones within the sample being much greater than the average macroscopic temperature.[32] These regions are not representative of the reaction conditions as a whole. The formation of hot spots due to local overheating effects has been demonstrated by D. M. P. Mingos [49] in the decomposition of H_2S over γ-Al_2O_3 and MoS_2–γ-Al_2O_3, where the higher decomposition rate under microwave irradiation was attributed to the presence of hot spots. The authors estimated the temperature in the hot spots to be about 100–200 ^oC higher than the bulk temperature. They claimed that hot spots may be created by local differences in the dielectric properties in the material, and/or by the uneven distribution of electromagnetic field strength. Hot spots can be problematic in certain cases if they cause the desired chemical reaction to not occur homogeneously. On the other hand, the occurrence of selective heating can sometimes be utilized to accelerate a reaction.

It is possible that in a composite material, depending on the characteristics of the specific phases (dielectric properties, size and structure) and their ability to couple to the electric and/or magnetic field of the microwaves, heating can occur preferentially in one phase as compared to the

others. Therefore, in case that certain materials couple poorly with the most frequently used 2.45 GHz microwaves, a radiation susceptor (such as SiC, graphite, activated carbon or metal powder) can be added to the precursor mixture. In case of metallic susceptors the microwave is reflected to large parts and absorption strongly increases. Alternatively, non-metallic radiation susceptors may simply couple better to the microwave and therefore exhibit increased temperature. The susceptor areas may always be regarded as artificial or deliberate "hot spots", which are well known to facilitate a more efficient microwave heating process.[50] However, most polar materials do couple to the electromagnetic wave sufficiently strong to reach high temperatures, no additives are necessary and the reaction time is often just a few minutes.[51]

In Table 2.3. the highest temperatures reached without a radiation susceptor in selected materials are summarized:

Table 2.3. Maximum temperatures reached within different materials after few minutes of exposure to microwaves.[12, 20, 41]

	T (K)	t (min)		T (K)	t (min)		T (K)	t (min)
B	1273	1	**MnO**	386	6	**Nb**	631	6
C amorphous	1556	1	**$MnCl_2$**	326	2	**Nb_2O_5**	387	6
SiC	1384	2	**Fe_3O_4**	1531	3	**MoS_3**	1379	7
C graphite	1053	6	**FeS_2**	1292	7	**Mo**	933	4
NaCl	356	7	**Fe**	1041	7	**MoO_3**	342	6
MgO	476	5	**Fe_2O_3**	407	7	**$SnCl_2$**	749	2
Mg	393	7	**$FeCl_3$**	314	4	**Sn**	570	6
Al	850	6	**Co_2O_3**	1563	3	**SnO**	375	30
Al_2O_3	351	4	**Co**	970	3	**$SnCl_4$**	322	8
Si	1272	1	**NiO**	1578	6	**Sb**	663	1
SiO_2	352	7	**Ni**	657	1	**$SbCl_3$**	497	2
S	436	6	**CuO**	1285	6	**La_2O_3**	392	6
CaO	389	4	**CuCl**	892	13	**CeO_2**	372	30
$CaCO_3$	334	7	**Cu**	501	7	**Ta**	450	7
Ti	1423	1	**Cu_2O**	362	7	**WO_3**	1543	6
TiB_2	1116	7	**$ZnCl_2$**	882	7	**W**	963	6
TiO_2	352	8	**Zn**	854	3	**Hg**	313	6
V_2O_5	987	11	**ZnO**	599	5	**PbS**	1229	7
V	830	1	**ZnS**	340	5	**Pb**	550	7
Cr_2O_3	403	7	**Y_2O_3**	388	7	**PbO_2**	455	7
MnO_2	1560	2	**Zr**	735	6	**Pb_3O_4**	395	30
Mn_2O_3	1453	6	**ZrO_2**	336	4	**PbO**	364	2

It is important to comment that SiC has turned out to be the ideal microwave susceptor for enhancing heating rates of non-polar reaction mixtures.[52] It strongly absorbs microwave energy and subsequently and rapidly transfers the generated thermal energy via conduction phenomena to the reaction mixture. Due to its high melting point (≈ 2700 ^{o}C) and low thermal expansion coefficient, SiC can be employed up to extremely high temperatures.[53, 54]

2.5. Microwave-Enhanced Reaction Rates.

The simplest chemical reaction can be represented by: A + B → AB. The reaction process starts with reactants A and B that must be activated to a higher-level energy state $[A\text{--}B]^{\neq}$. The difference between these energy levels is the activation energy (E_a) that is the energy that the system must absorb in order to react. Once enough activation energy is absorbed, the reaction occurs and leads to the product AB (Figure 2.10),[7] whereby parts of E_a (endothermic) or more energy than E_a (exothermic) are released.

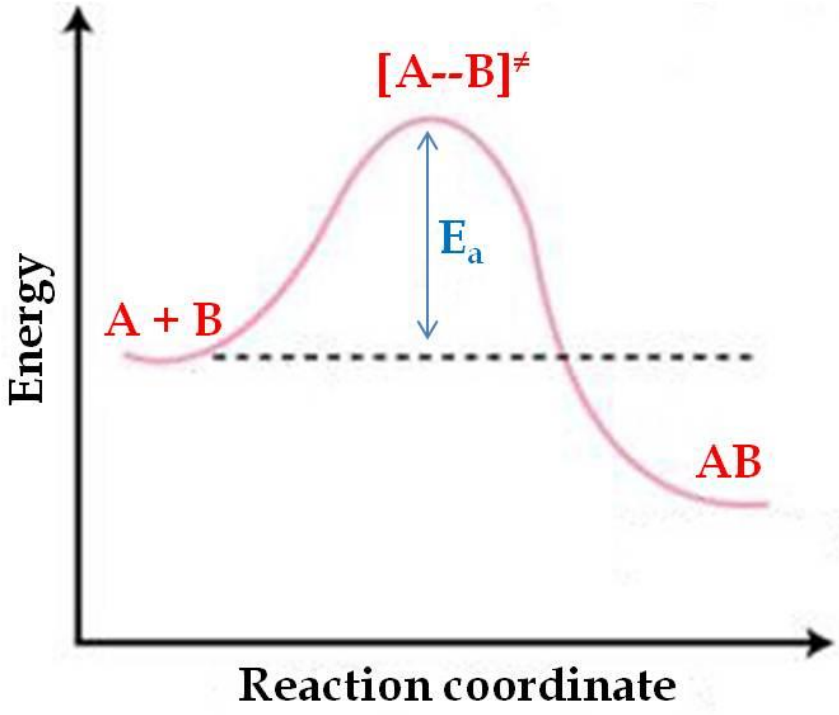

Figure 2.10. Reaction coordinates of a typical exothermic chemical reaction.

The reaction rate of the reaction can be described by the well-known Arrhenius rate equation (2.12):

$$K = Ae^{-Ea/RT} \quad [2.12]$$

Where *K* is the reaction rate constant, that depends on temperature, *A* is a pre-exponential factor constant, which describes the molecular mobility and depends on the frequency of vibrations of the molecules at the reaction interface[14], *R* is the gas constant and *T* the temperature.

Some authors[6, 7] claim that microwave irradiation does not affect the activation energy of the process and just provides the momentum to overcome this barrier and complete the reaction more quickly than for a conventional heating method. The fast energy transfer creates a non-equilibrium condition resulting in high instantaneous temperature. However, there are some reports that contradict this theory. C. Conner and G. A. Tompsett [55] claim that the variations in the reaction activation energy E_a exist because of the differences in dielectric properties of the reactions, intermediates and products. For example, Falamaki [56] reported a reaction activation energy of 12 kJ/mol for colloidal silica growth under the influence of microwaves, which is significantly lower than that reported for conventional synthesis (> 41 kJ/mol). This is not the only example, Brosnan *et al.* [57] claimed a significant difference in E_a between microwave-sintering (85 kJ/mol) and conventional sintering (520 kJ/mol) for alumina.

The change of E_a would be a rather significant phenomenon, which may be explained by changes in the intermediate energy states of the reactants during synthesis to manipulate the reaction kinetics significantly without changing the mechanism.[55]

This is a controversial topic, but it is clear that microwave heating is extremely useful in otherwise slower reactions with high reaction activation energies.

2.6. Microwave Assisted Synthesis Techniques

Microwave assisted synthesis of inorganic oxides may be performed by several alternative methodologies:

- Direct irradiation of a mixture of the solid precursor reactants.

- Combining microwaves with other synthetic procedures such as sol-gel, combustion or hydrothermal synthesis. The microwave-hydrothermal method is explained in detail in *section 2.6.3*.

The sol-gel process is a wet-chemical technique widely used in the synthesis of inorganic materials, typically metal oxides. The starting point is a chemical solution (sol) which acts as the precursor for a polymeric network (gel) formed upon hydrolysis and polycondensation reactions. Microwave thermal decomposition of a particular gel (usually containing high amounts of water which couple well to the microwave), leads to the formation of the desired phase.[58, 59]

Combustion reactions for the synthesis of oxide materials usually involve the mixing of metal nitrates and a solid fuel (urea, glycine, sacharose) in adequate quantities, where the later provides the necessary energy to ignite the (exothermic) reaction. The ignition can be performed by providing the energy in the form of microwaves. The high speed of the process together with the production of large quantities of gas produce sponge-like porous materials, yielding nano-sized particles.[60, 61]

2.6.1. Solid - State Microwave Synthesis

The term "Solid - State Microwave Synthesis" refers to microwave irradiation of solid precursors. The synthetic procedure consists in mixing the precursors and packing them into a pellet, which is then deposited in an adequate crucible (usually porcelain, alumina or SiC) and placed in a multimode microwave oven (a domestic one may be used). As mentioned

before (*section 2.4.3.*), in some cases the presence of a radiation susceptor is useful in order to significantly increase the reaction temperature and the reaction rate.

A schematic picture of a typical domestic microwave apparatus used for Solid State Microwave Synthesis is shown in Figure 2.11.[12]

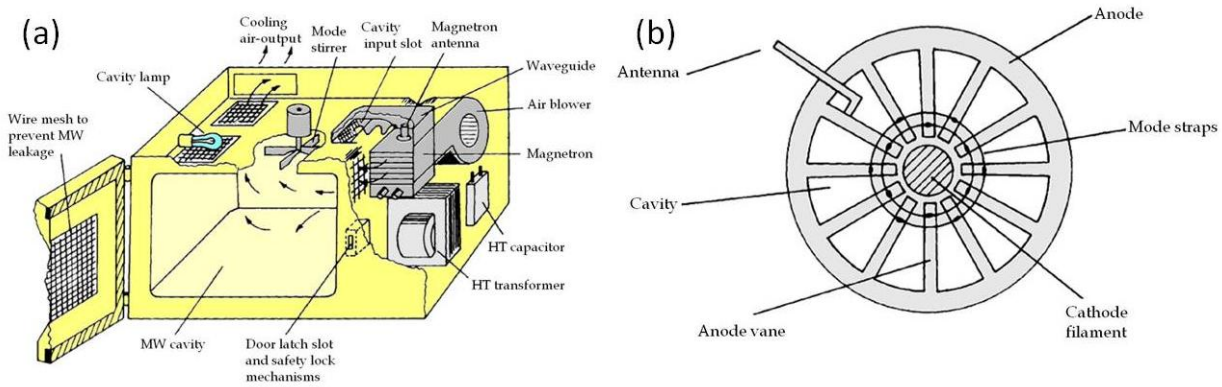

Figure 2.11. a) Domestic microwave oven scheme. b) Magnetron schematic illustration. [12]

The most important part of a microwave oven is the magnetron, which generates the microwave radiation and it is the main part in all the microwave-apparatus employed in this thesis (domestic microwave, single mode microwave, microwave-hydrothermal system).

A magnetron (Figure 2.11b) is a thermionic diode with an anode and a cathode. Electrons are emitted from the cathode and move along a spiral path, induced by the magnetic field, to the anode. As the electrons spiral outward, they form space charge groups, and the anode shape forms the equivalent of a series of resonant inductive-capacitive circuits. The microwave frequency generated in the anode is picked up by the antenna and is transmitted into the microwave cavity.[1,11] The variable power available in domestic ovens is produced by switching the magnetron on and off according to a duty cycle. For example a typical 800 W oven with a 30 s duty cycle can be made to deliver an average of 400 W by switching the magnetron on and off every 15 s.[12]

The waveguide is usually a rectangular channel made of sheet metal. Its reflective walls allow the transmission of microwaves from the magnetron to

the microwave cavity or applicator. The reflective walls of the microwave cavity are necessary to prevent leakage of radiation and to increase the efficiency of the oven. If the energy is reflected by the walls, absorbance in the sample is increased because the wave irradiates the sample and can be partially absorbed on each passage. This can be particularly important if the sample is dimensionally small. It should be noted though that the magnetron may be damaged if too much energy is reflected back into the waveguide.[1, 11, 12]

The microwave field in oven-like multimode instruments is distributed in a chaotic manner. Due to reflections from the cavity walls, multiple modes of the electromagnetic waves interact with the cavity load (Figure 2.12). In these large cavities, the field density (W/litre) is low and therefore the applied microwave power has to be high in order to achieve short heating rates.[54,62]

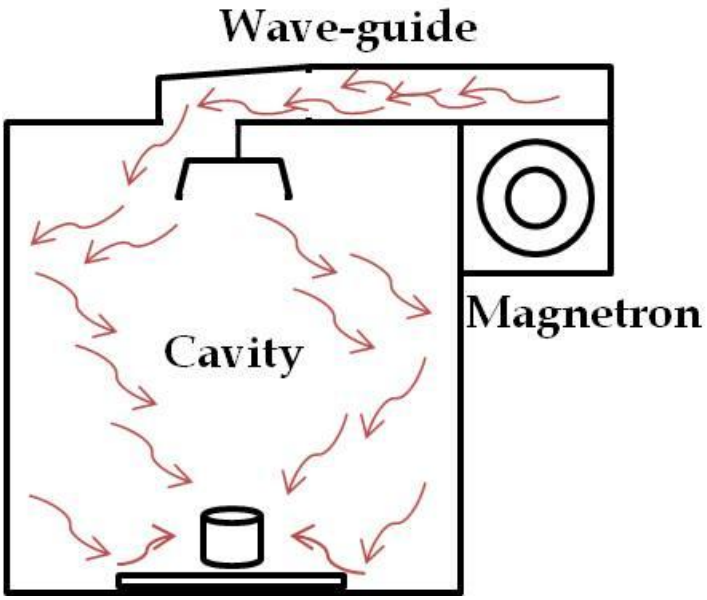

Figure 2.12. Schematic display of the field distribution in a multimode oven.

Figure 2.13 shows a domestic microwave oven image with a thermal infrared camera. With only a thin film of water present, the image illustrates the microwave intensity distribution in a nearly empty chamber. A pronounced horizontal mode structure also shows heterogeneous heating of the film.[35]

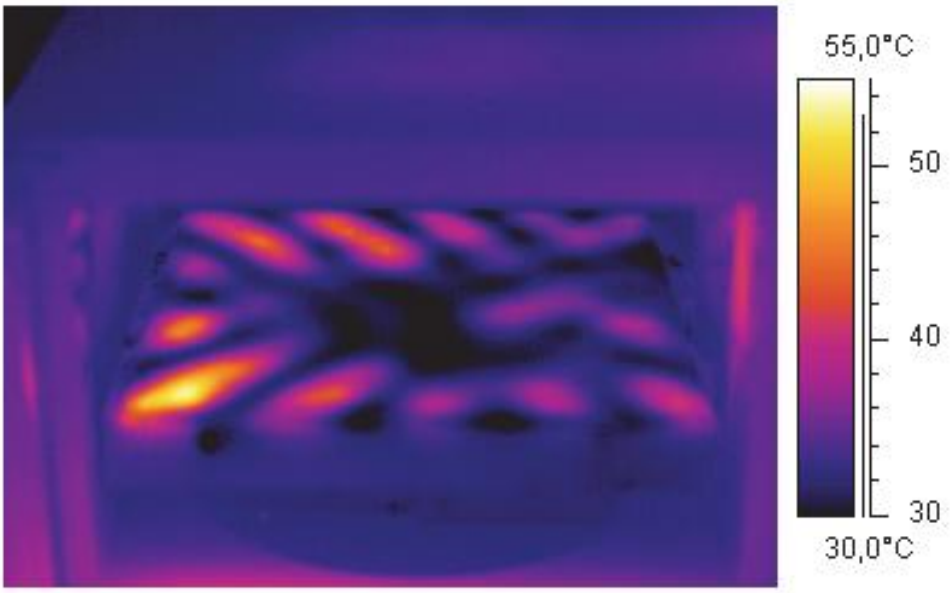

Figure 2.13. Infrared thermal imaging inside microwave oven.[35]

Due to the lack of temperature control in this type of microwave oven, the reactions are carried out at unknown temperature. However, the method has been applied to a large range of materials during the last years. Just a few examples are mentioned here to demonstrate the efficiency of the method for different types of materials.

1. Core-shell structures can be obtained with inverse organization, for example, a NiO core covered with a Ni shell can be obtained when using nickel acetate as precursor, or particles with a Ni core covered by a NiO shell when using nickel formate.[63] In both cases a small amount of active carbon as microwave susceptor was used. Such core-shell structures exhibit exchange bias in the magnetic hysteresis loops as a consequence of antiferromagnetic/ ferromagnetic interactions.

2. A wealth of perovskite structures can be formed by solid state microwave synthesis, where a selected few ones are summarized in Table 2.4. Vaidhyanathan *et al*. [64] showed a decade ago that the synthesis of niobates and titanates, among them ferroelectrics, piezoelectrics and insulators, can be performed by microwaves in minutes, reducing time and intermediate steps as compared to conventional synthesis.

3. It can be stated generally that the more complex the materials are the more difficult it is to prepare them by microwave assisted synthesis, as occurs generally with all synthesis techniques. In more complex systems better diffusion processes are required to uniformly disperse 3 or more cations across the sample during the synthesis. At the current stage this still poses a major challenge for the solid state chemist. As an example, the complex perovskites $CaCu_3Ti_4O_{12}$ (CCTO) can be synthesized by solid-sate microwave techniques.[65,66] This 1:3 A-site ordered perovskite related structure has recently attracted much attention due to its giant dielectric permittivity, which may be interesting for capacitors in microelectronic devices. It is quite well established though that the giant permittivity is not intrinsic but debited to a core-shell structure of conducting bulk and insulating grain boundaries, thus forming an Internal barrier layer capacitor (IBLC) structure.[67, 68] It has been reported that solid state microwave synthesis reduces the processing time and, more importantly, the IBLC structure is preserved and even higher values of the giant dielectric permittivity can be obtained.[65, 66]

Table 2.4. Synthesis conditions for some niobates and titanates produced by microwave and conventional routes.

Material	Reactants	Microwave	Conventional
$LiNbO_3$	Li_2CO_3, Nb_2O_5	15 minutes 800 W	12 h 500 ºC
$NaNbO_3$	Na_2CO_3, Nb_2O_5	17 minutes 800 W	t>>>, grindings 1250 ºC
$KNbO_3$	K_2CO_3, Nb_2O_5	12 minutes 800 W	30 h 1000 ºC
$BaTiO_3$	$BaCO_3$, TiO_2	25 minutes 1000 W	t>>>, grindings 1400 ºC
$PbTiO_3$	$PbNO_3$, TiO_2	9 minutes 600 W	8 h 360 ºC

4. Since many years ferrites with inverse spinel structure (AFe_2O_4) are used in the manufacture of inductors, transformers and other electronic devices. Vanetsev *et al*.[69] discussed the microwave synthesis of several ferrites ($NiFe_2O_4$, $CoFe_2O_4$, $CuFe_2O_4$) using nitrates as precursors within just 10 minutes reaction time.

5. It is also possible to synthesize various manganites by this route, for example lithium or nickel manganites.[70, 71] Lithium transition metal oxides such as spinel $LiMn_2O_4$ has been considered promising electrode material due to its

low cost, high environmental acceptability and high reduction potential.[71] $NiMn_2O_4$ is a material that is widely used in the industry for the manufacture of temperature sensors (negative thermal coefficient NTC material).[72]

6. Cathodic materials used as electrodes in lithium batteries such as $LiCoO_2$, $LiCo_{1-x}Ga_xO_2$ have been produced by solid - state microwave synthesis as well using nitrates or carbonates of the respective metals as precursors.[73]

Here in this work, the application of the solid - state microwave synthesis technique is demonstrated on several well-known phases for the first time. Such phases are (a) rare earth (RE) orthochromites ($RECrO_3$), (b) $LaMO_3$ (M = metal transition) perovskites, interesting for several applications such as solid oxide fuel cells (SOFCs) components, gas sensors, catalysis, and (c) rare earth titanates ($RE_2Ti_2O_7$) with pyrochlore structure exhibiting interesting magnetic properties and ionic conduction.

2.6.2. Single-Mode Solid State Microwave Synthesis

Conventional microwave ovens constitute a multi-mode cavity configuration, where the electric (E) and magnetic (H) components of the microwave are randomly oriented in the cavity. Single-mode or monomode reactors can be considered as the second generation of microwave instruments, where the microwave utilized for heating is polarized and exhibits minima and maxima in the amplitude. The field is well defined in space and the material to be heated needs to be placed at a certain position in the cavity.[74]

The single-mode microwave equipment used in this work is based on a microwave generator working at the standard 2.45 GHz frequency with a variable power up to 2 kW and a TE_{10p} microwave cavity. The experimental set-up includes a microwave generator, circulator (water cooled magnetron), 3-stub tuner (impedance agreement accord) and the resonant cavity, as despicted in Figure 2.14.

The amplitude distributions of the electric and magnetic component of the microwave can be utilized by carefully choosing the position of the sample during synthesis with respect to the respective maxima and minima of E and H (Figure 2.15a-b). [54, 75]

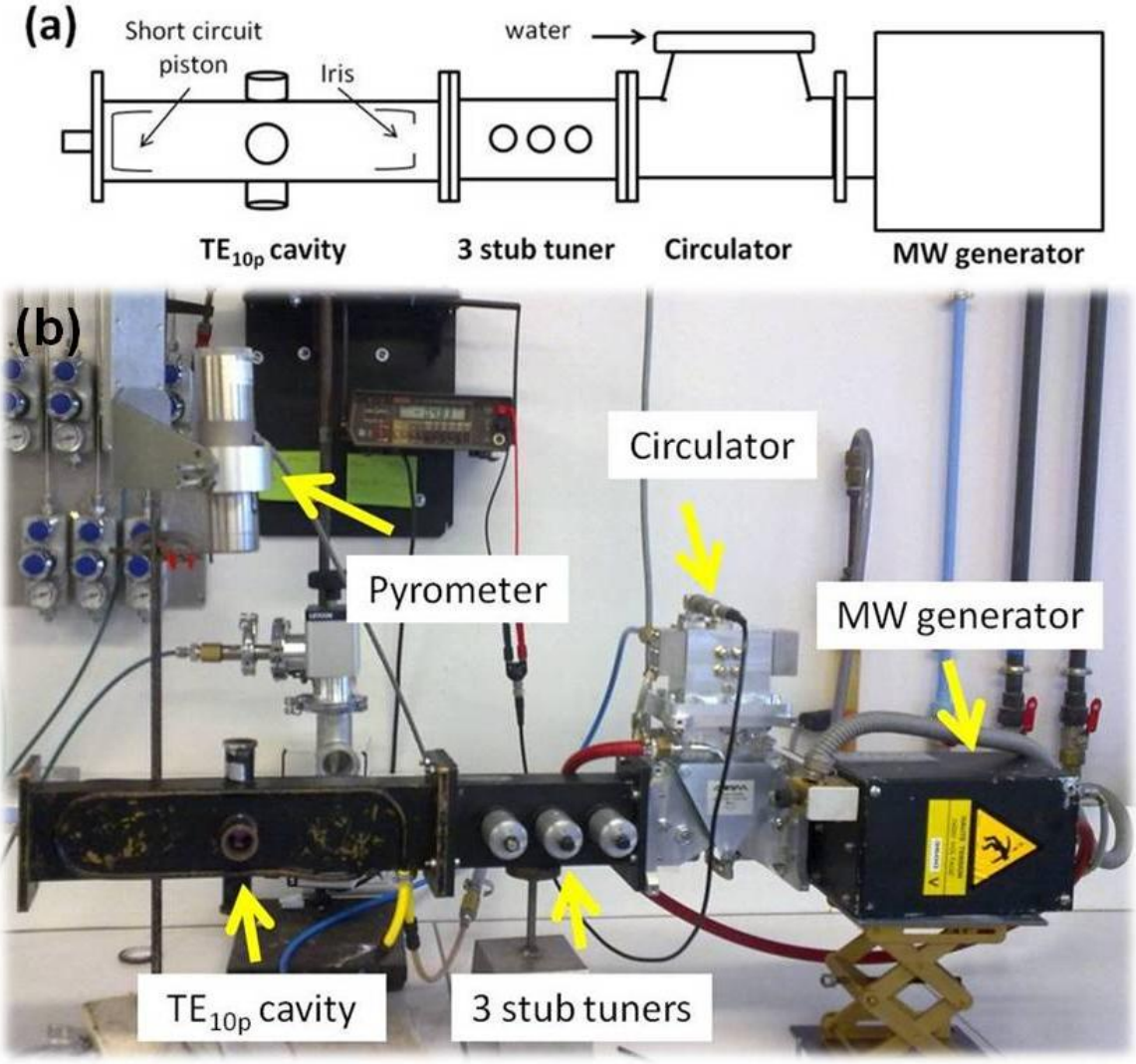

Figure 2.14. a) Single-mode microwave apparatus (schematic picture). b) Comercial single mode apparatus (SAIREM company), in CRISMAT- CNRS Caen laboratory.

By tuning the length of the cavity by moving a coupling iris and a short circuit piston it is possible to work in TE_{102} or TE_{103} resonant modes (Figure 2.15c-d). In the TE_{102} mode the sample is placed at the amplitude maximum of the magnetic field component of the microwave (H mode), whereas in the TE_{103} mode the sample is placed at the amplitude maximum of the E field (E mode).

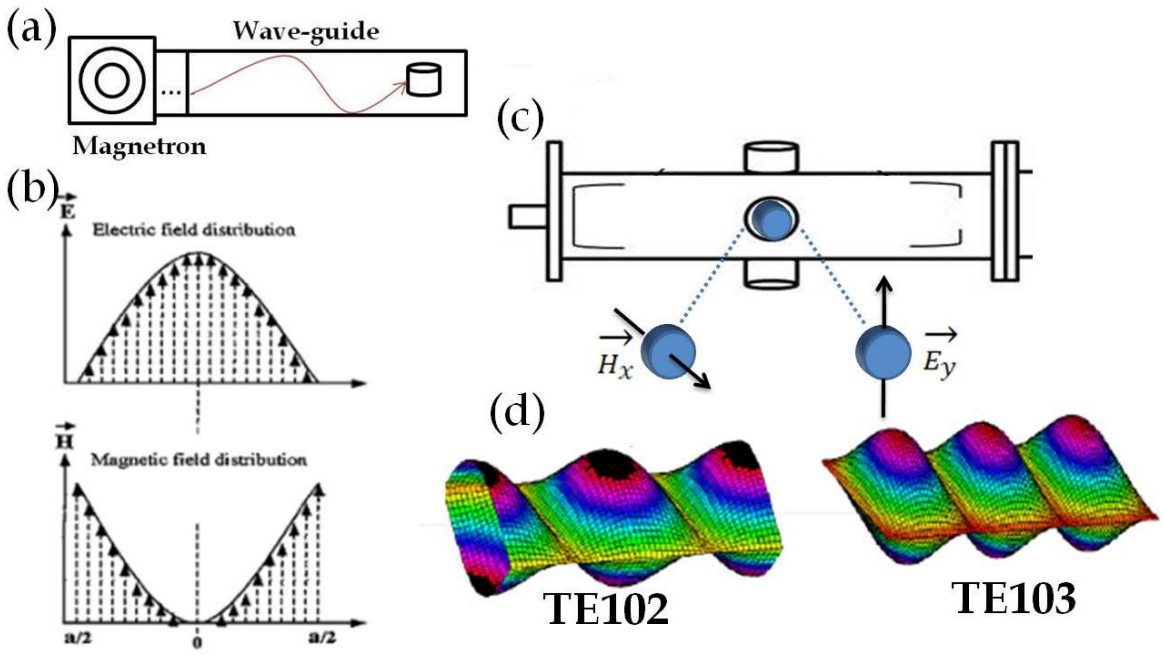

Figure 2.15. a) Schematic display of a single-mode resonant cavity. b) Amplitude distribution of the electromagnetic field: the sample is in the amplitude maximum of the electric E field where the magnetic field amplitude is minimum. Vice versa, the amplitude maximum of the magnetic H field corresponds to the minimum of the electric field E. c) Schematic drawing of the magnetic and electric field orientation of the polarized wave. d) Amplitude distribution of the magnetic field component for the TE_{102} mode. For the TE_{103} mode the amplitude distribution of the electric field component is shown.

During the synthesis process the sample temperature is usually monitored with a pyrometer, which consists in a non-contacting device that intercepts and measures thermal radiation.

It is well established that different materials exhibit greatly different heating behaviour in the E and H microwave fields respectively (Figure 2.16).[76, 77] In general, conductive samples such as metals can be much more efficiently heated in the magnetic field. On the contrary, ceramic insulators with low conductivity such as Al_2O_3 and ZnO show much higher heating rates in the electric field.[76] If ceramics and metals are combined (mixed systems), sample heating may be performed in both electric and magnetic fields.[76, 77] This feature clearly indicates that for a complete understanding of the interaction between microwaves and matter (see *section 2.2*) it is necessary to consider the interactions of the electric and magnetic parts of the microwave separately.

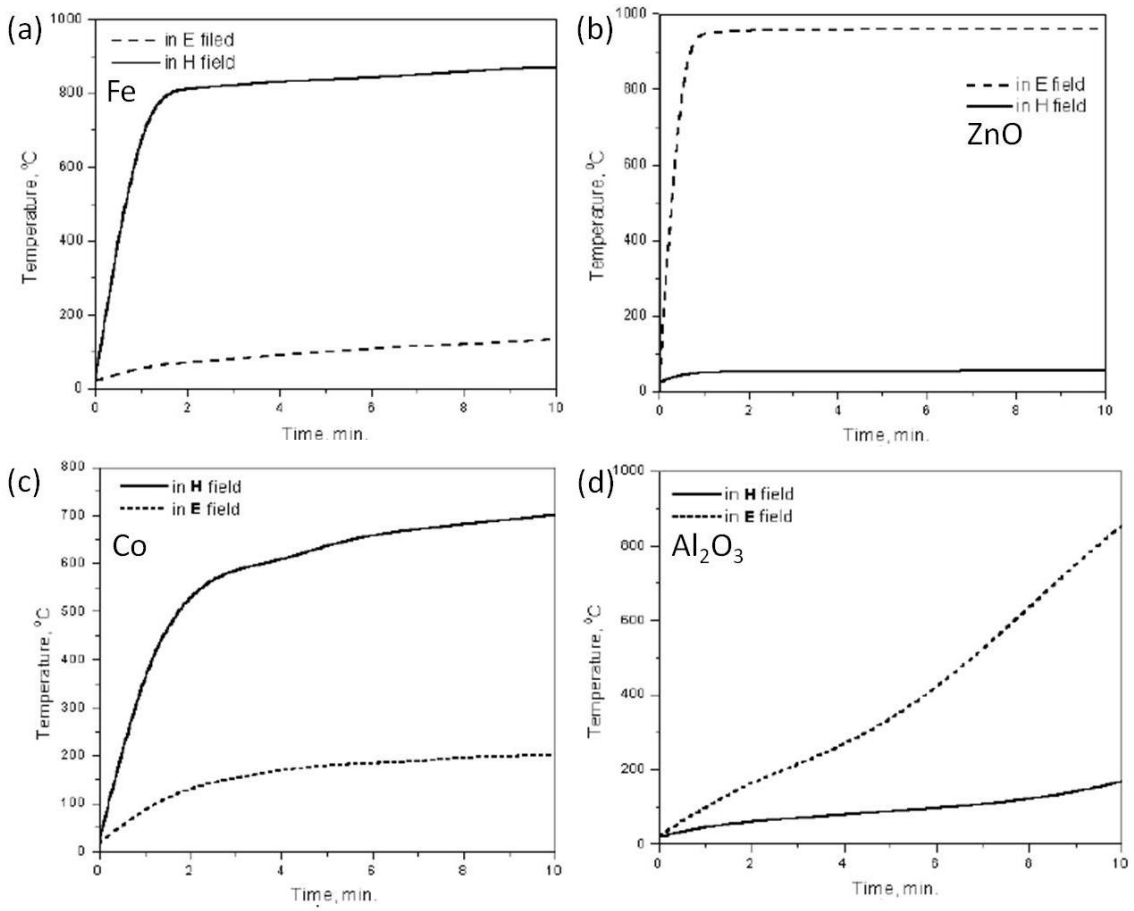

Figure 2.16. Comparison of heating rates of various compacted powder samples in microwave H and E fields. a) Fe, b) ZnO, c) Co, d) Al_2O_3.[76]

The following examples give a clear indication of the efficiency and potential use of this new methodology for the synthesis but also the sintering classification for a wide range of materials.[1, 78, 79]

1. Nano-sized cubic $BaTiO_3$ powder was prepared rapidly at 90 °C using TiO_2 and $Ba(OH)_2$ precursors by a single-mode microwave-assisted synthesis system. $BaTiO_3$ particles of 30 to 50 nm were obtained after microwave treatment for 5 min at 90 °C.[80] Unfortunately, the microwave mode employed in this work is not indicated.

2. D. Grossin *et al*.[81] demonstrated single mode microwave synthesis of $La_{0.8}Sr_{0.2}MnO_3$ using a microwave TE_{10p} cavity, where a SiC crucible was used as a microwave susceptor to facilitate an effective synthesis process within only

10 minutes. The properties of the microwave ceramics were equivalent to the properties obtained conventionally. The microwave mode employed was TE_{102}.

3. S. Marinel *et al*. [82] have observed fast sintering kinetics in CuO and ZnO for both resonant modes (TE_{102} and TE_{103}), which implies that the matter was coupling to the magnetic or electric field, and both may accelerate atomic diffusion. The overall enhancement in densification is attributed to lowering of activation energies of diffusion processes during exposure to microwave heating,[83] or more rapid delivery of the E_a necessary, as discussed before (*section 2.5*).

Here in this work single-mode microwave synthesis is applied for the preparation of the $Ba_{1.2}Mn_8O_{16}$ hollandite phase for the first time. This material has been recently studied for possible thermoelectric applications. Additionally, this technique is established for novel sintering procedures for rare earth doped ceria and $BiFeO_3$ ceramics.

2.6.3. Microwave – Hydrothermal Synthesis

In the early 1990s, Dr. Sridhar Komarneni at the University of Pennsylvania launched a pioneering work by studying and comparing the differences between hydrothermal syntheses performed with conventional means of heating and hydrothermal syntheses performed by heating special autoclaves with microwaves.[84, 85]

Hydrothermal synthesis is a "wet Chemistry", moderate-pressure method of synthesis, which consists in an aqueous solution that is heated above 100 ^{o}C in a sealed container (autoclave) and concomitantly the pressure increases. This results in an increase of the dispersion of the system components which react quickly. It should be further noted that "solvothermal" synthesis has become increasingly popular lately, where non-aqueous solvents are used.

For hydrothermal synthesis it is important to consider "subcritical" and "supercritical" synthesis conditions, where the temperature is below or above

the critical temperature of water (Tc = 374 °C) respectively. Above Tc the pressure in the synthesis autoclave raises rapidly with increasing temperature, which makes the reaction process difficult to control (Figure 2.17).[86, 87]

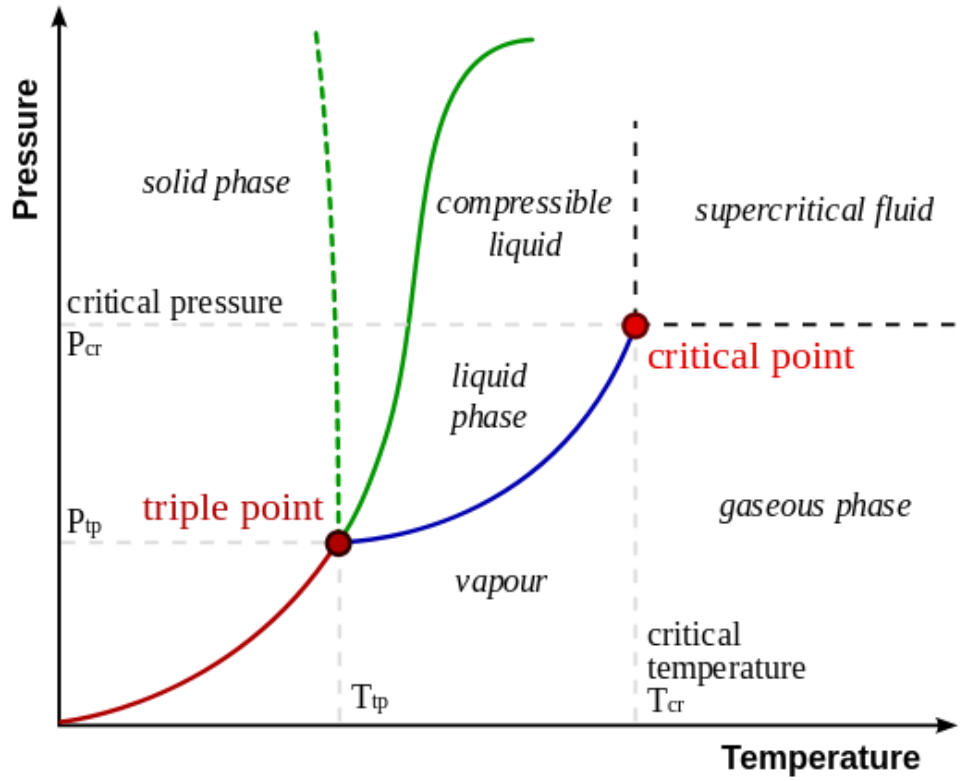

Figure 2.17. Phase diagram of water.[88]

The main difference between hydrothermal and solid-state reactions lies in the reactivity which is reflected in their different reaction mechanisms. Solid state reactions depend on the diffusion of the raw materials at their interfaces, whereas in hydrothermal or solvothermal reactions the reactant ions and/or molecules react in solution. The difference of reaction mechanisms may lead to different microstructure of the products, even if the same reactants are used.[86] Although the hydrothermal method is versatile, one of the main drawbacks is slow kinetics of solution/crystallization at any given temperature. In order to accelerate the kinetics of solution/crystallization, one may use microwaves for heating the solution, due to excellent coupling of the microwave to the water molecules in the solution.[89]

(a)

(b)

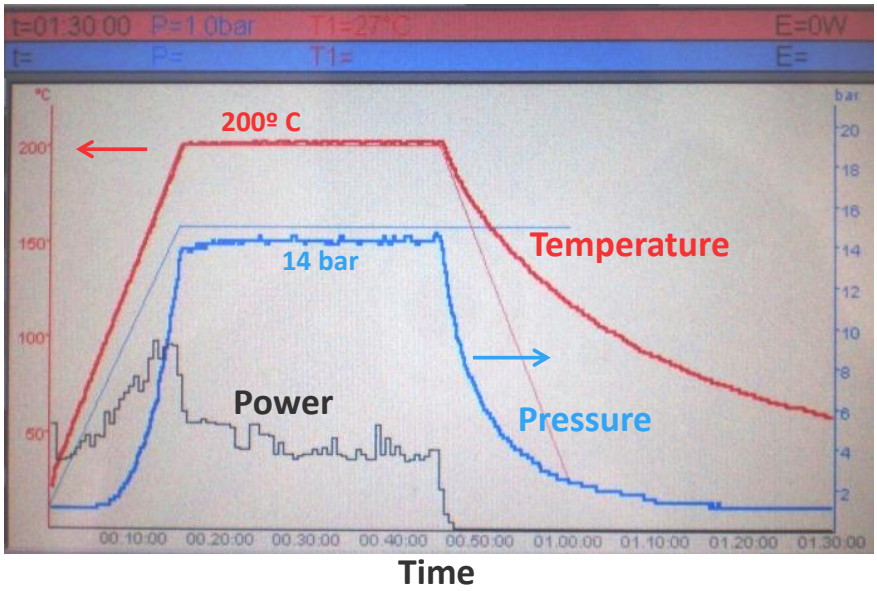

Figure 2.18. (a) Commercial Milestone Ethos One apparatus for microwave-hydrothermal synthesis. (b) Typical profile of the reaction parameters temperature, pressure and microwave power during a microwave-assisted hydrothermal synthesis process during 30 min at 200 °C and 14 bar.

Besides the characteristic microwave parameters of power and time, the method of microwave-assisted hydrothermal synthesis involves additional parameters such as the pH of the solution, the reaction temperature and pressure. Therefore, more advanced synthesis technology is required to control pressure and temperature in the subcritical region of water.

Typical commercial equipment used for microwave hydro-solvothermal processing in this work is shown in Fig. 2.18. There are several companies that

distribute microwave-hydrothermal synthesis equipment: Milestone, CEM, Biotage and Anton Paar.

In the work presented a Milestone ETHOS One apparatus was used, which is equipped with advanced reaction sensors, including direct temperature and pressure control in a single reference vessel and contact-less temperature and pressure control in all vessels.[90] Autoclaves are made out of Teflon, in which case the temperature and pressure are limited to 250 °C and 100 bars, or out of quartz (> 250 °C, 45 bars). The Milestone system releases only the excess pressure from the vessel: "Vent-and-reseal" vessels (US Patent 5,270,010)[91]. This ensures that there is no stress to the door of the microwave system, as it could happen in the case of a vessel bursting (Figure 2.19).

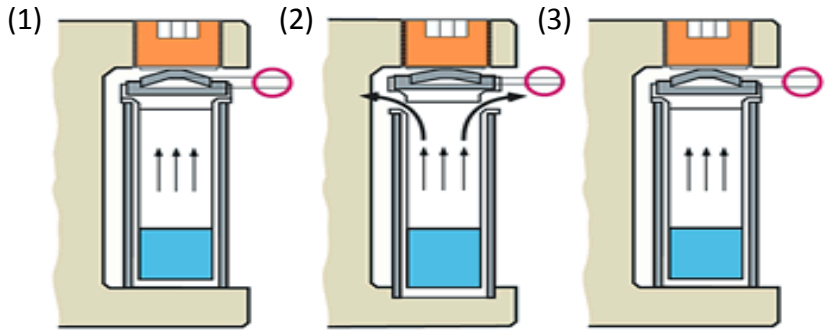

Figure 2.19. "Vent-and-reseal" Milestone technology: The "dome-shaped" spring is temporarily flattened in case of overpressure (1), allowing the cap to lift-up (2) slightly and release the pressure. Once the pressure has been released, the cap closes again (3), and the microwave program can continue.[90]

In contrast to domestic ovens, dedicated microwave-hydrothermal reactors feature a built-in magnetic stirrer, which is of great importance since without proper agitation the temperature distribution within the reaction mixture will not be uniform and the measured temperature will be dependent on the position of the temperature sensor, i.e., stirring helps the system to avoid "hot spots".[54]

Microwaves couple directly with the reactants and solvent mixture, leading to a rapid rise in temperature (Figure 2.20).

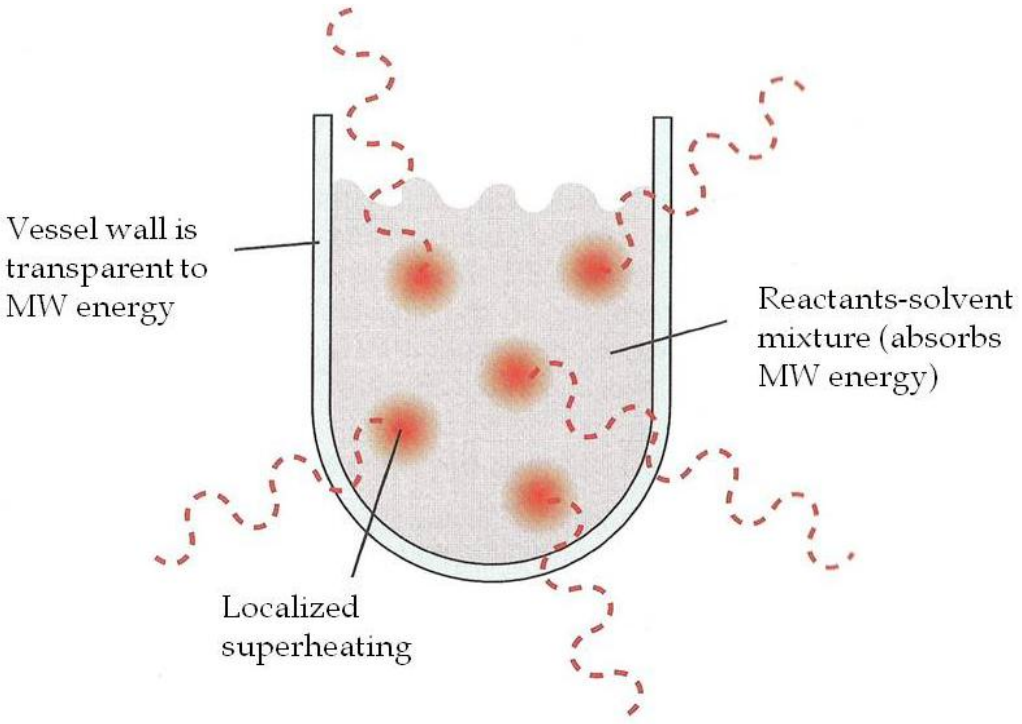

Figure 2.20. Schematic of sample heating by microwave-hydrothermal method.[7]

When microwave irradiation is combined with the hydrothermal method, an important factor is the choice of solvent.[92] The coupling efficiency of a solvent to the microwave determines the outcome of the reaction. The more efficient the solvent couples to the microwave is, the faster the temperature of reaction mixture increases. In a non-magnetic system there are two main dielectric parameters related to the ability of a solvent, in most cases water, to absorb microwave energy, which is commented in *section 2.2.*: (1) Dielectric loss (ε") and (2) dielectric constant (ε') of the solvent.[3, 7]

At 2.45 GHz, all dielectric parameters strongly depend on the temperature. As the temperature of the solvent increases, clear changes in the dielectric parameters can be observed, and hence, its coupling efficiency changes. A graphical representation of the temperature dependence of ε' and ε" in several standard solvents is shown in Figures 2.21 and 2.22.[7]

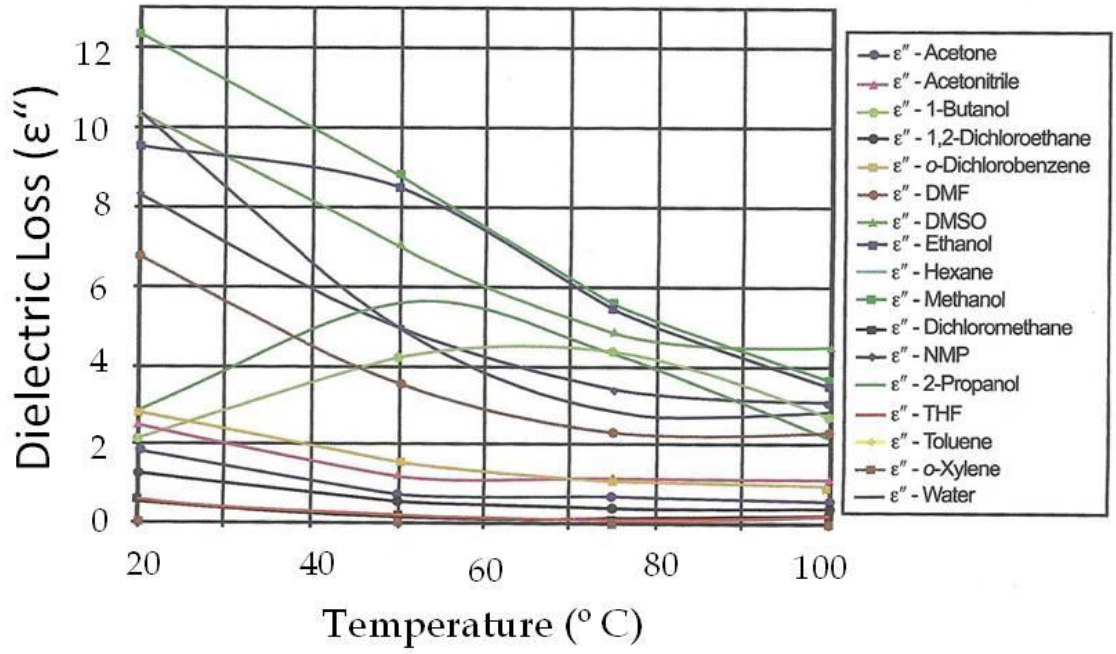

Figure 2.21. Dielectric loss vs Temperature.[7]

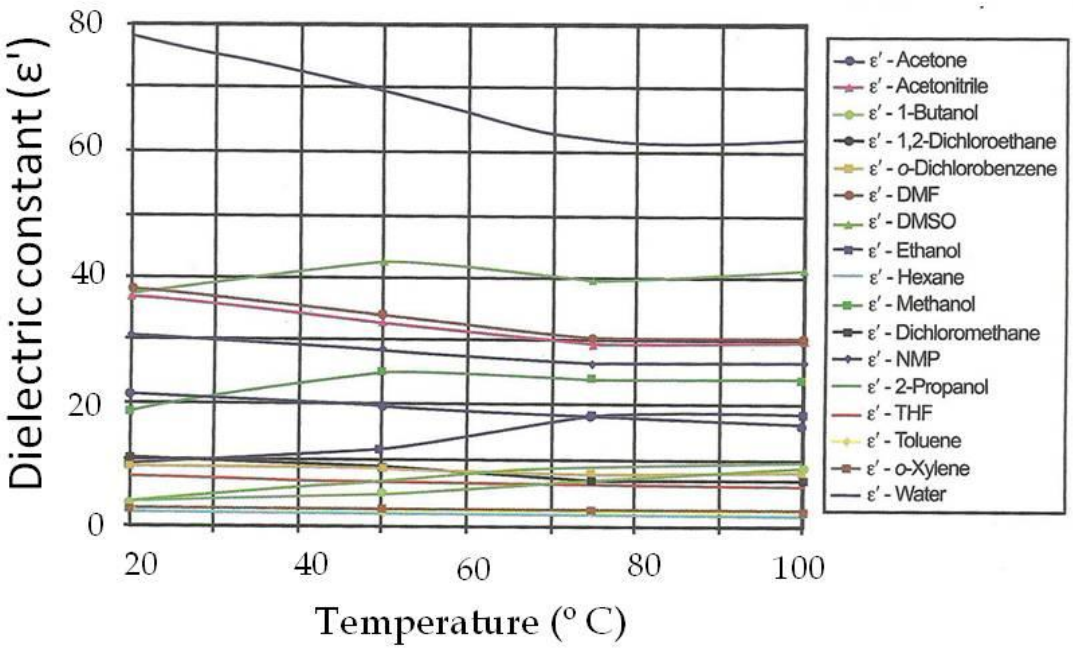

Figure 2.22. Dielectric constant vs Temperature.[7]

Solvents can easily be categorized into three different groups, examining the values of the dielectric parameters. The high microwave absorbing solvents exhibit dielectric losses higher than 14. Medium absorbers have dielectric loss values between 1 and 14, and low absorbing molecules have less than 1 (Table 2.5).[7]

Table 2.5. Dielectric constant and dielectric loss for common solvents, measured at room temperature and 2.45 GHz. Reproduced from reference 7.

Solvent (bp °C)	Dielectric Constant (ε′)	Solvent	Dielectric Loss (ε″)
Water (100)	80.4	Ethylene Glycol	49.950
Formic Acid (100)	58.5	Formic Acid	42.237
DMSO (189)	45.0	DMSO	37.125
DMF (153)	37.7	Ethanol	22.866
Acetonitrile (82)	37.5	Methanol	21.483
Ethylene Glycol (197)	37.0	Nitrobenzene	20.497
Nitromethane (101)	36.0	1-Propanol	15.216
Nitrobenzene (202)	34.8	2-Propanol	14.622
Methanol (65)	32.6	Water	9.889
NMP (215)	32.2	1-Butanol	9.764
Ethanol (78)	24.3	NMP	8.855
Acetone (56)	20.7	Isobutanol	8.248
1-Propanol (97)	20.1	2-Butanol	7.063
MEK (80)	18.5	2-Methoxyethanol	6.929
2-Propanol (82)	18.3	DMF	6.070
1-Butanol (118)	17.1	*o*-Dichlorobenzene	2.772
2-Methoxyethanol (124)	16.9	Acetonitrile	2.325
2-Butanol (100)	15.8	Nitromethane	2.304
Isobutanol (108)	15.8	MEK	1.462
1,2-Dichloroethane (83)	10.4	1,2-Dichloroethane	1.321
o-Dichlorobenzene (180)	9.9	Acetone	1.118
Dichloromethane (40)	9.1	Acetic Acid	1.079
THF (66)	7.4	Chloroform	0.437
Acetic Acid (113)	6.2	Dichloromethane	0.382
Ethyl Acetate (77)	6.0	Ethyl Acetate	0.354
Chloroform (61)	4.8	THF	0.348
Chlorobenzene (132)	2.6	Chlorobenzene	0.263
o-Xylene (144)	2.6	Toluene	0.096
Toluene (111)	2.4	*o*-Xylene	0.047
Hexane (69)	1.9	Hexane	0.038

Water has the highest dielectric constant (80.4) of the list of solvents, but dielectric loss values are medium (ε'' = 9.889, at room temperature and 2.45 GHz), so it should be classified as a medium absorber.

Microwave-hydrothermal synthesis has successfully been used for materials ranging from binary metallic oxides, oxyhydroxides and ternary oxides to more complex materials and structures such as zeolites or other mesoporous materials. It is an effective method for producing nanoparticles

and controlling the particle size through the nucleation and growth kinetics is feasible. Bellow some selected examples are listed:

1. Binary metallic oxides can be synthesized in just a few minutes: ZnO , CuO , PdO , CoO, MnO, TiO_2, CeO_2, SnO_2, HfO_2, ZrO_2, Nd_2O_3, In_2O_3, Tl_2O_3, Fe_2O_3, Fe_3O_4 and Mn_3O_4 are produced by microwave-assisted/ hydrothermal synthesis, many of them nanometer sized.[84, 93-97]

2. The synthesis of oxy-hydroxides is feasible: γ-AlOOH nanoparticules, *a*-FeOOH hollow spheres, or β-FeOOH architectures have been synthesized using the microwave-hydrothermal method with close control of temperature and pressure.[98, 99]

3. Furthermore, various ceramic perovskites have been synthesized by this technique, for example $KNbO_3$, $ATiO_3$ (A=Ba, Pb), $NaTaO_3$,[84, 100, 101] or spinels such as ZnM_2O_4 (M = Al, Ga) or AFe_2O_4 (A=Zn, Ni, Mn, Co).[102, 103]

4. In the last decade different structures of nanoporous materials, such as zeolites, have been prepared by combining the hydrothermal synthesis with microwaves. A review article published by G. A. Tompsett *et al.*,[104] presents a large number of these structures of aluminosilicates and aluminophosphates synthesized by microwave-hydrothermal: MFI, Sodalite, NaY (FAU), LSX (FAU), Analcime, Na-P1 (Gis), Ti-ZSM-5 (MFI), AlPO4, Toad, Cloverite, MnAPO-5VAPSO-44, MnAPO-5, MCM-41, SBA-15, UDF-1, PSU-1.

The main advantage of the combination of these two technologies in microwave-assisted hydrothermal synthesis may be the possibility to obtain nano-particles via quick chemical reactions.

Here in this work, the technique of hydrothermal-microwave synthesis is used for the first time to produce materials such as (a) nanosized rare-earth doped cerias which have potential application in SOFCs, (b) $BiFeO_3$ multiferroic material, and (c) $H_2V_3O_8$ nanobelts for application in lithium batteries.

2.7. References

1. Gupta, M.; Leong, E. W. W., *Microwaves and Metals*. Wiley: 2008; p 228.

2. Giordano, N., *College Physics, Volume 2, 2nd ed*. Cengage Learning: 2011.

3. Bilecka, I.; Niederberger, M., Microwave chemistry for inorganic nanomaterials synthesis. *Nanoscale* **2010,** 2, (8), 1358-1374.

4. Gabriel, C.; Gabriel, S.; H. Grant, E.; S. J. Halstead, B.; Michael P. Mingos, D., Dielectric parameters relevant to microwave dielectric heating. *Chemical Society Reviews* **1998,** 27, (3), 213-224.

5. Sanghi, R., Microwave Irradiation: way to Eco-friendly, Green Chemistry. *Resonance* **2000,** 3, 77-81.

6. Zhao, J.; Yan, W., Chapter 8 - Microwave-assisted Inorganic Syntheses. In *Modern Inorganic Synthetic Chemistry*, Elsevier: Amsterdam, 2011; pp 173-195.

7. Hayes, B. L., *Microwave synthesis: chemistry at the speed of light*. CEM Pub.: 2002; p 295.

8. Leadbeater, N. E., *Microwave Heating as a Tool for Sustainable Chemistry*. Taylor & Francis: 2010; p 290.

9. Clark, D. E.; Sutton, W. H.; Lewis, D. A., What is Microwave Processing? *Ceram. Trans.* **1997** 80, 61.

10. Clark, D. E.; Folz, D. C.; West, J. K., Processing materials with microwave energy. *Materials Science and Engineering: A* **2000,** 287, (2), 153-158.

11. Kingston, H. M.; Haswell, S. J., *Microwave-enhanced chemistry: fundamentals, sample preparation, and applications*. American Chemical Society: 1997; p 772.

12. Mingos, D. M. P.; Baghurst, D. R., Tilden Lecture. Applications of microwave dielectric heating effects to synthetic problems in chemistry. *Chemical Society Reviews* **1991,** 20, (1), 1-47.

13. Ramo, S.; Whinnery, J. R.; Van Duzer, T., *Fields and Waves in Communication Electronics*. John Wiley & Sons: 1994; p 864.

14. Lidström, P.; Tierney, J.; Wathey, B.; Westman, J., Microwave assisted organic synthesis - a review. *Tetrahedron* **2001,** 57, (45), 9225-9283.

15. Yin, C., Microwave-assisted pyrolysis of biomass for liquid biofuels production. *Bioresource Technology* **2012,** 120, 273-284.

16. Clark, D. E.; Sutton, W. H.; Lewis, D. A., What is Microwave Processing? *Ceram. Trans.* **1997** 80, 61.

17. Berteaud, A. J.; Badot, J. C., High Temperature Microwave Heating in Refractory Materials. *Journal of the Microwave Power and Electromagnetic Energy* **1976,** 11, 315-320.

18. Kumar, P. P.; Yashonath, S., Journal of Chemical Sciences. *Journal of Chemical Sciences* **2006,** 118, 135-154.

19. Whittaker, G., Microwave chemistry. *School Science Review* **2004,** 85, (312), 87-94.

20. Rao, K. J.; Vaidhyanathan, B.; Ganguli, M.; Ramakrishnan, P. A., Synthesis of Inorganic Solids Using Microwaves. *Chemistry of Materials* **1999,** 11, (4), 882-895.

21. Sahu, R.; Rao, M.; Manoharan, S. S., Microwave synthesis of magnetoresistive $La_{0.7}Ba_{0.3}MnO_3$ using inorganic precursors. *Journal of Materials Science* **2001,** 36, (17), 4099-4102.

22. Bogdal, D., *Microwave-assisted Organic Synthesis: One Hundred Reaction Procedures*. Elsevier Science: 2006; p 214.

23. Zhang, Y.; Zhai, Y., Magnetic Induction Heating of Nano-sized Ferrite Particles. In *Advances in Induction and Microwave Heating of Mineral and Organic Materials*, Grundas, S., Ed. InTech: 2011; pp 483-500.

24. Stoppels, D., Developments in soft magnetic power ferrites. *Journal of Magnetism and Magnetic Materials* **1996,** 160, 323-328.

25. Inoue, O.; Matsutani, N.; Kugimiya, K., Low loss MnZn-Ferrites : Frequency dependence of minimun power loss temperature. *IEEE Transactions on Magnetics* **1993,** 29, (6), 3532-3534.

26. Horikoshi, S.; Sumi, T.; Serpone, N., Unusual effect of the magnetic field component of the microwave radiation on aqueous electrolyte solutions. *Journal of Microwave Power and Electromagnetic Energy* **2012,** 46, (4), 215-228.

27. Moulson, A. J.; Herbert, J. M., *Electroceramics: Materials, Properties, Applications*. Wiley: 2003.

28. Hill, M. The Microwave Palaeointensity Technique and its Application to Lava. University of Liverpool, Liverpool, 2000.

29. Yoshikawa, N., Recent Studies on Fundamentals and Application of Microwave Processing of Materials. In *Advances in Induction and Microwave Heating of Mineral and Organic Materials*, Grundas, S., Ed. InTech: 2011; pp 3 - 26.

30. Herrero, M. A.; Kremsner, J. M.; Kappe, C. O., Nonthermal Microwave Effects Revisited: On the Importance of Internal Temperature Monitoring and Agitation in Microwave Chemistry. *The Journal of Organic Chemistry* **2007,** 73, (1), 36-47.

31. Wroe, R.; Rowley, A. T., Evidence for a non-thermal microwave effect in the sintering of partially stabilized zirconia. *Journal of Materials Science* **1996,** 31, (8), 2019-2026.

32. De la Hoz, A.; Diaz-Ortiz, A.; Moreno, A., Microwaves in organic synthesis. Thermal and non-thermal microwave effects. *Chemical Society Reviews* **2005,** 34, (2), 164-178.

33. Fini, A.; Breccia, A., Chemistry of microwaves. *Pure and Applied Chemistry* **1999,** 71, (4), 573-579.

34. Suvorov, S. A.; Turkin, I. A.; Printsev, L. N.; Smirnov, A. V., Microwave Synthesis of Materials from Aluminum Oxide Powders. *Refractories and Industrial Ceramics* **2000,** 41, (9-10), 295-299.

35. Saxena, V. K.; Chandra, U., Microwave Synthesis: a Physical Concept. In *Microwave Heating*, Chandra, U., Ed. InTech: 2011; pp 1-22.

36. Thostenson, E. T.; Chou, T. W., Microwave processing: fundamentals and applications. *Composites Part A: Applied Science and Manufacturing* **1999,** 30, (9), 1055-1071.

37. Tanaka, M.; Kono, H.; Maruyama, K., Selective heating mechanism of magnetic metal oxides by a microwave magnetic field. *Physical Review B* **2009,** 79, (10), 104420.

38. Stuerda, D., *Microwaves in Organic Synthesis: Microwave–Material Interactions and Dielectric Properties, Key Ingredients for Mastery of Chemical Microwave Processes*. Wiley: 2006; p 1-61.

39. Peng, Z.; Hwang, J.-Y.; Andriese, M., Magnetic Loss in Microwave Heating. *Applied Physics Express* **2012,** 5, (2), 027304.

40. Schanche, J.-S., Microwave synthesis solutions from personal chemistry. *Molecular Diversity* **2003,** 7, (2-4), 291-298.

41. Peng, J.; Binner, J.; Bradshaw, S., Microwave Initiated Self-Propagating High-Temperature Synthesis of materials. *Materials Science and Technology* **2002,** 18, 1419-1427.

42. Gerbec, J. A.; Magana, D.; Washington, A.; Strouse, G. F., Microwave-Enhanced Reaction Rates for Nanoparticle Synthesis. *Journal of the American Chemical Society* **2005,** 127, (45), 15791-15800.

43. Li, J.; Huang, J.; Wu, J.; Cao, L.; Li, Q.; Yanagisawa, K., Microwave-assisted growth of $WO_3 \cdot 0.33H_2O$ micro/nanostructures with enhanced visible light photocatalytic properties. *CrystEngComm* **2013,** 15, (39), 7904-7913.

44. Chung, S. L.; Tsai, T. I.; Huang, S. C., High thermal conductivity ceramics from combustion synthesized AlN powder through microwave sintering and reheating. *International Journal of Self-Propagating High -Temperature Synthesis* **2012,** 21, (1), 45-50.

45. Marinaro, M.; Nobili, F.; Tossici, R.; Marassi, R., Microwave-assisted synthesis of carbon (Super-P) supported copper nanoparticles as conductive agent for $Li_4Ti_5O_{12}$ anodes for Lithium-ion batteries. *Electrochimica Acta* **2013,** 89, 555-560.

46. Liu, Y.-Q.; Zhang, M.; Wang, F.-X.; Pan, G.-B., Facile microwave-assisted synthesis of uniform single-crystal copper nanowires with excellent electrical conductivity. *RSC Advances* **2012,** 2, (30), 11235-11237.

47. Komarneni, S.; Katsuki, H., Nanophase materials by a novel microwave-hydrothermal process. *Pure and Applied Chemistry* **2002,** 74, (9), 1537 - 1543.

48. Galema, S. A., Microwave chemistry. *Chemical Society Reviews* **1997,** 26, (3), 233-238.

49. Zhang, X.; Hayward, D. O.; Mingos, D. M. P., Apparent equilibrium shifts and hot-spot formation for catalytic reactions induced by microwave dielectric heating. *Chemical Communications* **1999,** 11, 975-976.

50. Das, S.; Mukhopadhyay, A. K.; Datta, S.; Basu, D., Prospects of microwave processing: An overview. *Bulletin of Material Science* **2009,** 32, (1), 1-13.

51. Bykov, Y. V.; Rybakov, K. I.; Semenov, V. E., High-temperature microwave processing of materials. *Journal of Physics D: Applied Physics* **2001,** 34, (13), R55.

52. Liu, X.; Zhang, Z.; Wu, Y., Absorption properties of carbon black/silicon carbide microwave absorbers. *Composites Part B: Engineering* **2011,** 42, (2), 326-329.

53. Kremsner, J. M.; Kappe, C. O., Silicon Carbide Passive Heating Elements in Microwave-Assisted Organic Synthesis. *The Journal of Organic Chemistry* **2006,** 71, (12), 4651-4658.

54. Kremsner, J. M.; Stadler, A., *A chemist's guide to microwave synthesis: Basics, equipment & application examples*. Anton Paar: 2013; p 94.

55. Conner, W. C.; Tompsett, G. A., How Could and Do Microwaves Influence Chemistry at Interfaces? *The Journal of Physical Chemistry B* **2008,** 112, (7), 2110-2118.

56. Falamaki, C., *Frontiers of Solid State Chemistry: Proceedings of the International Symposium on Solid State Chemistry in China, Changchun, China, 9-12 August, 2002*. World Scientific: 2002.

57. Brosnan, K. H.; Messing, G. L.; Agrawal, D. K., Microwave Sintering of Alumina at 2.45 GHz. *Journal of the American Ceramic Society* **2003,** 86, (8), 1307.

58. Tian, Y.; Zhang, P.; Zheng, Z.; Chai, Y., A novel approach for preparation of $Sr_3Al_2O_6:Eu^{2+}$, Dy^{3+} nanoparticles by sol-gel microwave processing. *Materials Letters* **2012,** 73, 157-160.

59. Phani, A. R.; Ruggieri, F.; Passacantando, M.; Santucci, S., Low temperature growth of nanocrystalline Fe_2TiO_5 perovskite thin films by sol-gel process assisted by microwave irradiation. *Ceramics International* **2008,** 34, (1), 205-211.

60. Rosa, R.; Veronesi, P.; Leonelli, C., A review on combustion synthesis intensification by means of microwave energy. *Chemical Engineering and Processing: Process Intensification* **2013**, 71, 2-18

61. Nehru, L. C.; Swaminathan, V.; Sanjeeviraja, C., Rapid synthesis of nanocrystalline ZnO by a microwave-assisted combustion method. *Powder Technology* **2012,** 226, 29-33.

62. Darcovich, K.; Biton, J.; Magnier, J., Calculation of the electromagnetic field in a multimode microwave cavity for sintering planar-perovskite SOFC ceramics. *Journal of Electroceramics* **2007,** 19, (2-3), 195-206.

63. Parada, C.; Morán, E., Microwave-Assisted Synthesis and Magnetic Study of Nanosized Ni/NiO Materials. *Chemistry of Materials* **2006,** 18, (11), 2719-2725.

64. Vaidhyanathan, B.; Raizada, P.; Rao, K. J., Microwave assisted fast solid state synthesis of niobates and titanates. *Journal of Materials Science Letters* **1997,** 16, (24), 2022-2025.

65. Hutagalung, S. D.; Ibrahim, M. I. M.; Ahmad, Z. A., Microwave assisted sintering of $CaCu_3Ti_4O_{12}$. *Ceramics International* **2008,** 34, (4), 939-942.

66. Yu, H.; Liu, H.; Luo, D.; Cao, M., Microwave synthesis of high dielectric constant $CaCu_3Ti_4O_{12}$. *Journal of Materials Processing Technology* **2008,** 208, (1-3), 145-148.

67. Chung, S.-Y.; Kim, I.-D.; Kang, S.-J. L., Strong nonlinear current-voltage behaviour in perovskite-derivative calcium copper titanate. *Nat Mater* **2004,** 3, (11), 774-778.

68. Schmidt, R.; Sinclair, D., $CaCu_3Ti_4O_{12}$ (CCTO) Ceramics for Capacitor Applications. In *Capacitors: Theory of Operation, Behavior and Safety Regulations*, Muller, K. N., Ed. 2013; p 91.

69. Vanetsev, A. S.; Ivanov, V. K.; Tret'yakov, Y. D., Microwave Synthesis of Lithium, Copper, Cobalt, and Nickel Ferrites. *Doklady Chemistry* **2002**, (387), 332-334.

70. Yan, H.; Huang, X.; Chen, L., Microwave synthesis of $LiMn_2O_4$ cathode material. *Journal of Power Sources* **1999,** 81-82, 647-650.

71. Ragupathy, P.; Vasan, H. N.; Munichandraiah, N., Microwave driven hydrothermal synthesis of $LiMn_2O_4$ nanoparticles as cathode material for Li-ion batteries. *Materials Chemistry and Physics* **2010,** 124, (1), 870-875.

72. Díez, A.; Schmidt, R.; Sagua, A. E.; Frechero, M. A.; Matesanz, E.; Leon, C.; Morán, E., Structure and physical properties of nickel manganite $NiMn_2O_4$ obtained from nickel permanganate precursor. *Journal of European Ceramic Society* **2010,** 30, 2617-2624.

73. Gonzalo, E. C.; Morán, E.; Parada, C.; Ehrenberg, H., Microwave-assisted synthesis of $LiCoO_2$ and $LiCo_{1-x}Ga_xO_2$: Structural features, magnetism and electrochemical characterization. *Materials Chemistry and Physics* **2010,** 121, (3), 484-488.

74. Kitchen, H. J.; Vallance, S. R.; Kennedy, J. L.; Tapia-Ruiz, N.; Carassiti, L.; Harrison, A.; Whittaker, A. G.; Drysdale, T. D.; Kingman, S. W.; Gregory, D. H., Modern Microwave Methods in Solid-State Inorganic Materials Chemistry: From Fundamentals to Manufacturing. *Chemical Reviews* **2014** DOI: 10.1021/cr4002353.

75. Rosa, R.; Veronesi, P.; Leonelli, C., A review on combustion synthesis intensification by means of microwave energy. *Chemical Engineering and Processing: Process Intensification* **2013,** 71, 2-18.

76. Cheng, J.; Roy, R.; Agrawal, D., Radically different effects on materials by separated microwave electric and magnetic fields. *Materials Research Innovations* **2002,** 5, 170-177.

77. Roy, R.; Peelamedu, R.; Hurtt, L.; Cheng, J.; Agrawal, D., Definitive experimental evidence for Microwave Effects: radically new effects of separated E and H fields, such as decrystallization of oxides in seconds. *Materials Research Innovations* **2002,** 6, 128-140.

78. Vetl , G.; Petzoldt, F.; Pueschner, P. A. In *Effects of microwave on sintering processes*, PM2004 World Congress, Vienna, October, 2004; EMPA: Vienna, 2004.

79. Borrell, A.; Salvador, M. D.; Peñaranda-Foix, F. L.; Cátala-Civera, J. M., Microwave Sintering of Zirconia Materials: Mechanical and Microstructural Properties. *International Journal of Applied Ceramic Technology* **2012,** 10, (2), 313-320.

80. Katsuki, H.; Furuta, S.; Komarneni, S., Semi-continuous and fast synthesis of nanophase cubic $BaTiO_3$ using a single-mode home-built microwave reactor. *Materials Letters* **2012,** 83, 8-10.

81. Grossin, D.; Marinel, S.; Noudem, J. G., Materials processed by indirect microwave heating in a single-mode cavity. *Ceramics International* **2006,** 32, (8), 911-915.

82. Marinel, S.; Savary, E.; Gomina, M., Sintering of CuO and ZnO in a Single Mode Microwave Cavity with Shrinkage Control. *Journal of Microwave Power and Electromagnetic Energy* **2010,** 44, (1), *57-63*.

83. Demirskyi, D.; Agrawal, D.; Ragulya, A., Densification kinetics of powdered copper under single-mode and multimode microwave sintering. *Materials Letters* **2010,** 64, 1433-1436.

84. Komarneni, S.; Roy, R.; Li, Q. H., Microwave-hydrothermal synthesis of ceramic powders. *Materials Research Bulletin* **1992,** 27, (12), 1393-1405.

85. Komarneni, S.; Katsuki, H., Nanophase materials by a novel microwave-hydrothermal process. *Pure and Applied Chemistry* **2002,** 74, (9), 1537-1543.

86. Feng, S.; Li, G., Hydrothermal ans Solvothermal Syntheses. In *Modern Inorganic Synthetic Chemistry*, Elsevier B.V.: 2011; pp 63-93.

87. Alario, M. A.; Morán, E., Materiales inorgánicos bajo presión. *Anales de Química* **2002,** 98, (2), 5-15.

88. Critical point (thermodynamics) http://en.wikipedia.org/wiki/Critical_point_(thermodynamics). **2013**.

89. Komarneni, S., Nanophase materials by hydrothermal, microwave-hydrothermal and microwave-solvothermal methods. *Current Science* **2003,** 85, (12), 1730-1734.

90. Favretto, L., Milestone's microwave labstation. *Molecular Diversity* **2003,** 7, 287-291.

91. Lautenschlager, W. Sample holder for decomposition or analysis of sample materials. 1993.

92. Rajamathi, M.; Seshadri, R., Oxide and chalcogenide nanoparticles from hydrothermal/solvothermal reactions. *Current Opinion in Solid State and Materials Science* **2002,** 6, (4), 337-345.

93. Bilecka, I.; Djerdj, I.; Niederberger, M., One-minute synthesis of crystalline binary and ternary metal oxide nanoparticles. *Chemical Communications* **2008,** 7, 886-888.

94. Huang, J.; Xia, C.; Cao, L.; Zeng, X., Facile microwave hydrothermal synthesis of zinc oxide one-dimensional nanostructure with three-dimensional morphology. *Materials Science and Engineering: B* **2008,** 150, (3), 187-193.

95. Patra, C. R.; Gedanken, A., Rapid synthesis of nanoparticles of hexagonal type In_2O_3 and spherical type Tl_2O_3 by microwave irradiation. *New Journal of Chemistry* **2004,** 28, (8), 1060-1065.

96. Komarneni, S.; Rajha, R. K.; Katsuki, H., Microwave-hydrothermal processing of titanium dioxide. *Materials Chemistry and Physics* **1999,** 61, (1), 50-54.

97. Wang, K.; Huang, T.; Liu, H.; Zhao, Y.; Liu, H.; Sun, C., Size control synthesis of palladium oxide nanoparticles by microwave irradiation. *Colloids and Surfaces A: Physicochemical and Engineering Aspects* **2008,** 325, (1-2), 21-25.

98. Zhang, L.; Zhu, Y.-J., Microwave-Assisted Solvothermal Synthesis of AlOOH Hierarchically Nanostructured Microspheres and Their Transformation to β-Al_2O_3 with Similar Morphologies. *The Journal of Physical Chemistry C* **2008,** 112, (43), 16764-16768.

99. Cao, S.-W.; Zhu, Y.-J., Iron oxide hollow spheres: Microwave-hydrothermal ionic liquid preparation, formation mechanism, crystal phase and morphology control and properties. *Acta Materialia* **2009,** 57, (7), 2154-2165.

100. Shi, J.; Liu, G.; Wang, N.; Li, C., Microwave-assisted hydrothermal synthesis of perovskite $NaTaO_3$ nanocrystals and their photocatalytic properties. *Journal of Materials Chemistry* **2012,** 22, (36), 18808-18813.

101. Zhu, X.; Wang, J.; Zhang, Z.; Zhu, J.; Zhou, S.; Liu, Z.; Ming, N., Perovskite Nanoparticles and Nanowires: Microwave–Hydrothermal Synthesis and Structural Characterization by High-Resolution Transmission Electron Microscopy. *Journal of the American Ceramic Society* **2008,** 91, (8), 2683-2689.

102. Conrad, F.; Massue, C.; Kuhl, S.; Kunkes, E.; Girgsdies, F.; Kasatkin, I.; Zhang, B.; Friedrich, M.; Luo, Y.; Armbruster, M.; Patzke, G. R.; Behrens, M., Microwave-hydrothermal synthesis and characterization of nanostructured copper substituted ZnM_2O_4 (M = Al, Ga) spinels as precursors for thermally stable Cu catalysts. *Nanoscale* **2012,** 4, (6), 2018-2028.

103. Komarneni, S.; D'Arrigo, M. C.; Leonelli, C.; Pellacani, G. C.; Katsuki, H., Microwave-Hydrothermal Synthesis of Nanophase Ferrites. *Journal of the American Ceramic Society* **1998,** 81, (11), 3041-3043.

104. Tompsett, G. A.; Conner, W. C.; Yngvesson, K. S., Microwave Synthesis of Nanoporous Materials. *ChemPhysChem* **2006,** 7, (2), 296-319.

3. *EXPERIMENTAL TECHNIQUES*

3.1. Introduction

Several instrumental techniques were used to characterize the composition and crystal structure of the powder and bulk morphologies in order to assess the powder quality and functionality of the materials synthesized by the different microwave techniques. X-Ray diffraction (XRD) was used for all samples in order to confirm the desired crystal structure. Other techniques were employed according to the requirements to validate the relevant parameters for applications. In general, the characterizations are important to assess the usefulness of the microwave-assisted synthesis techniques applied in terms of the possibility to obtain the correct crystal phase and the desired physical properties relevant for potential applications.

3.2. Powder X-ray Diffraction & Rietveld Refinement

X-Ray diffraction (XRD) is a fundamental technique in solid state chemistry. The most important use of the powder XRD method is the qualitative identification of crystalline phases. Furthermore, a high quality XRD pattern helps to quantify different phases presented in a sample, to refine unit cell size, atom positions, to measure thermal coefficients and to study phase transformations.[1]

Routine powder X-ray diffraction (XRD) patterns of all samples synthesized in this work were collected on a SIEMENS D-5000 diffractometer, using Cu K_α. The Cu source generates the X-ray beam at a wavelength of λ =

1.54056 Å. The working conditions were typically 2θ scanning between 5 – 90 º, with a 0.04 º step and a counting time of 1 s. Longer measurements were carried out on a Philips X'Pert PRO ALPHA1 Panalytical B.V. diffractometer with Cu $K_{\alpha 1}$ monochromatic radiation (λ = 1.54056 Å) equipped with a primary curved Ge111 primary beam monochromator and a speed X'Celerator fast detector, operating at 45 kV and 40 mA. XRD pattern were collected in the 2θ range of 5 – 120 ° at room temperature with an angle step size of 0.017 ° and 8 s counting time in order to ensure sufficient resolution for structural refinements.

Powder X-ray Thermodiffraction patterns were collected on an X'Pert PRO MPD diffractometer with an Anton Paar HTK1200 camera, using Cu K_{α} radiation. The standard working conditions were: 2θ range of 10 – 120 ° with angle step size of 0.033 º and 25 s counting time. The diffractometers utilized are located in the "CAI de Difracción de Rayos X" at the Universidad Complutense de Madrid.

High-resolution synchrotron X-ray powder diffraction patterns were collected at the SpLine beamline (BM25A) of the Spanish CRG at the European Synchrotron Radiation Facility (ESRF, Grenoble)[2] with a fixed wavelength of λ = 0.49684897Å (24954.112 eV) at room temperature.

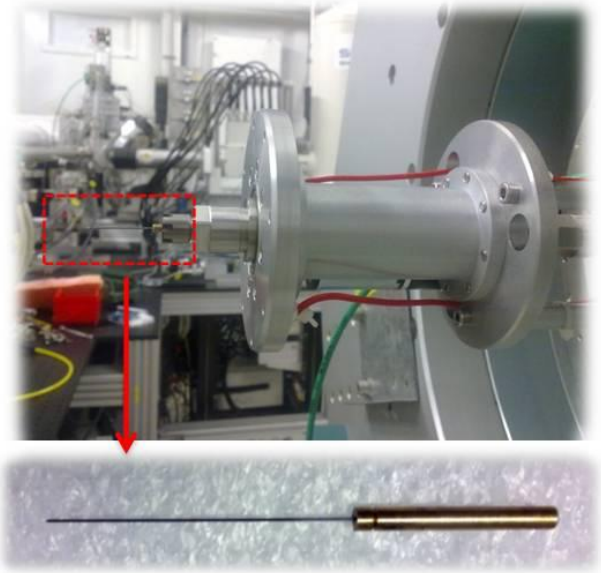

Figure 3.1. Loaded capillary stuck attached to the holder base. Zoom: 0.5 mm diameter capillary.

The radiation generated is of high brightness and high intensity, many orders of magnitude more than X-ray laboratory source. Furthermore, there is a wide choice of wavelengths available.

Powdered samples were placed inside a 0.2 - 0.5 mm diameter capillary (Figure 3.1.), which were rotated during exposure. Data were collected in a continuous 2θ-scan mode from 3° to 30°. Fullprof software[3] was employed to carry out structural refinements from both conventional and synchrotron XRD patterns using the Rietveld method. This method of refining powder diffraction data was used for refining several parameters:[4, 5] Zero shift, lattice parameters, background, peak width, shape and asymmetry, atomic positions and isotropic temperature factors. Thompson–Cox-Hastings pseudo-Voigt functions [6] with convoluted axial divergence asymmetry were used to describe the peak shape. Linear interpolation between a set of background points with refinable heights was used to determine the background. All values were refined to improve the agreement factors: weighted profile R-factor (R_{wp}), expected *R* factor (R_{exp}), R Bragg and goodness of fit (χ^2). Smaller error index values indicate a better fit of a model to the data.[7]

3.3. Scanning Electron Microscopy (SEM)

Scanning electron microscopy (SEM) uses a focused electron probe to extract topological and chemical information from a region of interest in the sample. The high spatial resolution of an SEM makes it a powerful tool to characterize a wide range of specimen at the nanometer to micrometer length scales.[8] The SEM allows both, wide angle images and high resolution spot analysis. This technique has a large depth of field, which allows a large amount of the sample to be in focus at one time.[9]

Because the SEM utilizes vacuum conditions and uses electrons to form an image, special preparations must be done to the sample. All water must be removed from the samples so it is necessary to dry each samples at 80 ^{o}C for

some hours. The sample surface has to be conductive and therefore all non-conducting samples needs to be covered with a thin layer of conductive material (gold or graphite) using a dc sputter coater using Argon gas.

It is possible to work in two different modes: (1) Secondary electron mode and (2) Backscattered electron mode.

Secondary electron imaging is more surface sensitive and has greater spatial resolution. The escape depth of backscattered electrons is greater than that of secondary electrons, consequently resolution of surface topographical characteristics may suffer. On the other hand, backscattered electrons have the advantage that they are sensitive to the atomic mass of the nuclei they scatter from. As a result, heavier elements which backscatter more efficiently appear brighter than lighter elements in a backscattered electron image.[10] A secondary electron image mainly displays topological contrast, whereas a backscattered electron image shows mainly elemental contrast.

Here in this work all samples investigated were sputter coated with Au using a EMITECH K550 apparatus and field-emission scanning electron microscopy (FE-SEM) was carried out by using a JEM 6335 F electron microscope with a field-emission gun operating at 10 kV and equipped with a LINK ISIS 300 detector for energy-dispersive analysis of X-rays (EDAX). The microscope is located at the "ICTS Centro Nacional de Microscopía Electrónica" (Universidad Complutense de Madrid).

3.4. Transmission Electron Microscopy (TEM)

A Transmission Electron Microscope (TEM) utilizes energetic electrons to provide morphologic, compositional and crystallographic information from thin samples. Electrons pass across the sample,[11] some fraction of them will be scattered to particular angles, determined by the crystal structure of the sample. As a result, the image on the screen of the TEM will be a series of spots—the

Selected area electron diffraction SAED pattern, where each spot corresponds to a satisfied diffraction condition of the sample's crystal structure and indicates a crystallographic direction.[12] It is possible to perform microdiffraction where the convergence angle is smaller (<0.01^{o}), which provides additional information, such as the symmetry of the lattice.

High-Resolution transmission electron microscopy (HRTEM) is a powerful tool in imaging defects. It shows directly a two-dimensional projection of the crystal with atomic resolution. The diffraction pattern corresponds to the Fourier transform of the periodic potential of the electron clouds associated to individual atoms in two dimensions.[13]

Samples for TEM techniques were prepared by ultrasonic dispersion of the powder in n-butanol. Drops of this dispersion were deposited on a carbon-coated copper grid to form a thin layer which would be electron transparent. JEOL 2000FX and JEOL Jem 2100, equipped with a LINK ISIS 300 analyzer have been used for selected area electron diffraction (SAED). HRTEM was performed using a JEOL 3000F TEM yielding a resolution limit of 1.1 Å. Images were recorded with an objective aperture of 70 μm centered on a sample spot within the diffraction pattern area. Fast Fourier Transforms (FFTs) of the HRTEM images were carried out to reveal the periodic image contents using the Digital Micrograph package.[14] The exit wave has been reconstructed from the focal series using the IWFR software[15]. The microscopes used are located at the "ICTS Centro Nacional de Microscopía Electrónica" (Universidad Complutense de Madrid).

The experimental HRTEM images were also compared to simulated images using MacTempas software.[16] Such computations were performed using information from the structural parameters obtained from the Rietveld refinement, the microscope parameters such as microscope operating voltage (300 kV) and spherical aberration coefficient (0.6 mm), and the specimen parameters such as zone axis and thickness. The defocus and sample thickness

parameters were optimized by assessing the agreement between model and data.

3.5. Electron Energy Loss Spectroscopy (EELS)

EELS measures the changes in the energy distribution of an electron beam transmitted through a thin electron transparent specimen. Each type of interaction between the electron beam and the specimen produces a characteristic change in the energy and angular distribution of scattered electrons. The energy loss process is the primary interaction event.[17] This technique helps to determine oxidation states of atoms.

EELS studies were performed in a Philips CM200FEG electron microscope (point resolution ≈ 0.23 nm, acceleration voltage of 200 kV), equipped with a Gatan Image Filter GIF200 spectrometer (energy resolution ≈ 0.70 eV). All the experiments were performed at the "ICTS Centro Nacional de Microscopía Electrónica" (Universidad Complutense de Madrid).

3.6. Thermal Analysis

Thermogravimetric Analysis (TGA) measures the amount and rate of change in the weight of a material as a function of temperature and time in a controlled atmosphere. Measurements are used primarily to determine the composition of materials and to predict their thermal stability at temperatures up to 1000 °C. The technique can characterize materials that exhibit weight loss or gain due to decomposition, oxidation, reduction or dehydration.[18] Differential Thermal Analysis (DTA) measures the temperature difference of the sample versus a reference, caused by thermal events in a material. It provides similar information to differential scanning calorimetry (DSC). DTA usually complements TGA with detailed information on phase transitions. Both analyses were carried out in a TA Instruments apparatus (SDT Q600 model)

located in the Departamento Química Inorgánica I (Universidad Complutense de Madrid).

The oxygen content of certain samples was determined by using thermogravimetric analysis (TGA) on a Cahn D-200 electrobalance on samples of about 50 mg in a H_2 (200 mbar)/He (400 mbar) atmosphere heating until 700ºC at 5 ºC/min ratio. The apparatus is located in the Departamento Química Inorgánica I (Universidad Complutense de Madrid).

Specific Heat Capacity (C_p) corresponds to the quantity of heat required to raise the temperature of a substance. C_p measurements were performed on a thermal analyzer NETZSCH STA 449 F3 Jupiter located in the CRISMAT – CNRS laboratories (Caen, France).

3.7. Raman Spectroscopy

Raman spectroscopy helps to determine the chemical structure of a sample and identify different phases present by measuring molecular vibrations, similar to Fourier Transform Infrared Spectroscopy (FTIR). However, the Raman method yields better spatial resolution and enables the analysis of smaller samples. Raman spectroscopy as such is based on the inelastic scattering of monochromatic light laser when the frequency of photons changes upon interaction with a sample. The photons of the laser light are absorbed by the sample and subsequently reemitted. The frequency of the reemitted photons is shifted up or down in comparison with the original monochromatic frequency, which is known as the Raman shift. The Raman shift provides information about vibrational and rotational energies of molecular bonds.[19]

Raman spectroscopy was carried out at room temperature on sintered and polished pellets using a WITec Alpha-300R confocal Raman microscope with a 532 nm laser. At least 20 measurements were done in different points of

the samples studied to investigate the possible presence of secondary phases. The instrument is located at the Instituto de Cerámica y Vidrio, ICV-CSIC, Madrid.

3.8. Fourier Transform Infrared Spectroscopy (FTIR)

In FTIR analysis, a spectrum of molecular vibrations is obtained in order to identify or characterize different materials, similar as for Raman spectroscopy. For infrared spectroscopy, samples were analyzed by grinding and mixing the powder sample together with potassium bromide and pressing the mix into a disc. The choice of KBr is due to its wide spectral range. This salt is transparent from the near ultraviolet to long-wave infrared wavelengths.

Infrared (IR) spectra of a KBr pellet (≈ 150 mg), containing approximately 2 mg of sample dried previously at 80 ^{o}C were recorded by using an FTIR Thermo-Nicolet 200 spectrophotometer in the 4000-400 cm^{-1} frequency range. This apparatus is lacoated in the Departamento Química Inorgánica I (Universidad Complutense de Madrid).

3.9. Inductively Coupled Plasma Optical Emission Spectrometry (ICP-OES)

Inductive Coupled Plasma (ICP) spectroscopy can quantitatively measure the elemental content of a material from the ppt to the wt% range. The only elements that cannot be measured by ICP methods are C, H, O, N and the halogens. Solid samples are dissolved in a liquid, usually an acidic aqueous solution. The sample solution is then sprayed into the core of and inductively coupled argon plasma, which can reach temperatures of approximately 8000 °C. At such high temperature, the species under investigation are atomized, ionized and thermally excited, and they can then be detected and quantified with either an optical emission spectrometer (OES).[20]

An inductively coupled plasma optical emission spectrometer with axial and radial viewing plasma configuration (ICP-OES Perkin-Elmer Model Optima 3300 DV) operating at a 40 MHz free running ratio-frequency and provided with a TRACYC44 autosampler (Perkin-Elmer) was utilized to determine the vanadium content of certain samples. The ICP-OES spectrometer is located at the "CAI de Técnicas Geológicas" (Universidad Complutense de Madrid).

3.10. Specific surface area (SSA) measurements by the Brunauer, Emmett and Teller method (BET)

SSA measures the surface area of a powder. There are several techniques to measure it. The most common is the Brunauer, Emmett and Teller (BET) method.[21] The theoretical concept of this technique is an extension of the Langmuir theory considering multilayered gas molecule adsorption.[22]

Nitrogen adsorption-desorption isotherms were recorded using a Micromeritics ASAP 200 surface analyzer at 77 K. Prior to measurement the powder samples were placed in a glass cell and heated in vacuum at 110 ^{o}C for 180 minutes in order to achieve the removal of water and other contaminants by degassing, which is essential to facilitate accurate surface area determination. The BET analysis port was cooled by immersion into a liquid nitrogen dewar in order to maintain constant temperature of 77 K during measurement. Such low temperature is required to ensure sufficient interaction between the gas molecules and the surface of the sample for measurable amounts of adsorption to occur. Nitrogen adsorption layers are formed on the particle surfaces, the sample is removed from the nitrogen atmosphere and the release of the adsorbed nitrogen is quantified during heating. The data collected are displayed in the form of BET isotherms, which plot the amount of gas adsorbed and desorbed as a function of the relative pressure. This apparatus is located in

the Departamento Química Inorgánica I (Universidad Complutense de Madrid).

3.11. Magnetic properties

Magnetic properties were measured in a MPMS-SQUID (Magnetic Properties Measurement System- Superconducting Quantum Interference Device), Quantum Design. This instrument is based on the tunneling of superconducting electrons across a narrow insulating gap, between two superconductors.[23]

The temperature dependence of the magnetization was recorded according to the following protocol: First the as-prepared samples were cooled from room temperature (RT) down to 2 K with no applied field, the Zero Field Cooled (ZFC) temperature dependent magnetization was then measured in an applied field H = 0.1 T while increasing the temperature. Subsequently, the samples were demagnetized at RT and cooled down again with an applied magnetic field of 0.1 T. Finally, the Field Cooled (FC) magnetization was recorded with an applied magnetic field H = 0.1 T. Magnetization vs magnetic field measurements were carried out in the ZFC mode at constant temperature. When the required temperature is stable, the magnetic field is increased until 5 T and then decreased until - 5 T. Finally, the field is returned to the initial zero condition to close the loop.

All the magnetic measurements were performed at the "CAI de medidas físicas" (Universidad Complutense de Madrid), with the exception of the $Ba_{1.2}Mn_8O_{16}$ samples, measured in CRISMAT – CNRS laboratories (Caen, France).

3.12. Thermal conductivity

Thermal conductivity (λ) is an intrinsic property of a material which relates its ability to conduct heat. λ is defined as the quantity of heat transmitted through a unit thickness in a direction normal to a surface of unit area due to a unit temperature gradient under steady state conditions and the heat transfer only depends on the temperature gradient.[24, 25]

To measure the thermal conductivity it is necessary to know different sample parameters: Thermal diffusivity (a), Specific Heat (Cp) and density (ρ).

$$\lambda(T) = a(T) \cdot Cp(T) \cdot \rho(T) \qquad [3.1]$$

For measuring the thermal diffusivity, a sintered pellet was positioned on a LFA 447 NanoFlash NETZSCH sample robot, located in a small furnace. This furnace is then held at a predetermined temperature. At this temperature the sample surface is then irradiated with a programmed energy pulse (laser flash). This energy pulse results in a homogeneous temperature rise at the sample surface. The resulting temperature rise of the rear surface of the sample is measured by a high speed IR detector and thermal diffusivity values are computed from the temperature rise versus time data. This apparatus is located in the CRISMAT – CNRS laboratories (Caen, France).

3.13. Seebeck coefficient & Electronic Conductivity

The Seebeck coefficient (S) is related to the thermoelectric effect, where a temperature difference (ΔT) between two points in a conductor or semiconductor results in a voltage difference (ΔV) between these two points.[26-28]

$$S = \Delta V/\Delta T \qquad [3.2]$$

The sign of the Seebeck coefficient depends on the type of charge carriers. If the dominant carriers are electrons, S will be negative. If the dominant carriers are holes S will be positive.

Electrical conduction occurs by the long range migration of either electrons as a response to an applied electric field (voltage). Furthermore, in electrically insulating materials the possibility exits than mobile ions move across the material as a response to the applied electric field. For any material and charge carriers, the specific conductivity is given by:

$$\sigma = \sum_i n_i e_i \mu_i \qquad [3.3]$$

where n_i is the number of charge carrier of species (i), e_i is their charge and μ_i their mobility. For electrons and monovalent ions, e is the elementary charge of an electron ($1.6 \cdot 10^{-19}$ C).[1] Typical conductivities for a range of materials are given in Table 3.1.

Table 3.1. Typical values of electrical conductivity[1]

	Material	**σ (ohm^{-1} cm^{-1})**
Ionic conduction	Ionic crystals	$< 10^{-18} - 10^{-4}$
	Solid electrolytes	$10^{-3} - 10^{1}$
Electronic conduction	Metals	$10^{1} - 10^{5}$
	Semiconductors	$10^{-5} - 10^{2}$
	Insulators	$< 10^{-12}$

The inverse of conductivity is called resistivity (ρ).

$$\sigma = 1/\rho \qquad [3.4]$$

For a given material, the resistance is inversely proportional to the cross-sectional area.

$$R = \rho\,(d/A) \qquad [3.5]$$

Where R is the resistance of the material, d is the electrode distance, A is the cross-section area of the conductor measured. The electrical resistivity of a material is most commonly measured in ohm-centimetres ($\Omega \cdot$ cm).

Low temperature measurements (from 125 to 320 K) of electrical Seebeck coefficient were performed in a Physical Properties Measurements System (PPMS Quantum Design) using an adequate probe and a bar sintered sample (Figure 3.2a). High temperature measurements (from 330 to 625 K) of Seebeck coefficient and electrical resistivity have been carried out with a Seebeck Coefficient / Electric Resistance Measuring System (ZEM-3), as shown in Figure 3.2b. Both apparati are located in the CRISMAT – CNRS laboratories (Caen, France).

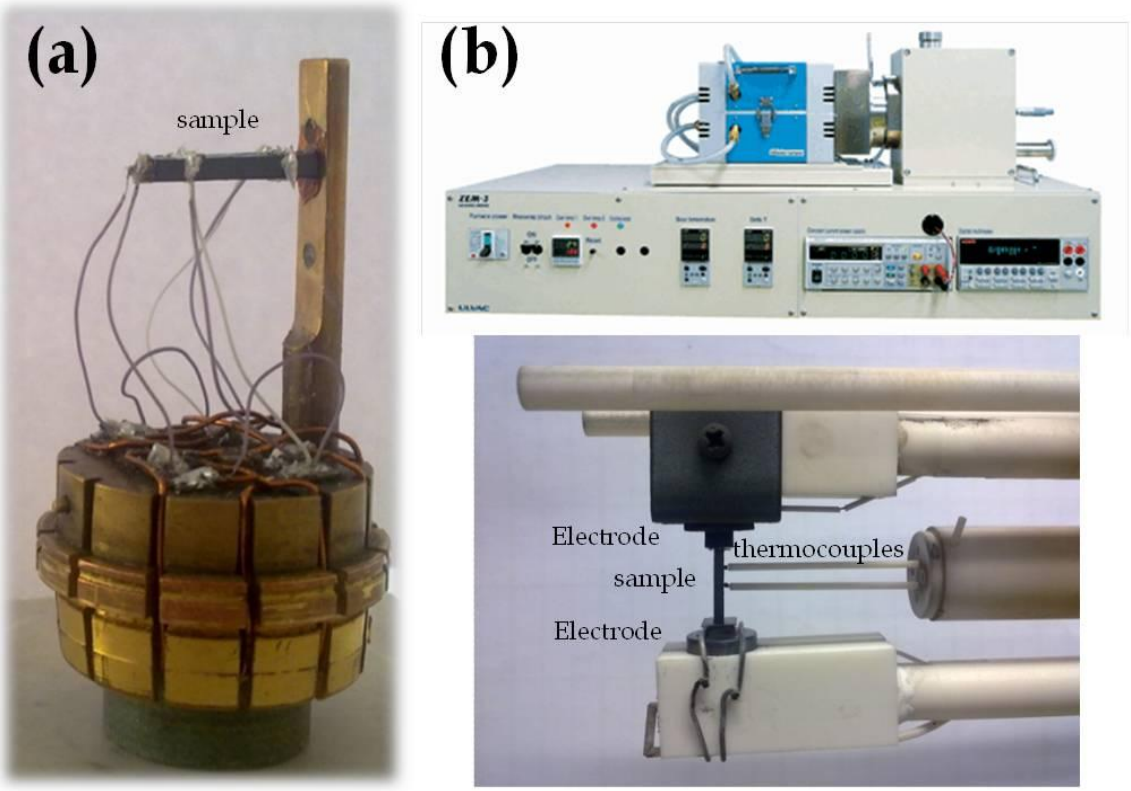

Figure 3.2. (a) PPMS probe for measuring Seebeck coefficient at low temperature. (b) ZEM-3 Seebeck Coefficient / Electric Resistance Measuring System.

3.14. Impedance Spectroscopy

Impedance spectroscopy (IS) is a powerful technique that enables the many contributions to the dielectric and resistive properties of electroceramic materials to be deconvoluted and characterized separately. The charge transport mechanism and the macroscopic dielectric constant in polycrystalline materials commonly consist of several contributions such as sample-electrode

interface, grain boundary and bulk resistance/capacitance. In order to gain precise understanding of the functionality of polycrystalline electroceramic materials it is essential to deconvolute these contributions.[29] AC impedance measurements are typically performed over a wide range of frequencies: 10^{-2} to 10^{7} Hz.

IS data are often obtained in the complex impedance notation Z* (= Z′ + iZ′′), i.e. real and imaginary part of the complex impedance at each frequency are measured separately. For data interpretation it can be useful to transform the data into the modulus (M*), capacitance (C*), admittance (Y*) or dielectric (ε*) notation.[29] Conventionally, different dielectric relaxations in an impedance spectrum correspond to different regions of a ceramic sample. Ideal dielectric relaxations are usually characterized by a resistor and a capacitor in parallel, i.e. the well-known RC - element.[30] The following classification scheme (Table 3.2.) has been proposed by Irvine, Sinclair and West[30] to identify the origin of a dielectric relaxation according to its capacitance ($C = \varepsilon_o \cdot \varepsilon'$) of the RC element.

Table 3.2. Capacitance values and their possible interpretation.[30]

Specific Capacitance (F/cm)	Origin of the RC element
10^{-12}	Bulk
10^{-11}	Minor secondary phase
10^{-11} - 10^{-8}	Grain boundary
10^{-10} - 10^{-9}	Bulk ferroelectric
10^{-9} - 10^{-7}	Surface layer
10^{-7} - 10^{-5}	Sample – electrode interface
10^{-4}	Electrochemical reaction

The most common used model for impedance spectroscopy data analysis is the so-called the Brick Work Layer model (Figure 3.3.), where it is assumed that a polycrystalline sample, contacted with appropriate electrodes, consists of several distinct regions, dominated by (1) grain boundary (GB) effects, (2) electrode sample interface and (3) grain interior properties. In order to account for potentially different dielectric and resistive behaviour in GBs compared to bulk regions, it is required that all GB areas across the sample show similar

properties, such that they can be averaged by a single equivalent circuit component, and that GBs show distinctively different properties compared to grain interior regions or other contributions to allow discrimination.[29]

Impedance Spectroscopy was carried out on sintered pellets with dc sputtered Au electrodes between 150 – 550 K using a Novocontrol Alpha-A High Performance Frequency Analyzer equipped with a liquid nitrogen cooled sample chamber. A 100 mV amplitude alternating voltage signal was employed and the data were recorded between 0.5 Hz – 3 MHz in terms of the real and imaginary parts of the impedance (Z' – Z''). The analyzer is located in the Departamento Física Aplicada III, Facultad de CC. Físicas, GFMC (Universidad Complutense de Madrid).

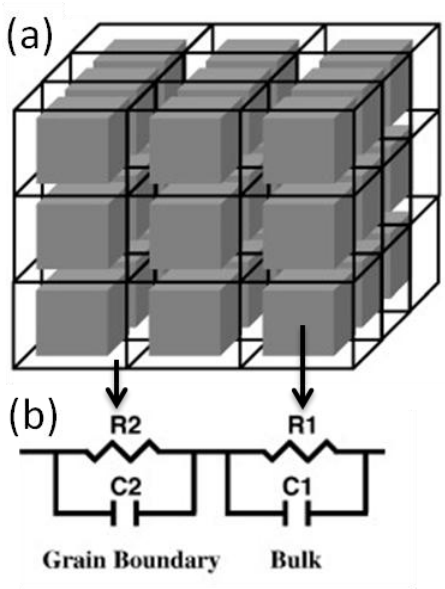

Figure 3.3. Brick work layer model.[31] (a) Ceramic grains are represented schematically by cubes (solid lines). The bulk areas are represented by smaller grey cubes. The surrounding grain boundary areas are colourless. (b) Idealized equivalent circuit model to account for GB and bulk dielectric relaxation processes.

3.15. Electrochemical characterization

Electrochemical characterization of microwave - hydrothermally synthesized $H_2V_3O_8$ for battery applications was performed in a CR2032 coin cell to investigate the lithium insertion and deinsertion reactions.

The battery performance is based on the spontaneous chemical reactions taking place by a process of charge transfer (redox process). During battery discharge, electrons flow from the negative electrode (anode) to the positive electrode (cathode) and this provides energy.[32] One of the most important quantities to determine the technological use of a battery is the potential difference between the electrodes (E) since it measures the tendency of the system that the electrochemical process occurs. The potential is related to the free energy change of the process (ΔG) through the Nernst expression (eq. 3.6):

$$\Delta G = - n F E \qquad [3.6]$$

Where n is the number of moles of active species involved in the reaction and F the Faraday constant (96485.3 C mol^{-1}). The above equation is strictly true only when no current flows through the cell. Another characteristic parameter is the specific capacity of a battery (C), which gives an idea of the amount of electrons (or power) flowing through the external circuit during the electrochemical reaction. C is calculated by:

$$C = n \cdot z \cdot F / W \qquad [3.7]$$

Where z is the number of electrons transferred per mole of the active species and the molecular weight W thereof. The capacitance of batteries is usually expressed in units of mAh $\cdot g^{-1}$. [33-35]

A lithium foil was used as the negative electrode, while the prepared material serves as the positive electrode. The material was dried at 80 ^{o}C and manually mixed with carbon black and a binder agent (Kynarflex) in a 75 : 20 : 5 weight ratio. Pellets of 8 mm diameter containing typically 11 - 14 mg of sample were formed by uniaxial pressing. A 1M LiPF6 solution in EC:DMC (1:1) was used as the electrolyte (commercial battery electrolyte LP30, Selectipure). Cells were run using a MacPile II system. Galvanostatic experiments at constant current corresponding to different C/n discharge rates (n stands for the number of hours needed to insert 1 Li/f.u.) were carried out to characterize the response of the electrode material. Experiments close to equilibrium were carried out

using the potentiostatic intermittent titration technique (PITT) at 25 ^{o}C by changing the potential in intervals of ±10 mV every 12 h. All the electrochemical experiments were carried out in the Departamento de Química, Facultad de Farmacia (Universidad San Pablo CEU).

3.16. References

1. West, A. R., *Solid State Chemistry and Its Applications*. Wiley: 1991.

2. ESRF A Light for Science (http://www.esrf.eu/UsersAndScience/Experiments/Beamlines/beamline-snapshot?BeamlineID=BM25A).

3. Rodriguez-Carvajal, J. In *FULLPROF: a program for Rietveld refinement and pattern matching analysis*, Satellite Meeting on Powder diffraction of the XV Congress of the IUCr, 1990; 1990.

4. Rietveld, H., Line profiles of neutron powder-diffraction peaks for structure refinement. *Acta Crystallographica* **1967,** 22, (1), 151-152.

5. Rietveld, H., A profile refinement method for nuclear and magnetic structures. *Journal of Applied Crystallography* **1969,** 2, (2), 65-71.

6. Finger, L. W.; Cox, D. E.; Jephcoat, A. P., A correction for powder diffraction peak asymmetry due to axial divergence. *Journal of Applied Crystallography* **1994,** 27, (6), 892-900.

7. Toby, B. H., R factors in Rietveld analysis: How good is good enough? *Powder Diffraction* **2006,** 21, (1), 67-70.

8. Durham University. Scanning Electron Microscopy http://www.dur.ac.uk/resources/electron.microscopy.facility/06879ScanningElectronMicroscopy.pdf.

9. ElectronMicroscopy http://web.utk.edu/~prack/MSE%20300/SEM.pdf

10. SEM Illustrative Example: Secondary Electron and Backscatter Electron Images http://www.andersonmaterials.com/sem/sem-secondary-backscatter-images.html.

11. Transmission Electron Microscope Uses. In Microscopy Advantages and Disadvantages http://www.microscopemaster.com/transmission-electron-microscope.html.

12. Williams, D. B.; Carter, C. B., *Transmission Electron Microscopy: A Textbook for Materials Science*. Springer: 2009; p 760.

13. Spence, J. C. H., *Experimental high-resolution electron microscopy*. Oxford University Press: 1988; p 427.

14. Gatan Software http://www.gatan.com/products/software.

15. Allen, L. J.; McBride, W.; O'Leary, N. L.; Oxley, M. P., Exit wave reconstruction at atomic resolution. *Ultramicroscopy* **2004,** 100, (1-2), 91-104.

16. McTempas Software for High Resolution Electron Microscopy http://www.totalresolution.com/index.html.

17. Zaluzec, N. J. Brief Review of Energy Loss Processes, http://tpm.amc.anl.gov/Lectures/EELSAEMShortCourse.pdf.

18. Thermogravimetric analysis, http://www1.chm.colostate.edu/Files/CIFDSC/TGA-MS.pdf

19. Princeton Instruments. Confocal Raman Microscopy General Overview, http://content.piacton.com/Uploads/Princeton/Documents/Library/UpdatedLibrary/Confocal_raman_microscopy_note.pdf.

20. Group, E. A. Materials Characterization http://www.eaglabs.com/mc/inductively-coupled-plasma-spectroscopy.html.

21. Brunauer, S.; Emmett, P. H.; Teller, E., Adsorption of Gases in Multimolecular Layers. *Journal of the American Chemical Society* **1938,** 60, (2), 309-319.

22. Rouquerol, J.; Rouquerol, F.; Sing, K. S. W., *Adsorption by Powders and Porous Solids*. Elsevier Science: 1998; p 467.

23. Cullity, B. D.; Graham, C. D., *Introduction to Magnetic Materials*. Wiley: 2011; p 568.

24. Center, N. R. Thermal Conductivity (http://www.ndt-ed.org/EducationResources/CommunityCollege/Materials/Physical_Chemical/ThermalConductivity.htm).

25. Shinde, S. L.; Goela, J., *High Thermal Conductivity Materials*. Springer: 2006; p 271.

26. Alam, H.; Ramakrishna, S., A review on the enhancement of figure of merit from bulk to nano-thermoelectric materials. *Nano Energy* **2013,** 2, (2), 190-212.

27. Li, J.-F.; Liu, W.-S.; Zhao, L.-D.; Zhou, M., High-performance nanostructured thermoelectric materials. *NPG Asia Mater* **2010,** 2, 152-158.

28. Snyder, G. J.; Toberer, E. S., Complex thermoelectric materials. *Nat Mater* **2008,** 7, (2), 105-114.

29. Schmidt, R., Impedance Spectroscopy of electroceramics. In *Ceramic Materials Research Trends*, Lin, P. B., Ed. Nova Science Publishers, Inc.: 2007; pp 321-351.

30. Irvine, J. T. S.; Sinclair, D. C.; West, A. R., Electroceramics: Characterization by Impedance Spectroscopy. *Advanced Materials* **1990,** 2, (3), 132-138.

31. Schmidt, R.; Stennett, M. C.; Hyatt, N. C.; Pokorny, J.; Prado-Gonjal, J.; Li, M.; Sinclair, D. C., Effects of sintering temperature on the internal barrier layer capacitor (IBLC) structure in $CaCu_3Ti_4O_{12}$ (CCTO) ceramics. *Journal of the European Ceramic Society* **2012,** 32, (12), 3313-3323.

32. Perez-Flores, J. C.; Garcia-Alvarado, F.; Hoelzel, M.; Sobrados, I.; Sanz, J.; Kuhn, A., Insight into the channel ion distribution and influence on the lithium insertion properties of hexatitanates $A_2Ti_6O_{13}$ (A = Na, Li, H) as candidates for anode materials in lithium-ion batteries. *Dalton Transactions* **2012,** 41, (48), 14633-14642.

33. Marom, R.; Amalraj, S. F.; Leifer, N.; Jacob, D.; Aurbach, D., A review of advanced and practical lithium battery materials. *Journal of Materials Chemistry* **2011,** 21, (27), 9938-9954.

34. Scrosati, B.; Garche, J., Lithium batteries: Status, prospects and future. *Journal of Power Sources* **2010,** 195, (9), 2419-2430.

35. Tirado, J. L., Inorganic materials for the negative electrode of lithium-ion batteries: state-of-the-art and future prospects. *Materials Science and Engineering: R: Reports* **2003,** 40, (3), 103-136.

4. SOLID STATE - MICROWAVE SYNTHESIS

4.1. Introduction

The synthesis of mixed-metal oxide materials is traditionally performed in a conventional high temperature furnace following the standard ceramic route. It is perfectly feasible though to perform the synthesis by a solid state microwave route, as was previously explained in *Chapter 2.6.1.* The focus of this chapter is on solid state microwave synthesis and characterization of different oxide materials with two common structures, ABO_3 perovskites and $A_2B_2O_7$ pyrochlores.

The perovskite is probably the most studied structure in materials science. The mineral perovskite is $CaTiO_3$, although the ideal, aristotype structure (the highest symmetry, *Pm-3m*, #221 cubic form) is adopted by $SrTiO_3$ under ambient conditions. The perovskite structure can be described as A cations surrounded by twelve anions (oxygen in this work) in cubo-octahedral coordination and B cations surrounded by six anions in octahedral coordination. The anions are coordinated by two B-site cations and four A-site cations (Figure 4.1). The large A cations and O-anions, are cubic close packed, with the smaller B cations occupying the octahedral holes between the O-anions.[1]

It is possible to have perovskites with different sets of cations: $A^{+}B^{5+}O_3$ (i.e. $NaNbO_3$), $A^{2+}B^{4+}O_3$ (i.e. $SrTiO_3$) and $A^{3+}B^{3+}O_3$ (i.e. $GdFeO_3$) or the special case of A –site vacancies $B^{6+}O_3$ (i.e. ReO_3). Furthermore it is possible to have multiple combinations of these like bronzes A_xBO_3 (i.e. $Na_{0.23}BO_3$) with partial A – site vacancies or double perovskite $AA'BB'O_6$ (i.e. Sr_2FeMoO_6).[1]

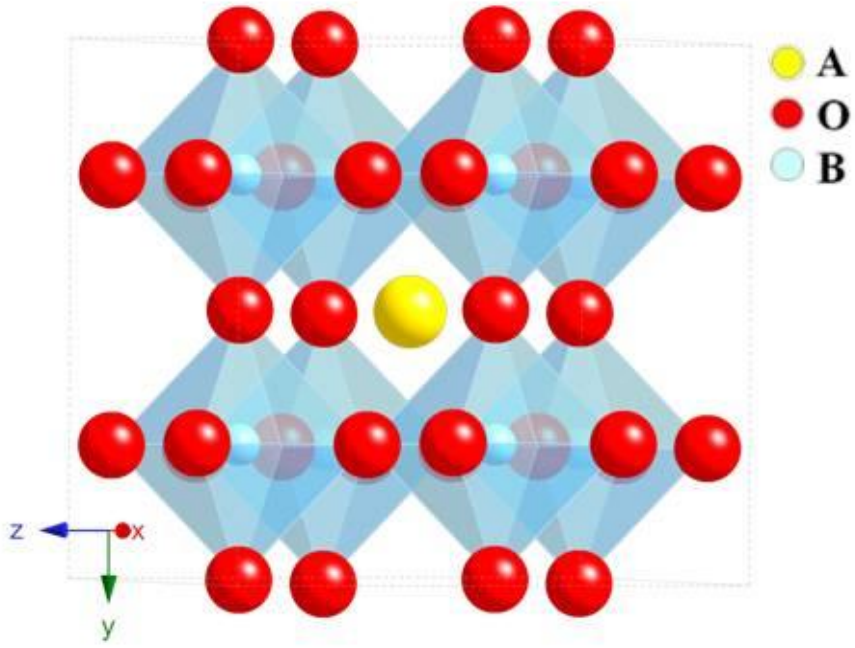

Figure 4.1. The ideal ABO_3 perovskite structure showing the octahedral coordination of the B-site cation.

All the microwave-synthesized perovskite materials presented in this chapter are included in the set of cations $A^{3+}B^{3+}O_3$. The structure exhibits some flexibility and can accommodate smaller A-site cations than might be expected on the basis of tabulated radii: the B–O–B bond angles can be within a certain range, giving concerted tilting patterns of the (BO_6) motifs to bring oxide ions closer to the A site.[2] This degree of distortion may be predicted to some extent using simple geometric parameters, such as the Goldschmidt tolerance factor (t):[3]

$$t = (r_A + r_O)/\sqrt{2}(r_B + r_O) \qquad [4.1]$$

where r_A, r_B and r_O are the ionic radii of the respective ions. The ideal cubic structure has $t = 1$. This is the case for $SrTiO_3$, where r_A = 1.44 Å, r_B = 0.605 Å and r_O = 1.40 Å. If the A cation is smaller than the ideal value the tolerance factor is smaller than 1. As a result, the [BO_6] octahedral will tilt in order to fill space. The cubic perovskite structure occurs if $0.89 < t < 1$. Lower values of t

will lower the symmetry of the crystal structure, for example to an orthorhombic symmetry. On the other hand, if the value is larger than 1, hexagonal variants of the perovskite structure are stable.[4-6]

Pyrochlore materials take their name from the mineral $NaCaNb_2O_6F$ pyrochlore. This is a crystal structure type that may be understood in several ways. One possibility is to describe it as an anion-deficient fluorite lattice, in which 1/8 of the anions are removed in an ordered manner (Figure 4.2a), such that one half of the cations maintain their coordination number of 8 (albeit distorted) and the other half have a lower coordination number of 6 (regular octahedral). The parent structure is an F-centered cubic lattice with space group (S.G): *Fd-3m* (# 227) and cell parameter $\boldsymbol{a} \approx 10$ Å, corresponding to the double of the fluorite parameter. A - cations are located on 16d eight-coordinated sites while B – cations are located on 16c six-coordinated sites. The O^{2-} anions are located on two different sites:

1) four-coordinated 48f positions with two A - cations and two B - cations as the nearest neighbours.
2) four-coordinated 8b sites with four A cation as nearest neighbors. The oxygen vacancies are four-coordinated 8a sites surrounded by four B cation neighbours (Figure 4.2b and 4.2c).

The structure may similarly accommodate various charged combinations of A and B site metals, with $(A^{3+})_2(B^{4+})_2O_7$ (i.e. $Gd_2Zr_2O_7$) and $(A^{2+})_2(B^{5+})_2O_7$ (i.e. $Ni_2Sb_2O_7$) being the most common possibilities in oxide pyrochlores. In these materials the two most important crystal defects are (i) cation antisite, and (ii) anion Frenkel defects.

Cation antisite defects essentially consists in a positional exchange of an A^{3+} for a B^{4+} cation, whereas Frenkel anion disorder proceeds when a 48f site oxygen ion is displaced to an 8a interstitial vacancy site, thus leaving the 48f site empty.[7-10]

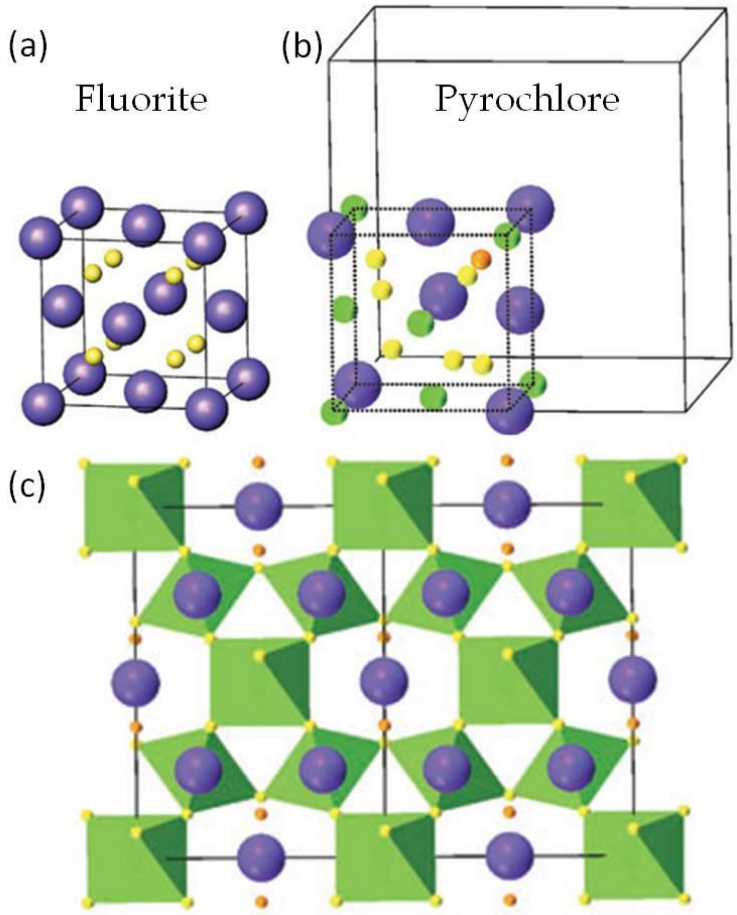

Figure 4.2. Different views of the $A_2B_2O_6O'$ pyrochlore structure showing the relationship between (a) the fluorite and (b) the pyrochlore structures in which one octant of the pyrochlore unit cell is shown by the dotted cube, (c) octahedral connectivity of (BO_6) units with *A* sites and *O'* anions as "extra-framework ions". *A* metals are shown as purple spheres, *B* metals as green spheres, the *O* atoms as yellow spheres and the *O'* atoms as orange spheres. The unit cell is shown by the full line in each view. A metals are shown as purple spheres, *B* metals as green spheres, the *O* atoms as yellow spheres and the *O'* atoms as orange spheres. Reproduced from Modeshia *et al.*[2]

4.2. $LaMO_3$ and $La_{1-x}A'_xMO_3$ (A' = Sr, M = Al, Cr, Mn, Fe, Co)

Lanthanum perovskites ($LaMO_3$) containing metals of the first transition series (M) are appealing functional materials because of their immense technological potential: some of them are used as components for solid oxide fuel cells (SOFCs), others are efficient catalysts, some are used as membranes for separation processes or as gas sensors in automobiles, several show magneto-optic or magnetoresistance properties. Moreover some of these materials, where different properties coexist, are multifunctional.[11-14] In the case of $LaAlO_3$ it is a well-known substrate for depositing superconducting thin

films because of its excellent lattice and thermal expansion matching with 1-2-3 superconductors.[14] Furthermore, $LaCoO_3$ is regarded as a model compound for many cobaltites in terms of the thermally induced spin-state transition, which has triggered a great deal of fundamental research into this compound.[15-17]

$LaCoO_3$

$LaCoO_3$ exhibits a magnetic spin-state transition due to the crystal field splitting of the octahedral Co d-electron energy levels into t_{2g} and e_g levels where the energy gap between t_{2g} and e_g levels is only marginally larger (≈ 80 K) than Hund's coupling energy. This small energy difference can be overcome by thermal activation, and Co^{3+} t_{2g} electron(s) can transfer into the e_g level above T_{s1} ≈ 80 K. The compound was suggested to adopt a diamagnetic low-spin (LS) state below T_{s1} (S = 0, $t_{2g}^6 e_g^0$) and an intermediate-spin (IS) state (S = 1, t_{2g}^5 e_g^1) above. Alternatively, a high-spin (HS) state above T_{s1} has been suggested as well (S = 2, t_{2g}^4 e_g^2).[18-20] Both, IS and HS models cannot correctly describe the magnetic susceptibility in $LaCoO_3$ and large controversy in the literature has arisen over the validity of the IS or HS models.[21]

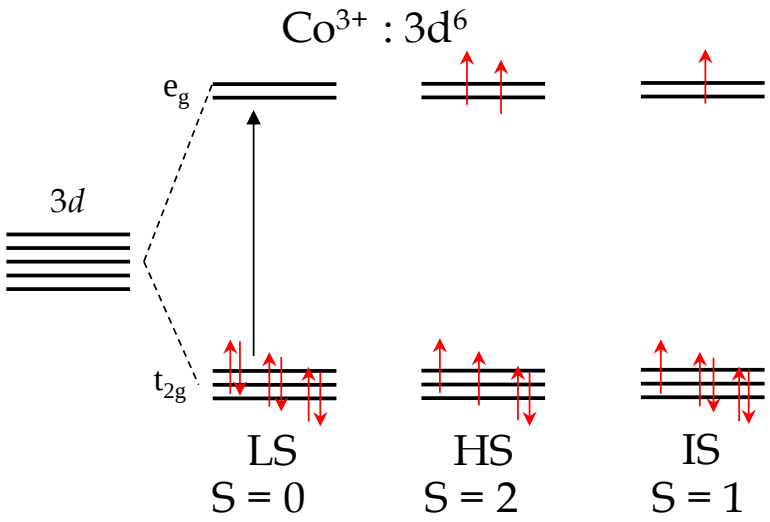

Figure 4.3. Electron energy levels of the LS, IS, and HS states in $LaCoO_3$ with $3d^6$ Co^{3+} electron configuration.Reproduced from Schmidt *et al.*[22]

All $LaMO_3$ materials are usually synthesized by the traditional solid state method at high temperatures (>1000 ^oC) for extended periods (> 24 h), and by means of other chemical methods, such as sol-gel,[23, 24] citrate complexation route,[25,26] combustion,[27,28] hydrothermal[29-31] and sonochemistry[32], but their synthesis using microwave radiation in a reproducible way is quite scarce and just a few authors have reported partial studies.[33, 34]

4.2.1. Synthetic aspects

In this work, the $LaMO_3$ family was synthesized starting from metal nitrates precursor materials. The equimolar amounts of metal nitrates were weighed according to the nominal composition of $LaMO_3$ (M = Al, Cr, Mn, Fe, Co) and mixed with 5 % weight of carbon black, which can enhance microwave absorption. The mixtures were mechanically homogenized and compacted in pellets of 12 mm diameter. The pellets were placed in a porcelain crucible, which were again placed inside another larger one stuffed with mullite.

$LaCoO_3$ and $LaMnO_3$ materials are directly obtained after 30 minutes of irradiation. On the other hand, $LaAlO_3$, $LaCrO_3$ and $LaFeO_3$ need to be irradiated by microwaves for 30 minutes and, heated afterwards in air in a conventional furnace for 2 hours at specific temperatures (500 ^oC for $LaFeO_3$, 800 ^oC for $LaCrO_3$ and 1000 ^oC for $LaAlO_3$). To prepare doped materials, such as $La_{0.8}Sr_{0.2}FeO_3$ and $La_{0.8}Sr_{0.2}Fe_{0.5}Co_{0.5}O_3$, it is necessary to combine the described microwave method with the sol-gel methodology. The sol-gel process followed is similar to that reported by Liu *et al*[35]. The equimolar amounts of metal nitrates are dissolved in distilled water and a saturated polyvinyl alcohol (PVA) (Fluka, 98%) solution is added as the complexing agent. The amount of PVA added is such that the ratio of total number of moles of cations to that of PVA was 1:2. Then the final solution is heated at 80 ^oC for 3 h to remove water and a viscous solution (gel) is formed. This gel is irradiated by microwaves during 30 minutes. The resulting polymeric and sponge-like-precursor is then calcinated in air at 500 ^oC for 2 hours in order to decompose the organic remnants, rendering a black powder as final product.

The scheme of the synthesis is summarized in Figure 4.4.:

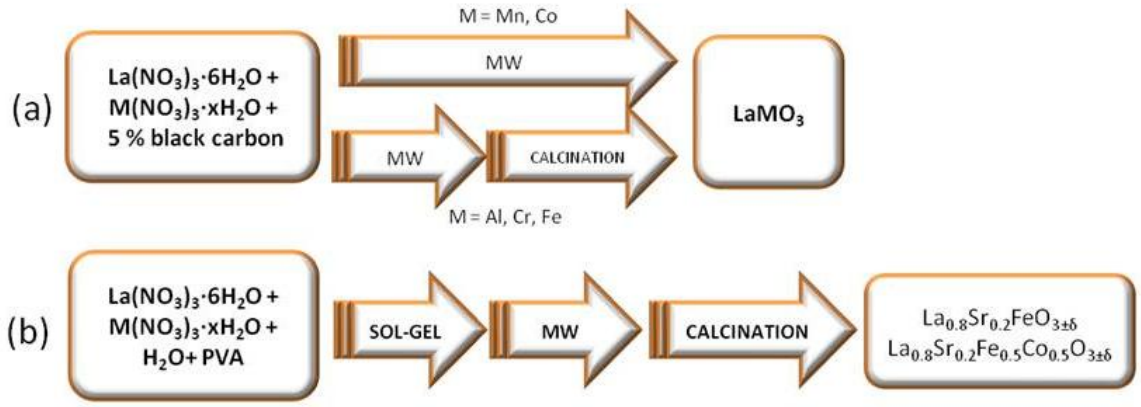

Figure 4.4. Microwave routes followed to produce different lanthanum perovskites.

The fact that 30 minutes of microwave irradiation are sufficient to get pure and crystalline $LaMnO_3$ and $LaCoO_3$ materials without any additional thermal treatment seems to be due to the metallic character of $LaMnO_3$ and $LaCoO_3$. The first $LaMnO_3$ and $LaCoO_3$ clusters formed from the precursors may act in a similar way as the black carbon added as susceptor: the first metallic clusters produced do scatter the radiation and speed up the reaction until completion.

The microwave heating does not proceed in the same way for $LaMO_3$ (M= Al, Cr, Fe), mainly due to their semiconducting character, and an amorphous material is obtained after 30 minutes of microwave irradiation. Figure 4.5. shows an example of the X-ray diffraction pattern evolution for $LaFeO_3$.

On the other hand, for $La_{0.8}Sr_{0.2}FeO_3$ and $La_{0.8}Sr_{0.2}Fe_{0.5}Co_{0.5}O_3$, the microwave heating proceeds in an even more complicated way as for the other samples, and even longer times of microwave irradiation (up to 2 hours) do not yield crystalline materials. Obviously, this synthetic route is not successful for doped $LaMO_3$ materials, and another intermediate step is necessary such as the preparation of a gel.

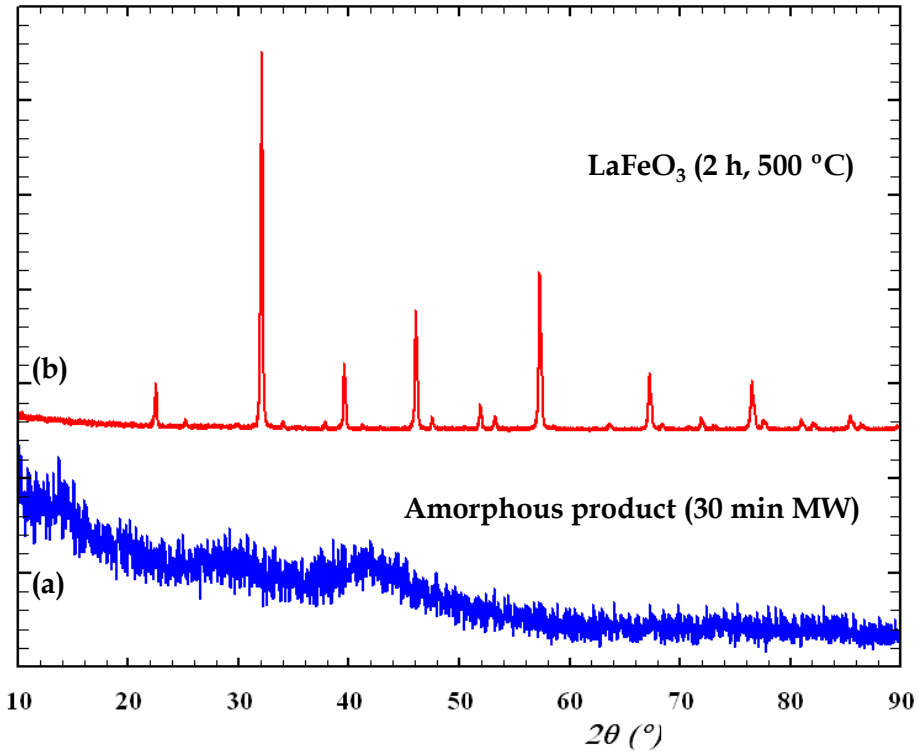

Figure 4.5. a) X-ray diffraction patterns of (a) Amorphous La-Fe-O product obtained after 30 min microwave irradiation (b) Crystalline $LaFeO_3$ synthesized after calcination of the previously amorphous powder during 2 h at 500 ºC.

4.2.2. Structural characterization

The X-ray diffraction (XRD) patterns of all simple $LaMO_3$ perovskites – shown in Figures 4.6- exhibit the basic reflections corresponding to the perovskite structure and all the Bragg reflections of the materials can be indexed by comparison with the respective JCPDS cards. $LaCrO_3$, $LaMnO_3$ and $LaFeO_3$ all crystallize in the *Pnma* space group and a displacement of the main peaks towards lower angles can be observed by comparison of the XRD patterns. This is the expected trend, taking into account the respective high spin ionic radii $^{VI}Cr^{3+}$: 0.615 Å, $^{VI}Mn^{3+\,[HS]}$: 0.65 Å, and $^{VI}Fe^{3+\,[HS]}$: 0.645 Å.[36] $LaAlO_3$ and $LaCoO_3$ crystallize in the R3c and R-3c (hexagonal setting) space groups, respectively. The diffraction patterns of the doped and undoped Fe – containing perovskites are shown in Fig. 4.6b. It can be observed that the diffraction maxima shift to higher angles, which corresponds to smaller lattice parameters, in contrast to the expected shift from the respective ionic radii of $^{VIII}La^{3+}$ 1.18 Å

and $^{VIII}Sr^{2+}$ 1.25 Å. This can be explained by taking into account the presence of some Fe^{4+} induced by doping. It is worth noting that the doped samples remain nanocrystalline, as can be inferred from the width of the diffraction maxima if compared to the undoped ferrite.

Rietveld analysis has been performed to refine the respective crystal structures and Figure 4.7 shows the observed and calculated diffraction patterns. The results obtained for $LaMO_3$ (M = Al, Cr, Fe and Co) concerning cell parameters and atoms positions are in good agreement with the values reported in the literature.[37-43] The fits all showed reasonable errors as indicated by the R-factors which are summarized in Table 4.1a and Table 4.1b.

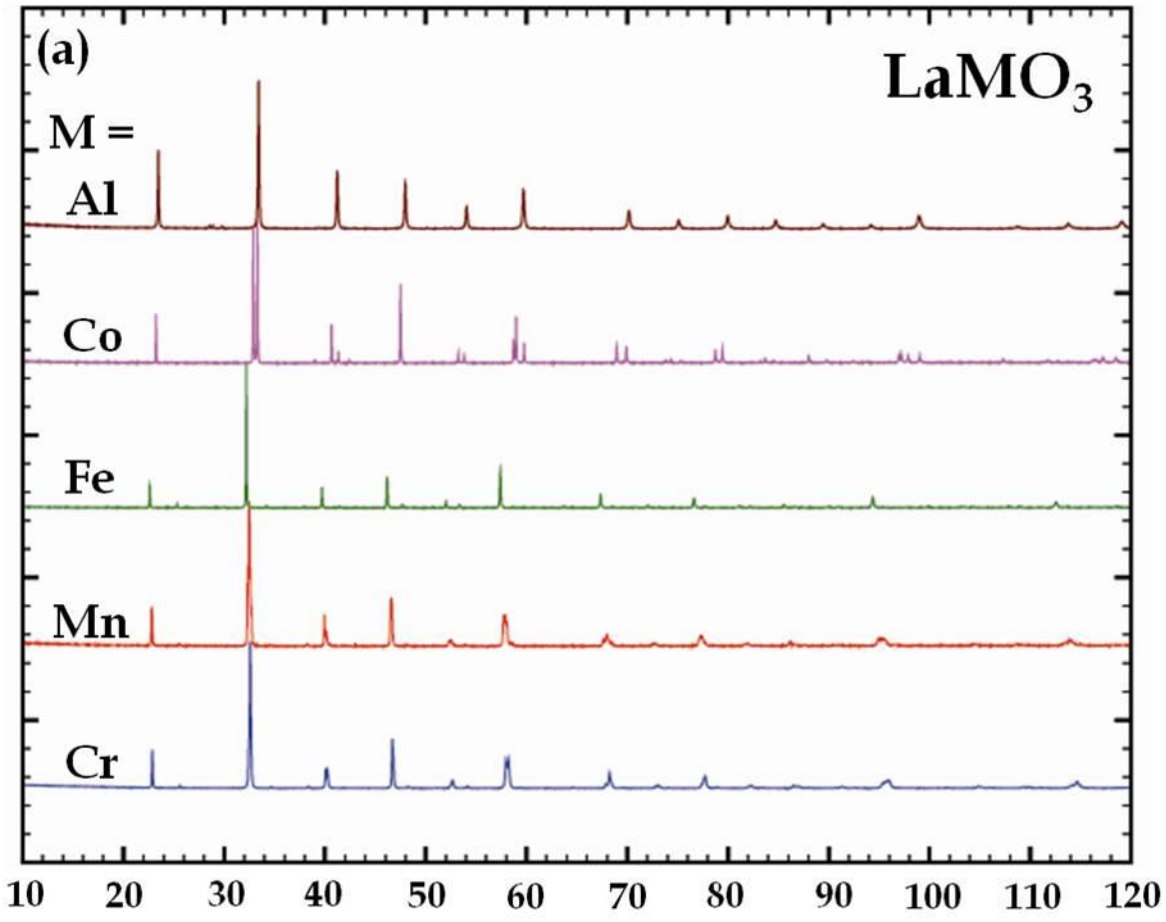

Fig. 4.6 to be continued on next page.

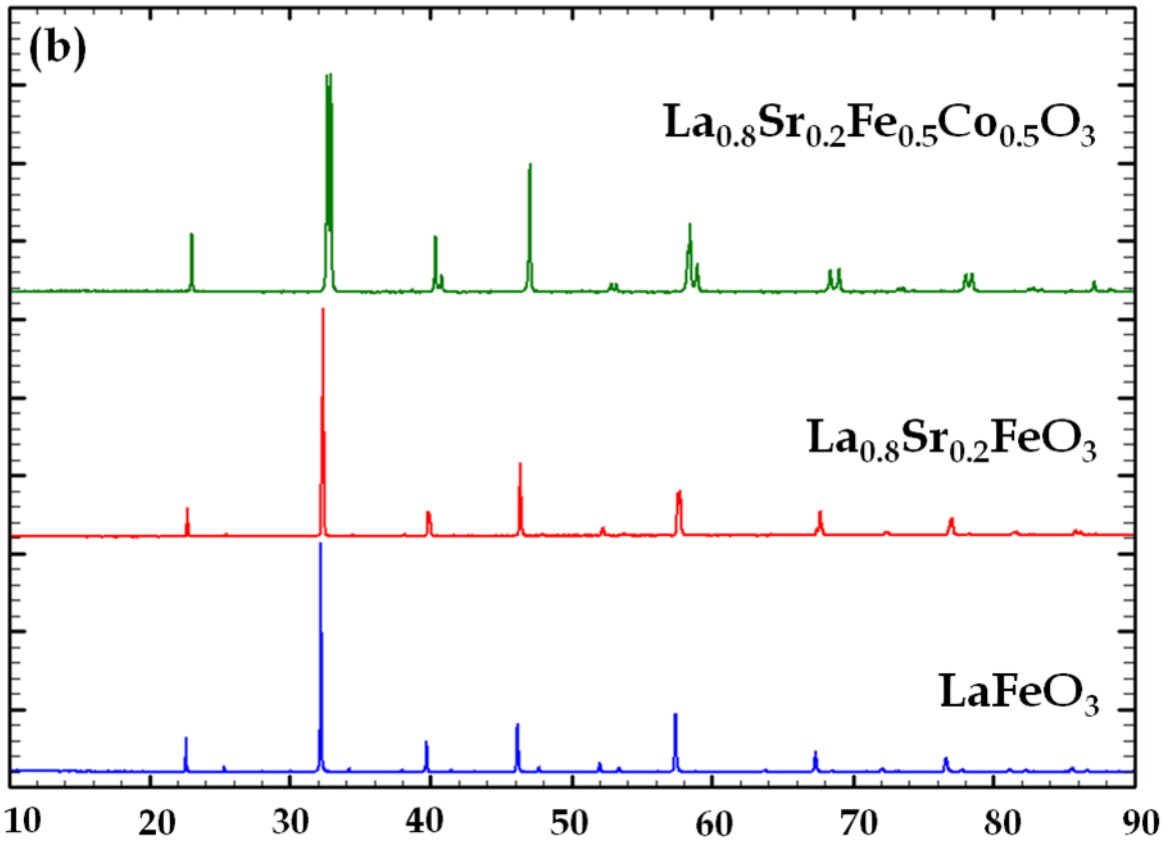

Figure 4.6. a) X-ray diffraction patterns of undoped lanthanum perovskites. b) X-ray diffraction patterns of doped - lanthanum ferrites and $LaFeO_3$. The increased width of the reflexions in the doped samples shows that the particle size is in the nanometric range.

Only for the lanthanum manganite the R-factors are relatively high, and further Rietveld analysis showed the coexistence of two different phases crystallizing in the *R-3c* and *Pnma* space groups, in agreement with the observations made by Wold and Arnott in 1959.[44] They suggested that a phase transition takes place from orthorhombic to rombohedral structure at ≈ 600 ^{o}C. It is worth to note that the literature is plenty of data concerning lantanum manganites, doped or not, and there is general agreement about the intrinsic complexity of these materials where different features may exist: Mn^{3+}/ Mn^{4+} mixed valence and oxygen hyperstoichiometry due to cationic vacancies and different symmetries.[45] It has been demonstrated that the common notation "$LaMnO_{3+\delta}$", which would indicate an excess of interstitial oxygen in the lattice, does not represent the correct unit cell, which should be written as $La_{1-\varepsilon}Mn_{1-\varepsilon}O_3$ (with $\varepsilon = \delta/[3+\delta]$), a notation which indicates a fully occupied oxygen lattice, showing, however, cation vacancies.[45, 46]

Table 4.1a. Structural parameters for rhombohedral lanthanum perovskites obtained by solid state microwave synthesis.

	$LaAlO_3$	$LaCoO_3$	$La_{0.8}Sr_{0.2}Fe_{0.5}Co_{0.5}O_3$
$a = b$ (Å)	5.36116(6)	5.44315(2)	5. 4818(1)
c (Å)	13.13391(8)	13.09436(6)	13.2751(3)
La position	6a	2a	2a (La/Sr)
M position	6b Al	2b Co	2b (Fe/Co)
O position	18e	6e	6e
x	0.5276(3)	0.549(1)	0.547(1)
χ^2	1.82	3.71	2.10
R_{wp} / R_{exp} (% / %)	6.51 / 4.83	4.29 / 2.23	3.81 / 2.63
R_{Bragg}	2.20	2.51	4.78
Space Group	*R3c* (#161): 6a (0 0 ¼), 6b (0 0 0), 18e (x 0 ¼)	*R-3c* (#167): 2a (0 0 ¼), 2b (0 0 0), 6e (x 0 ¼)	

Table 4.1b. Structural parameters for orthorhombic lanthanum perovskites obtained by solid state microwave synthesis.

	$LaFeO_3$	$LaMnO_3$ *	$LaCrO_3$	$La_{0.8}Sr_{0.2}FeO_3$
a (Å)	5.56304(4)	5.4858(2)	5.4790(1)	5.5511(1)
b (Å)	7.85346(4)	7.7907(2)	7.7616(2)	7.8223(1)
c (Å)	5.55623(4)	5.5390(4)	5.5164(1)	5.5263(1)
La position 4c				
x	0.0281(5)	0.5179(5)	0.0178(2)	0.0121(3)
z	0.0019(3)	0.0182(4)	-0.0035(5)	-0.0033(4)
M position 4b				
O(1) position 4c				
x	0.488(6)	-0.008(1)	0.496(4)	0.448(3)
z	0.091(4)	-0.004(2)	0.064(4)	0.093(2)
O(2) position 8d				
x	0.291(4)	0.289(3)	0.280(2)	0.261(3)
y	0.029(4)	-0.001(2)	0.033(1)	0.025(6)
z	-0.297(1)	0.797(2)	-0.271(3)	-0.294(3)
χ^2	1.05	4.69	1.28	1.09
R_{wp} / R_{exp} (% / %)	4.60 / 4.36	6.91/7.22	4.70 / 4.15	4.58 / 4.20
R_{Bragg}	4.67	8.90	4.29	4.43
Space Group	*Pnma* (#62) : 4*c* (*x* ¼ *z*), 4*b* (0 0 ½), 8*d* (*xyz*)			

* $LaMnO_3$ secondary phase. *R-3c*: $a = b = 5.5311(2)$Å , $c = 13.4858(1)$ Å

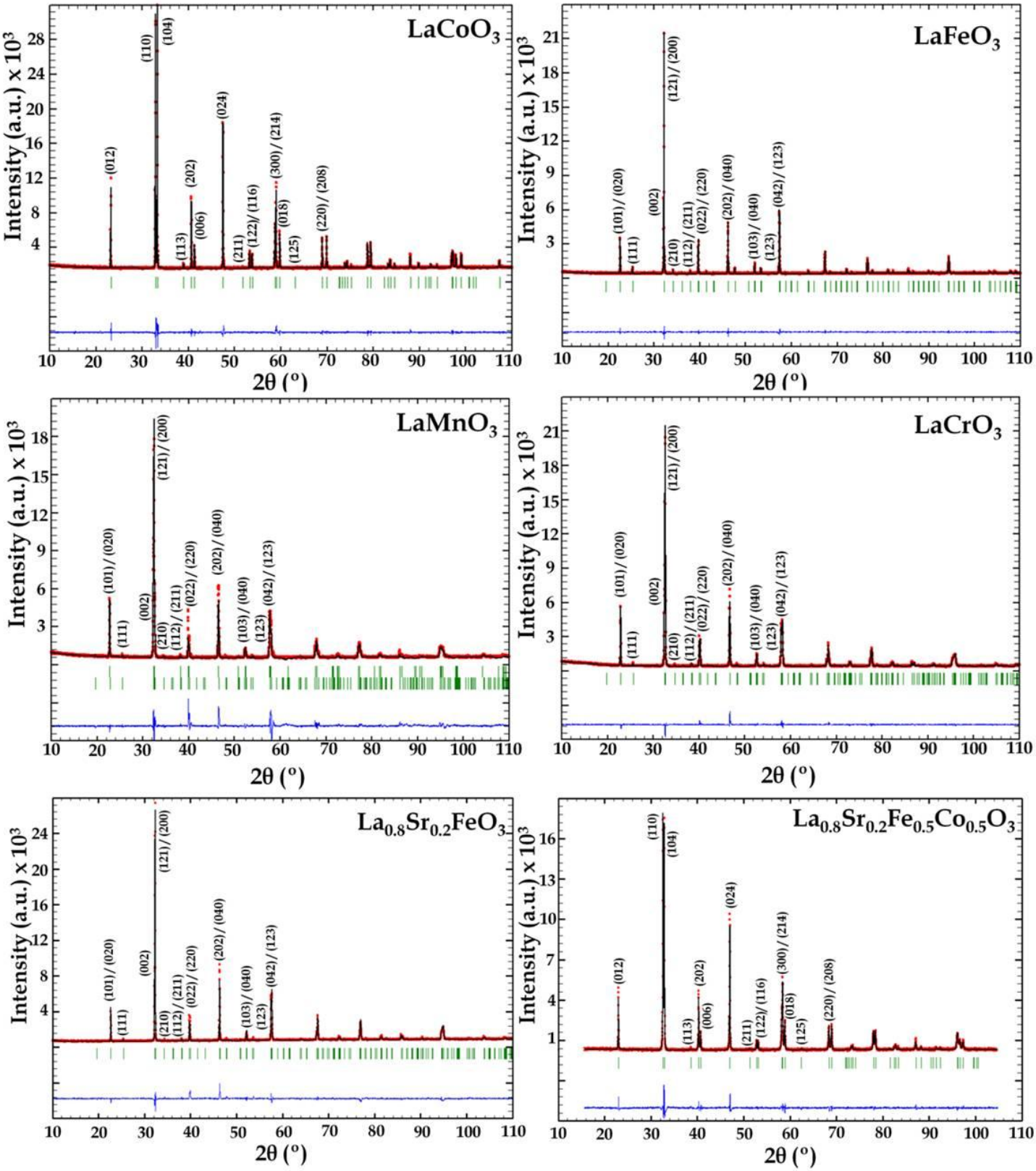

Figure 4.7. Rietveld refinement of XRD patterns: observed (red dotted lines), refined (black solid lines), and their difference (blue bottom line). Green vertical bars indicate the X-ray reflection positions.

4.2.3. Microstructural characterization

SEM micrographs and EDS analysis results from all $LaMO_3$ materials are shown in Figure 4.8 and Table 4.2, respectively. The micrographs clearly indicate the agglomeration of polyhedral particles of submicronic or nanometric size, with the exception of $LaCoO_3$ showing much larger crystals. These features are important for processing at higher temperatures in order to fabricate devices. To give two representative examples, $LaMnO_3$ and $LaCoO_3$ ceramics sintered in air at 1300 ºC are shown: compact, void-free and, consequently, high density pellets can be produced. Regarding the chemical EDS analysis, the metallic proportions as detected from EDS are sufficiently close to the nominal ones to postulate correct stoichiometry. Furthermore, the distribution of elements in the bulk materials was found to be rather homogeneous.

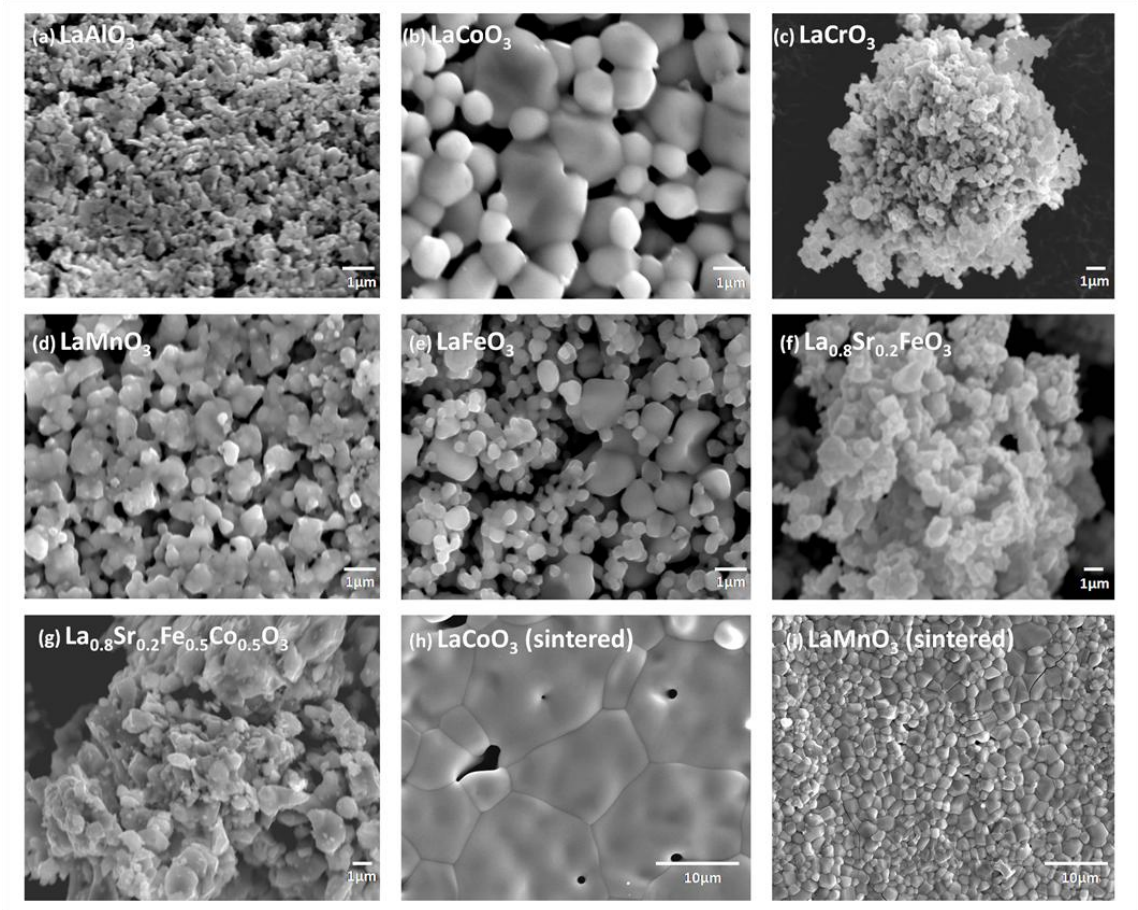

Figure 4.8. SEM micrographs of lanthanum perovskites. (a) to (g): as prepared polycrystalline powders; (h) and (i): pellets sintered at 1300 ºC.

Table 4.2. EDS analysis of metallic contents (atomic %) for lanthanum perovskites powders. Ideal values are 50% both in the A or the B perovskite position.

ABO_3	$LaAlO_3$	$LaCoO_3$	$LaCrO_3$	$LaMnO_3$	$LaFeO_3$	$La_{0.8}Sr_{0.2}FeO_3$	$La_{0.8}Sr_{0.2}Fe_{0.5}Co_{0.5}O_3$
A	50.5	52.9	51.7	51.2	50.9	La: 36.0 Sr: 12.3	La: 40.4 Sr: 12.0
B	49.5	47.1	48.3	48.8	49.1	51.7	Fe: 23.9 Co: 23.7

TEM images obtained for selected doped and undoped $LaMO_3$ powders show highly agglomerated particles (Figure 4.9). The particle sizes are clearly in the nanometric range. The corresponding SAED patterns (insets of Figure 4.9) show the diffraction rings commonly observed in polycrystalline materials.

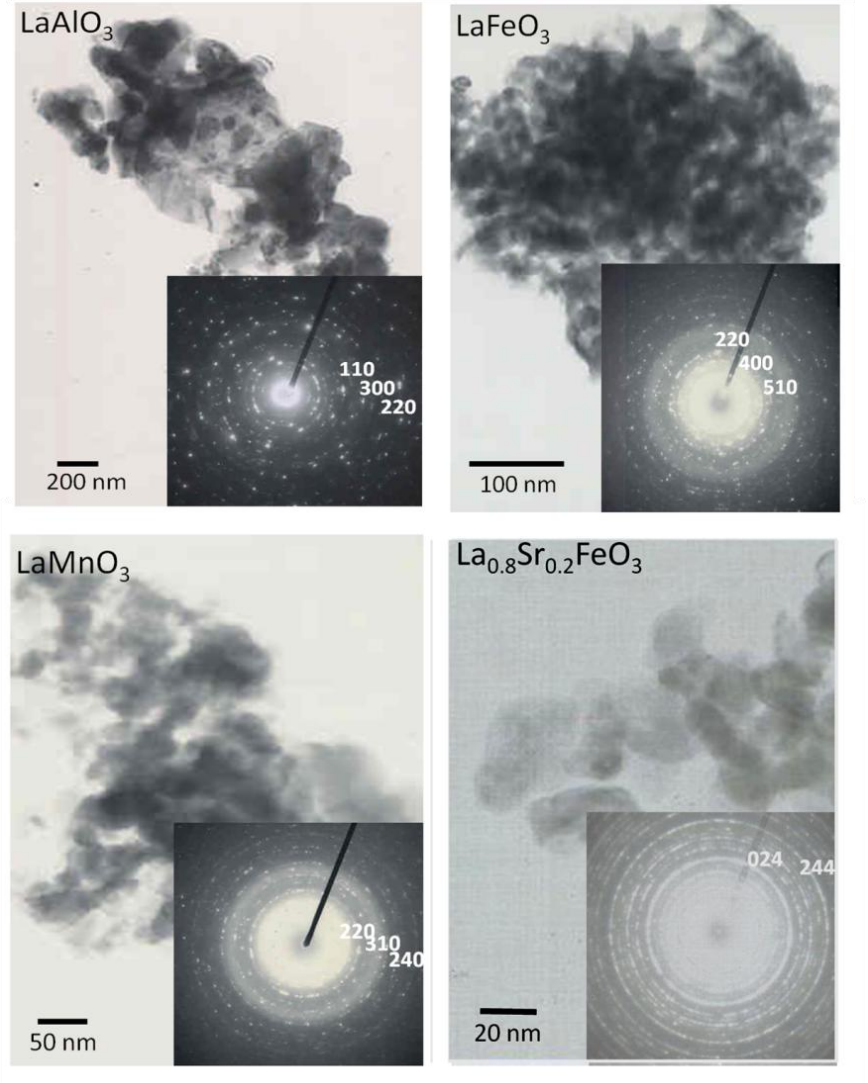

Figure 4.9. TEM micrographs and SAED patterns of different Lanthanum perovskites

In order to evaluate the structural modifications in the $LaCoO_3$, HRTEM images along the [-2201] and [12-32] zone axes are displayed in Figure 4.10. The parameters from the refined structures were used to calculate the theoretical HRTEM images which show excellent agreement to the experimentally observed structure (Fig.4.10). This confirms that the refined structure may be a valid reflection of the actual crystal structure. The experimental HRTEM images were recorded at the defocus value of -35 nm, near to the optimum Scherzer defocus. The contrast of the black dots corresponds to the atomic columns from the ionic La and Co sublattices, showing a long range ordering without any defects.

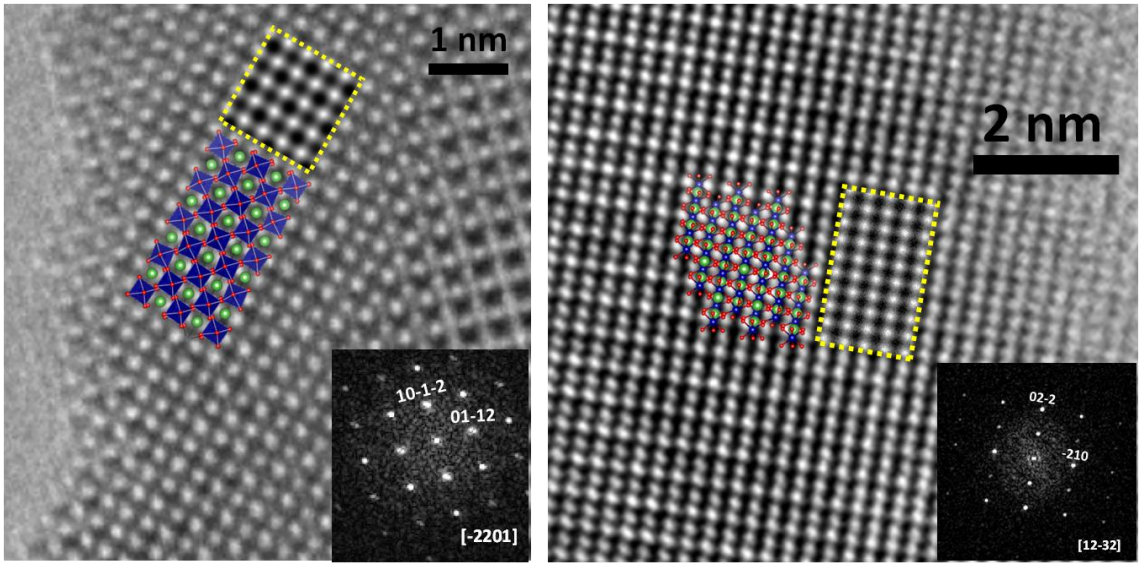

Figure 4.10. Experimental HRTEM micrographs along the [-2201] and [12-32] zone axis for $LaCoO_3$. No streaking or extra spots are evident (see the FFT images in the figure insets). A good match between experimental and simulated images (rectangle marked with yellow dots) is demonstrated. Structural pictures of the $LaCoO_3$ are shown inside the micrographs.

4.2.4. Oxygen contents

The oxygen contents have been determined by thermogravimetric analysis in a hydrogen atmosphere. Table 4.3 shows the analysis of the reduction products and the weight loss together with the cationic stoichiometry data for all perovskites synthesized.

Table 4.3. TGA results for the reduction of lanthanum perovskites in H_2 (200 mbar)/He (400 mbar) atmosphere performed at 700 ºC.

$LaMO_{3\pm\delta}$	Intermediate products	Final products	% Weight loss	Composition
Cr	----	$LaCrO_3$	0.20	$LaCrO_{3.00(3)}$
Mn	$LaMnO_3$	La_2O_3 + MnO	4.06	$LaMnO_{3.12(1)}$
Fe	La_2O_3 + FeO	La_2O_3 + Fe	9.60	$LaFeO_{2.97(3)}$
Co	La_2O_3 + CoO	La_2O_3 + Co	9.69	$LaCoO_{2.99(2)}$
Sr, Fe	La_2O_3 + SrO + FeO	La_2O_3 + SrO + Fe	12.55	$La_{0.8}Sr_{0.2}FeO_{3.21(3)}$
Sr, Fe, Co	La_2O_3 + SrO + FeO + CoO	La_2O_3 + SrO + Fe + Co	12.52	$La_{0.8}Sr_{0.2}Fe_{0.5}Co_{0.5}O_{3.23(1)}$

As an example, the thermogravimetric reduction plots for "$LaMnO_{3.12}$" and $LaCoO_3$ are presented in Figure 4.11. Two different steps in the reduction processes are apparent. The correct formula with a fully occupied oxygen lattice for "$LaMnO_{3.12}$" can be expressed as $La^{3+}_{0.962}(Mn^{3+}_{0.76}Mn^{4+}_{0.24})_{0.962}O_3$. By heating between 300 and 550 ºC, manganites with different oxygen contents can be isolated. Above this temperature, the perovskite starts to decompose into La_2O_3 and MnO. In the case of $LaCoO_3$, the first step in the TGA plots corresponds to the reduction to La_2O_3 and CoO between 300 ºC to 450 ºC. At higher temperatures, the CoO decomposes to metallic Co.

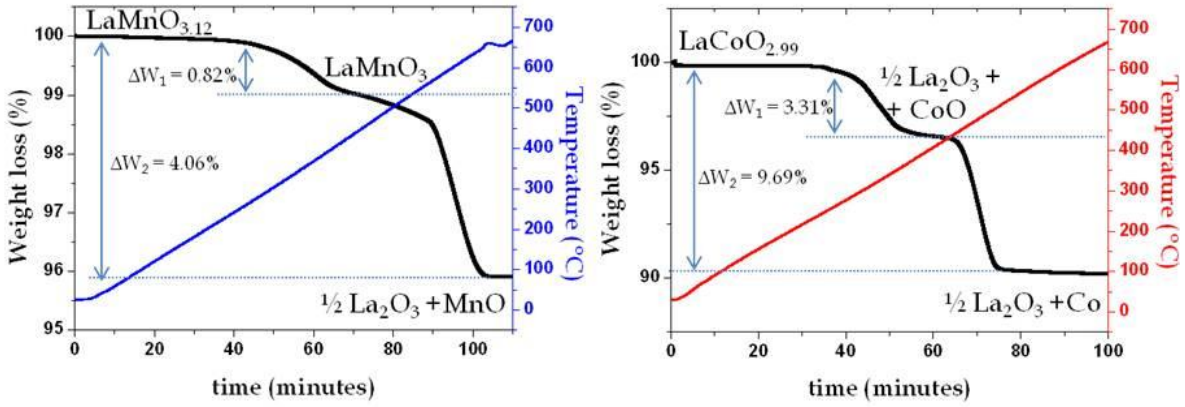

Figure 4.11. TGA plots corresponding to the H_2/He reduction of "$LaMnO_{3.12}$" and $LaCoO_3$.

There is no weight loss in the case of stoichiometry $LaCrO_3$ in the measurement range up to 700 ºC. In the case of $La_{0.8}Sr_{0.2}FeO_3$ and

$La_{0.8}Sr_{0.2}Fe_{0.5}Co_{0.5}O_3$ different reduction steps to La_2O_3, SrO and metallic Fe and/or Co have been observed.

4.2.5. Relation between magnetic and dielectric properties in $LaCoO_3$

A comparative study of impedance spectroscopy (IS) and magnetisation measurements on microwave (MW) and conventionally synthesized ceramics was performed. By comparison of $LaCoO_3$ synthesised from different routes, it is possible to ensure that the observed effects are intrinsic and inherent to the material. More importantly, such comparison allows studying the effect of magnetic oxygen vacancy defects, which naturally possess different concentrations and properties for different chemical synthesis routes. The difference in the concentration of oxygen vacancy defects may be related to the different thermodynamic conditions: conventional synthesis is performed in thermodynamic equilibrium, whereas the chemical reaction in MW synthesis occurs far away from such equilibrium.

In Figure 4.12 temperature dependent impedance spectroscopy data for the MW synthesized $LaCoO_3$ ceramic sample is presented as the real part of the complex dielectric permittivity (ε') plotted vs frequency (f) on a double logarithmic scale. Two ε' permittivity plateaus (bulk and GB) can be seen at T = 60 K, which suggests an inhomogeneous electronic structure due to two different relaxation processes. Such double permittivity plateaus are typical for ceramics containing two dielectric relaxation processes. At the specific temperature and frequency ranges displayed the two relaxations may well reflect the intrinsic bulk and a GB contribution.[22, 47] The bulk dielectric permittivity ε_r in MW synthesised $LaCoO_3$ was found to be about 17 including a small correction for the contribution from the GB capacitance. This is in close agreement with conventional $LaCoO_3$, and no significant effects on the intrinsic bulk permittivity ε_r due to the different synthesis methods are indicated. At the low frequency ends of the 120 K and 140 K curves in Fig. 4.12 typical signs of an electrode sample interface effect (labelled “Electrode”) are displayed. At

temperatures above the thermally induced spin-state transition T_{s1} > 80 K an additional dielectric relaxation at intermediate frequency appears which directly points towards a coupling of the magnetic and dielectric properties. In strongly correlated electron systems it is common that magnetic and dielectric properties are coupled via the lattice due to the localised character of electrons and the concomitant strong electron lattice interactions. Therefore, changes in magnetisation due to varying electron-spin configurations may well be reflected in the dielectric permittivity and/or the charge transport properties.

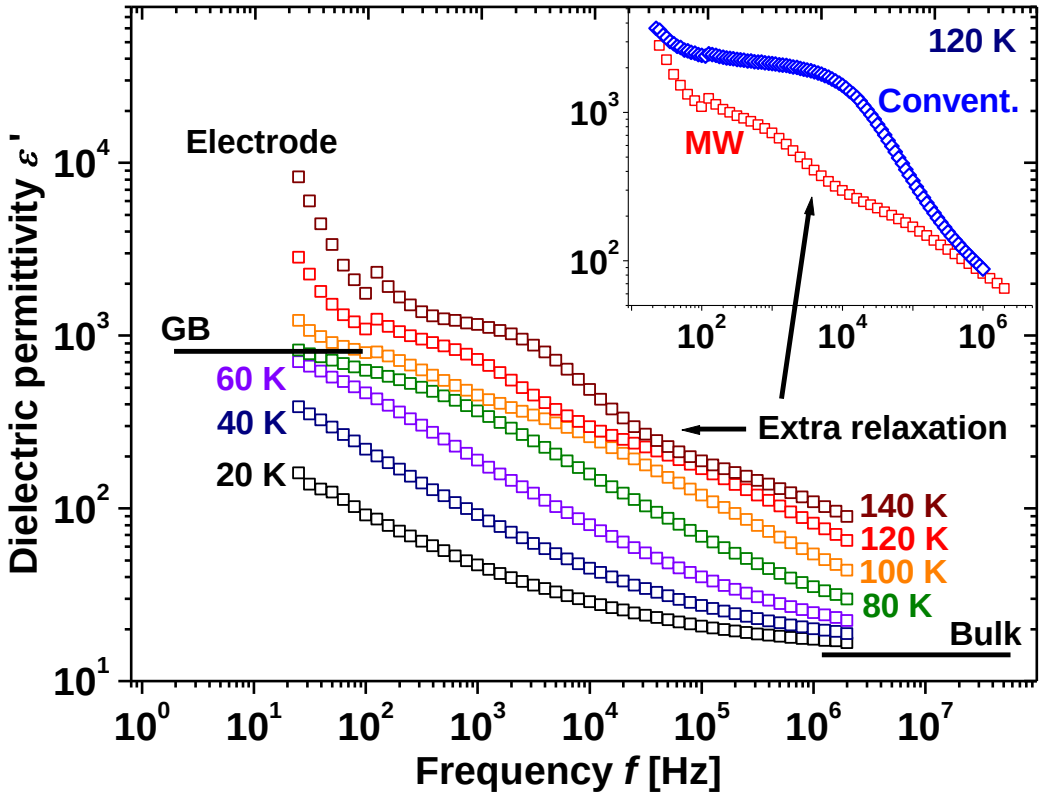

Figure 4.12. Dielectric permittivity ε' vs frequency of MW synthesised $LaCoO_3$. An additional relaxation appears at $T \geq 80$ K. Black solid lines represent GB and bulk plateaus. Inset: Comparison of Conventionally (Convent.) and MW synthesised $LaCoO_3$ at 120 K.

In conventionally (Convent.) synthesized $LaCoO_3$ the additional "extra" dielectric relaxation above T_{s1} cannot be observed in plots of ε' vs f as demonstrated in the inset of Fig.4.12 although it does clearly exist[22] as confirmed in the inset Fig. 4.13. The coexistence of this additional dielectric relaxation with the normal GB and bulk contributions is a sign of phase –

coexistence, where LS and IS/HS may coexist above T_{s1}. The additional "extra" relaxation may represent sample areas that have adopted a IS/HS state.

Plots of the imaginary parts of the impedance -Z'' vs frequency f for the MW samples are shown in Figure 4.13 and again demonstrate the dielectric phase separation at $T_{s1} \approx 80$ K. Comparative -Z'' vs f plots for MW and conventional $LaCoO_3$ are shown in the inset of Figure 4.13. The "extra" dielectric relaxation can be identified clearly in form of an additional peak (labelled with an arrow) and appears at T_{s1} now for both types of $LaCoO_3$. Clear differences are indicated though in the relaxation peak frequency (see both black vertical arrows). Nevertheless, the appearance of the "extra" relaxation is independent of the synthesis route and the apparent dielectric phase separation at T_{s1} constitutes an intrinsic property of $LaCoO_3$.

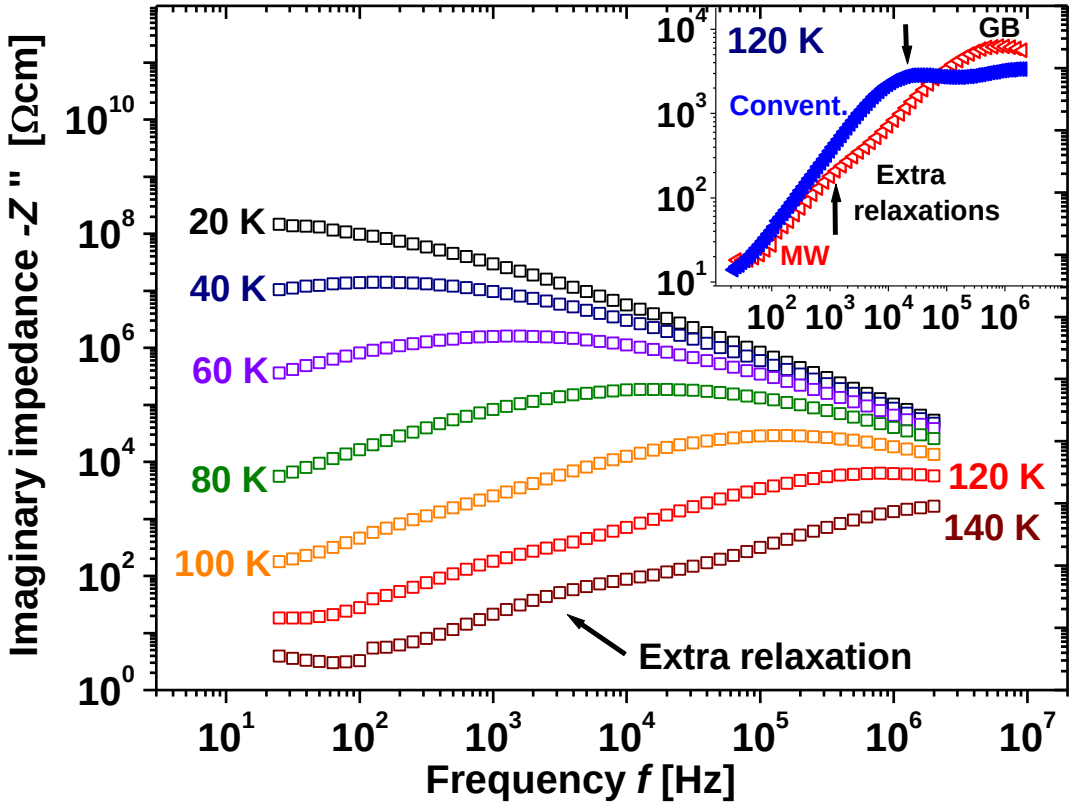

Figure 4.13. Imaginary impedance –Z'' vs frequency f of MW synthesized $LaCoO_3$. At $T \geq 80$ K an additional relaxation peak appears. Inset: Comparison of Conventionally (Convent.) and MW $LaCoO_3$ at 120 K.

Note that the "extra" dielectric relaxation process cannot be attributed to secondary material phase such as Co_3O_4 or La_2O_3, because the resistance and

capacitance values may be unrealistic and the appearance of this relaxation is clearly correlated to the spin state transition temperature. The occurrence of this "extra" relaxation implies that the dc resistance can contain 2 (GB & bulk for T < 80 K) or 3 components (additional "extra relaxation" for T > 80 K), and T_{s1} is reflected in distinct changes in the dc activation energy.

The combined plots of Z '' vs f and M '' vs f for MW and conventional $LaCoO_3$ in Figure 4.14 show the dielectric relaxation peaks of the GB and bulk dielectric relaxations respectively at T = 60 K below T_{s1} (no "extra" phase). The GB and bulk relaxations exhibit strong overlap in both type of $LaCoO_3$, because they cannot be resolved as separated semicircles in complex plane plots of $-Z$ '' vs Z ' in the inset of Figure 4.14.

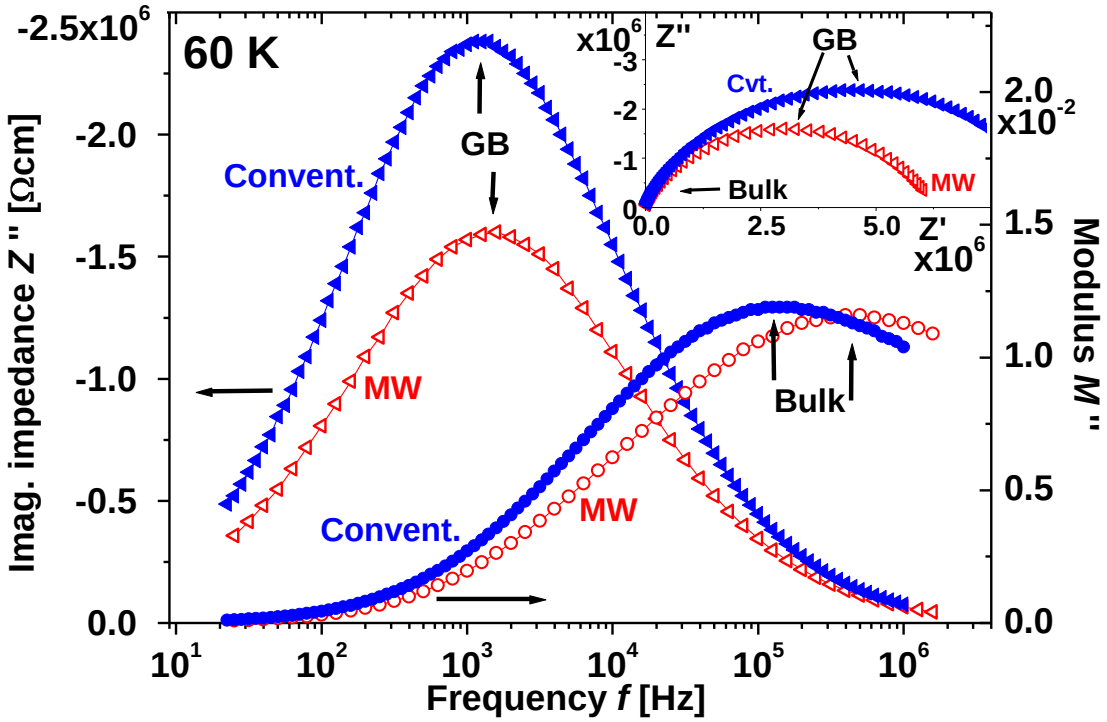

Figure 4.14. Imaginary impedance Z '', and modulus M '' vs frequency at 60 K; GB and bulk can be resolved. **Inset:** Z '' vs Z '; overlap of GB and bulk semicircles prevents resolution of both relaxations.

Possible differences in defect properties or concentration in MW and conventional $LaCoO_3$ were confirmed from magnetization vs temperature measurements from pellet fragments as shown in Fig.4.15. The sharp upturn in magnetization in a Curie-Tail fashion below 30 K in Fig.4.15 is a manifestation

of the magnetic defect structure which is related to oxygen vacancy defects.[48, 49] The Curie Weiss plots of χ^{-1} vs T in the main Figure 4.15 for MW and conventionally synthesized $LaCoO_3$ show 2 approximately linear regimes (solid lines) as expected from the Curie-Weiss law.

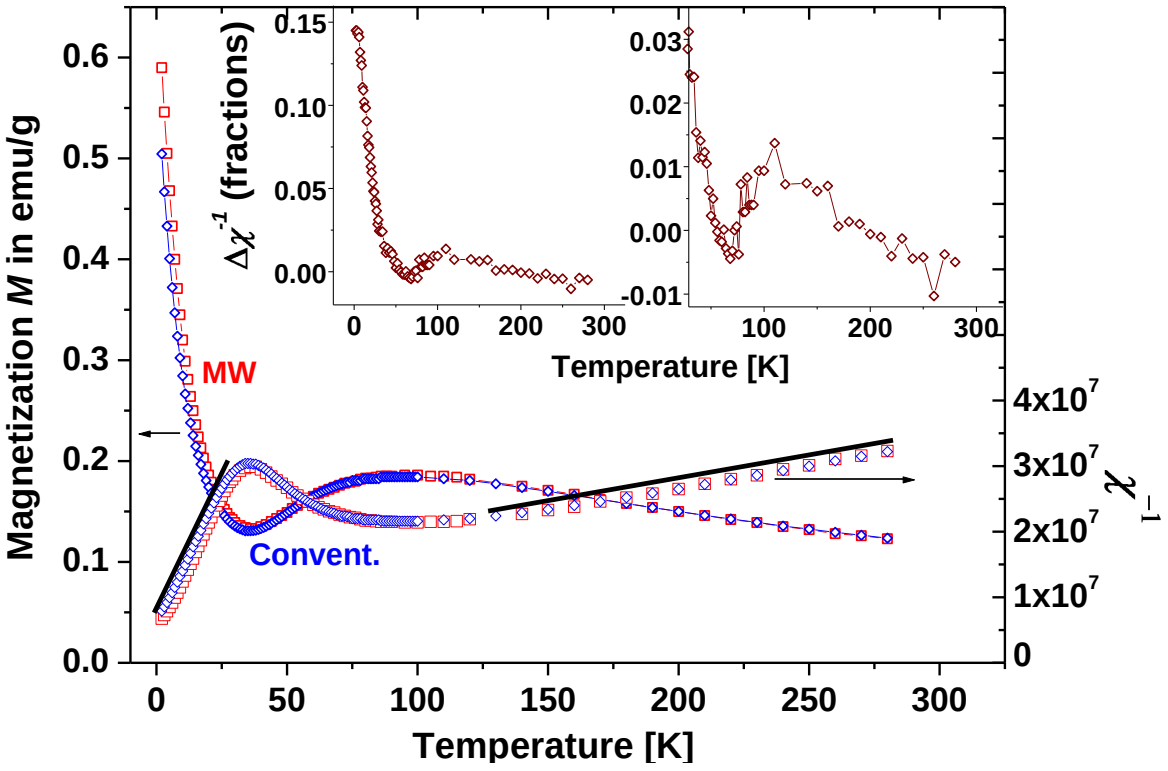

Figure 4.15. Field cooled (10 kOe) mass magnetization M and reciprocal magnetic susceptibility χ^{-1} vs T for MW and conventionally synthesized $LaCoO_3$. **Inset**: Fractional difference of reciprocal magnetic susceptibility $\Delta\chi^{-1}$ vs T. $\Delta\chi^{-1} = (\chi^{-1}_{cvt.} - \chi^{-1}_{mw})/(\chi^{-1}_{cvt/mw})$.

The slope of the Curie-Weiss plot in Fig.4.15 for the low temperature defect magnetism ($T \leq 30$ K) is larger by a factor of about 10 as compared to the regular magnetism ($T \geq 130$ K). This highlights the different origin and the different properties of the magnetic defect phase. In this context it is interesting to note that the extrapolated Θ values from the Curie Weiss plots vary for MW and conventional $LaCoO_3$. Both Θ values are negative indicating anti-ferromagnetism, but for MW synthesized $LaCoO_3$ the value changes by a factor of ≈ 0.7 and is closer to zero. The varied defect properties in MW synthesized

$LaCoO_3$ may drive the $LaCoO_3$ defect magnetism closer to a ferromagnetic state, where Θ would become positive.

The magnetization is slightly higher for the MW synthesized sample by a factor of ≈ 1.16 at the end of the Curie-tail, which implies that the properties of the magnetic defect structure may be different in the two samples. On the other hand, the regular magnetic structure at T > 50 K shows little changes with the different synthesis routes. The difference in magnetisation between MW and conventional $LaCoO_3$ is illustrated in the two insets of Fig.4.15 in terms of the magnetic susceptibility χ^{-1}: $\Delta\chi^{-1} = [(\chi^{-1}_{cvt.} - \chi^{-1}_{mw})/(\chi^{-1}_{cvt/mw})]$ is plotted vs T as a fraction of the conventional ($\Delta\chi^{-1} > 0$) or the MW ($\Delta\chi^{-1} < 0$) susceptibility. Whereas the defect magnetism is clearly reflected at $T \leq 30$ K in the $\Delta\chi^{-1}$ vs T data only a rather weak peak structure is visible around T_{s1}. It is interesting to note that these features resemble the magnetisation vs T curve in the main figure. This is not expected by any means and it implies that the difference between the 2 curves is not constant nor can it be accounted for by a constant factor. Therefore, an experimental artefact as the origin of $\Delta\chi^{-1}$ can safely be ruled out. Clear differences in the defect magnetism are indicated by large $\Delta\chi^{-1}$ values within the Curie-tail temperature region. The small peak in $\Delta\chi^{-1}$ near T_{s1} may suggest the following model: magnetic oxygen vacancy defects act as nucleation centres for IS/HS state regions and differences in the magnetic defect structure may be reflected in slightly different nucleation behaviour near T_{s1} leading to differences in magnetisation.

Significant diamagnetic contributions to $\Delta\chi^{-1}$ in the LS state of the two different $LaCoO_3$ samples are unlikely, because $\Delta\chi^{-1}$ reduces to basically zero at 60 K although diamagnetic contributions should increase when large parts of the material adopt the diamagnetic LS state. It should be pointed out that the minimum in $\Delta\chi^{-1}$ at 60 K does not coincide with the minimum in χ at 30 K, which again rules out an experimental artefact as the main contribution to $\Delta\chi^{-1}$.

Magnetisation was measured as a macroscopic average over the full sample, whereas dielectric spectroscopy is capable of deconvoluting and

separately displaying different relaxation processes even if the respective areas are microscopically small in real space such as thin GB layers and possibly the "extra" phase. The dielectric and magnetic differences between MW and conventional $LaCoO_3$ may be small in a macroscopic sense, but dielectric spectroscopy may exhibit a superior resolution power at microscopic level as compared to magnetisation measurements, a feature which is in fact well established.

4.3. (RE)CrO_3 (RE = Rare Earth)

Rare-earth (RE) orthochromites (RE)CrO_3 with distorted perovskite structure are currently attracting research interest due to their potential application as multifunctional materials.[50] Chromites in general are under intense investigation nowadays,[51] where the particular interest into the RE species is debited to potential magneto-electric coupling. Initial studies had claimed that certain rare-earth chromites belong to a new family of ferroelectric and antiferromagnetic multiferroics.[52] Such claims are somewhat surprising though, because (RE)CrO_3 chromites adopt a centrosymmetric orthorhombic structure with space group *Pnma* (#62). Ferroelectricity in centrosymmetric space groups is unusual and it was attempted recently to explain this by Cr off-centering with a local character and a small value of displacement leading to weak polarization.[53]

The magnetic properties of the (RE)CrO_3 series contain a rich variety of different magnetic spin interactions, where 3 different types may occur: (1) Cr^{3+}-Cr^{3+}, (2) Cr^{3+}-$(RE)^{3+}$, and (3) RE^{3+}-RE^{3+}, with isotropic, symmetric, and antisymmetric anisotropic exchange interactions, respectively.[54, 55] A weak ferrimagnetic moment in some of the species was claimed to arise from Dzyaloshinskii–Moriya (D–M) interactions between Cr^{3+} spins.[56,57] The antiferromagnetic Néel temperature T_{N1} for Cr^{3+}-Cr^{3+} ordering increases with

the RE ionic radius,[58] which is associated with diminishing lattice distortions and the increasing Cr^{3+}-O^{2-}-Cr^{3+} bond angles approaching the ideal 180 °.[59] The charge transport properties in (RE)CrO_3 materials have been claimed to involve p-type semiconductivity with sensitivity towards humidity, methanol, ethanol, and several gases, which is useful for potential sensor applications.[60, 61] Furthermore, $LaCrO_3$ and its doped variants are candidates for application as interconnecting materials in solid oxide fuel cells[62] and as catalysts for hydrocarbon oxidation.[63]

4.3.1. Synthetic aspects

The synthetic procedure is the same as is described above for $LaCrO_3$ (see *Section 4.2.1*). The resulting powders for the full (RE)CrO_3 series plus the Y-specie were all compacted into pellets in a 1 ton die press for 5 minutes and densification sintering was performed in air at 1300 °C for 15 hours.

The reaction pathway for (RE)CrO_3 formation from nitrate precursors can be described by a 3-step process as indicated by the XRD patterns in Fig.4.16:

(a) Formation of an amorphous phase after 10 min microwave irradiation.
(b) Formation of polycrystalline (RE)CrO_4 at 500 °C (2h).
(c) Formation of (RE)CrO_3 at 800 °C (2 h).

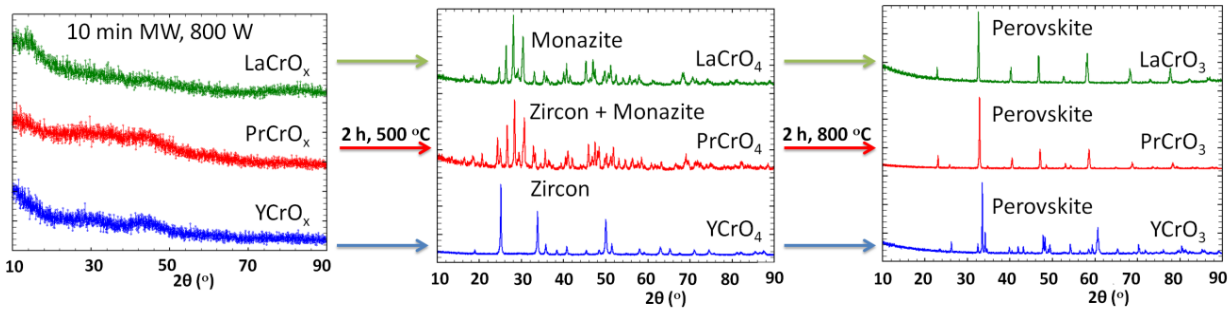

Fig.4.16: (a) Powder XRD pattern of the MW as-synthesized $PrCrO_x$ powder (amorphous), (b) XRD pattern of the 500 °C annealed powders showing monazite ($LaCrO_4$), mixed monazite and zircon ($PrCrO_4$), and pure zircon ($YCrO_4$) structure, (c) XRD pattern of the 800 °C annealed powders all showing pure perovskite phase ($LaCrO_3$, $PrCrO_3$, $YCrO_3$).

Notably, most of the intermediate (RE)CrO_4 phases show the zircon-type structure with tetragonal symmetry, S.G. $I4_1/amd$ (# 141), except in the case of $LaCrO_4$ and $PrCrO_4$. For $LaCrO_4$ the monazite-type structure with monoclinic symmetry, S.G. $P2_1/n$ (# 14), is obtained due to the large La^{3+} ionic radius, whereas in $PrCrO_4$ zircon and monazite phases coexist. Another point of interest is the unusual Cr^{5+} oxidation state in these intermediate phases. The (RE)CrO_3 final products adopt a distorted perovskite structure and orthorhombic symmetry, S.G. *Pnma* (# 62) upon heating at 800 ^oC as expected with the more common Cr^{3+} oxidation state.

4.3.2. Structural characterization

All microwave synthesized (RE)CrO_3 and $YCrO_3$ powders are single-phase as confirmed by XRD. Figure 4.17 shows the powder X-ray diffraction (XRD) patterns of the (RE)CrO_3 series. It is clear that the increasing diffraction angles with decreasing RE ionic radius lead to a decrease in unit cell size. Tables 4.4a and 4.4b summarize all structural parameters obtained from Rietveld refinements of the XRD pattern. Tables 4.5a and 4.5b summarize additional parameters such as bonding angles and bonding distances.

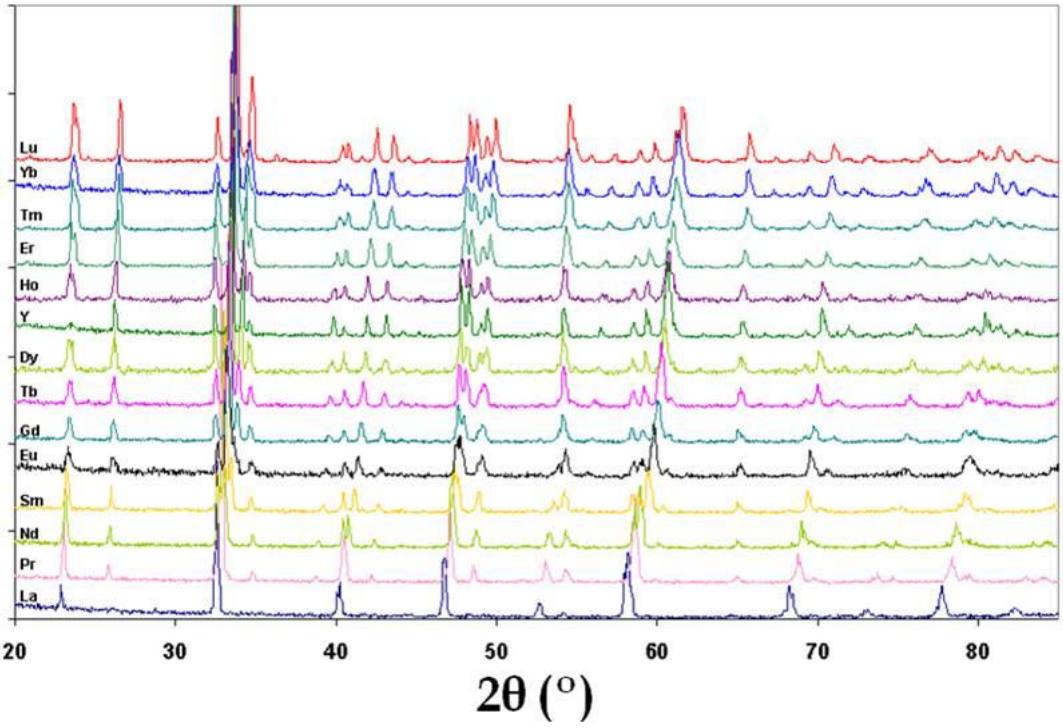

Figure 4.17: XRD patterns of (RE)CrO_3 powders

Table 4.4a: Structural parameters for (RE)CrO_3 from refining XRD data

	$LaCrO_3$	$PrCrO_3$	$NdCrO_3$	$SmCrO_3$	$EuCrO_3$	$GdCrO_3$	$TbCrO_3$
a (Å)	5.4790(1)	5.47986(7)	5.48649(3)	5.48848(6)	5.51039(9)	5.52582(7)	5.51909(5)
b (Å)	7.7616(2)	7.7154(1)	7.69419(5)	7.62627(8)	7.6255(1)	7.60635(9)	7.57856(7)
c (Å)	5.5164(1)	5.45034(7)	5.42108(3)	5.35381(6)	5.34191(8)	5.31376(7)	5.29434(5)
RE position 4c							
x	0.0178(2)	0.0354(1)	0.0419(1)	0.0505(1)	0.0541(2)	0.0585(2)	0.0604(2)
z	-0.0035(5)	-0.0074(4)	-0.0087(2)	-0.0103(3)	-0.0119(5)	-0.0131 (4)	-0.0144(3)
U*100 (Å²)	0.19(2)	0.15(2)	0.27(3)	0.09(2)	0.10(3)	0.28(6)	0.17(3)
Cr position 4b							
U*100 (Å²)	0.11(2)	0.12(2)	0.17(3)	0.26(3)	0.13(2)	0.13(3)	0.14(2)
O(1) position 4c							
x	0.496(4)	0.483(2)	0.480(1)	0.480 (1)	0.463(2)	0.468(2)	0.465(2)
z	0.064(4)	0.081 (2)	0.089(1)	0.088 (1)	0.095(2)	0.098 (2)	0.100(2)
Occ	1.00(1)	1.00(1)	1.00(2)	1.00(1)	1.00(2)	1.00(2)	1.00(1)
U*100 (Å²)	0.24(5)	0.11(3)	0.07(2)	0.10(2)	0.24(3)	0.14(3)	0.17(2)
O(2) position 8d							
x	0.280(2)	0.290(2)	0.285(1)	0.285(2)	0.282(2)	0.292 (2)	0.296 (2)
y	0.033(1)	0.033(1)	0.0403(7)	0.0434(9)	0.048(1)	0.048(1)	0.0500(9)
z	-0.271(3)	-0.287(2)	-0.287(1)	-0.290(1)	-0.289(2)	-0.294(2)	-0.298(1)
Occ	1.01(1)	1.00(1)	1.00(1)	1.00(2)	1.00(1)	1.00(2)	1.01(2)
U*100 (Å²)	0.24(5)	0.11(3)	0.07(2)	0.10(2)	0.24(3)	0.14(3)	0.17(2)
χ^2	1.28	0.93	1.14	2.02	1.41	0.92	0.97
R_{wp} / R_{exp} (%/%)	4.70 / 4.15	4.52 / 4.69	4.53 / 4.25	1.77 / 1.24	3.04 / 2.70	2.68 / 2.78	3.19 / 3.24
R_{Bragg}	4.29	3.07	3.89	4.02	4.58	4.68	2.27

S.G. *Pnma*: 4*c* (*x* ¼ *z*), 4*b* (0 0 ½), 8*d* (*xyz*)

Table 4.4b: Structural parameters for (RE)CrO_3 from refining XRD data

	$DyCrO_3$	$YCrO_3$	$HoCrO_3$	$ErCrO_3$	$TmCrO_3$	$YbCrO_3$	$LuCrO_3$
a (Å)	5.50805(5)	5.52267(6)	5.50728(5)	5.50289(4)	5.50850(6)	5.48912(5)	5.50150(7)
b (Å)	7.53767(7)	7.53555(8)	7.52026(6)	7.50370(6)	7.50506(8)	7.47059(7)	7.4811(1)
c (Å)	5.25436(5)	5.24376(5)	5.23164(4)	5.21377(4)	5.21114(6)	5.18258(5)	5.17911(7)
RE position 4c							
X	0.0635(1)	0.0666(1)	0.06509(9)	0.06698(7)	0.06766(8)	0.06912(9)	0.0704(1)
Z	-0.0159(2)	-0.0170(2)	-0.0172(1)	-0.0179(1)	-0.0182(1)	-0.0184(1)	-0.0187(2)
U*100 (Å²)	0.11(2)	0.30(4)	0.14(4)	0.04(1)	0.21(1)	0.14(4)	0.08(2)
Cr position 4b							
U*100 (Å²)	0.18(2)	0.29(3)	0.06(2)	0.05(1)	0.18(3)	0.10(4)	0.07(2)
O(1) position 4c							
X	0.467(1)	0.4652 (8)	0.4686(9)	0.4647(7)	0.453 (1)	0.464(1)	0.466(1)
Z	0.101 (1)	0.1044(8)	0.0990(9)	0.1081(7)	0.1136(9)	0.108(1)	0.110(1)
Occ	1.00(1)	1.01(2)	1.01(2)	1.00(1)	1.00(1)	1.01(2)	1.00(2)
U*100 (Å²)	0.31(3)	0.18(3)	0.10(2)	0.13(3)	0.14(5)	0.08(3)	0.11(3)
O(2) position 8d							
X	0.297(1)	0.3023(6)	0.2991(8)	0.3022(6)	0.3019(8)	0.3072(8)	0.303(1)
Y	0.0520 (6)	0.0538(4)	0.0492 (5)	0.05195(4)	0.0562(5)	0.0538(5)	0.0539(7)
Z	-0.3016(9)	-0.3073(6)	-0.3030(8)	-0.3060(6)	-0.3092(7)	-0.3115(8)	-0.307(1)
Occ	1.00(1)	1.01(1)	1.01(2)	1.00(1)	1.00(1)	1.00(1)	1.00(1)
U*100 (Å²)	0.31(3)	0.18(3)	0.10(2)	0.13(3)	0.14(5)	0.08(3)	0.11(3)
χ^2	2.03	1.07	5.05	3.88	1.37	6.32	3.06
R_{wp} / R_{exp} (%/%)	1.62 / 1.13	5.20 / 5.03	4.06 / 1.81	3.43 / 1.74	5.19 / 4.25	4.59 / 1.82	8.15 / 4.66
R_{Bragg} (%)	5.31	2.46	3.20	2.33	1.68	4.40	5.71

S.G. *Pnma*: 4*c* (*x* ¼ *z*), 4*b* (0 0 ½), 8*d* (*xyz*)

Table 4.5a. Selected structural information for (RE)CrO_3 obtained from XRD data. Angles are given in degrees and distances in [Å]

	$LaCrO_3$	$PrCrO_3$	$NdCrO_3$	$SmCrO_3$	$EuCrO_3$	$GdCrO_3$	$TbCrO_3$
tolerance factor	0.92338	0.91006	0.90431	0.89315	0.88883	0.88415	0.87984
[a] **Tilt angle** θ	9.4	11.5	12.2	12.9	13.4	14.4	15.2
[b] **Tilt angle** φ	9.4	11.5	12.2	12.9	13.4	14.4	15.2
[c] **Tilt angle** μ	10.3	13.2	14.4	14.2	16.0	16.1	16.5
Cr-O(1) × 2	1.972(2)	1.981(2)	1.986(2)	1.967(2)	1.968(1)	1.980(3)	1.976(2)
Cr-O(2) × 2	1.94(2)	1.96(1)	1.967(6)	1.955(8)	1.970(3)	1.974(9)	1.970(8)
Cr-O(2)' × 2	2.00(2)	1.98(1)	1.977(6)	1.978(8)	1.985(4)	1.984(9)	1.992(8)
Average *B*'-O	1.971(6)	1.975(4)	1.977(2)	1.966(3)	1.974(1)	1.979(3)	1.980(3)

For S.G. *Pnma* only a *B*-site exists with co-ordination: *B*'-O(1) × 2, *B*'-O(2) × 2 and *B*'-O(2)' × 2

For S.G. *Pnma* the tilting scheme in Glazer's notation ($a^-a^-c^+$) implies that $\theta \approx \varphi$

[a] With [101] for *Pnma*

[b] With [10-1] for *Pnma*

[c] With [010] for *Pnma*

Table 4.5b. Selected structural information for (RE)CrO_3 obtained from XRD data. Angles are given in degrees and distances in [Å]

	$DyCrO_3$	$YCrO_3$	$HoCrO_3$	$ErCrO_3$	$TmCrO_3$	$YbCrO_3$	$LuCrO_3$
tolerance factor	0.87552	0.87264	0.87156	0.86796	0.86436	0.86076	0.85716
[a] **Tilt angle** θ	15.9	17.00	15.8	16.6	17.4	17.7	17.0
[b] **Tilt angle** φ	15.9	17.00	15.8	16.6	17.4	17.7	17.0
[c] **Tilt angle** μ	16.6	17.1	16.2	17.6	19.0	17.6	17.8
Cr-O(1) × 2	1.966(2)	1.971(1)	1.958(1)	1.968(1)	1.984(2)	1.960(2)	1.965(2)
Cr-O(2) × 2	1.979(5)	1.988(4)	1.968(4)	1.970(3)	1.983(4)	1.972(5)	1.968(6)
Cr-O(2)' × 2	1.979(5)	1.993(3)	1.978(4)	1.985(4)	1.991(4)	1.990(5)	1.984(6)
Average *B*'-O	1.975(2)	1.984(1)	1.968(2)	1.974(1)	1.986(1)	1.974(2)	1.972(2)

For S.G. *Pnma* only a *B*-site exists with co-ordination: *B*'-O(1) × 2, *B*'-O(2) × 2 and *B*'-O(2)' × 2

For S.G. *Pnma* the tilting scheme in Glazer's notation ($a^-a^-c^+$) implies that $\theta \approx \varphi$

[a] With [101] for *Pnma*

[b] With [10-1] for *Pnma*

[c] With [010] for *Pnma*

Fig. 4.17 shows representative examples of the Rietveld refinement fits for RE = La, Nd, Sm, Tb, Tm and.Lu. The distorted perovskite structure with orthorhombic symmetry (S.G. *Pnma*, #62) was confirmed in all RE-chromites, in agreement with previous work.[64, 65] The unit cell vectors can be represented by $\sqrt{2}\boldsymbol{a}_p \times 2\boldsymbol{a}_p \times \sqrt{2}\boldsymbol{a}_p$ where $\boldsymbol{a}_p$ refers to the simple cubic perovskite cell. The perovskite tolerance factors for (RE)CrO_3 are t = 0.85 – 0.93, which is within the reported limits of t = 0.8 - 1 for perovskite structures of cubic (t = 1) or lower symmetry (t < 1).[1]

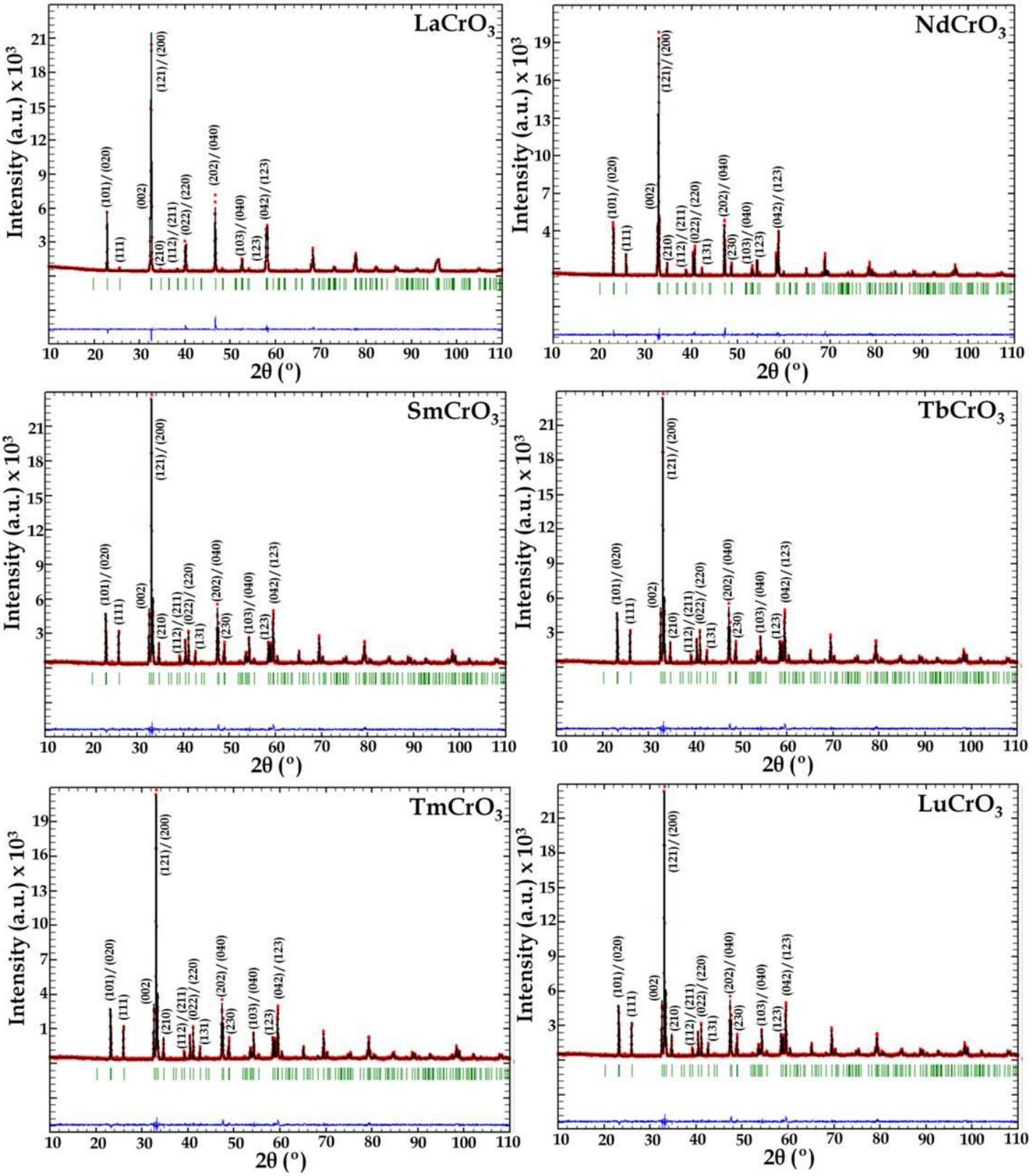

Figure 4.17. Rietveld refinement of XRD patterns: Observed (red dotted lines), refined (black solid lines), and their difference (blue bottom line). Green vertical bars indicate the X-ray reflection positions.

The cell parameters ***a***, ***b*** and ***c*** for the RE family are given in Fig. 4.18 as a function of the RE ionic radius (IOR) and the tolerance factor *t*. IOR values were taken from Shannon's tables,[36] where the coordination number 9 was considered for all RE cations consistently. Fig. 4.18 shows approximately constant cell parameter ***a***, whereas ***b*** and ***c*** increase with increasing IOR.

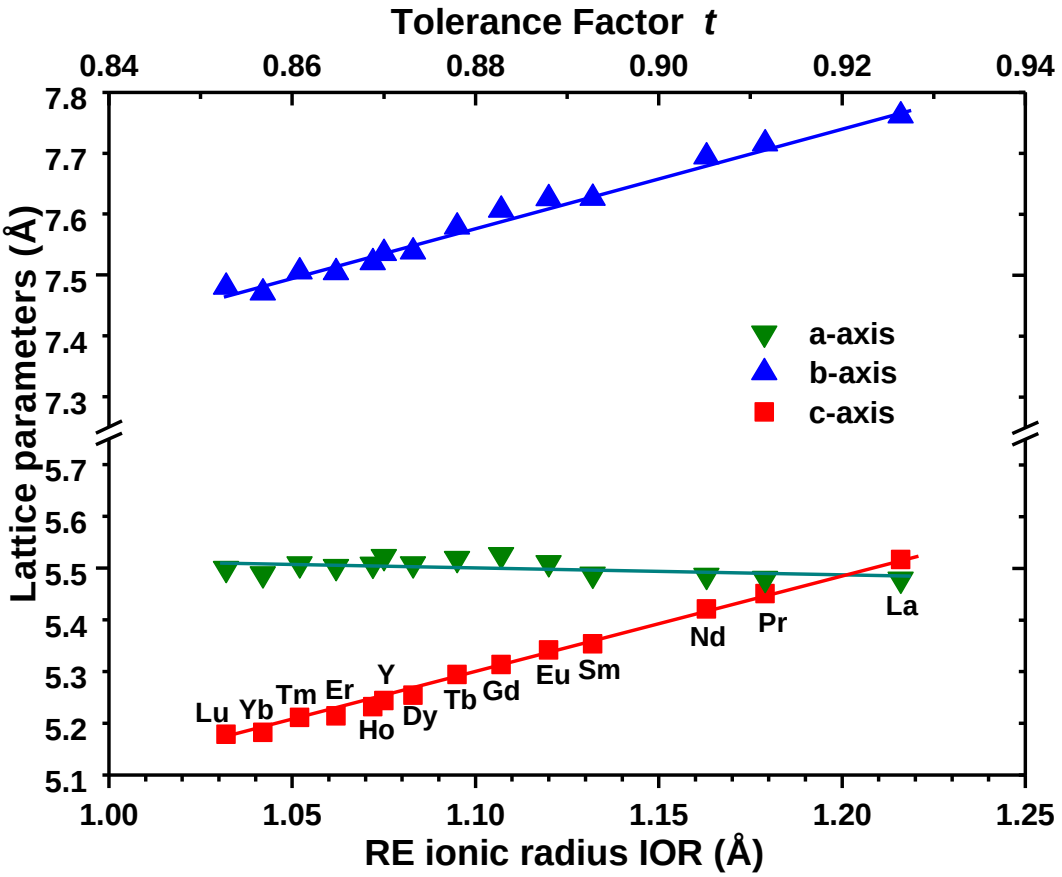

Figure 4.18. Lattice parameters ***a***, ***b*** and ***c*** vs the RE ionic radius IOR and the perovskite tolerance factor for the (RE)CrO_3 series. An approximately linear increase of ***b*** and ***c*** with IOR implies an increasing unit cell size.

It is well known that X-ray diffraction is not the optimum technique to deal with structural features related to light atoms such as oxygen, however, some useful structural information can be extracted from the XRD data being consistent along the full series (Table 4.5). The Cr^{3+}-O^{2-} bonding distances were determined with relatively low resolution, but all these distances appear to be similar (≈ 1.97 Å) and close to the expected value (1.9805 Å)[66]. The main effect of the RE size is observed in the octahedral tilting of the perovskite cell. θ, φ, and μ

represent the tilting angles of the BO_6 octahedra along the three main directions of the ideal ABO_3-cubic perovskite structure, which implies that the larger these angles are, the more distorted the structure.[4] All angles decrease quite consistently away from the ideal 180° with decreasing IOR and increasing RE atomic number, because the rigid CrO_6 octahedra accommodate A-site RE cations of decreasing size by decreasing unit cell size and increasing degrees of octahedral tilting.

4.3.3. Microstructural characterization

As a representative example, the SEM micrographs of $ErCrO_3$ powder and the $ErCrO_3$ sintered pellet are shown in Fig. 4.18a & b, respectively. In powder form the $ErCrO_3$ particles form a brain-shaped structure and exhibit intra-granular fractures (Figure 4.19a). These fractures were healed out during sintering, and the sintered pellet displays no significant porosity.

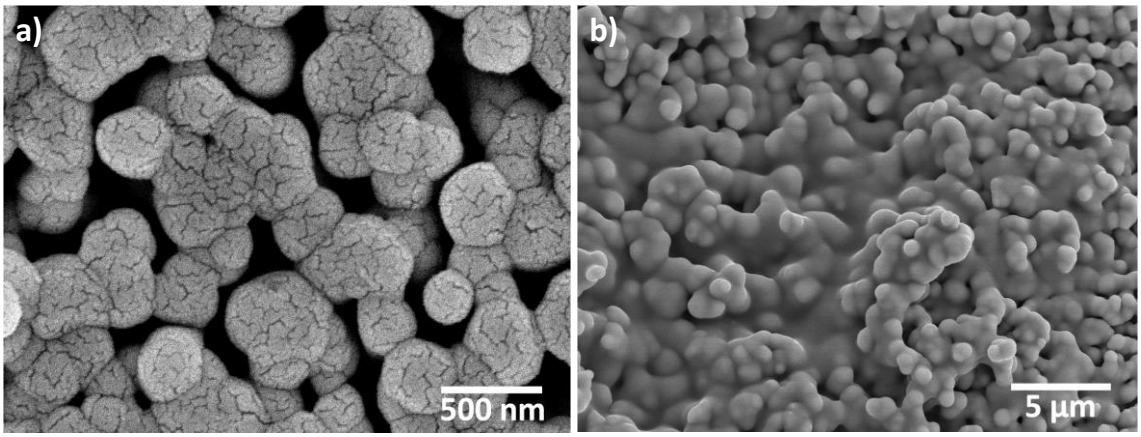

Figure 4.19. Scanning electron micrograph of (a) $ErCrO_3$ powder as prepared. (b) $ErCrO_3$ pellet after densification sintering at 1300 ° C for 15 hours.

A full set of SEM micrographs for $(RE)CrO_3$ powders is presented in Figure 4.20 where clear evidence for agglomeration of sub-micrometer particles is presented. EDS analysis yielded an average ratio (RE):Cr of ≈ 1:1 which corresponds to the nominal stoichiometry.

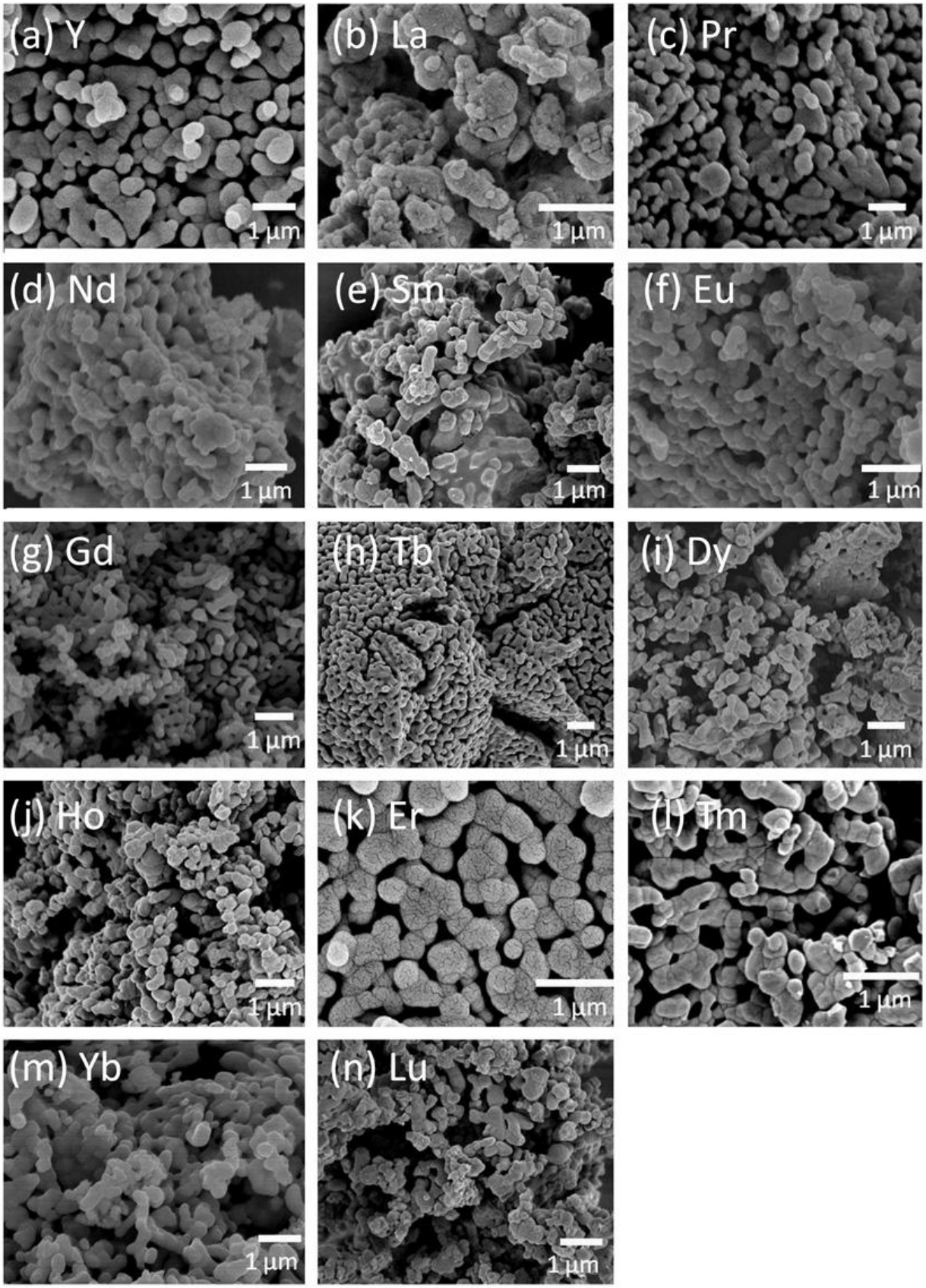

Figure 4.20. SEM micrographs of (RE)CrO_3 powder

HRTEM images for (RE)CrO_3 (RE = La, Nd, Y and Lu) are displayed in Fig. 4.21. The experimental images taken along the [001] zone axis show excellent agreement with the calculated images depicted within the rectangles marked with (yellow) asterisks. In all images the black dots are the projections of the atomic columns from the cationic RE and Cr sublattices, showing a well ordered crystal without the formation of superstructures or defects such as dislocations and stacking faults. This is evidenced by a regular contrast across the HRTEM images and the absence of extra spots or streaking lines in the FFTs (Fig. 4.21 insets).

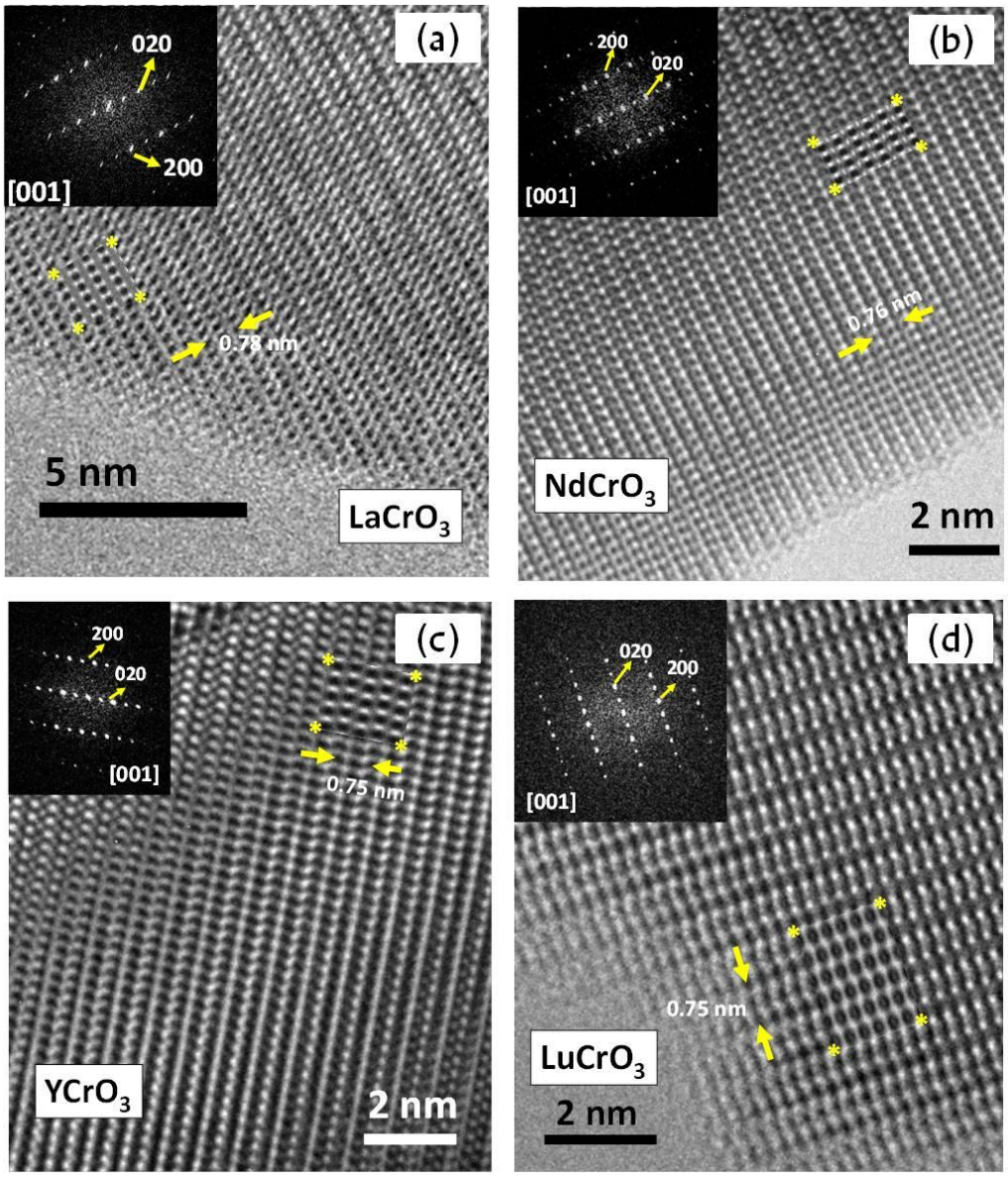

Figure 4.21. Experimental HRTEM micrograph along the [001] zone axis. No streaking or extra spots are evident (see the FFT images in the figure insets). A good match between experimental and simulated images (rectangles marked by yellow asterisks) is demonstrated.

An enlargement of the HRTEM images with the projected model from each material set on top of the experimental image is displayed in Fig. 4.22 showing good agreement. By carefully analyzing the contrast of the images it can be noticed that the darker dots (RE) and the less darker ones (Cr columns) are oriented in zigzag fashion along the [010] direction with increasing amplitude from $LaCrO_3$ < $NdCrO_3$ < $YCrO_3$ < $LuCrO_3$. This feature is related to increasing octahedral tilting to accommodate RE cations of decreasing size into the octahedral framework.

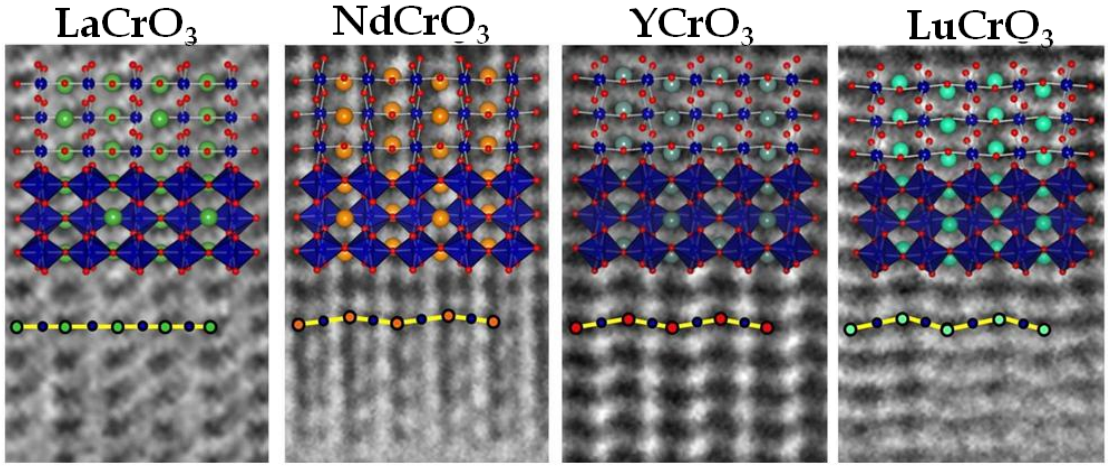

Figure 4.22. Magnified HRTEM micrograph along the [010] zone axis. The increasing octahedral tilting with decreasing IOR is evidenced by stronger zig-zag orientation of the atoms along the [010] direction.

Although HRTEM shows generally a well ordered structure in most of the crystals in all studied samples, in few cases it reveals the presence of local dislocation defects, (Figure 4.23) responsible for the extra diffuse spots along $\boldsymbol{a}^*$ observed in the Fast Fourier Transform (FFT) pattern (Inset Figure 4.23) for $ErCrO_3$. The local dislocation here appears as a distinct area of a locally dislocated lattice of the width of five unit cells (see white arrows). The contrast in the image in Figure 4.23 corresponds to a defect of width ≈ 28 Å (5 x $\boldsymbol{a}$) displayed in the image centre shifted ½ along $\boldsymbol{c}$. This defect can, therefore, be explained by a structural displacement of ½ along $\boldsymbol{c}$ which is stabilized by sharing the edges of consecutive octahedra as it can be observed in the schematic structural sketch inserted into the experimental image. This lattice

displacement defect was found to be the dominant type of defect within these samples.

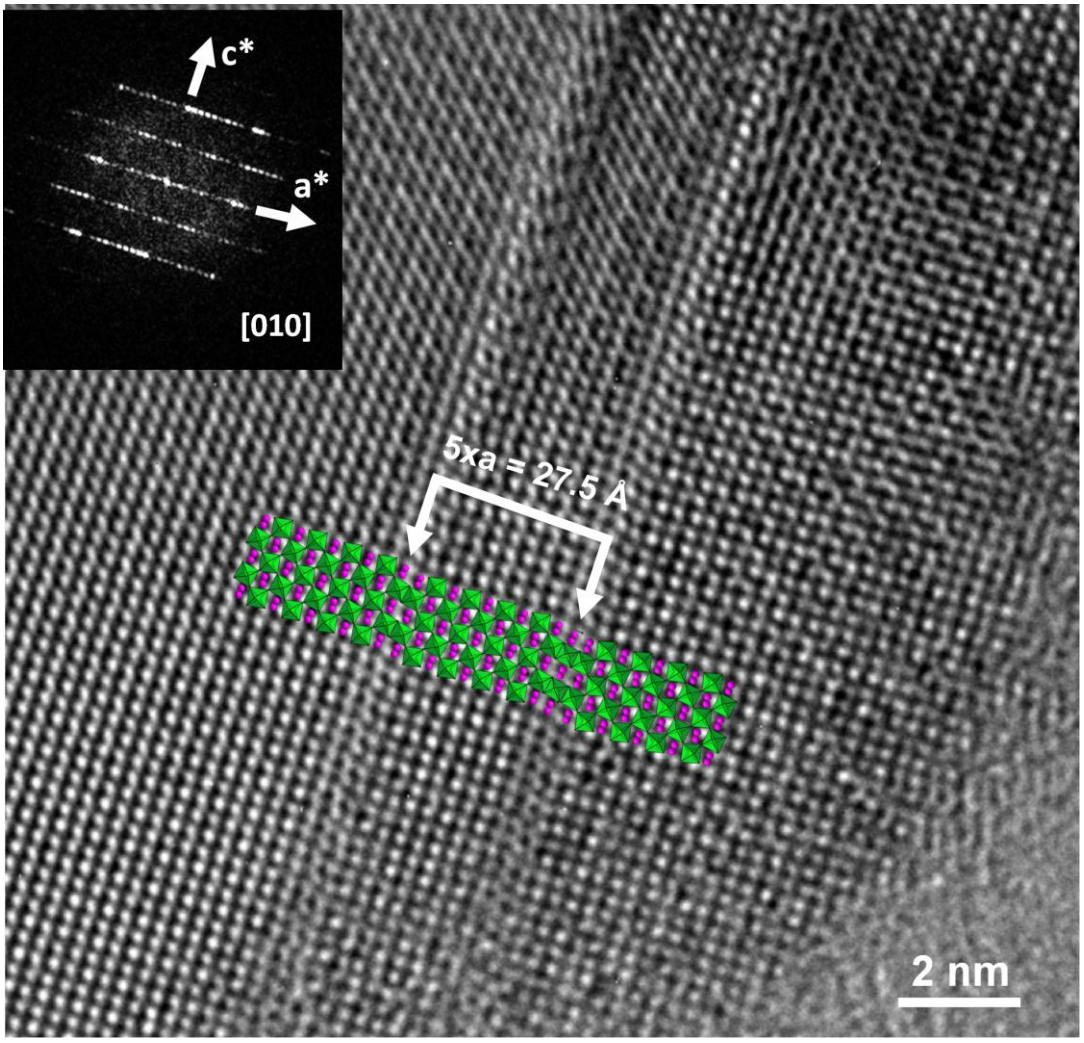

Figure 4.23. HRTEM micrograph from a crystal of $ErCrO_3$ along [010] zone axis, where a dislocation defect of ≈ 28 Å (5 x ***a***) is clearly identified. See the FFT in the inset where the extra spots observed along ***a**** confirm the presence of this defect.

Figure 4.24 shows the microdiffraction patterns for the $ErCrO_3$ sample, which revealed the presence of glide lanes and screw axes of the specimen in the particular sample. The ideal symmetry of the Zero Order Laue Zone (ZOLZ) for the [010] and [110] zone axes patterns (Figure 4.24) are 2mm indicating that the crystal system must present orthorhombic symmetry, in agreement with the *Pnma* space group. In addition, when looking carefully at the rows of the k00 and 00l reflections in the [010] zone axis (Figure 4.24a), dark lines crossing the reflections with k = 2n+1 and l = 2n+1 are obvious, which are forbidden reflections for the *Pnma* space group. These lines of dynamic absence, known as

Gjønnes-Moodie lines,[67] indicate that these reflections are cinematically forbidden, here in this particular case due to the presence of 2_1 screw axes parallel to ***a*** and ***c***, but appear here due to multiple diffraction.

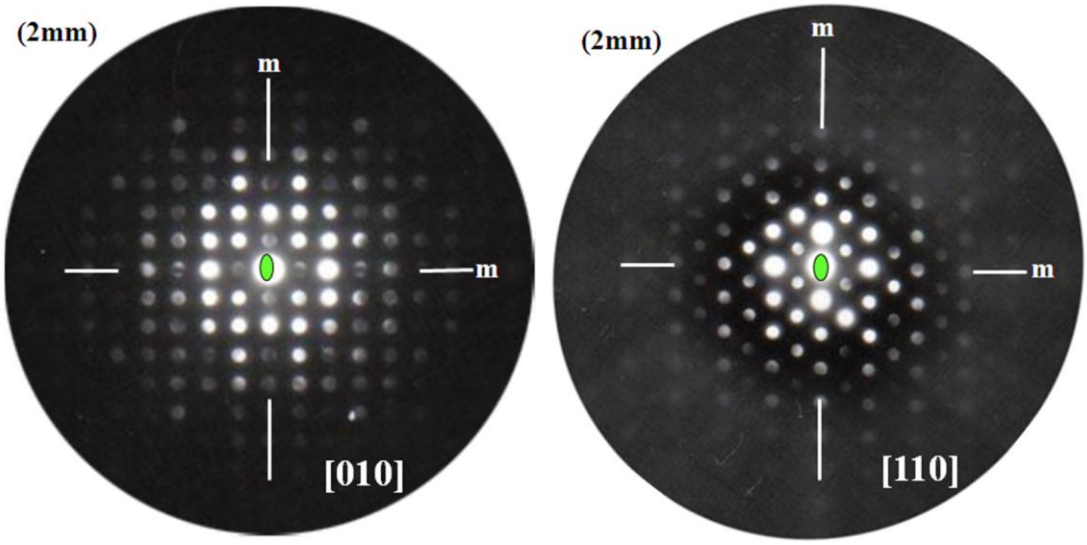

Figure 4.24. Microdiffraction patterns of orthorhombic $ErCrO_3$ along [010] and [110] showing (2mm) ideal symmetry. The characteristic Gjønnes-Moodie lines crossing the odd k00 and 00l reflections in the [010] zone axis, indicate forbidden reflections appearing due to multiple diffraction.

4.3.4. Raman spectroscopy

Fig. 4.25 shows the Raman spectra of all chromite pellets. No secondary phases could be found on any of the samples, indicating a high degree of material homogeneity. Altogether 24 Raman modes are predicted by group theory for the orthorhombic and centro-symmetric *Pnma* structure with 4 formula units per unit cell.[68] Only 9 of those Raman modes are easily observed in all the samples (these modes are labeled in Fig. 4.25) due to the measurement range used in this work. Additional symmetrically forbidden Raman modes characteristic for a potential (local) non-centrosymmetry were not encountered and the observed spectra are in good agreement with a previous study[69] and references therein.

The lower energy modes (100 – 200 cm^{-1}) are quite stable across the full series, with the exception of $YCrO_3$. Since these modes are mainly related to the vibrations of the A cations they are independent of structural changes but highly sensitive to the mass of the cation.

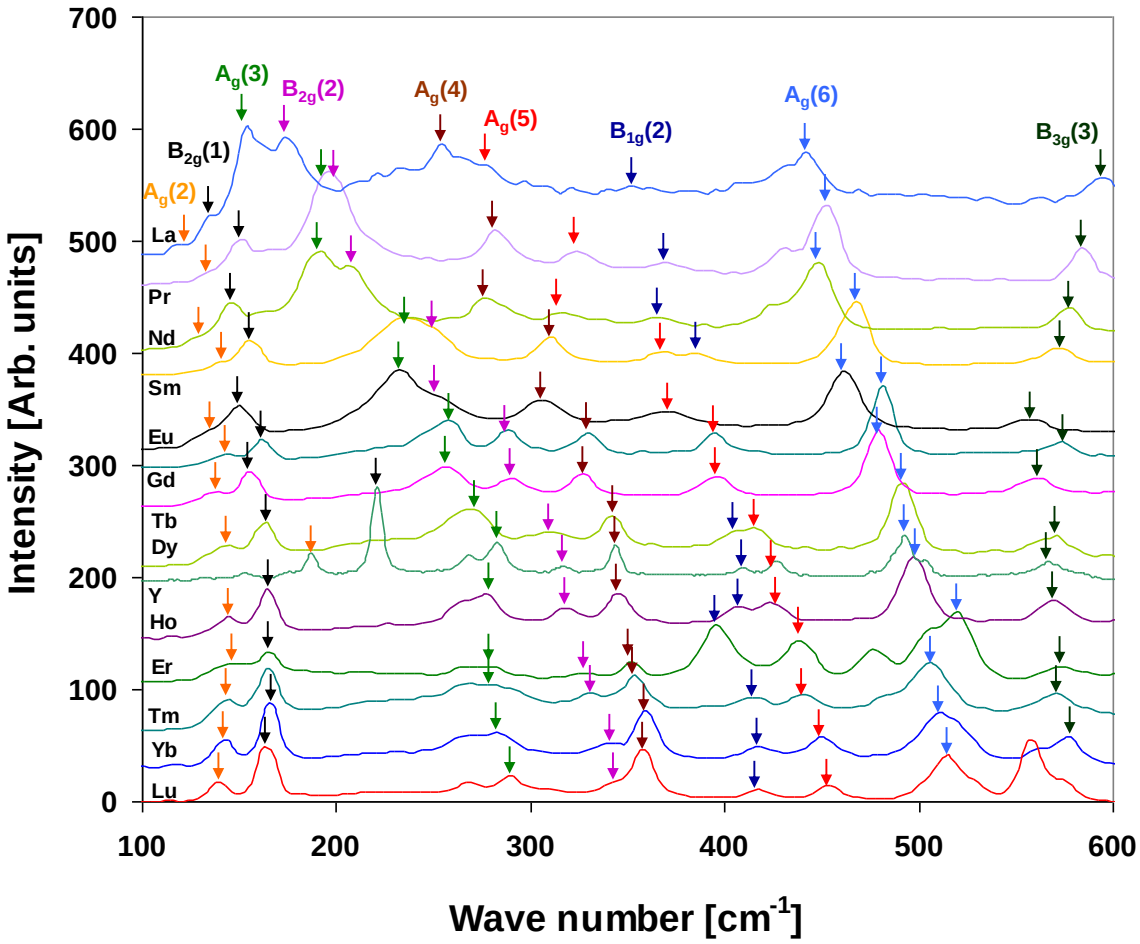

Figure 4.25. Raman spectra collected at room temperature for the $(RE)CrO_3$ series. Colored arrows indicate different Raman modes and how they develop through the series.

Most of the remaining Raman modes show a continuous tendency of decreasing mode position with increasing ionic radius (IOR) as it is shown in Figure 4.26 (see also Table 4.6), which can be associated with the increase of the unit cell volume. Certain Raman modes display a higher dependence on IOR, for example the mode Ag(3),which changes from 291 cm^{-1} in $LuCrO_3$ to 154 cm^{-1} in $LaCrO_3$ or the mode $A_g(5)$, which changes from 454 cm^{-1} in $LuCrO_3$ to 278 cm^{-1} in $LaCrO_3$. Furthermore, a modes crossing can be observed between $A_g(5)$ and $B_{1g}(2)$ for samples with IOR between 1.107 Å (Gd) and 1.12 Å (Eu), where

both modes are almost indistinguishable. The $A_g(5)$ mode has been previously associated with the [101] rotation of the CrO_6 octahedra and is therefore strongly dependent on the different octahedral tilting angles. A plot of the $A_g(5)$ mode position vs the octahedral tilt angle obtained from Rietveld refinement (θ-angle in Tables 4.5a and 4.5b) is shown in Figure 4.27, displaying a linear dependence for all samples (including $YCrO_3$) with a slope of ≈ 21 cm^{-1}/ degree. This value is near to, but slightly smaller than that previously reported.[37] The $A_g(3)$ Raman mode position also exhibits a linear tendency with the tilting angle with a slope of ≈ 16 cm^{-1}/deg.

Table 4.6. Wave numbers of selected Raman modes for $(RE)CrO_3$

$(RE)CrO_3$	**Raman mode wave numbers (cm^{-1})**							
	$A_g(2)$	$A_g(3)$	$A_g(4)$	$A_g(5)$	$A_g(6)$	$B_{1g}(2)$	$B_{2g}(1)$	$B_{3g}(3)$
$LaCrO_3$	120	154	254	278	442	353	135	594
$PrCrO_3$	133	196	281	324	454	371	152	583
$NdCrO_3$	130	192	278	320	451	367	144	579
$SmCrO_3$	140	235	312	368	470	387	155	572
$EuCrO_3$	135	235	306	372	460		149	557
$GdCrO_3$	143	257	328	394	482		162	574
$TbCrO_3$	139	259	329	395	478		154	561
$DyCrO_3$	145	269	344	415	492	405	164	572
$YCrO_3$	(189)	284	345	429	495	412	(221)	569
$HoCrO_3$	144	278	344	423	500	409	163	571
$ErCrO_3$	149	282	353	442	(520)	(395)	168	575
$TmCrO_3$	144	282	353	442	506	414	163	571
$YbCrO_3$	144	282	358	451	511	418	168	580
$LuCrO_3$	138	291	356	454	515	417	162	

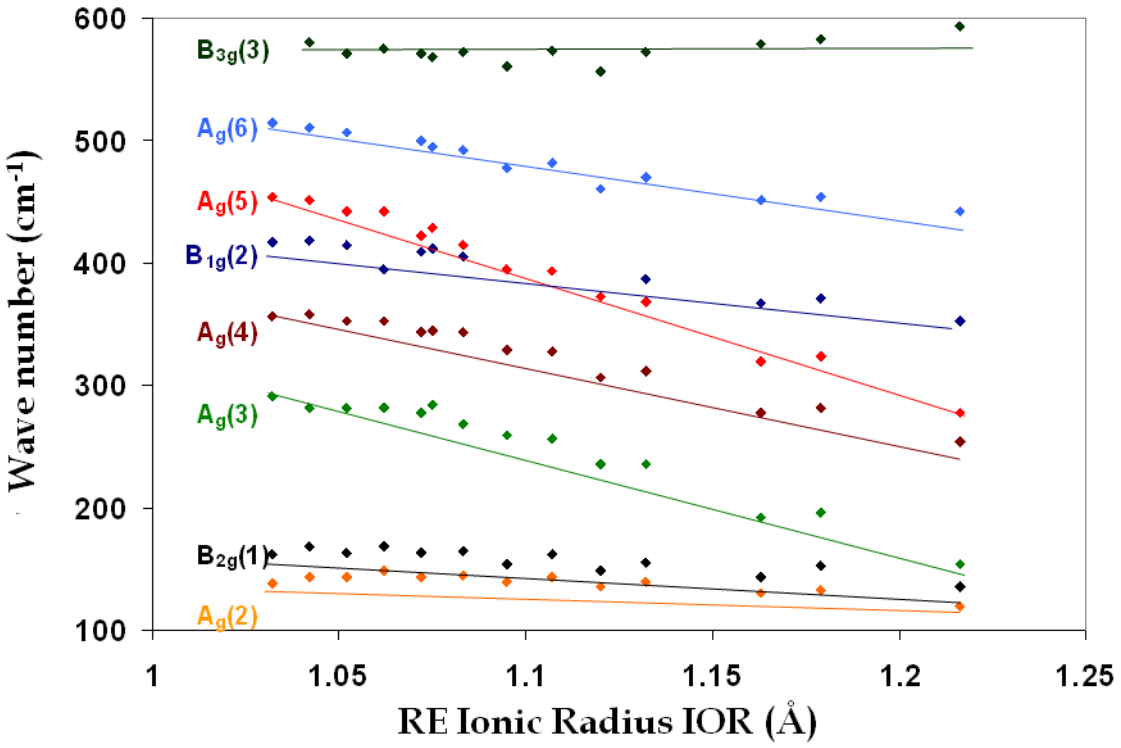

Figure 4.26. Wave number of selected Raman modes in (RE)CrO_3 vs IOR

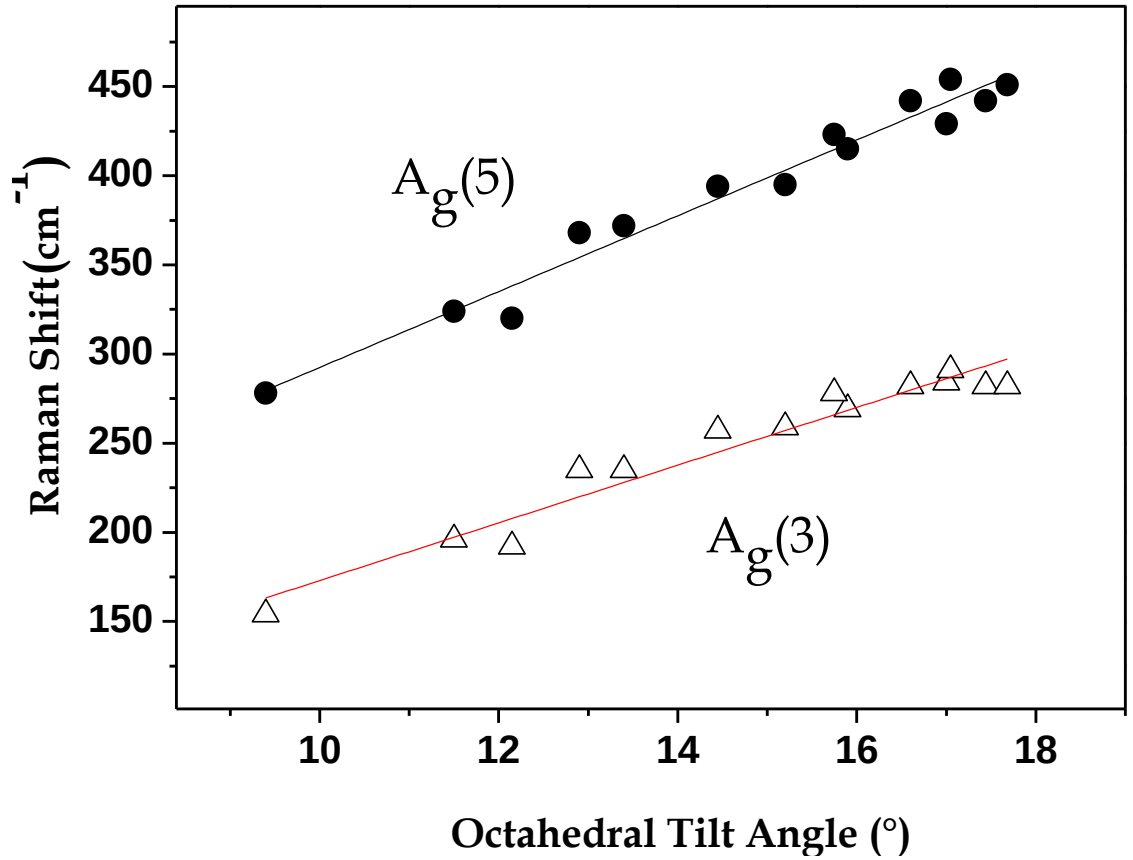

Figure 4.27. Wave number vs octahedral tilt angle θ. Solid lines are guide to the eyes.

4.3.5. Magnetic properties

(RE)CrO_3 orthochromites are paramagnetic at room temperature and undergo several magnetic transitions upon cooling. The chromium Cr^{3+}-Cr^{3+} sublattice is first to order at the Néel temperature T_{N1}, which increases monotonically with IOR from 109 K in $LuCrO_3$ to 288 K in $LaCrO_3$ as demonstrated in Fig. 4.28.

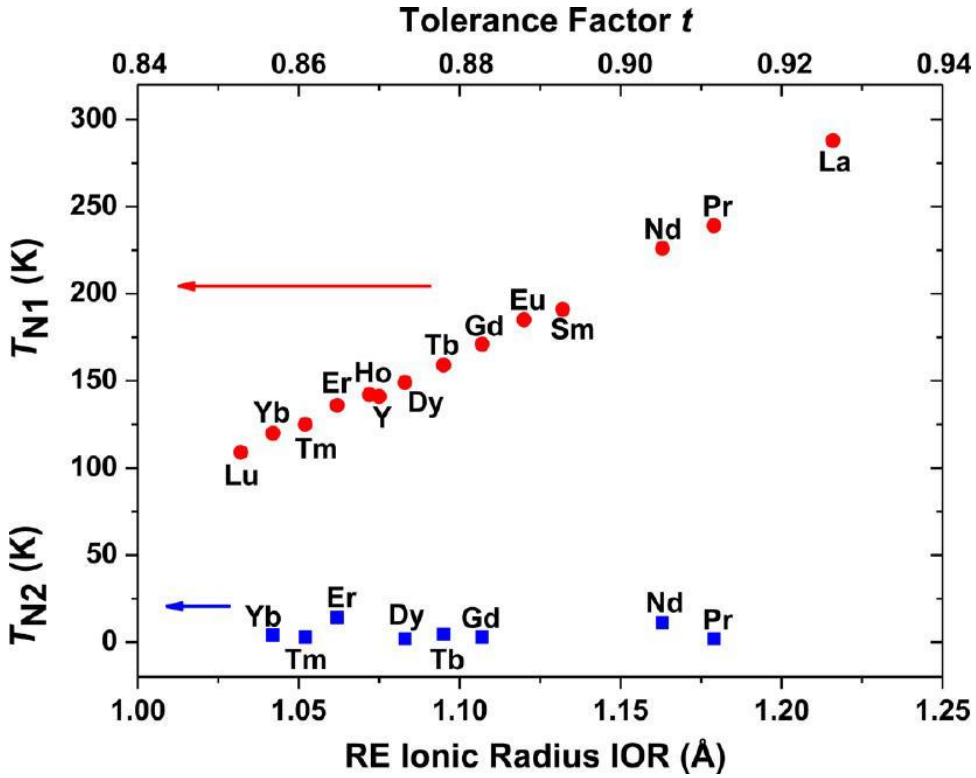

Figure 4.28. Neel temperature for the Cr^{3+}-Cr^{3+} ordering (T_{N1}) and RE^{3+} ordering (T_{N2}) vs the RE ionic radius IOR and the perovskite tolerance factor. The increasing T_{N1} with IOR reflects a decreasing tilting angle approaching the ideal 180° Cr^{3+}-O^{2-}-Cr^{3+} angle.

Upon further cooling, RE^{3+}-Cr^{3+} interactions appear for certain RE cations, which leads to unusual ZFC-FC magnetic susceptibility (χ) vs temperature (T) characteristics below T_{N1} in the range of ≈ 50 – 100 K as demonstrated in Fig.4.29. The RE^{3+}-RE^{3+} sublattice orders last at very low temperature (T_{N2}) in the range of ≈ 2 – 15 K for certain species, where the variation of T_{N2} does not appear to be correlated with IOR (see Fig. 4.28). The χ vs T curves recorded at 1 kOe fall into two different classes according to the magnitude of the magnetic susceptibility χ below T_{N1}. The samples with

relatively low χ include RE = Y, La, Nd, Sm, Eu, Tm, Yb and Lu, whereas χ is higher for RE = Pr, Gd, Tb, Dy, Ho and Er. Fig.4.29 shows the temperature dependence of χ for three representative powders each from the low (Fig. 4.29a) and the high χ (Fig. 4.29b) species.

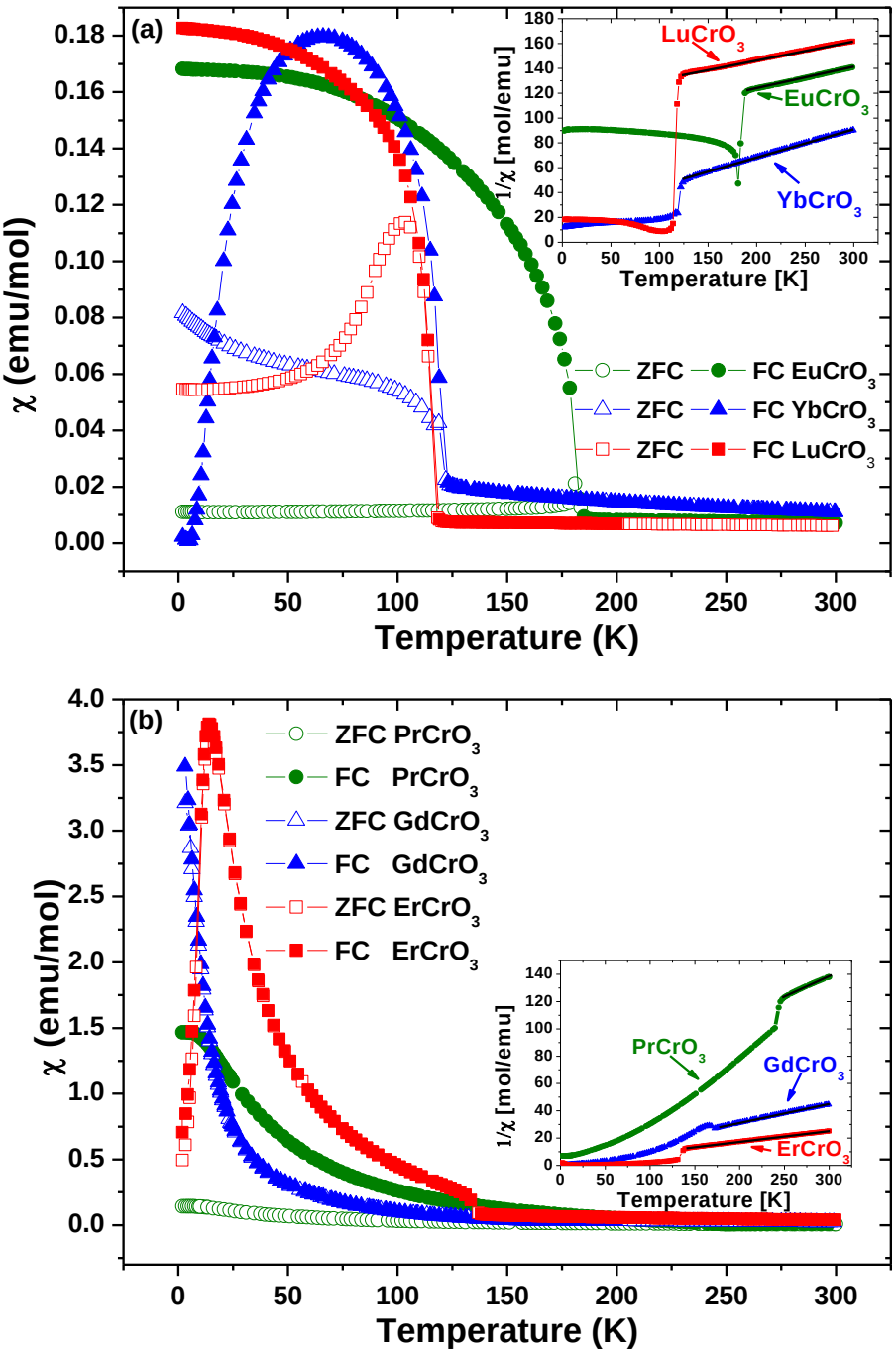

Figure 4.29. Magnetic susceptibility χ (emu/mol) vs temperature T. The data fall into a low and a high χ regime. (a) 3 representative examples for the low χ regime. Inset: Inverse magnetic susceptibility $1/\chi$ vs T. Solid lines indicate the Curie-Weiss plots for determining the effective magnetic susceptibility $\chi_{eff.}$ (b) 3 representative examples for the high χ regime. Lower inset: Inverse magnetic susceptibility $1/\chi$ vs T. Solid lines indicate the Curie-Weiss plots.

In Fig. 4.29a the low χ representative samples $EuCrO_3$, $YbCrO_3$, and $LuCrO_3$ exhibit ferrimagnetic moments below T_{N1} as is indicated by clear differences between ZFC and FC curves. Such moments are attributed to a small canting angle of the antiferromagnetic Cr^{3+} spins.[70] In the case of $EuCrO_3$ and $LuCrO_3$ the RE magnetic ground state is diamagnetic and, therefore, the low T magnetic properties are dominated by the Cr^{3+} spin system. The $YCrO_3$, $LaCrO_3$ and $SmCrO_3$ species (data not shown for simplifying the figure) exhibit features in χ vs T equivalent to $EuCrO_3$, taking into account the variation of Néel temperature T_{N1} as demonstrated in Fig. 4.28. The ZFC magnetic susceptibility curve for $YbCrO_3$ exhibits a maximum at 66 K and crosses the ZFC curve at 16 K. This behaviour seems unusual, since it may suggest that the applied magnetic field during cooling (FC) supports the suppression of the low T magnetism. This finding is in agreement though with previous reports,[54] and has been attributed to an antiparallel coupling between the moments of the RE = Yb^{3+} and the weak ferrimagnetic component of the Cr^{3+} spins.[71] This behaviour could also be involved with a magnetic memory effect. At 4 K, the magnetic susceptibility in FC mode increases modestly, which indicates the onset of antiferromagnetic ordering of Yb^{3+} spins (T_{N2}).

The main panel of Fig. 4.29b shows the magnetic properties of $GdCrO_3$, $ErCrO_3$ and $PrCrO_3$ as representative members of the high χ species. $GdCrO_3$ and $ErCrO_3$ show no significant differences between ZFC and FC susceptibility curves and Cr^{3+} ferrimagnetic ordering is not indicated. Contrarily, the $PrCrO_3$ sample does show differences between ZFC and FC curves appearing below T_{N1} = 239 K and Cr^{3+} ferrimagnetism is indicated. The RE ordering temperature T_{N2} can be identified by a peak-like structure in the χ vs T curves at $T_{N2} \approx 2$ K.[72] T_{N2} can be identified more clearly in the $ErCrO_3$ sample ($T_{N2} \approx 14$ K) as is the case in $TbCrO_3$ and $DyCrO_3$ (data not shown for simplifying the figure), whereas the $GdCrO_3$ sample does not reach the T_{N2} peak at low T.

The lower insets in Fig. 4.29a and Fig. 4.29b show the temperature dependence of the reciprocal magnetic susceptibility $1/\chi$ for the respective samples. Above T_{N1}, the paramagnetic state follows the Curie–Weiss law. The Curie–Weiss fits are indicated by the solid lines. In Table 4.7 all fitted parameters are summarized and compared to the theoretical values for μ_{eff} from Landolt-Börnstein tables,[73] and generally good agreement is encountered. The Θ – values obtained from the fits are all negative, which indicates predominantly antiferromagnetic exchange interactions.

Table 4.7. Magnetic parameters for $(RE)CrO_3$ obtained from magnetization measurements.

	T_{N1} Cr^{3+} (K)		T_{N2} RE^{3+} (K)		C (μ_B)	Θ (K)	Total μ_{eff} (μ_B)	
$(RE)CrO_3$	Experim.	Literature	Experim	Literature[50, 73]			Experim.	Theoretical
$LaCrO_3$	288	282	-	-	-	-	-	3.87
$PrCrO_3$	239	239	2	2	3.3	-160	5.15	5.21
$NdCrO_3$	226	224	11	10	3.8	-189	5.54	5.29
$SmCrO_3$	191	193	-	-	3.4	-314	5.21	5.46
$EuCrO_3$	185	181	-	-	3.4	-198	5.23	5.15
$GdCrO_3$	171	170	3	4	7.3	-29	7.65	8.83
$TbCrO_3$	159	158	4.5	4	12.9	-26	10.17	10.46
$DyCrO_3$	149	146	2	2	15.7	-24	11.21	11.33
$YCrO_3$	141	140	-	-	2.51	-408	4.48	3.87
$HoCrO_3$	142	141	-	12	15.7	-21	11.22	11.28
$ErCrO_3$	136	133	14	17	12.8	-24	10.12	10.33
$TmCrO_3$	125	124	3	4	8.6	-32	8.30	8.49
$YbCrO_3$	120	118	4	3	4.4	-99	5.92	5.97
$LuCrO_3$	109	112	-	-	2.4	-174	4.42	3.87

The effective magnetic moments μ_{eff}, originating from the Cr^{3+} cations were calculated from the Curie constants *C* according to equation 4.2.

$$\mu_{eff}{}^2 = 8C \qquad [4.2]$$

The theoretical value for μ_{eff} was regarded a combination of Cr^{3+} and $(RE)^{3+}$, where $\mu_{eff}(Cr^{3+})$ = 3.87 μB, obtained from the equation [4.3]

$$\mu_{eff} = 2[S(S+1)]^{1/2} \qquad [4.3]$$

with the multiplicity S = 3/2.

For $(RE)^{3+}$:

$$\mu_{eff} = g_L[J(J+1)]^{1/2} \qquad [4.4]$$

where g_L is the Lande g-factor ($g_L = (3/2)+[(S(S+1)-L(L-1))/2J(J+1)]$), J is the total angular momentum and L corresponds to the maximum orbital angular momentum. All μ_{eff} values are displayed in Figure 4.30, together with theoretical values in agreement with Landolt-Bornstein tables. For the $LaCrO_3$ sample T_{N1} is high and no sufficient $1/\chi$ vs *T* data points were available at high *T* to perform a Curie-Weiss fit.

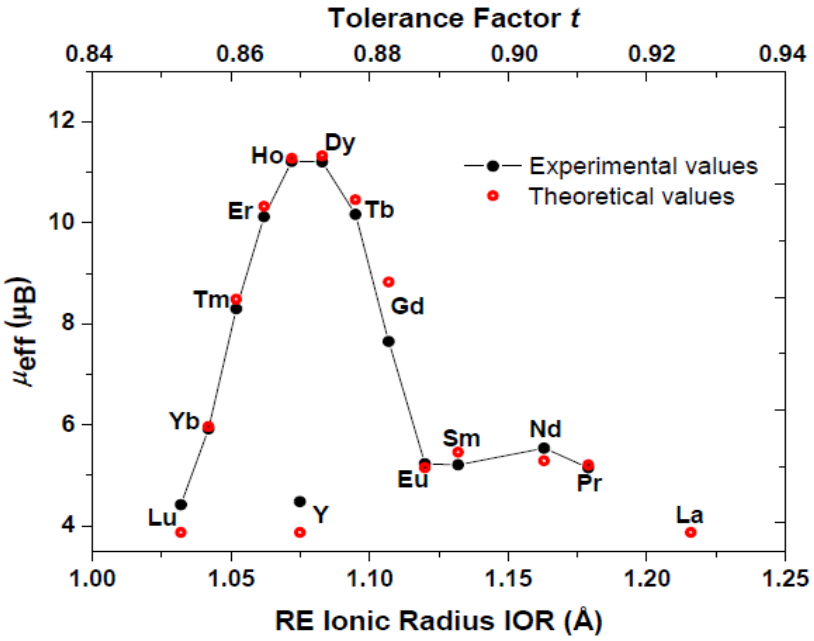

Figure 4.30. Effective magnetic moment μ_{eff} for the $(RE)CrO_3$ series as determined from the respective Curie-Weiss fits and plotted vs IOR. Theoretical values were taken from Landolt-Börnstein tables.[73]

Fig. 4.31 presents the magnetization vs applied field plots at 10 K for $DyCrO_3$, $HoCrO_3$ and $TmCrO_3$, which all show weak ferrimagnetic hysteresis as a result of Cr^{3+} spin canting.

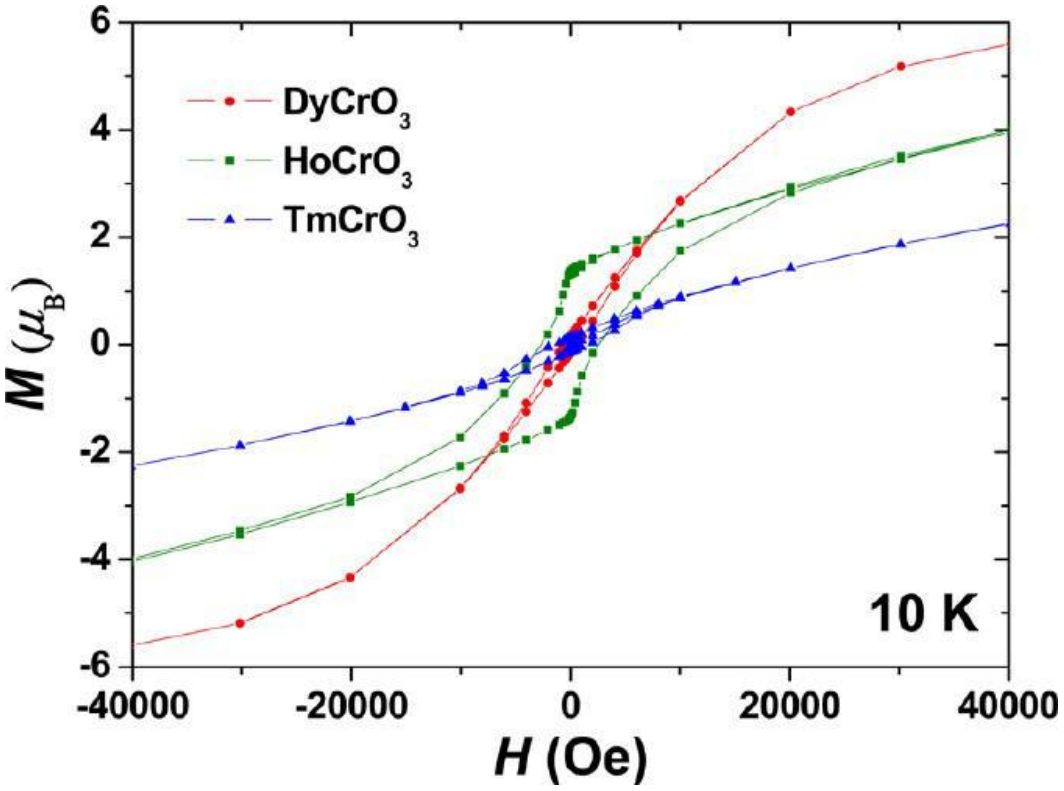

Figure 4.31. Magnetization (μ_B) vs applied magnetic field H (Oe) curves at 10 K for 3 representative species from the (RE)CrO_3 series.

In previous studies such weak ferromagnetic moment of the Cr^{3+} spins has been explained with Dzialoshinski–Moriya (D–M) interactions.[56, 57]

4.3.6. Dielectric properties

Impedance spectroscopy data for the (RE)CrO_3 series were collected from sintered pellets. Selected impedance spectra are shown in Fig. 4.32 in terms of the complex impedance plane plot of -Z'' vs Z'. The spectra for the Ho-, Gd-, Pr- and Y-containing samples are normalized and shifted up the Z'' y-axes by increasing amounts for demonstration purposes. For the different compositions two or three semicircles are displayed in -Z'' vs Z', which is consistent with 2 or 3 conventional dielectric relaxation processes in series.[47, 64] Not all semicircles

are fully developed and considerable overlap occurs, which is highlighted in the spectrum for $TmCrO_3$ by the dotted semicircles. All semi-circles in Fig. 4.32 are slightly suppressed in a way such that the semicircle center seems to be slightly suppressed below the Z' x-axis. This indicates a certain degree of non-ideality of the relaxation process, which can be associated with a broadening of the distribution of dielectric relaxation times τ.[74, 75]

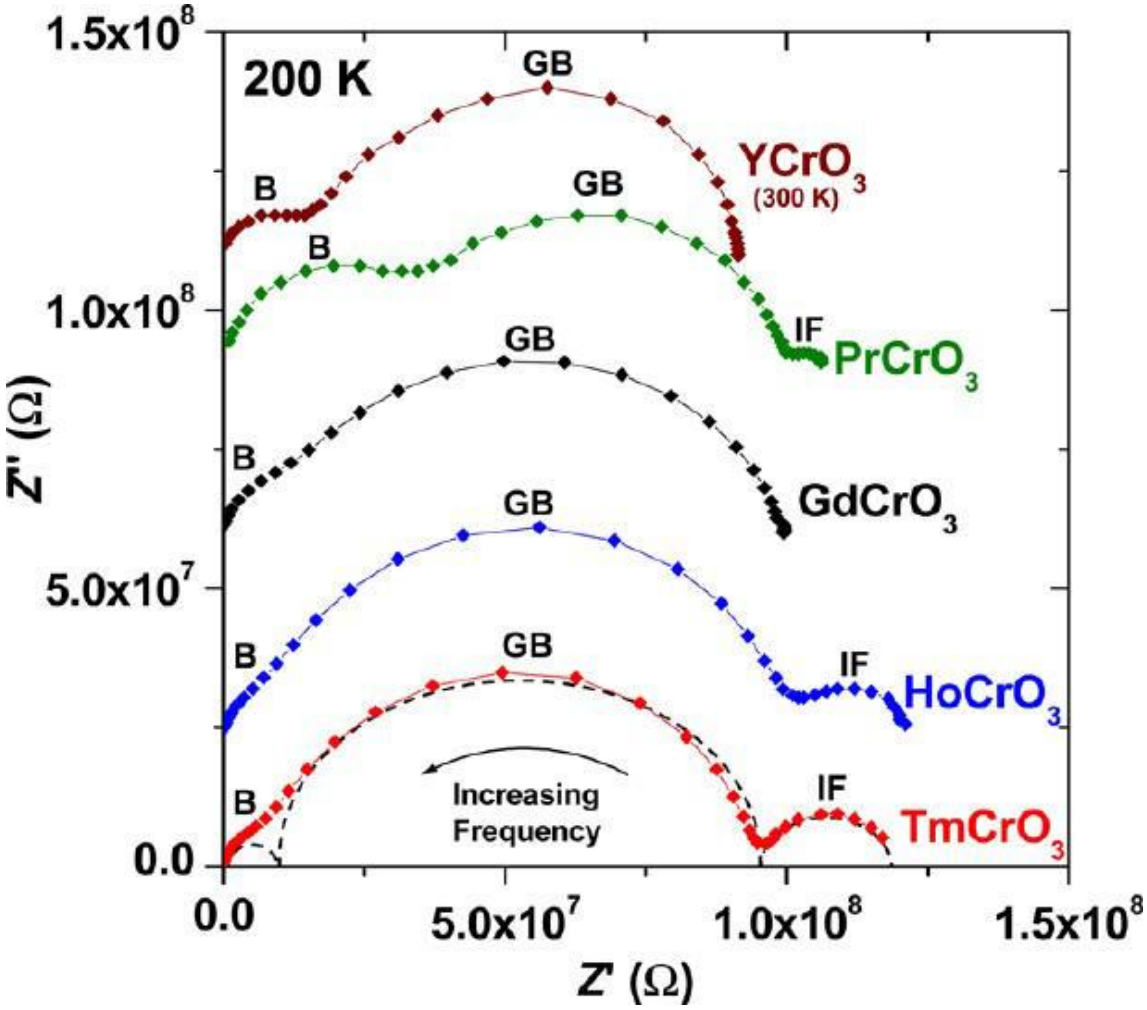

Figure 4.32. Plots of the imaginary vs real part of the impedance (-Z'' vs Z') at 200 K for 5 representative examples from the $(RE)CrO_3$ series. $YCrO_3$ data is shown for 300 K. The Ho, Gd, Pr and Y containing samples were shifted up the y –axis for demonstration purposes. The overlapping of several semicircles is highlighted by the dotted lines in the $TmCrO_3$ spectrum, where each semicircle can be associated with a bulk (B), grain boundary (GB) or electrode – sample interface (IF) effect.

The two semicircles at high and intermediate frequency are associated with intrinsic bulk (B) and extrinsic grain boundary (GB) relaxation processes respectively. In the case of the Tm-, Ho- and Pr-containing samples a third

semicircle at low frequency is associated with an electrode-sample interface effect (IF), which also occurs in the, Nd-, Sm-, Dy-, Er-,[76] Yb and Lu-containing species. To extract the resistivity ρ and relative dielectric permittivity ε values for the bulk and GB relaxations from impedance spectroscopy data for each (RE)CrO_3 sample, equivalent circuit fitting[76] was attempted but did not succeed for all samples. Therefore, bulk and GB ρ and ε values were extracted from the respective impedance spectra by a manual procedure to be identical for all samples to render the extracted parameters comparable to each other. The bulk and GB relaxations were approximated by an equivalent circuit consisting of two ideal RC elements connected in series (see Inset in Fig.4.33), where the non-ideality was neglected. R1 and C1 describe the intrinsic bulk resistivity ρ_1 and bulk permittivity ε_1 respectively, whereas R2 and C2 describe the extrinsic GB resistivity ρ_2 and GB permittivity ε_2 respectively.

Fig. 4.33 shows the comparison of modulus and impedance spectroscopy for 5 representative examples from the (RE)CrO_3 series. The bulk dielectric relaxation peaks dominate the M'' vs f curves, whereas the GB peaks are strongly pronounced in the $-Z''$ vs f curves. The approximate conditions for a bulk or GB relaxation peak maximum to occur are shown in equation 4.5 for both notations, M'' vs f and $-Z''$ vs f, using the framework of the brick work layer and RC element model for ideal relaxations. The approximate peak ordinates are distinctively different for $M''(f_{max})$ and $-Z''(f_{max})$ (equation 4.6), which guarantees that in the M'' vs f notation the smallest capacitance (bulk) and in the $-Z''$ vs f notation the largest resistance (GB) are most strongly pronounced.

The curves of Fig 4.33 for the Ho-, Gd-, Pr-, and Y-containing samples are shifted up the M'' and $-Z''$ y-axes by increasing amounts for demonstration purposes. The $-Z''$ vs f curves were normalized to render the peak heights comparable to enable equivalent resolution for all samples within the same graph. The approximate conditions for a bulk or GB relaxation peak maximum to occur are shown in equation 4.5 for both notations, M'' vs f and $-Z''$ vs f,

using the framework of the brick work layer model for ideal relaxations. The approximate peak ordinates are distinctively different for $M''(f_{max})$ and $-Z''(f_{max})$ (eq. 4.6), which guarantees that in the M'' vs f notation the smallest capacitance (bulk) and in the $-Z''$ vs f notation the largest resistance (GB) are most strongly pronounced in form of a relaxation peak. This is clearly evident in Fig.4.33, where the main bulk peaks in M'' vs f clearly dominate over the secondary GB peaks, whereas the main GB peaks in $-Z''$ vs f clearly dominate over the secondary bulk peaks. In fact, some of the secondary peaks cannot be resolved at all in the respective notation.

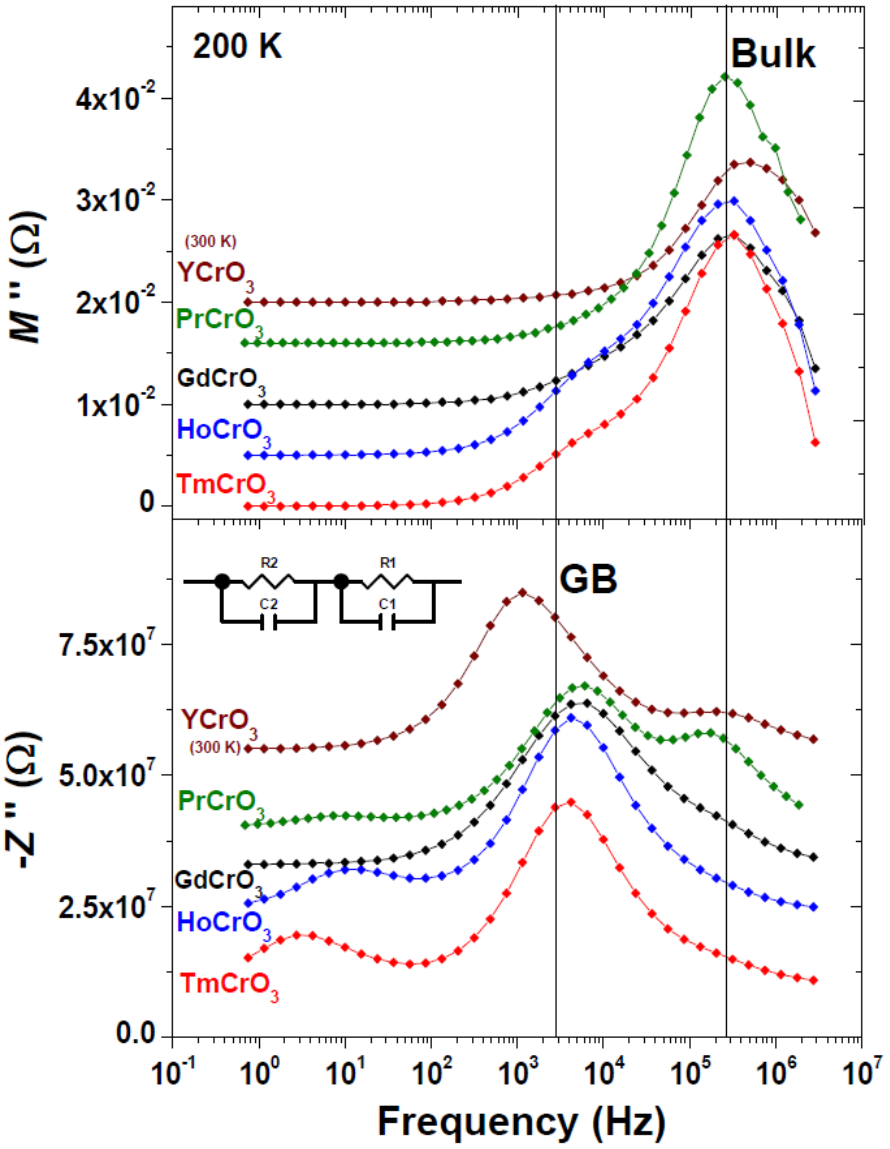

Figure 4.33. Comparison of modulus and impedance spectroscopy for 5 representative examples from the $(RE)CrO_3$ series. The bulk dielectric relaxation peaks dominate the M'' vs f curves, whereas the GB peaks are strongly pronounced in the $-Z''$ vs f curves.

$$f_{max}(M'') \approx \frac{1}{2\pi\ \rho_1\varepsilon_0\varepsilon_1}\ ;\ f_{max}(-Z'') \approx \frac{1}{2\pi\ \rho_2\varepsilon_0\varepsilon_2}\ ; \qquad [4.5]$$

$$M''(f_{max}) \approx \frac{1}{2\varepsilon_1}\ ;\ -Z''(f_{max}) \approx \frac{\rho_2}{2}\ ; \qquad [4.6]$$

The bulk and GB resistivity values ρ_1 and ρ_2 obtained from the impedance spectra at the respective temperature are plotted on Arrhenius axes, showing good linearity for all (RE)CrO_3 samples (see Figures 4.34 and 4.35).

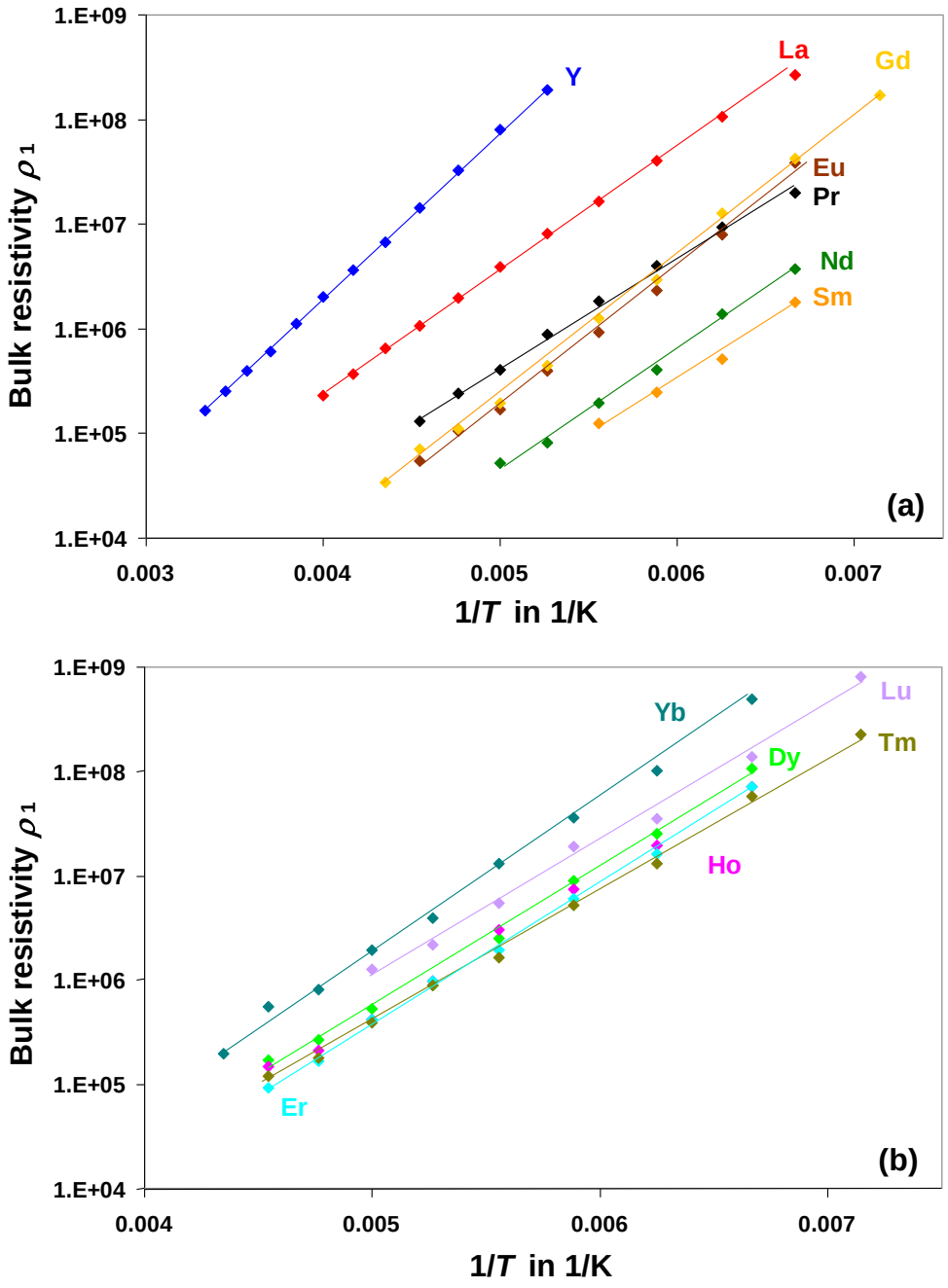

Figure 4.34.a-b Bulk resistivity ρ_1 plotted vs reciprocal temperature 1/T. Solid lines are guide to the eyes, indicating good linearity and Arrhenius behaviour.

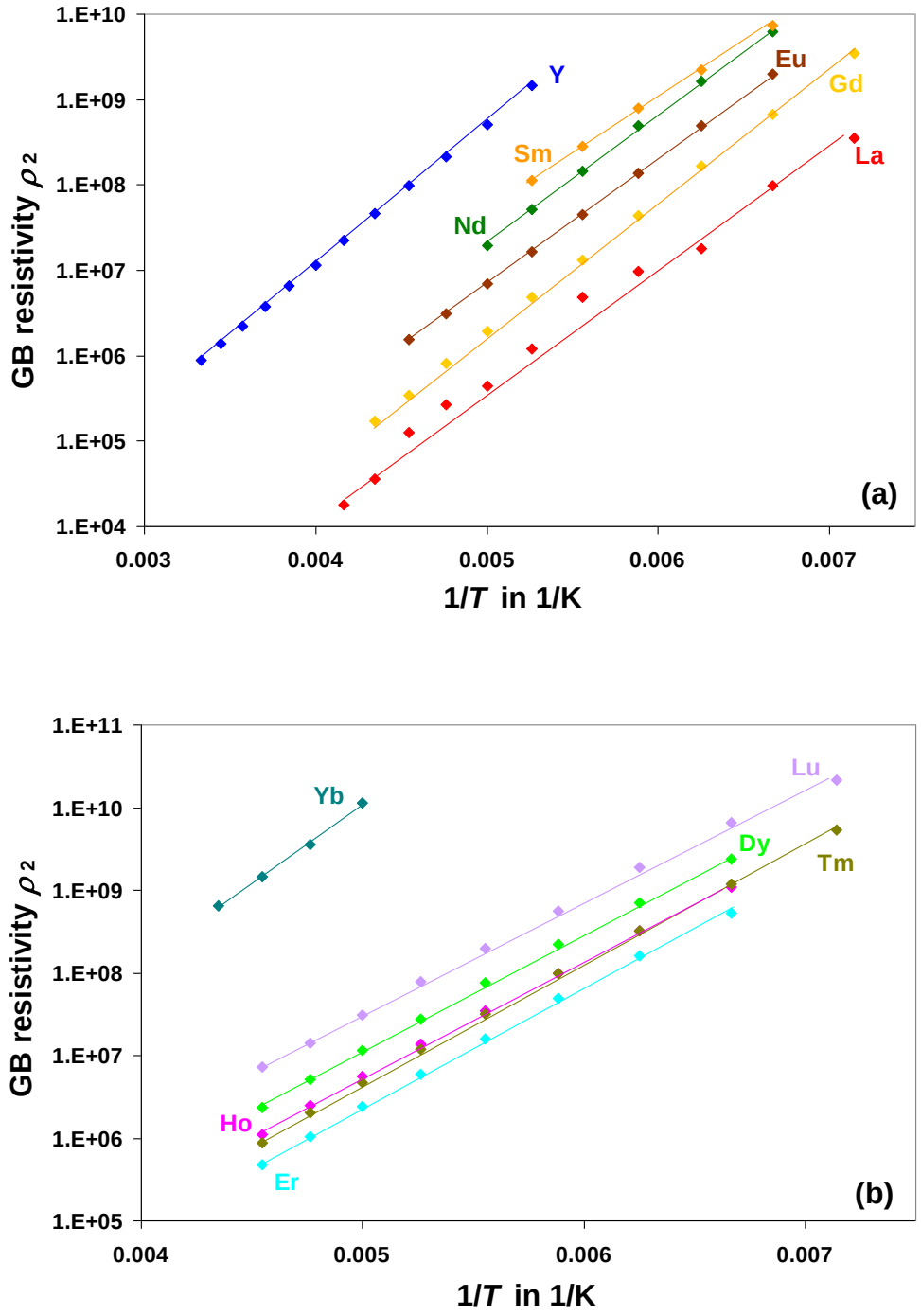

Figure 4.35.a-b Grain boundary GB resistivity ρ_2 plotted vs reciprocal temperature 1/T. Solid lines are guide to the eyes, indicating good linearity and Arrhenius behaviour.

From the slopes of such graphs the bulk and GB activation energies E_A can be determined and are plotted vs IOR in Fig.4.36 (upper curves). Although the absolute ρ_1 and ρ_2 values at 200 K and other example temperatures do not show any clear trends with IOR (see Table 4.8), the E_A values are quite consistent. Especially the intrinsic bulk E_A trend seems to show a slight decrease

with increasing IOR above the Gd sample, whereas for lower IOR the bulk E_A trend appears approximately constant. A similar trend is observed in the intrinsic dielectric permittivity ε_1 vs IOR (lower curve in Fig. 4.36), where again the trend seems to change near the Gd sample.

The $YCrO_3$ sample on the other hand falls out of all the ρ and ε trends presented in Fig. 4.36, which is consistent with the trends in effective magnetization μ_{eff}. The RE electron configuration seems to play a major role here in determining the electronic charge transfer rate (resistivity) and the electron cloud polarizability (permittivity) in $(RE)CrO_3$ chromites.

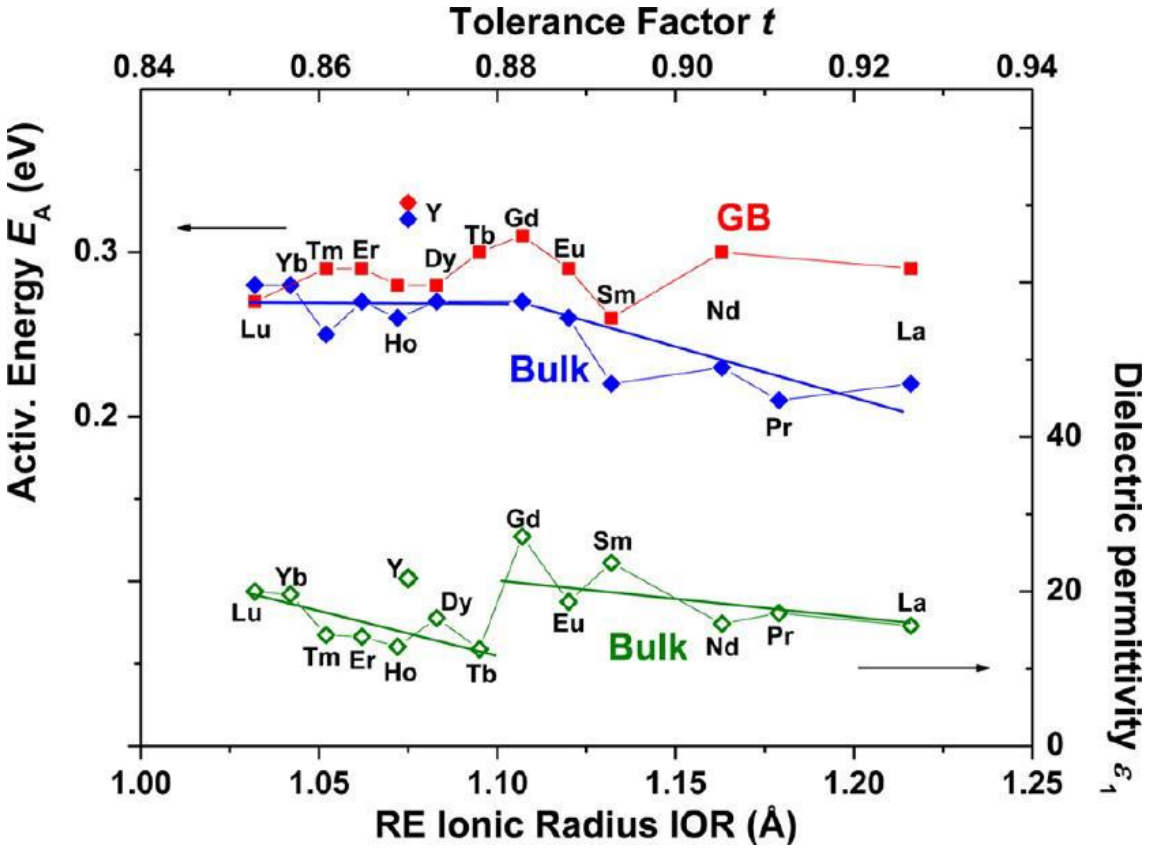

Figure 4.36. Bulk and GB charge transport activation energies E_A and bulk dielectric permittivity ε_1 plotted vs IOR and the perovskite tolerance factor.

Most importantly, the permittivity ε_1 values are all relatively low and the electron cloud polarizability may well be the only contribution to the overall measurable polarizability in the $(RE)CrO_3$ series. Furthermore, the ε_1 values

determined did not show any clear temperature dependence (see Table 4.8). Therefore, a contribution from an ionic displacement to the overall polarisability, typical for ferroelectricity, is unlikely and previous reports on ferroelectricity in these materials cannot be confirmed. The absence of ferroelectricity may be consistent though with the centro-symmetric space-group used for Rietveld refinements of XRD patterns and the Raman spectra presented here. None of the trends of the magnetic parameters (T_{N1}, T_{N2}, μ_{eff}) vs IOR are correlated with any of the trends of the dielectric parameters (E_A, ε_1) vs IOR, and obvious magneto-electric coupling effects are not indicated.

Table 4.8. Dielectric parameter for (RE)CrO_3 obtained from impedance spectroscopy

(RE)CrO_3	**Activation Energy E_A (eV)**		**Dielectric permittivity**		**Resistivity at 200 K in (Ω cm)**	
	Bulk	GB	Bulk ε_1	GB ε_2	Bulk ρ_1	GB ρ_2
$LaCrO_3$	0.22	0.29	15.6	2520	3.92×10^6	4.45×10^5
$PrCrO_3$	0.21		17.2	407	4.11×10^5	8.89×10^5
$NdCrO_3$	0.23	0.3	15.8	258	5.17×10^4	1.96×10^7
$SmCrO_3$	0.22	0.26	23.7	90.2		
$EuCrO_3$	0.26	0.29	18.7	283	1.70×10^5	6.93×10^6
$GdCrO_3$	0.27	0.31	27.1	177	1.96×10^5	1.93×10^6
$TbCrO_3$		0.30	12.5	318	1.05×10^7	8.40×10^6
$DyCrO_3$	0.27	0.28	17.3	47.4	5.40×10^5	1.15×10^7
$YCrO_3$	0.32	0.33	21.7	1740	8.00×10^7	5.04×10^8
$HoCrO_3$	0.26	0.28	12.9	76.8	4.27×10^5	5.62×10^6
$ErCrO_3$	0.27	0.29	14.1	181	4.27×10^5	2.42×10^6
$TmCrO_3$	0.25	0.29	14.4	102	3.93×10^5	4.66×10^6
$YbCrO_3$	0.28		19.6	164	1.97×10^6	1.14×10^{10}
$LuCrO_3$	0.28	0.27	20.0	97.4	1.28×10^6	3.11×10^7

4.4. $(RE)_2Ti_2O_7$ (RE = Gd, Ho)

$RE_2Ti_2O_7$ pyrochlore oxide compounds are materials[77] that can possess a wide range functional properties such as ionic conductivity, exotic magnetic properties and multiferroic behaviour.[78-81] Furthermore, due to their high chemical stability and the flexibility to form solid solutions with many cations they have been proposed as a host matrix for immobilizing toxic nuclear wastes.[82]

The crystal structure (see *section 4.1.*) may be regarded a superstructure of oxygen deficient fluorite ($RE_{0.5}Ti_{0.5}O_{1.75}$) with ordered RE^{3+} and Ti^{4+} cations, where an amount of 0.25 of the anions would be missing which allows ionic oxygen vacancy conduction to occur. Traditionally, $(RE)_2Ti_2O_7$ compounds are prepared by solid state reaction, which requires long firing times (> 1 day) with temperatures higher than 1400 ^oC and intermediate grinding to achieve single phase material. In the last decades several alternative routes have been proposed such as co-precipitation of hydroxides, sol-gel, citrate based method and mechanical milling, reducing significantly the time and temperature requirements. However, for all such methods, a second firing step in a conventional furnace is necessary to obtain the phase pure materials and total reaction time increases.[83-85] in the following, the solid state microwave synthesis of the two representative species $Gd_2Ti_2O_7$ and $Ho_2Ti_2O_7$ and their structural and physical property characterizations are presented.

4.4.1. Synthetic aspects

The synthetic procedure is basically the route described in *section 4.2.1.* Here in this case, after 20 minutes of microwave irradiation a second firing step was necessary, in a conventional furnace during 2 h at 1100 ^oC (Fig. 4.37). For sintering, the samples were ground again and pressed into 5 mm pellets and fired for 4 h at 1400 ^oC with a ramp of 2 ^oC/min. The density in both samples, $Gd_2Ti_2O_7$ and $Ho_2Ti_2O_7$, was ≈ 95%.

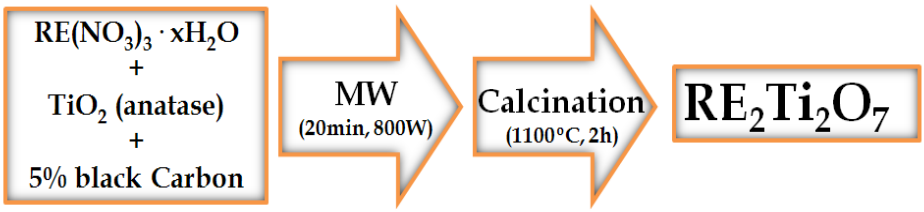

Figure 4.37. Microwave-assisted route followed to produce $RE_2Ti_2O_7$ (RE = Gd, Ho).

4.4.2. Structural characterization

Figure 4.38 presents the results relating to the Gd-sample second reaction procedure after microwave irradiation. First treatment at 800 ºC was performed in order to remove all possible residual carbon and complete the reaction. From the XRD data, it is observed that the reaction is not complete and a mixture of low-temperature fluorite-like and pyrochlore structures coexists. Then a new batch was treated at 1000 ºC during 2 h. The XRD data reveals single-phase pyrochlore-like structure but is still not very crystalline. The best result was obtained after firing at 1100 ºC for 2 h producing a single phase.

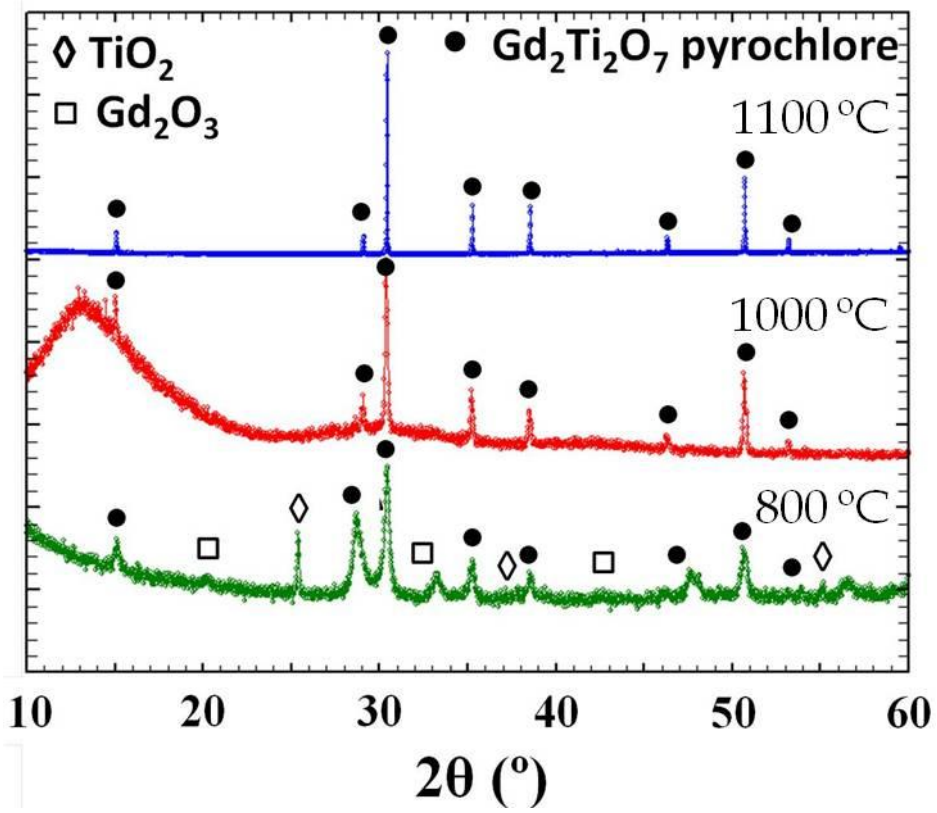

Figure 4.38. Temperature dependence of X-ray diffraction patterns of microwave-assisted $Gd_2Ti_2O_7$.

The calcinated powders (2 hours, 1100 ºC) are single phases and show highly crystalline XRD pattern with the pyrochlore-like structure characteristic reflections. Rietveld refinements of synchrotron X-ray diffraction data collected at the SPLINE beamline in ESRF Grenoble were carried out for the $RE_2Ti_2O_7$ (RE = Gd, Ho) samples at different temperatures (from 1100 ºC to 1400 ºC) in order to study the temperature dependence of the anti-site defects. The results of the Rietveld refinements are summarized on Table 4.9. The good agreement factors confirm the model, and the results are in good agreement with the ICSD database[86] for both $Gd_2Ti_2O_7$ and $Ho_2Ti_2O_7$ samples. Figure 4.39 shows the observed and calculated patterns with Miller planes indexed on top for $Ho_2Ti_2O_7$ at 1100 ºC and 1200 ºC, and Figure 4.39 shows the same for $Gd_2Ti_2O_7$ at 1300 ºC and 1400 ºC.

A – B antisite defects are commonly observed in pyrochlore structure, especially when the A and B – site ionic radii are similar. Here in this case, the ionic radii are in fact quite different:[87,88] Gd^{3+} (r_{viii} = 1.107 Å), Ho^{3+} (r_{viii} = 1.015 Å) and Ti^{4+} (r_{viii} = 0.74 Å). Nevertheless, the anti-site defect percentages obtained are relatively high: 3.6 % for $Gd_2Ti_2O_7$ and 2.4 % for $Ho_2Ti_2O_7$ at 1100 ºC, which is a remarkable result. The anti-site defects may be responsible for the distortions in the lattice detected, which became higher when the more defects are present. In a previous study, the anti-site defects have also been linked with changes in the ionic conduction of these compounds.[89]

When increasing the temperature, the main difference between the Ho and Gd 1100 ºC synthesized samples is the anti-site defects extension and an obvious narrowing of peak widths. A clear reduction of anti-site defects is observed with increasing temperature as reported by A. Fuentes *et al*[85]. This may be related with the low temperature fluorite structure, which can be regarded as a disordered pyrochlore structure. By increasing the temperature and moving away from the phase transition, the structural order may still improve and anti-site defects disappear. It should be noted though that another irreversible phase transition from a pyrochlore to a high temperature fluorite

type structure occurs at 1600 ºC.[89] The detected anti-site defects may be responsible for the expansion of the unit cell due to the distortions induced by the difference in size of the A and B cations.

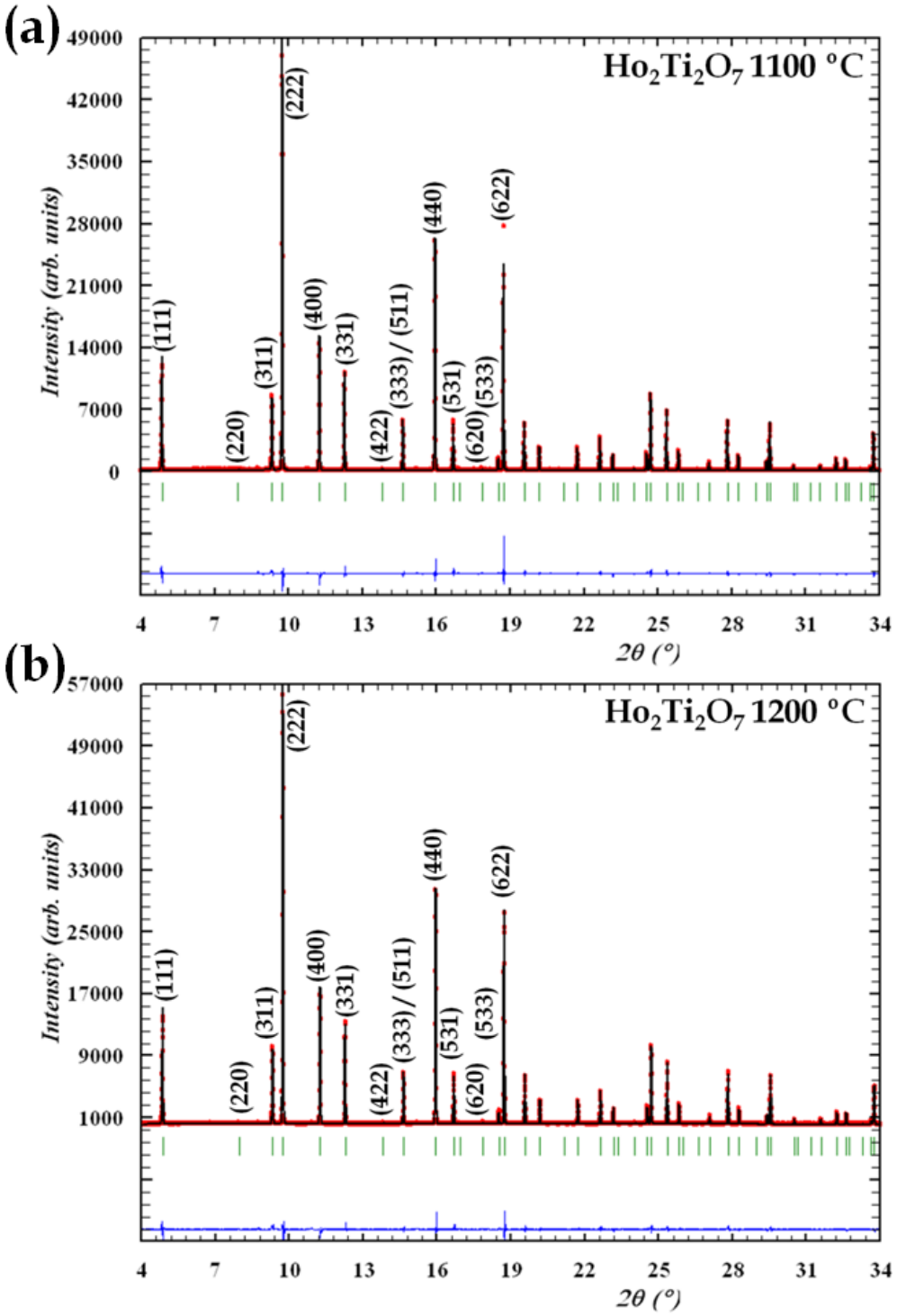

Figure 4.39. Rietveld refinement of synchrotron XRD patterns of $Ho_2Ti_3O_7$ at different temperatures: a) 1100 ºC, b) 1200 ºC. Observed (red dotted lines), refined (black solid lines), and their difference (blue bottom line). Green vertical bars indicate the X-ray reflection positions.

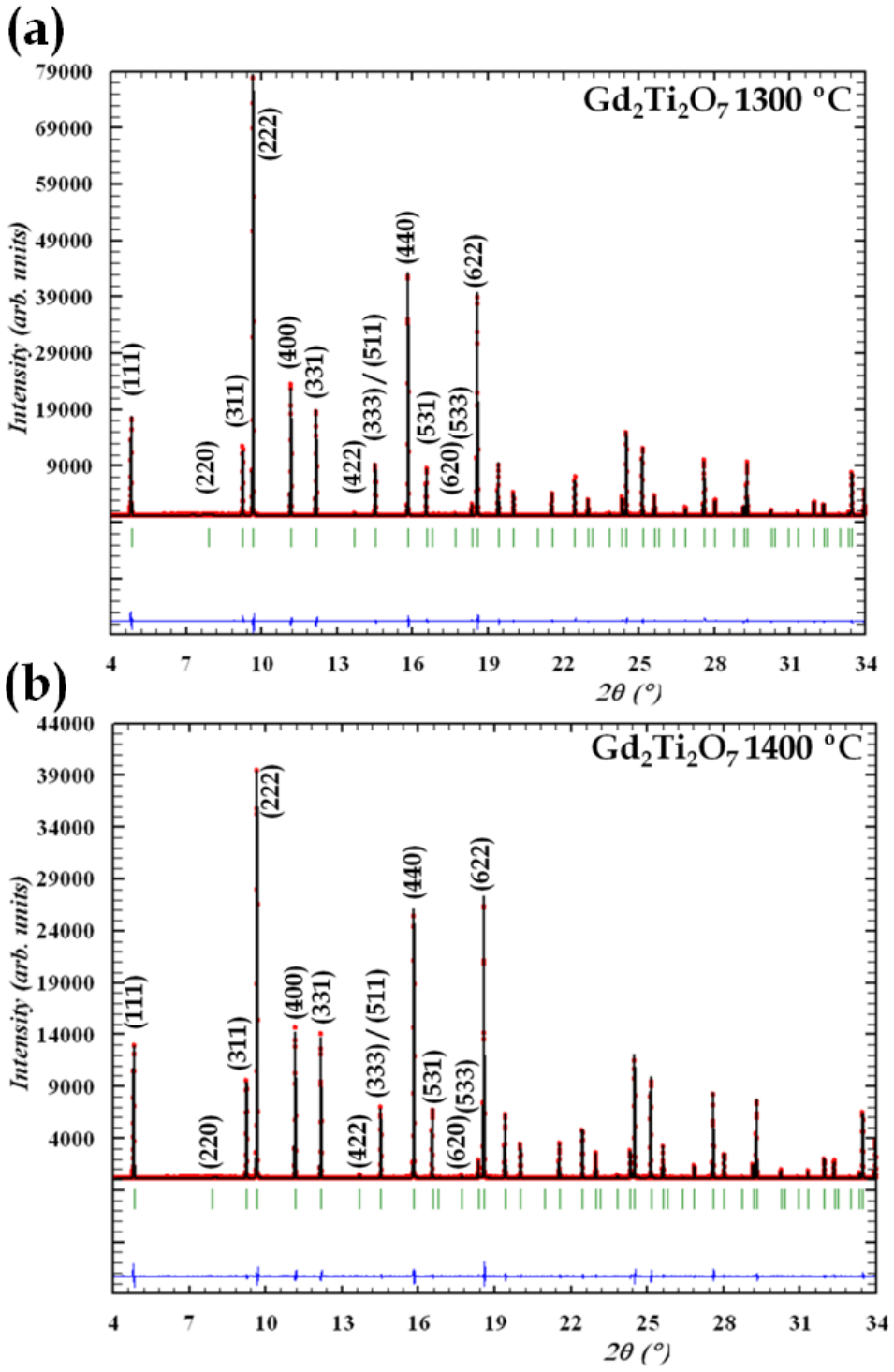

Figure 4.40. Rietveld refinement of synchrotron XRD patterns of $Gd_2Ti_3O_7$ at different temperatures: a) 1300 °C, b) 1400 °C. Observed (red dotted lines), refined (black solid lines), and their difference (blue bottom line). Green vertical bars indicate the X-ray reflection positions.

As it will be discussed below *(section 4.4.5)*, $Gd_2Ti_2O_7$ shows higher ionic conductivity while $Ho_2Ti_2O_7$ is significantly more insulating. From the structural point of view, the pyrochlore structure is not a compact one and presents empty oxygen sites (8a) surrounded by 4 B cations which can be occupied by mobile O^{2-} anions. In $Gd_2Ti_2O_7$ and $Ho_2Ti_2O_7$, the B cation is the same (Ti^{4+}) but the larger Gd^{3+} cation, expands the lattice and thus enhances the mobility of the O^{2-} through the empty 8a sites.[90]

Table 4.9. Structural parameters for $RE_2Ti_2O_7$ (RE = Gd, Ho) obtained by using synchrotron X-ray diffraction Rietveld refinements. Data was taken for samples at different temperatures in order to study the anti-site defects.

	$Ho_2Ti_2O_7$			**$Gd_2Ti_2O_7$**			
	1100°C	**1200°C**	**1400°C**	**1100°C**	**1200°C**	**1300°C**	**1400°C**
***a* (Å)**	10.10004 (6)	10.09882 (5)	10.09828 (3)	10.18126 (8)	10.18407 (5)	10.18496 (5)	10.18507 (6)
A position	16d			16d			
U*100 (Å²)	0.72(1)	0.74(2)	0.38(3)	0.84(1)	0.62(2)	0.56(3)	0.45(2)
Occ RE/Ti	1.952 / 0.048	1.952 / 0.048	2.000 / 0.000	1.929 / 0.071	1.952 / 0.048	1.976 / 0.024	2.000 / 0.000
B position	16c			16c			
U*100 (Å²)	1.01(5)	1.03(3)	0.39(2)	1.22(2)	0.83(1)	0.65(2)	0.95(4)
Occ Ti/RE	1.952 / 0.048	1.952 / 0.048	2.000 / 0.000	1.929 / 0.071	1.952 / 0.048	1.976 / 0.024	1.976 / 0.024
O(1) position	48f			48f			
x	0.4229(4)	0.4232(4)	0.4227(4)	0.4239(4)	0.4244(3)	0.4253(3)	0.42877(5)
U*100 (Å²)	0.71(2)	0.71(2)	0.42(1)	0.82(3)	1.13(1)	0.88(2)	0.93(1)
O(2) position	8b			8b			
U*100 (Å²)	0.09(2)	0.02(4)	0.51(3)	0.09(2)	0.16(3)	0.01(2)	0.23(3)
χ^2	4.24	4.43	4.60	4.78	4.74	3.57	6.21
R_{wp}/ R_{exp} (%/%)	9.63 / 4.67	9.13 / 4.34	9.36 / 4.36	10.7 / 4.92	9.23 / 4.24	7.59 / 4.02	12.3 / 3.94
R_{Bragg}	2.42	2.35	2.83	2.40	2.16	1.90	5.50
Space group	*Fd-3m (#227)*: 16d (½ ½ ½), 16c (0 0 0), 48f (x ⅛ ⅛),4b (⅜ ⅜ ⅜)						

4.4.3. Microstructural characterization

Figures 4.41a and 4.41b show the SEM micrographs of the pyrochlore powder in backscattered-electron mode, obtained after the first 20 minutes of microwave treatment and 2 hours at 1100ºC in air. Powders are composed by agglomerations of submicron and nanometric spherical particles, with high homogeneity and a sponge-like texture. This morphology is probably due to the big amount of gases produced during the synthesis from the decomposition of the starting nitrates and oxidation of the carbon microwave susceptor to CO_2. The small particle size may be adequate for processing ceramic materials with high sintering activity. After the sintering process, materials show high density and strongly increased particle size due to the high sintering activity of the initial powders as revealed in Fig. 4.41c and 4.41d.

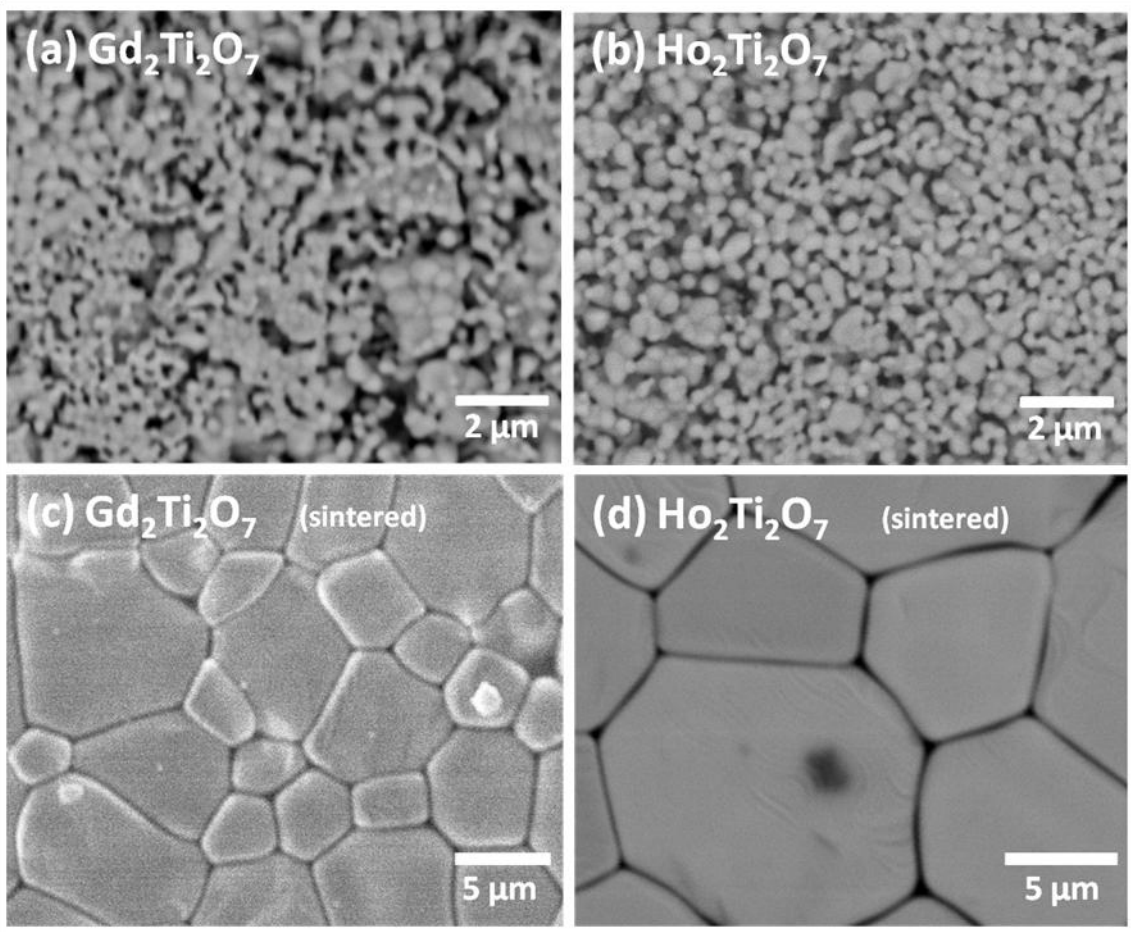

Figure 4.41. SEM micrographs of the $RE_2Ti_2O_7$ samples. (a) and (b) corresponds to $Gd_2Ti_2O_7$ and $Ho_2Ti_2O_7$ powder sample, respectively. (c) and (d) corresponds to pellets sintered at 1400 ºC during 4 h.

Chemical analyses were carried out by EDS. In both samples, the cations distributions are in good agreement with the expected ones (RE 50% and Ti 50%). Furthermore, the metal elements are distributed well all over the samples confirming a good degree of homogeneity.

4.4.4. Magnetic properties

In $RE_2Ti_2O_7$ (RE = Gd, Ho) pyrochlores the RE cations are located in a tetrahedral arrangement (4 RE cations form a tetrahedron) and $(RE)^{3+}$-$(RE)^{3+}$ antiferromagnetic interaction can lead to strong magnetic frustration. As the RE^{3+} cations, in both compounds, have a large moment the superexchange interaction is significant.[91] In the case of $Ho_2Ti_2O_7$ the spins are correlated but a spin ice ground state may occur, which involves that a "two spins in, two spins out" configuration is satisfied on every tetrahedra.[92, 93]

Figure 4.42 shows the temperature dependence of the magnetic susceptibility for both samples. There are no significant differences between ZFC (solid marks) and FC (hollow marks) susceptibility curves. The insets in Fig. 4.42 show the temperature dependence of the reciprocal magnetic susceptibility $1/\chi$ for the respective samples at low temperature, indicating a deviation from the Curie-Weiss law below 10 K in the two different samples. Above this temperature, the paramagnetic states do follow the Curie–Weiss law.

The Curie–Weiss fits are indicated by the black solid lines. In the case of $Gd_2Ti_2O_7$, a linear regression of $1/\chi$ vs T yields μ_{eff} of 5.7 μ_B /Gd^{3+}. The Weiss constant was calculated to $\Theta \approx$ -9.8 K, where the negative value suggests predominantly antiferromagnetic interactions. For $Ho_2Ti_2O_7$, μ_{eff} = 7.3 μ_B/Ho^{3+}, and $\Theta \approx$ + 0.2, consequently, the material may exhibit a slight ferromagnetic character. In both samples the extracted magnetic moments are smaller than the theoretical, μ_{eff} = 7.9 μ_B for the free ion $^8S_{7/2}$ ground state of Gd^{3+} and 10.6 for $^5I_8$ Ho^{3+} ground state.

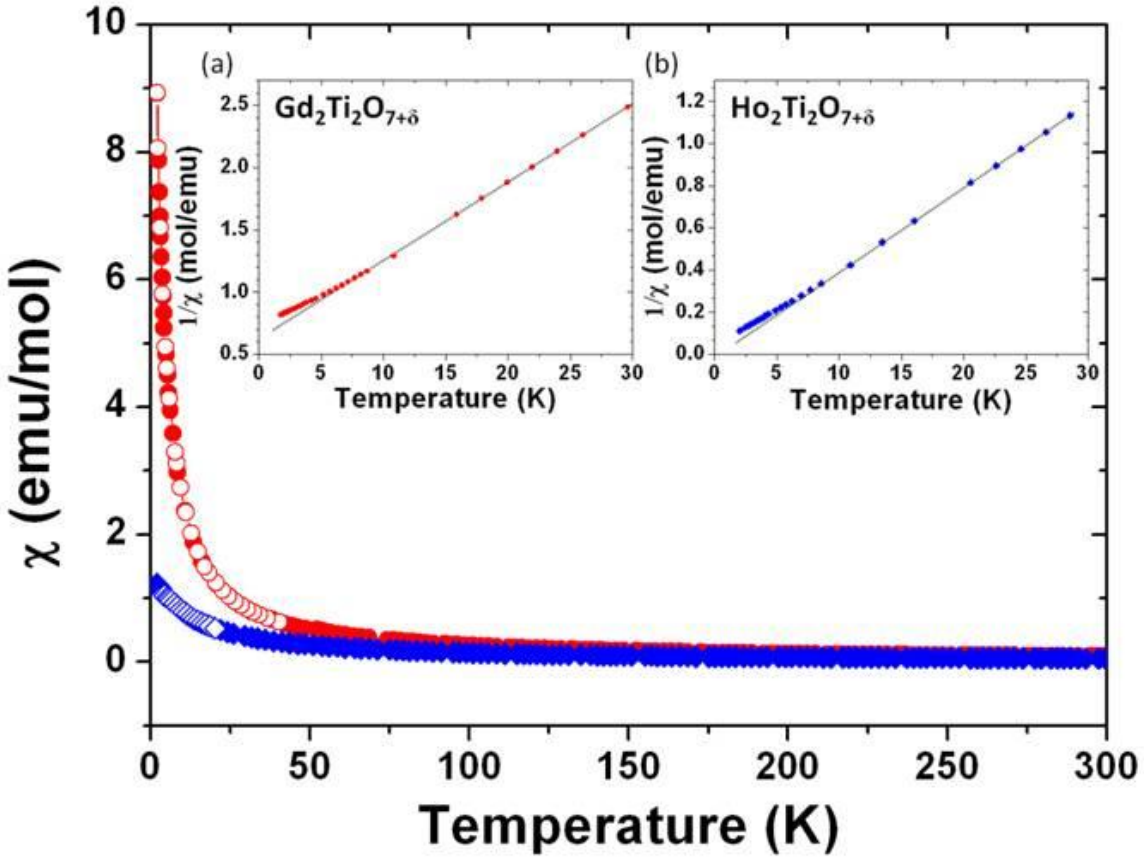

Figure 4.42. Temperature dependence of the magnetic susceptibilities χ of $Gd_2Ti_2O_7$ (red circles) and $Ho_2Ti_2O_7$ (blue squares) at 1 kOe. Solid symbols represents ZFC measurements and hollow simbols are FC data. **Insets:** Inverse susceptibility 1/χ. The black line represents the fit of the data to the Curie–Weiss law and their desviation below 10 K.

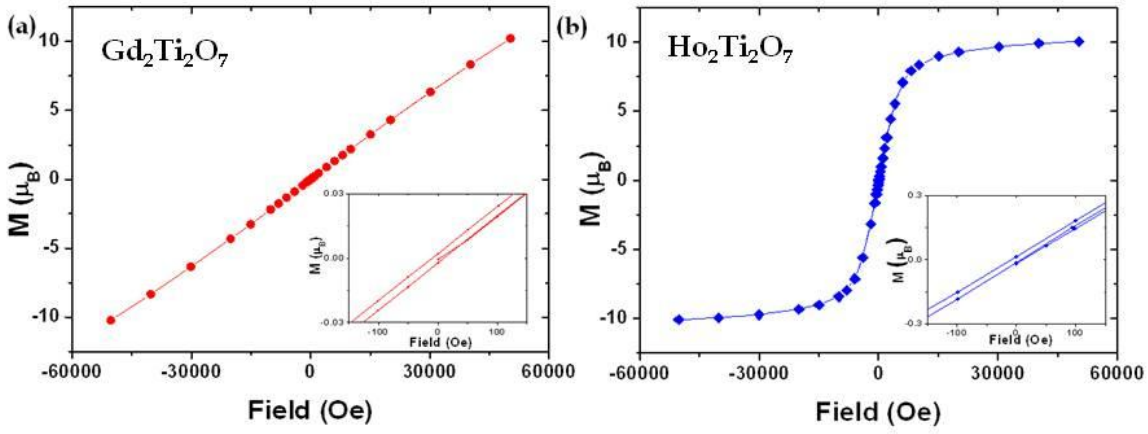

Figure 4.43. Magnetic hysteresis loop at 1.7 K in the magnetic field range of -50 to 50 kOe. Inset: Magnification of the hysteresis loop for (a) $Gd_2Ti_2O_7$ and (b) $Ho_2Ti_2O_7$.

Figure 4.43 presents the magnetization vs applied field plots at 1.7 K for $Gd_2Ti_2O_7$ and $Ho_2Ti_2O_7$, where a magnetic hysteresis loop is observed, indicating that a weak ferromagnetic component also contributes to the magnetic behaviour of the samples.

4.4.5. Dielectric properties

Impedance Spectroscopy (IS) data collected for $Gd_2Ti_2O_7$ at 570 K and for $Ho_2Ti_2O_7$ at 560 K are shown in Fig. 4.44 in terms of the complex impedance plane plots of -Z'' vs Z'. For the $Gd_2Ti_2O_7$ sample (Fig. 4.44a) two regular semicircles are displayed, which are consistent with a series connection of two conventional dielectric relaxation processes. The data can therefore be modeled by a series of two parallel resistor-capacitor (RC) elements where the resistance R corresponds to the respective semicircle diameter. The high frequency semicircle can be ascribed to an intrinsic bulk contribution, whereas the intermediate frequency semi-circle is interpreted as a GB response. It should be noted though that the semi-circles in Fig. 4.44a are slightly suppressed in such a way that the semicircle center seems to be slightly suppressed below the Z' x-axis. This indicates a certain degree of non-ideality of the relaxation process, which can be accounted for by replacing the ideal capacitor in the RC element with a constant phase element (CPE).

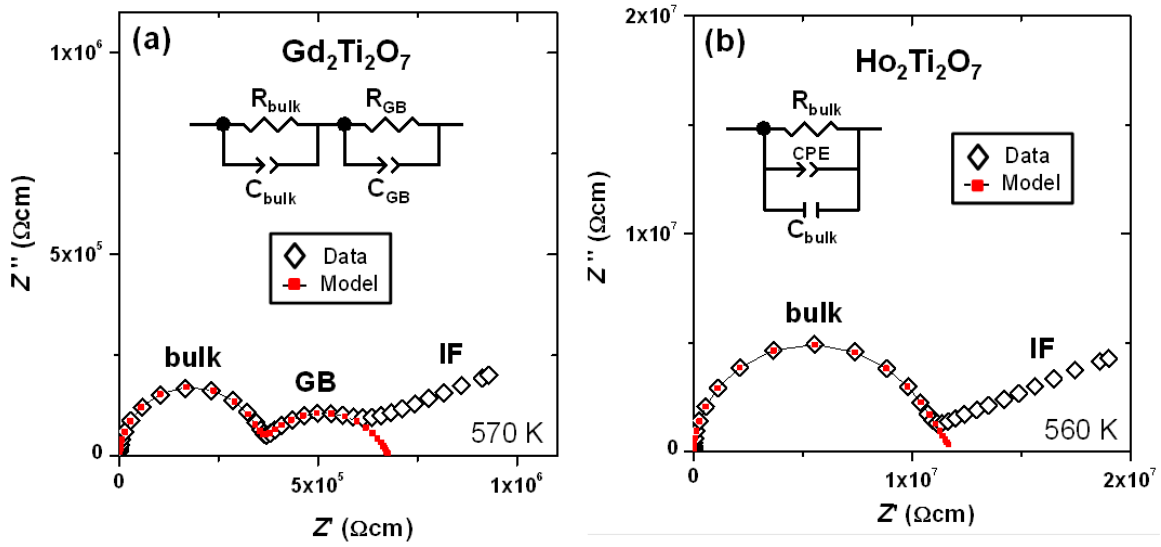

Figure 4.44. Complex impedance plane plots of Z'' vs Z' for **(a)** $Gd_2Ti_2O_7$ and **(b)** $Ho_2Ti_2O_7$. The equivalent circuits used for fitting the data are depicted in the figure insets.

The resulting equivalent circuit used for data fitting is displayed in the inset of Fig. 4.44a and a good fit to the data can be obtained in the high and intermediate frequency range where the GB and bulk relaxations are dominant. The CPE behaviour is usually explained in the framework of a broadening of the distribution of relaxation times τ across the macroscopic sample, where $\tau = R \cdot C$, with R being the resistance and C the capacitance of an ideal RC element. At the low frequency end the data points in $-Z''$ vs Z' (Fig. 4.44) align linearly in a "pike"-like fashion, which is inconsistent with the conventional RC element model and is commonly interpreted as a blocking effect of the electrode sample interface (IF). This constitutes clear evidence for ionic charge transport where the blocking effect of the interface occurs as a result of the different types of dominating charge carriers in the Au electrodes (electrons) and in the ceramics (ions). Therefore, ionic conductivity in the $Gd_2Ti_2O_7$ sample is indicated most likely due to oxygen vacancy conduction, and electronic contributions are not evident. The charge transport across blocking electrode interfaces is usually by diffusion, which was not accounted for in the equivalent circuit model here, because rather complex circuit components such as Warburg elements are needed to describe diffusion processes.[74]

In the case of the $Ho_2Ti_2O_7$ only one semicircle is evident from Fig. 4.44b. Although the pike-like interface contribution suggests ionic type charge transport, only one semicircle can be resolved. This is rather unusual, because ionic charge transport is usually understood to be inhibited by Schottky-type charge transport barriers at the GB regions, and both bulk and GB contributions are expected to appear in form of a semicircle in $-Z''$ vs Z' plots. The single semicircle in $Ho_2Ti_2O_7$ is interpreted as a bulk response due to the associated capacitance (more details are given below). The reasons for the disappearance of the GB contribution in $Ho_2Ti_2O_7$ ceramics are not entirely clear but the GB Schottky model possibly may be not valid here. The data was modelled with an unconventional ideal RC element with a CPE in parallel, which has been shown previously to be appropriate to model bulk ceramic relaxations in oxide ion conductors.[94]

The ionic conductivity in the $Gd_2Ti_2O_7$ sample appears to be much larger as compared to $Ho_2Ti_2O_7$, which is obvious from the increased semicircle diameter (the difference is almost a factor of 20). This effect can be interpreted as a result of the larger RE ionic size of Gd^{3+} (1.10 Å) as compared to Ho^{3+} (1.01 Å), which leads to a slightly larger $Gd_2Ti_2O_7$ unit cell size. This may open up conduction pathways for the oxygen anions to move across the $Gd_2Ti_2O_7$ sample more easily, whereas in $Ho_2Ti_2O_7$ oxygen anion transport may be inhibited due to a denser packing of the oxygen anions in a smaller unit cell.

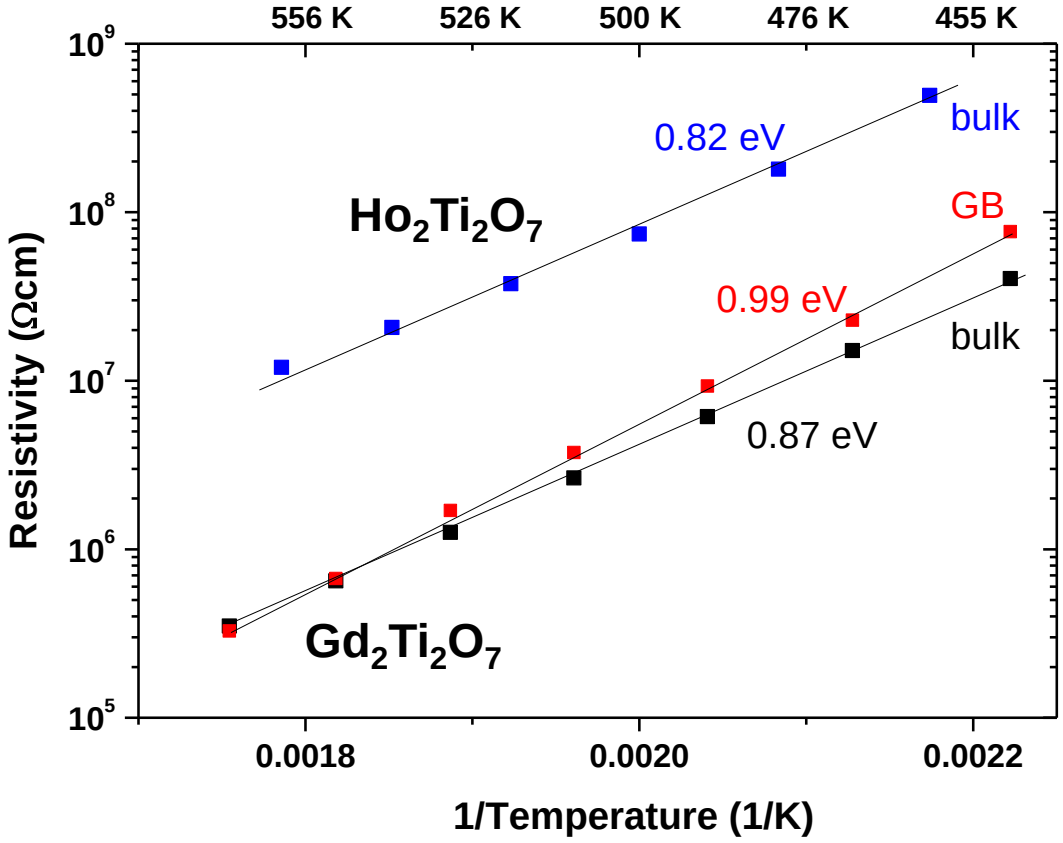

Figure 4.45. Arrhenius plots using the resistivity values for the bulk and GB contributions of $Gd_2Ti_2O_7$ and $Ho_2Ti_2O_7$ obtained from the equivalent circuit fits. The respective charge transport activation energies are indicated.

The difference in RE ionic radius is small though and the massive effect on the oxygen ion conduction is rather surprising. This massive difference in resistivity is illustrated clearly in Figure 4.45, where plots of logarithmic resistivity vs reciprocal temperature are depicted. The resistivity represents the values obtained from the resistors in the equivalent circuits depicted in the insets of Fig. 4.44a-b.

4.5. Conclusions

Solid state microwave synthesis is an effective method for the preparation of different oxide materials featuring the ABO_3 perovskite and $A_2B_2O_7$ pyrochlore structures. Despite the simplicity of this method, pure materials, sometimes nanosized, either in a single step or after a further annealing can be synthesized. The crystal quality of the powder samples obtained is high and permits the Rietveld refinement of the structure.

- For $LaMO_3$ and $La_{1-x}A'_xMO_3$ (A' = Sr, M = Al, Cr, Mn, Fe, Co) materials, different synthetic procedures have been established: $LaCoO_3$ and $LaMnO_3$ are directly obtained after microwave irradiation while a second calcination step is necessary for $LaAlO_3$, $LaCrO_3$ and $LaFeO_3$. On the other hand, to obtain doped more complex materials it is crucial to combine sol-gel methodology with microwaves.

$LaCoO_3$ ceramics contain oxygen vacancy defects, which vary in concentration or in the physical properties with the synthesis route (conventional vs. solid - state microwave). Such defects may act as nucleation centres for the gradual population of e_g levels above T_{s1} across the thermally induced spin state transition. Such gradual population of higher spin areas is reflected by the appearance of an additional dielectric relaxation at the transition T_{s1}, which indicates dielectric and magnetic phase separation, and coupling of dielectric and magnetic properties via the lattice. The use of different synthesis techniques implies that such observations constitute an intrinsic material property of $LaCoO_3$. The dielectric and, to a lesser extent, the magnetic properties in $LaCoO_3$ are influenced perceptibly by the magnetic defect structure.

- A comprehensive characterization in terms of the structural and physical properties was performed for the perovskite $(RE)CrO_3$ series. The ***b*** and ***c*** unit cell parameters showed a consistent increase with increasing IOR of the RE cation. The concomitant increase in octahedral tilt-angle approaching

180° resulted in a consistent increase of the Cr^{3+}-Cr^{3+} antiferromagnetic ordering temperature T_{N1}. The magnetic susceptibility χ vs temperature characteristics revealed a rich variety of different spin interactions. The intrinsic bulk charge transport activation energy and bulk dielectric permittivity in sintered ceramics showed a change in the trend with IOR near the Gd-containing sample. No clear correlations of the magnetic and dielectric properties were found, and major magneto-electric coupling effects could not be detected. A summary picture is presented in Figure 4.46 where it is possible to observe the structural, magnetic and dielectric correlation depending on the $(RE)^{3+}$ cation.

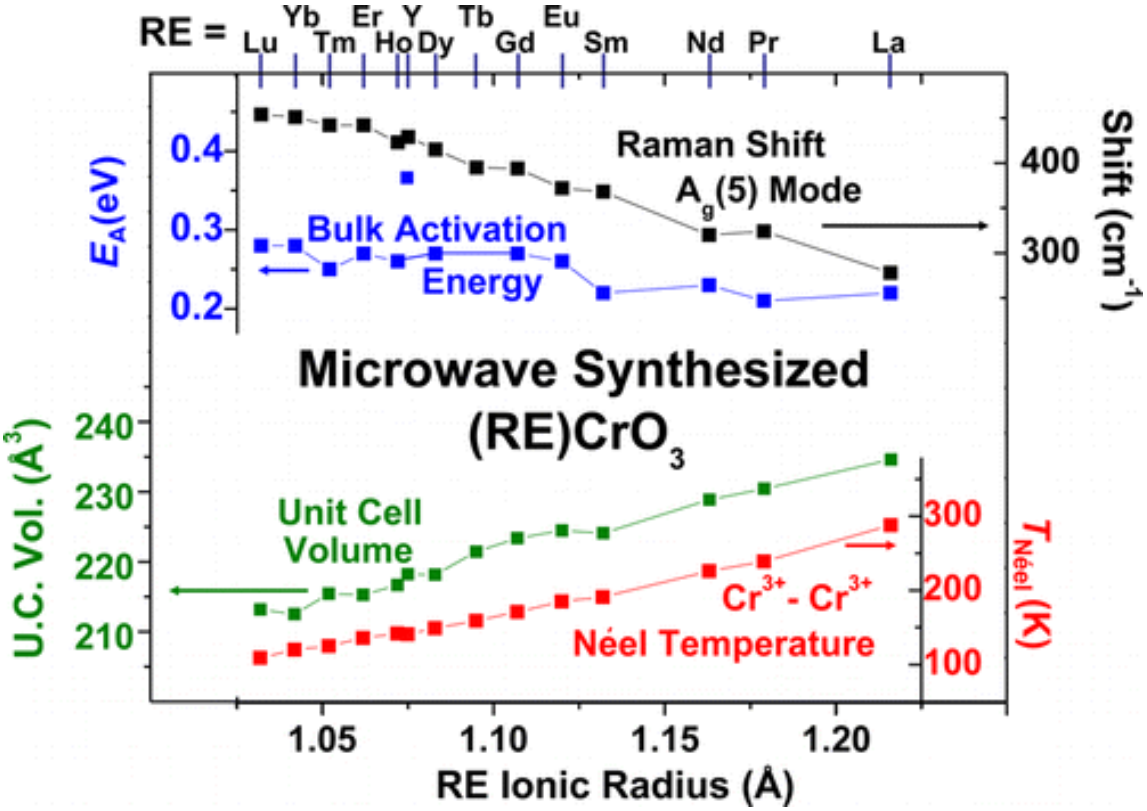

Figure 4.46. Structural, magnetic and dielectric properties summary picture

No indications for a non-centrosymmetric space-group and associated ferroelectricity were detected from XRD pattern, Raman spectroscopy and temperature dependent dielectric permittivity data. Microwave synthesized $(RE)CrO_3$ chromites may therefore not to be classified as magneto-electric or multiferroic materials.

- Synchrotron X-ray diffraction experiments were carried out in order to study cation anti-site defects in pyrochlore $(RE)_2Ti_2O_7$ (RE = Gd, Ho) and the temperature influence of this effect. Antisite defect concentration of 3.6 % for $Gd_2Ti_2O_7$ and 2.4 % for $Ho_2Ti_2O_7$ at 1100 ^oC were observed, where the antisite defect concentration decreases with the increasing of temperature. In pyrochlores, antiferromagnetic interactions can lead to strong magnetic frustration. In both studied samples a weak ferromagnetic component was observed at 1.7 K. Impedance spectroscopy reveals that $Gd_2Ti_2O_7$ ceramics shows higher ionic conductivity as compared to $Ho_2Ti_2O_7$.

4.6. References

1. Mitchell, R. H., *Perovskites: Modern and Ancient*. Almaz Press Incorporated: 2002; p 318.

2. Modeshia, D. R.; Walton, R. I., Solvothermal synthesis of perovskites and pyrochlores: crystallisation of functional oxides under mild conditions. *Chemical Society Reviews* **2010,** 39, (11), 4303-4325.

3. Goldschmidt, V. M., *Geochemisce Verterlungsgesetze der Elemente*. Norske Videnskap: 1927.

4. Galasso, F. S., *Structure, properties, and preparation of perovskite-type compounds*. Pergamon Press: 1969; p 207.

5. Howard, C. J.; Stokes, H. T., Group-theoretical analysis of octahedral tilting in perovskites. *Acta Crystallographica B* **1998,** 54, 782.

6. Lufaso, M. W.; Woodward, P. M., Jahn-Teller distortions, cation ordering and octahedral tilting in perovskites. *Acta Crystallographica Section B* **2004,** 60, (1), 10-20.

7. Stanek, C. R.; Minervini, L.; Grimes, R. W., Nonstoichiometry in $A_2B_2O_7$ Pyrochlores. *Journal of the American Ceramic Society* **2002,** 85, (11), 2792–2798.

8. Nachimuthu, P.; Thevuthasan, S.; Engelhard, M. H.; Weber, W. J.; Shuh, D. K.; Hamdan, N. M.; Mun, B. S.; Adams, E. M.; McCready, D. E.;

Shutthanandan, V.; Lindle, D. W.; Balakrishnan, G.; Paul, D. M.; Gullikson, E. M.; Perera, R. C. C.; Lian, J.; Wang, L. M.; Ewing, R. C., Probing cation antisite disorder in $Gd_2Ti_2O_7$ pyrochlore by site-specific near-edge x-ray-absorption fine structure and x-ray photoelectron spectroscopy. *Physical Review B* **2004,** 70, (10), 100101.

9. Minervini, L.; Grimes, R. W.; Sickafus, K. E., Disorder in Pyrochlore Oxides. *Journal of the American Ceramic Society* **2000,** 83, (8), 1873-1878.

10. Moreno, K. J.; Fuentes, A. F.; Maczka, M.; Hanuza, J.; Amador, U.; Santamaría, J.; León, C., Influence of thermally induced oxygen order on mobile ion dynamics in $Gd_2(Ti_{0.65}Zr_{0.35})_2O_7$. *Physical Review B* **2007,** 75, (18), 184303.

11. Backhaus-Ricoult, M., SOFC - A playground for solid state chemistry. *Solid State Sciences* **2008,** 10, (6), 670-688.

12. Choi, Y.; Mebane, D. S.; Lin, M. C.; Liu, M., Oxygen Reduction on $LaMnO_3$-Based Cathode Materials in Solid Oxide Fuel Cells. *Chemistry of Materials* **2007,** 19, (7), 1690-1699.

13. Petrovic, S.; Terlecki-Baricevic, A.; Karanovic, L.; Kirilov-Stefanov, P.; Zdujic, M.; Dondur, V.; Paneva, D.; Mitov, I.; Rakic, V., $LaMO_3$ (M = Mg, Ti, Fe) perovskite type oxides: Preparation, characterization and catalytic properties in methane deep oxidation. *Applied Catalysis B: Environmental* **2008,** 79, (2), 186-198.

14. Cui, X. M.; Tao, B. W.; Xiong, J.; Liu, X. Z.; Li, Y. R., YBCO Superconducting Film Coated on $LaAlO_3$ Substrate by TFA-MOD Process. *Journal of Superconductivity* **2005,** 18, (2), 291-294.

15. Koehler, W. C.; Wollan, E. O., Neutron-diffraction study of the magnetic properties of perovskite-like compounds $LaBO_3$. *Journal of Physics and Chemistry of Solids* **1957,** 2, (2), 100-106.

16. Goodenough, J. B., An interpretation of the magnetic properties of the perovskite-type mixed crystals $La_{1-x}Sr_xCoO_3$. *Journal of Physics and Chemistry of Solids* **1958,** 6, (2-3), 287-297.

17. Klie, R. F.; Zheng, J. C.; Zhu, Y.; Varela, M.; Wu, J.; Leighton, C., Direct Measurement of the Low -Temperature Spin-State Transition in $LaCoO_3$. *Physical Review Letters* **2007,** 99, (4), 047203.

18. Korotin, M. A.; Ezhov, S. Y.; Solovyev, I. V.; Anisimov, V. I.; Khomskii, D. I.; Sawatzky, G. A., Intermediate-spin state and properties of $LaCoO_3$. *Physical Review B* **1996,** 54, (8), 5309-5316.

19. Ishikawa, A.; Nohara, J.; Sugai, S., Raman Study of the Orbital-Phonon Coupling in $LaCoO_3$. *Physical Review Letters* **2004,** 93, (13), 136401.

20. Jonker, G. H., Magnetic and Semiconducting Properties of Perovskites Containing Manganese and Cobalt. *Journal of Applied Physics* **1966,** 37, (3), 1424-1430.

21. Kozlenko, D. P.; Golosova, N. O.; Jirák, Z.; Dubrovinsky, L. S.; Savenko, B. N.; Tucker, M. G.; Le Godec, Y.; Glazkov, V. P., Temperature- and pressure-driven spin-state transitions in $LaCoO_3$. *Physical Review B* **2007,** 75, (6), 064422.

22. Schmidt, R.; Wu, J.; Leighton, C.; Terry, I., Dielectric response to the low-temperature magnetic defect structure and spin state transition in polycrystalline $LaCoO_3$. *Physical Review B* **2009,** 79, (12), 125105.

23. Vázquez-Vázquez, C.; Kögerler, P.; López-Quintela, M. A.; Sánchez, R. D.; Rivas, J., Preparation of $LaFeO_3$ particles by sol-gel technology. *Journal of Materials Research* **1998,** 13, (02), 451-456.

24. Rida, K.; Benabbas, A.; Bouremmad, F.; Peña, M. A.; Sastre, E.; Martínez-Arias, A., Effect of calcination temperature on the structural characteristics and catalytic activity for propene combustion of sol-gel derived lanthanum chromite perovskite. *Applied Catalysis A: General* **2007,** 327, (2), 173-179.

25. Krupicka, E.; Reller, A.; Weidenkaff, A., Morphology of nanoscaled $LaMO_3$-particles (M=Mn, Fe, Co, Ni) derived by citrate precursors in aqueous and alcoholic solvents. *Crystal Engineering* **2002,** 5, (3-4), 195-202.

26. Shabbir, G.; Qureshi, A. H.; Saeed, K., Nano-crystalline $LaFeO_3$ powders synthesized by the citrate-gel method. *Materials Letters* **2006,** 60, (29-30), 3706-3709.

27. Najjar, H.; Batis, H., La-Mn perovskite-type oxide prepared by combustion method: Catalytic activity in ethanol oxidation. *Applied Catalysis A: General* **2010,** 383, (1-2), 192-201.

28. Tian, Z.-Q.; Yu, H.-T.; Wang, Z.-L., Combustion synthesis and characterization of nanocrystalline $LaAlO_3$ powders. *Materials Chemistry and Physics* **2007,** 106, (1), 126-129.

29. Rendón-Angeles, J. C.; Yanagisawa, K.; Matamoros-Veloza, Z.; Pech-Canul, M. I.; Mendez-Nonell, J.; Torre, S. D.-d. l., Hydrothermal synthesis of perovskite strontium doped lanthanum chromite fine powders and its sintering. *Journal of Alloys and Compounds* **2010,** 504, (1), 251-256.

30. Bernard, C.; Durand, B.; Verelst, M.; Lecante, P., Hydrothermal synthesis of $LaMnO_{3+\delta}$: F.T.I.R. and W.A.X.S. investigations of the evolution from amorphous to crystallized powder. *Journal of Materials Science* **2004,** 39, (8), 2821-2826.

31. Zheng, W.; Liu, R.; Peng, D.; Meng, G., Hydrothermal synthesis of $LaFeO_3$ under carbonate-containing medium. *Materials Letters* **2000,** 43, (1-2), 19-22.

32. Das, N.; Bhattacharya, D.; Sen, A.; Maiti, H. S., Sonochemical synthesis of $LaMnO_3$ nano-powder. *Ceramics International* **2009,** 35, (1), 21-24.

33. Panneerselvam, M.; Rao, K. J., Microwave preparation and sintering of industrially important perovskite oxides: $LaMO_3$ (M = Cr, Co, Ni). *Journal of Materials Chemistry* **2003,** 13, (3), 596-601.

34. Farhadi, S.; Momeni, Z.; Taherimehr, M., Rapid synthesis of perovskite-type $LaFeO_3$ nanoparticles by microwave-assisted decomposition of bimetallic $La[Fe(CN)_6]\cdot 5H_2O$ compound. *Journal of Alloys and Compounds* **2009,** 471, (1-2), L5-L8.

35. Liu, S.; Qian, X.; Xiao, J., Synthesis and characterization of $La_{0.8}Sr_{0.2}Co_{0.5}Fe_{0.5}O_{3\pm\delta}$ nanopowders by microwave assisted sol-gel route. *Journal of Sol-Gel Science and Technology* **2007,** 44, (3), 187-193.

36. Shannon, R. D.; Prewitt, C. T., Effective ionic radii in oxides and fluorides. *Acta Crystallographica Section B* **1969,** 25, (5), 925-946.

37. Jadhav, A. D.; Gaikwad, A. B.; Samuel, V.; Ravi, V., A low temperature route to prepare $LaFeO_3$ and $LaCoO_3$. *Materials Letters* **2007,** 61, (10), 2030-2032.

38. Taguchi, H.; Matsu-ura, S.-i.; Nagao, M.; Kido, H., Electrical properties of perovskite-type $La(Cr_{1-x}Mn_x)O_{3+\delta}$. *Physica B: Condensed Matter* **1999,** 270, (3-4), 325-331.

39. Sathe, V. G.; Paranjpe, S. K.; Siruguri, V.; Pimpale, A. V., Novel magnetic phases in $La_{0.7}Sr_{0.3}Co_{1-y}Fe_yO_3$ ($0.0 < y < 1.0$): a neutron diffraction study. *Journal of Physics: Condensed Matter* **1998,** 10, (18), 4045.

40. Dann, S. E.; Currie, D. B.; Weller, M. T.; Thomas, M. F.; Al-Rawwas, A. D., The Effect of Oxygen Stoichiometry on Phase Relations and Structure in the System $La_{1-x}Sr_xFeO_{3-\delta}$ ($0 < x < 1$, $0 < \delta < 0.5$). *Journal of Solid State Chemistry* **1994,** 109, (1), 134-144.

41. Fedulov, S. A.; Venevtsev, Y. N.; Dzhmukhadze, D. F., X-ray and electrical studies of the $PbTiO_3$ - $LaAlO_3$ system. *Kristallografiya* **1962,** 7, 408-411.

42. Marezio, M.; Dernier, P. D., The bond lengths in $LaFeO_3$. *Materials Research Bulletin* **1971,** 6, (1), 23-29.

43. Elemans, J. B. A. A.; Van Laar, B.; Van Der Veen, K. R.; Loopstra, B. O., The crystallographic and magnetic structures of $La_{1-x}Ba_xMn_{1-x}Me_xO_3$ (Me = Mn or Ti). *Journal of Solid State Chemistry* **1971,** 3, (2), 238-242.

44. Wold, A.; Arnolt, R. J., Preparation and crystallographic properties of the systems $LaMn_{1-x}Mn_xO_{3-\delta}$ and $LaMn_{1-x}Ni_xO_{3+\delta}$. *Journal of Physics and Chemistry of Solids* **1959,** 9, 176-180.

45. Ramirez, A. P., Colossal magnetoresistance. *Journal of Physics: Condensed Matter* **1997,** 9, (39), 8171.

46. Rodríguez-Carvajal, J.; Hennion, M.; Moussa, F.; Moudden, A. H.; Pinsard, L.; Revcolevschi, A., Neutron-diffraction study of the Jahn-Teller transition in stoichiometric $LaMnO_3$. *Physical Review B* **1998,** 57, (6), R3189-R3192.

47. Irvine, J. T. S.; Sinclair, D. C.; West, A. R., Electroceramics: Characterization by Impedance Spectroscopy. *Advanced Materials* **1990,** 2, (3), 132-138.

48. Giblin, S. R.; Terry, I.; Clark, S. J.; Prokscha, T.; Prabhakaran, D.; Boothroyd, A. T.; Wu, J.; Leighton, C., Observation of magnetic excitons in $LaCoO_3$. *EPL (Europhysics Letters)* **2005,** 70, (5), 677.

49. Nagaev, E. L.; Podel'shchikov, A. I., Phase separation and resistivity jumps in Co compounds and other materials with low-spin - high-spin transitions. *Journal of Physics: Condensed Matter* **1996,** 8, (30), 5611.

50. Sardar, K.; Lees, M. R.; Kashtiban, R. J.; Sloan, J.; Walton, R. I., Direct Hydrothermal Synthesis and Physical Properties of Rare-Earth and Yttrium Orthochromite Perovskites. *Chemistry of Materials* **2011,** 23, (1), 48-56.

51. Belik, A. A.; Matsushita, Y.; Tanaka, M.; Takayama-Muromachi, E., Crystal Structures and Properties of Perovskites $ScCrO_3$ and $InCrO_3$ with Small Ions at the A Site. *Chemistry of Materials* **2012,** 24, (11), 2197-2203.

52. Sahu, J. R.; Serrao, C. R.; Ray, N.; Waghmare, U. V.; Rao, C. N. R., Rare earth chromites: a new family of multiferroics. *Journal of Materials Chemistry* **2007,** 17, (1), 42-44.

53. Ramesha, K.; Llobet, A.; Proffen, T.; Serrao, C. R.; Rao, C. N. R., Observation of local non-centrosymmetry in weakly biferroic $YCrO_3$. *Journal of Physics: Condensed Matter* **2007,** 19, (10), 102202.

54. Su, Y.; Zhang, J.; Feng, Z.; Li, L.; Li, B.; Zhou, Y.; Chen, Z.; Cao, S., Magnetization reversal and Yb^{3+}/Cr^{3+} spin ordering at low temperature for perovskite $YbCrO_3$ chromites. *Journal of Applied Physics* **2010,** 108, (1), 013905.

55. Cooke, A. H.; Martin, D. M.; Wells, M. R., Magnetic interactions in gadolinium orthochromite, $GdCrO_3$. *Journal of Physics C: Solid State Physics* **1974,** 7, (17), 3133.

56. Dzyaloshinsky, I., A thermodynamic theory of "weak" ferromagnetism of antiferromagnetics. *Journal of Physics and Chemistry of Solids* **1958,** 4, (4), 241-255.

57. Moriya, T. r., Anisotropic Superexchange Interaction and Weak Ferromagnetism. *Physical Review* **1960,** 120, (1), 91-98.

58. Shamir, N.; Shaked, H.; Shtrikman, S., Magnetic structure of some rare-earth orthochromites. *Physical Review B* **1981,** 24, (11), 6642-6651.

59. Jaiswal, A.; Das, R.; Vivekanand, K.; Maity, T.; Abraham, P. M.; Adyanthaya, S.; Poddar, P., Magnetic and dielectric properties and Raman spectroscopy of $GdCrO_3$ nanoparticles. *Journal of Applied Physics* **2010,** 107, (1), 013912.

60. Russo, N.; Mescia, D.; Fino, D.; Saracco, G.; Specchia, V., N_2O Decomposition over Perovskite Catalysts. *Industrial & Engineering Chemistry Research* **2007,** 46, (12), 4226-4231.

61. Tsushima, K.; Aoyagi, K.; Sugano, S., Magnetic and Magneto Optical Properties of Some Rare-Earth and Yttrium Orthochromites. *Journal of Applied Physics* **1970,** 41, (3), 1238-1240.

62. Fergus, J. W., Lanthanum chromite-based materials for solid oxide fuel cell interconnects. *Solid State Ionics* **2004,** 171, (1-2), 1-15.

63. Beckers, J.; Rothenberg, G., "Hot Spot" Hydrocarbon Oxidation Catalysed by Doped Perovskites—Towards Cleaner Diesel Power. *A European Journal of ChemPhysChem* **2005,** 6, (2), 223-225.

64. Geller, S., Crystallographic studies of perovskite-like compounds. IV. Rare earth scandates, vanadites, galliates, orthochromites. *Acta Crystallographica* **1957,** 10, (4), 243-248.

65. Subba Rao, G. V.; Wanklyn, B. M.; Rao, C. N. R., Electrical transport in rare earth ortho-chromites, -manganites and -ferrites. *Journal of Physics and Chemistry of Solids* **1971,** 32, (2), 345-358.

66. García-Lastra, J. M.; Barriuso, M. T.; Aramburu, J. A.; Moreno, M., Microscopic origin of the different colors displayed by $MgAl_2O_4:Cr^{3+}$ and emerald. *Physical Review B* **2008,** 78, (8), 085117.

67. Gjønnes, J.; Moodie, A. F., Extinction conditions in the dynamic theory of electron diffraction. *Acta Crystallographica* **1965,** 19, (1), 65-67.

68. Iliev, M. N.; Abrashev, M. V.; Lee, H. G.; Popov, V. N.; Sun, Y. Y.; Thomsen, C.; Meng, R. L.; Chu, C. W., Raman spectroscopy of orthorhombic perovskitelike $YMnO_3$ and $LaMnO_3$. *Physical Review B* **1998,** 57, (5), 2872-2877.

69. Weber, M. C.; Kreisel, J.; Thomas, P. A.; Newton, M.; Sardar, K.; Walton, R. I., Phonon Raman scattering of $RCrO_3$ perovskites (R=Y, La, Pr, Sm, Gd, Dy, Ho, Yb, Lu). *Physical Review B* **2012,** 85, (5), 054303.

70. Widatallah, H. M.; Al-Harthi, S. H.; Johnson, C.; Klencsar, Z.; Gismelseed, A. M.; Moore, E. A.; Al-Rawas, A. D.; Wynter, C. I.; Brown, D. E., Formation, ionic site exchange and surface structure of mechanosynthesized $EuCrO_3$ nanocrystalline particles. *Journal of Physics D: Applied Physics* **2011,** 44, (26), 265403.

71. Kojima, N.; Tsushima, K.; Kurita, S.; Tsujikawa, I., Optical Investigations of $YbCrO_3$. II. Metamagnetic Transition in $YbCrO_3$. *Journal of the Physic Society Japon* **1980,** 49, 1456-1462

72. Van Laar, B.; Elemans, J. B. A. A., On the magnetic structure of $DyCrO_3$. *Journal de Physique* **1971,** 32, (4), 301-304.

73. Goodenough, J. B.; Longo, J. M., *Landolt−Bőrnstein New Series III*. 1970; Vol. 4, p 228.

74. Barsoukov, E.; Macdonald, J. R., *Impedance Spectroscopy: Theory, Experiment, and Applications*. 2005; p 608.

75. Schmidt, R., Impedance Spectroscopy of electroceramics. In *Ceramic Materials Research Trends*, Lin, P. B., Ed. Nova Science Publishers, Inc.: 2007; pp 321-351.

76. Aguilar-Garib, J. A.; García, F.; Valdez, Z., Estimating resistive and dielectric effects during microwave heating of $Fe_{0.22}Ni_{0.67}Mn_{2.11}O_4$. *Journal of the Ceramic Society of Japan* **2009,** 117, (1367), 801-807.

77. Greedan, J. E., Geometrically Frustrated Magnetic Materials. In *Functional Oxides*, Bruce, D. W.; O'Hare, D.; Walton, R. I., Eds. Wiley: 2011; pp 41-117.

78. Holtappels, P.; Poulsen, F. W.; Mogensen, M., Electrical conductivities and chemical stabilities of mixed conducting pyrochlores for SOFC applications. *Solid State Ionics* **2000,** 135, (1-4), 675-679.

79. Subramanian, M. A.; Aravamudan, G.; Subba Rao, G. V., Oxide pyrochlores: A review. *Progress in Solid State Chemistry* **1983,** 15, (2), 55-143.

80. Morris, D. J. P.; Tennant, D. A.; Grigera, S. A.; Klemke, B.; Castelnovo, C.; Moessner, R.; Czternasty, C.; Meissner, M.; Rule, K. C.; Hoffmann, J.-U.; Kiefer, K.; Gerischer, S.; Slobinsky, D.; Perry, R. S., Dirac Strings and Magnetic Monopoles in the Spin Ice $Dy_2Ti_2O_7$. *Science* **2009,** 326, (5951), 411-414.

81. Dong, X. W.; Wang, K. F.; Luo, S. J.; Wan, J. G.; Liu, J. M., Coexistence of magnetic and ferroelectric behaviors of pyrochlore $Ho_2Ti_2O_7$. *J. Appl. Phys.* **2009,** 106, (10), 4.

82. Wang, S. X.; Wang, L. M.; Ewing, R. C.; Govindan Kutty, K. V., Ion irradiation of rare-earth- and yttrium-titanate-pyrochlores. *Nuclear Instruments and Methods in Physics Research Section B: Beam Interactions with Materials and Atoms* **2000,** 169, (1), 135-140.

83. Shlyakhtina, A. V.; Karyagina, O. K.; Shcherbakova, L. G., Order-Disorder Transformations in $Ln_2Ti_2O_7$(Ln = Lu, Yb, Tm, Gd). *Inorganic Materials* **2004,** 40, (1), 59-65.

84. Zhang, L.; Zhong, H.; Zhang, W.; Lu, L.; Yang, X.; Wang, X., Fabrication of $Dy_2Ti_2O_7$ nanocrystalline at 700°C and its photocatalytic activity. *Journal of Alloys and Compounds* **2008,** 463, (1-2), 466-470.

85. Fuentes, A. F.; Boulahya, K.; Maczka, M.; Hanuza, J.; Amador, U., Synthesis of disordered pyrochlores, $A_2Ti_2O_7$ (, Gd and Dy), by mechanical milling of constituent oxides. *Solid State Sciences* **2005,** 7, (4), 343-353.

86. Brixner, L. H., Preparation and Properties of the $Ln_2Ti_2O_7$-Type Rare Earth Titanate. *Inorganic Chemistry* **1964,** 3, (7), 1065-1067.

87. Shannon, R., Revised effective ionic radii and systematic studies of interatomic distances in halides and chalcogenides. *Acta Crystallographica Section A* **1976,** 32, (5), 751-767.

88. Moon, P. K.; Tuller, H. L., Intrinsic Fast Oxygen Ionic Conductivity in the $Gd_2(Zr_xTi_{1-x})_2O_7$, and Y_2 $(Zr_xTi_{1-x})_2O_7$, Pyrochlore Systems. *MRS Online Proceedings Library* **1988,** 135.

89. Lian, J.; Wang, L. M.; Wang, S. X.; Chen, J.; Boatner, L. A.; Ewing, R. C., Nanoscale Manipulation of Pyrochlore: New Nanocomposite Ionic Conductors. *Physical Review Letters* **2001,** 87, (14), 145901.

90. Williford, R. E.; Weber, W. J.; Devanathan, R.; Gale, J. D., *J. Electroceramics* **1999,** 3-4, 409.

91. Matsuhira, K.; Hinatsu, Y.; Tenya, K.; Sakakibara, T., Low temperature magnetic properties of frustrated pyrochlore ferromagnets $Ho_2Sn_2O_7$ and $Ho_2Ti_2O_7$. *Journal of Physics: Condensed Matter* **2000,** 12, (40), L649.

92. Fennell, T.; Deen, P. P.; Wildes, A. R.; Schmalzl, K.; Prabhakaran, D.; Boothroyd, A. T.; Aldus, R. J.; McMorrow, D. F.; Bramwell, S. T., Magnetic Coulomb Phase in the Spin Ice $Ho_2Ti_2O_7$. *Science* **2009,** 326, (5951), 415-417.

93. Sazonov, A. P.; Gukasov, A.; Mirebeau, I., The spin ice $Ho_2Ti_2O_7$ versus the spin liquid $Tb_2Ti_2O_7$: field-induced magnetic structures. *Journal of Physics: Condensed Matter* **2011,** 23, (16), 164221.

94. Abram, E. J.; Sinclair, D. C.; West, A. R., A Strategy for Analysis and Modelling of Impedance Spectroscopy Data of Electroceramics: Doped Lanthanum Gallate. *Journal of Electroceramics* **2003,** 10, (3), 165-177.

5. *SINGLE-MODE MICROWAVE SYNTHESIS*

5.1. Introduction

In this chapter the preparation of $Ba_{1.2}Mn_8O_{16}$ hollandite rods using only the magnetic component of a microwave in a novel single-mode microwave synthesis set-up is described.

The hollandite family has drawn growing interest in recent years as they are appealing functional materials for potential technological applications such as cathodes for lithium batteries,[1-3] ion sieving sorption [4, 5] and catalysis.[6, 7] The hollandite structure was reported for the first time by Byström and Byström[8] in 1950 for oxides which have a composition of $A_XM_8O_{16}$ (A = Ba, K, Sr, Li, or Bi; M = Mn, V, Ru, Rh, Cr, Ti, or Mo) and a crystal structure which is made up of double chains (zigzag chains) formed by edge-sharing MO_6 octahedra. Such double chains are interconnected through common corners to form an M_8O_{16} framework with tunnels[9] (Figure 5.1). The structure is closely related to the structure of rutile MO_2, except that the single chains in rutile are replaced by double chains.[10, 11]

The hollandite symmetry can be tetragonal *I4/m* (#*87*) or monoclinic *I2/m* (#*12*), β = 90 - 91.5°. [12] The monoclinic symmetry results from a deformation and rotation of the MO_6 octahedra. The deformation can be described as a coupled rotation of the double chains. The square channel is deformed into a slightly smaller, lozenge-shaped one. The dimensional characteristics of the channels are thus controlled by the octahedral deformations which in turn depend on the channel cations.[13, 14]

Hollandites are usually synthesized by the traditional solid state method[1, 10, 15] or alternative routes, for example by the molten salts method,[16] by hydrothermal synthesis[17] and high pressure techniques.[18] There is no previous work of hollandite phases prepared by any microwave-assisted method.

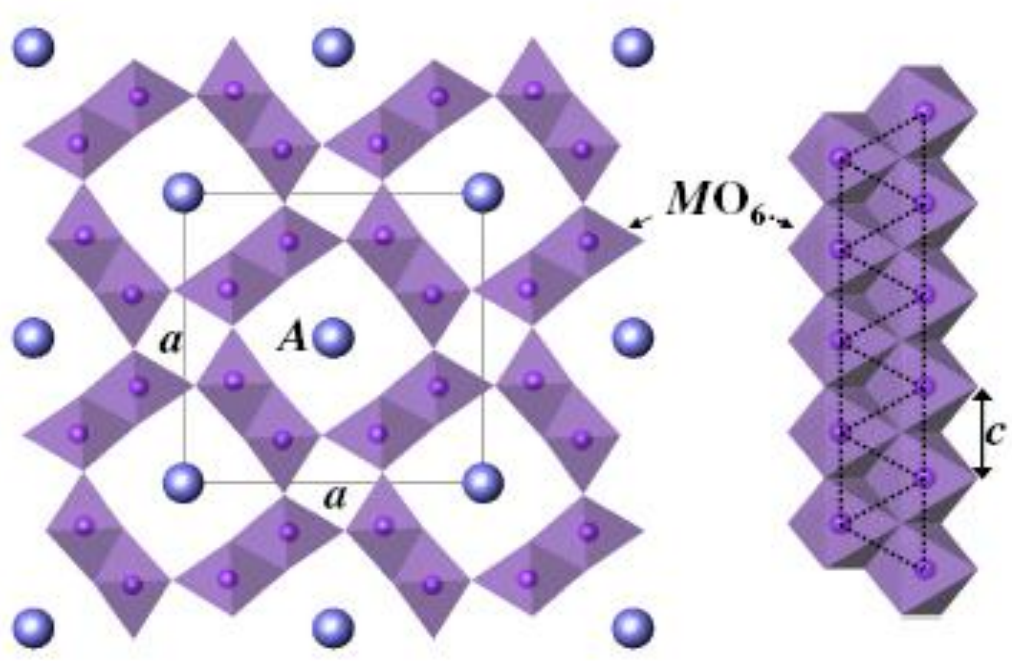

Figure 5.1. Hollandite-type oxide represented by the chemical formula $A_2M_8O_{16}$, (a) the crystal structure in the c-direction and (b) the double (zig-zag) chain made up fo edge-sharing MO_6 octahedra. The M_8O_{16} framework is constructed from double chains and has rectangular tunnels surrounded by four double chains. A-cations occupy sites within each rectangular tunnel.[10]

Transition-metal oxides for thermoelectric devices have been extensively investigated since the discovery of large thermopower in Na_xCoO_2.[19, 20] It has been found that the presence of mixed-valent cations $M^{n+}/M^{(n+1)+}$ with spin values S_n and S_{n+1} plays a crucial role in the large thermopower.[21] Furthermore, thermoelectric oxides containing mixed-valence Mn^{3+}/Mn^{4+} also exhibit interesting physical properties related to the fact that different oxidation states of Mn possess different magnetic moments (Mn^{2+}, Mn^{3+}, Mn^{4+} with S = 5/2, 2, 3/2, respectively). [10, 17, 21, 22] Thus, $Ca_{0.97}La_{0.03}MnO_3$ with the perovskite structure has been used in thermoelectric generators with the highest figure of merit (ZT=

0.3 at 1000 K) for such manganites. It is well known that oxides with empty electronic bands which can be partially filled by doping are the best candidates as n-type legs.[21]

5.2. $Ba_{1.2}Mn_8O_{16}$ hollandite

$Ba_{1.2}Mn_8O_{16}$ hollandite is a naturally occurring mineral, which can also be synthesized in the laboratory by the ceramic route. Table 5.1 shows a summary of the results obtained for the lattice parameters of $Ba_{1.2}Mn_8O_{16}$ synthesized in the laboratory and for the mineral species.

Table 5.1. Literature data summary of $Ba_{1.2}Mn_8O_{16}$ hollandite.

	Synthesis method / Mineral	*a* (Å)	*b* (Å)	*c* (Å)	*β* (º)
Barbato *et al,*[12] 2001	Solid state reaction, decomposition of carbonates and oxides in air	9.979	2.864	9.754	90.59
Ishiwata *et al.,*[15] 2006	Solid state reaction, obtained using KCl mineralizer	10.052	2.8579	9.7627	89.96
Bystrom,[8] 1950	Mineral	10.00	2.879	9.72	91.10
Miura *et al.,*[9] 1986	Mineral	10.006	2.866	9.746	91.17
Nistor *et al.,*[13] 1993	Mineral	10.00	2.87	9.73	91.00

In this chapter the structural and microstructural characterization, and magnetic and charge transport transport properties have been performed for $Ba_{1.2}Mn_8O_{16}$ hollandite rods produced by single mode microwave. Such properties have been compared with the ceramic route material obtained by using Ishiwata *et al.* procedure.[15]

5.2.1. Synthetic aspects

A mixture of $Ba(NO_3)_2$, Mn_2O_3 and KCl used as mineralizer (Sigma-Aldrich) in a molar ratio of 1.2 : 4 : 12 was ground during 15 minutes in an agate mortar and pressed into pellets. KCl is added to the metal precursors as a mineralizer to avoid the formation of the perovskite phase $BaMnO_3$, which in fact more stable than the hollandite phase.

The pellet was placed into a SiC crucible. Different times of synthesis were performed from 5 to 20 minutes in a single-mode microwave apparatus where the radiation was guided along a commercial TE_{10p} microwave cavity. The length of the microwave cavity was tuned to excite the TE_{102} mode and the temperature was measured using a pyrometer focused on the sample surface. The thermal cycle included a ramp of ≈ 300 °C/min and a dwell time of 5 - 20 minutes at 900 °C by adjusting both 3 stub tuners and the incident power. The incident power required to reach ≈ 900 °C is roughly 200 W. After the specific holding time at high temperature (900 °C), the power was switched off and the sample cooled down to room temperature with a cooling ramp of ≈ 300 °C/min The full ramp is displayed in Fig. 5.2 a. The powder obtained was washed in distilled water to dissolve KCl and is dried afterwards in an oven at 80 °C. This route is easier than the conventional procedure described by S. Ishiwata *et al* [12]: They heated the pellet in an alumina crucible up to 850 °C (100 °C/h), the holding time at 850 °C was 72 h, which was followed by another 900 °C treatment for 48 h in air after an intermediate grinding.

The sintering procedure consisted in heating a pellet at 900 °C for 24 h (100 °C/h) in a conventional furnace in air.

The temperature of the sample was measured during microwave synthesis by using an infra-red pyrometer and was automatically recorded through a computer. Figure 5.2a shows the temperature profiles (T/t) used for different $Ba_{1.2}Mn_8O_{16}$ samples synthesized through microwave heating.

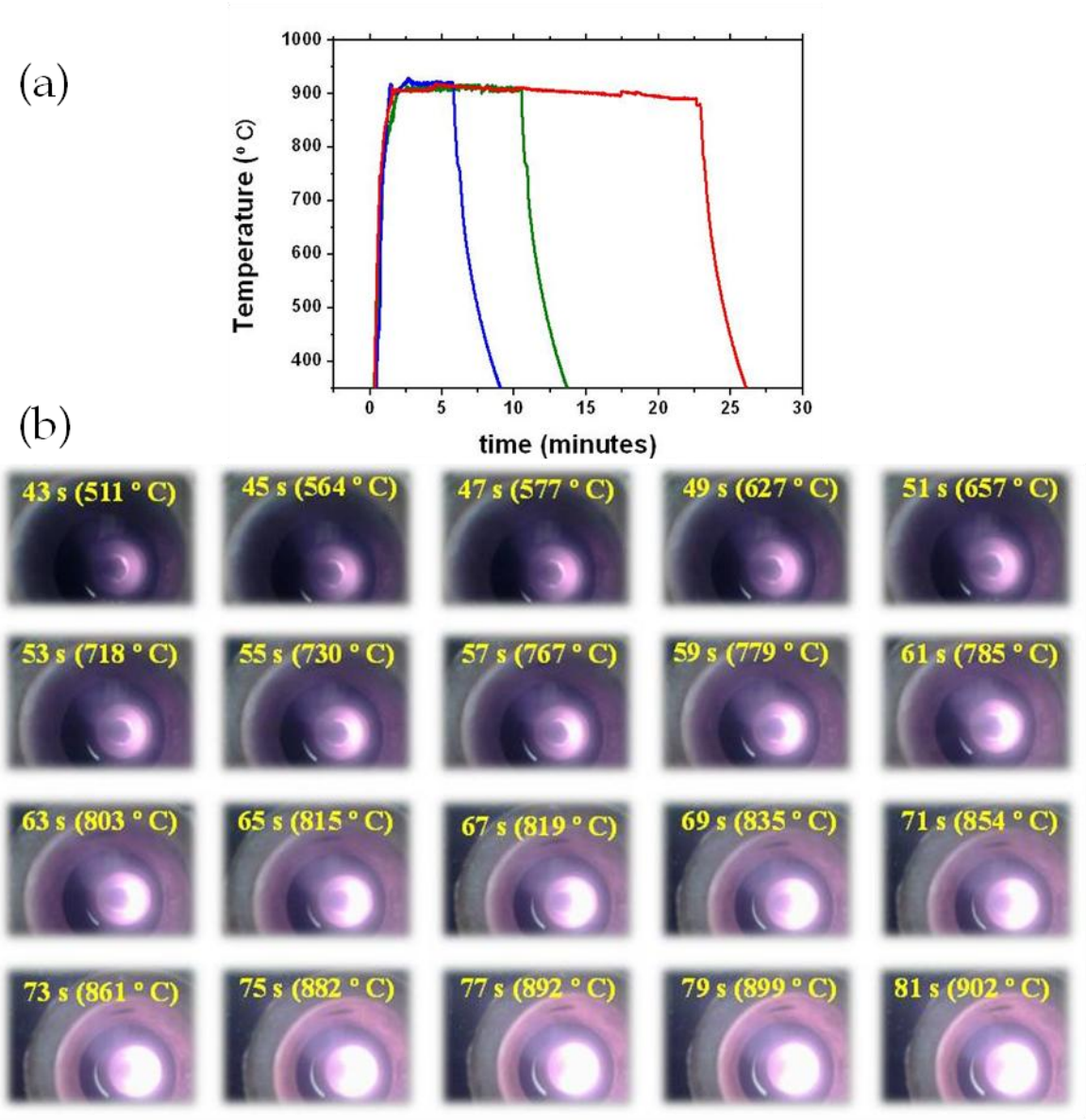

Figure 5.2. a) Temperature control of $Ba_{1.2}Mn_8O_{16}$ microwave experiments: 5 minutes (blue), 10 minutes (green) and 20 minutes (red) microwave irradiation. b) Sequence pictures of the 5 minutes microwave synthesis experiment.

Worth to be noted, the heating starts from the sample surface before propagating in few seconds to the whole sample (see the sequence in Figure 5.2b). This heat propagation mechanism reminds to the auto-propagation front movement that occurs in combustion methods.

5.2.2. Structural characterization.

The addition of KCl as a mineralizer leads to the phase pure hollandite phase, which is demonstrated in the X-ray diffraction patterns (XRD) presented in Figure 5.3

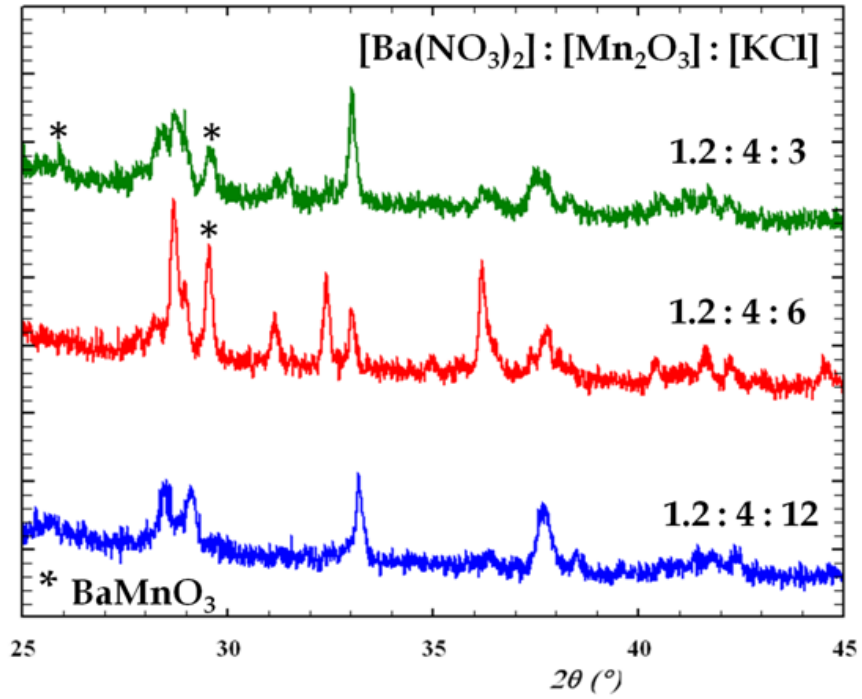

Figure 5.3. XRD pattern of $Ba_{1.2}Mn_8O_{16}$ obtained after 5 minutes microwave irradiation using different concentrations of KCl. The secondary phase $BaMnO_3$ is marked with an asterisk.

At 900 ^{o}C, KCl is molten and works as a flux,[23-25] dissolving the rest of the components and keeping the product free of atmospheric oxygen, which makes the hollandite phase to be preferentially formed. On the other hand it is interesting to recall that microwaves strongly affect the ion movements and therefore it would much improve the capability of the molten salt to act as a solvent.

The phase structure and purity of the material were examined by X-ray diffraction (XRD) for the sample prepared by conventional method and for samples prepared by microwave heating during 5, 10 and 20 minutes of microwave irradiation. All diffraction peaks could be indexed according to the

monoclinic phase $BaMn_8O_{16}$ *I2/m* (#12), Joint Committee on Powder Diffraction Standards (JCPDS) file number 38-0476 (Figure 5.4).[26]

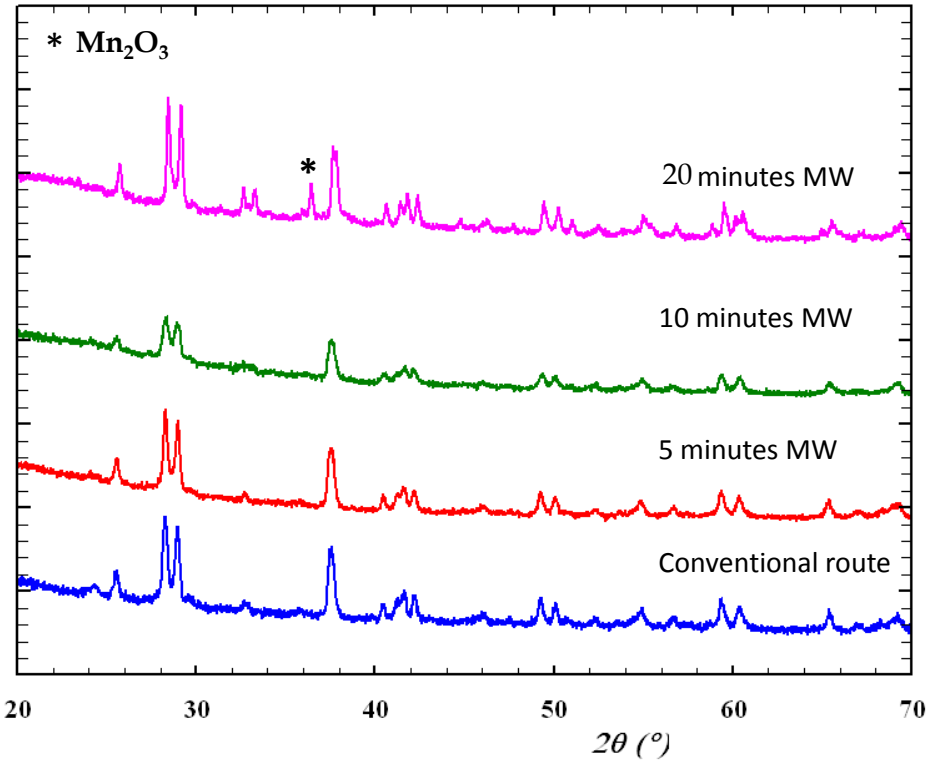

Figure 5.4. X-ray diffraction patterns of $Ba_{1.2}Mn_8O_{16}$ synthesized by single-mode microwave route and by conventional ceramic route.

Rietveld refinements of a 5 minutes microwave-sample and one control sample synthesized by the conventional ceramic route are shown in Figure 5.5. Cell parameters, atomic positions, thermal B factors and agreement factors of all the refined samples are summarized in Table 5.2.

The thermal parameters (U) are high for the Ba *4g* site, possibly due to the diffusion of Ba ions in the hollandite tunnels. It should be noted that large thermal parameter in this position were also reported in the literature for this material [15] and for other hollandites such as $K_2Cr_8O_{16}$ or $K_{2-x}V_8O_{16}$.[18, 27]

An X-ray thermo-diffraction study was performed from room temperature up to 300 °C to detect possible phase transitions in the material. A clear difference between the data collected above and below 140 °C is observed.

This phenomenon occurs in all samples (microwave and ceramic route synthesized) and is completely reversible as evidenced by the XRD data obtained at room temperature after the high-temperature treatment (blue curve at the top of Figure 5.6).

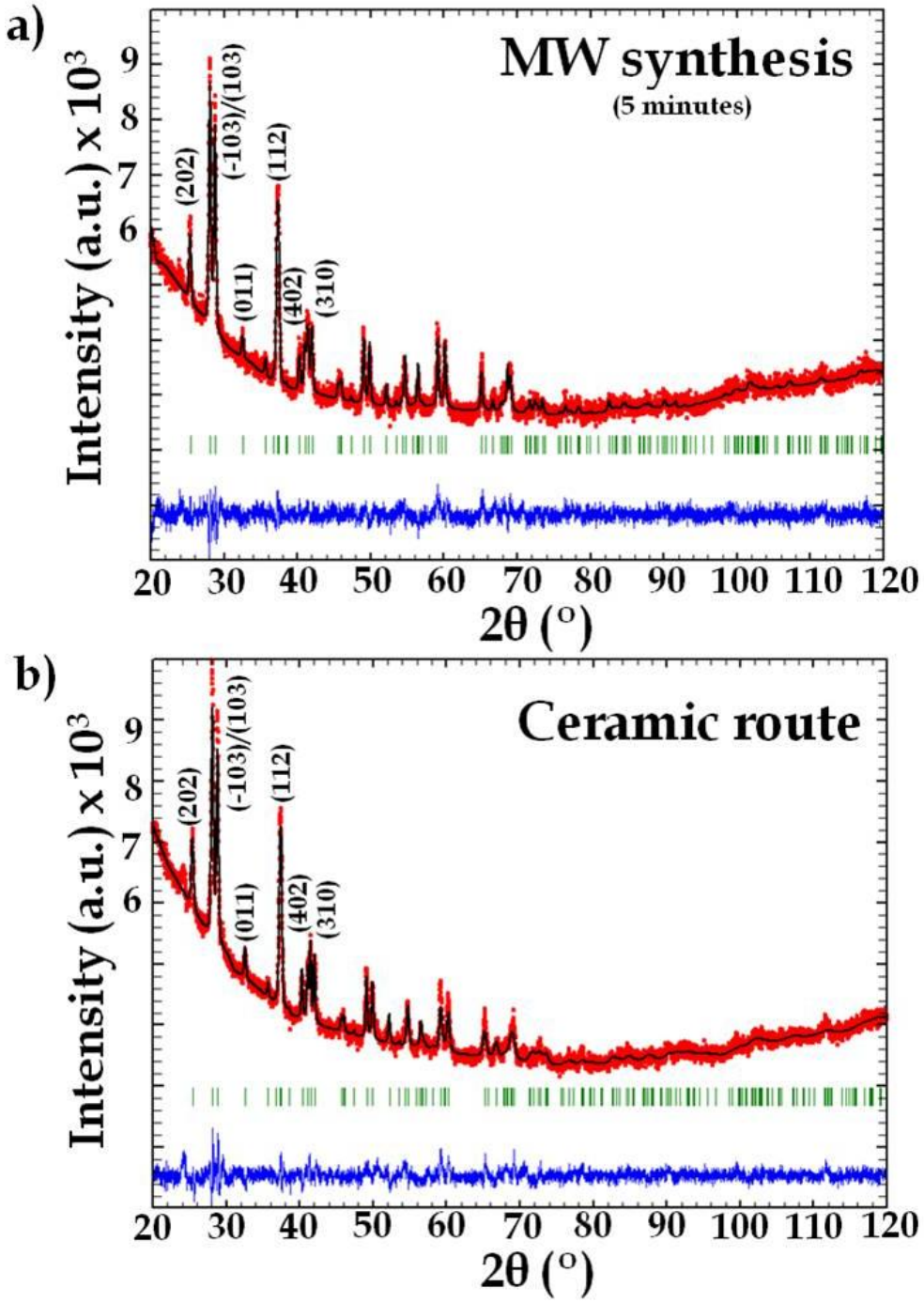

Figure 5.5. Rietveld refinement of powder X-ray diffraction patterns $Ba_{1.2}Mn_8O_{16}$ from (a) 5 minutes microwave irradiation and (b) the conventional ceramic route: observed (red dotted lines), refined (black solid lines), and their difference (blue bottom line). Green vertical bars indicate the X-ray reflection positions.

Table 5.2. Cell parameters and atomic positions of $Ba_{1.2}Mn_8O_{16}$ obtained by Rietveld refinement.

	5 minutes synthesis	10 minutes synthesis	20 minutes synthesis	Ceramic route
***a* (Å)**	10.0576(3)	10.0454(6)	10.0567(7)	10.0523(8)
***b* (Å)**	2.86094(9)	2.8580(2)	2.8584(3)	2.8578(3)
***c* (Å)**	9.7659(3)	9.7697(6)	9.7700(7)	9.7565(7)
***β*(º)**	90.020(4)	89.960(7)	89.986(6)	90.013(8)
Ba position 4g				
y	0.379(3)	0.414(4)	0.420(5)	0.401(3)
U*100 (Å^2)	2.9(1)	2.7(2)	2.8(3)	1.19(6)
Mn(1) position 4i				
x	0.1634(8)	0.165(1)	0.164(1)	0.160(1)
z	0.3536(7)	0.351(1)	0.354(1)	0.3512(9)
U*100 (Å^2)	0.418(2)	0.47(3)	0.49(1)	0.35(2)
Mn(2) position 4i				
x	0.3500(9)	0.351(1)	0.351(1)	0.346(1)
z	0.8317(8)	0.838(1)	0.834(1)	0.836(1)
U*100 (Å^2)	0.403(2)	0.425(3)	0.403(4)	0.33(3)
O(1) position 4i				
x	0.191(1)	0.175(3)	0.191(2)	0.198(2)
z	0.151(2)	0.169(3)	0.161(3)	0.145(2)
U*100 (Å^2)	0.2	0.2	0.2	0.2
O(2) position 4i				
x	0.163(2)	0.158(3)	0.159(3)	0.164(3)
z	0.807(1)	0.814(2)	0.796(2)	0.794(2)
U*100 (Å^2)	0.2	0.2	0.2	0.2
O(3) position 4i				
x	0.166(2)	0.1821(2)	0.197(2)	0.158(2)
z	0.525(1)	0.544(3)	0.552(3)	0.522(2)
U*100 (Å^2)	0.2	0.2	0.2	0.2
O(4) position 4i				
x	0.548(2)	0.541(2)	0.543(3)	0.546(2)
y	0.802(1)	0.800(2)	0.796(2)	0.805(2)
U*100 (Å^2)	0.2	0.2	0.2	0.2
χ^2	1.78	1.49	1.77	1.54
R_{wp}/R_{exp} (%/%)	2.1 / 1.57	1.85 / 1.52	2.00 / 1.50	2.21 / 1.78
R_{Bragg}	6.35	7.46	5.58	5.43
S.G. *I 2/m*: 4g (0 y 0), 4i (x 0 z)				

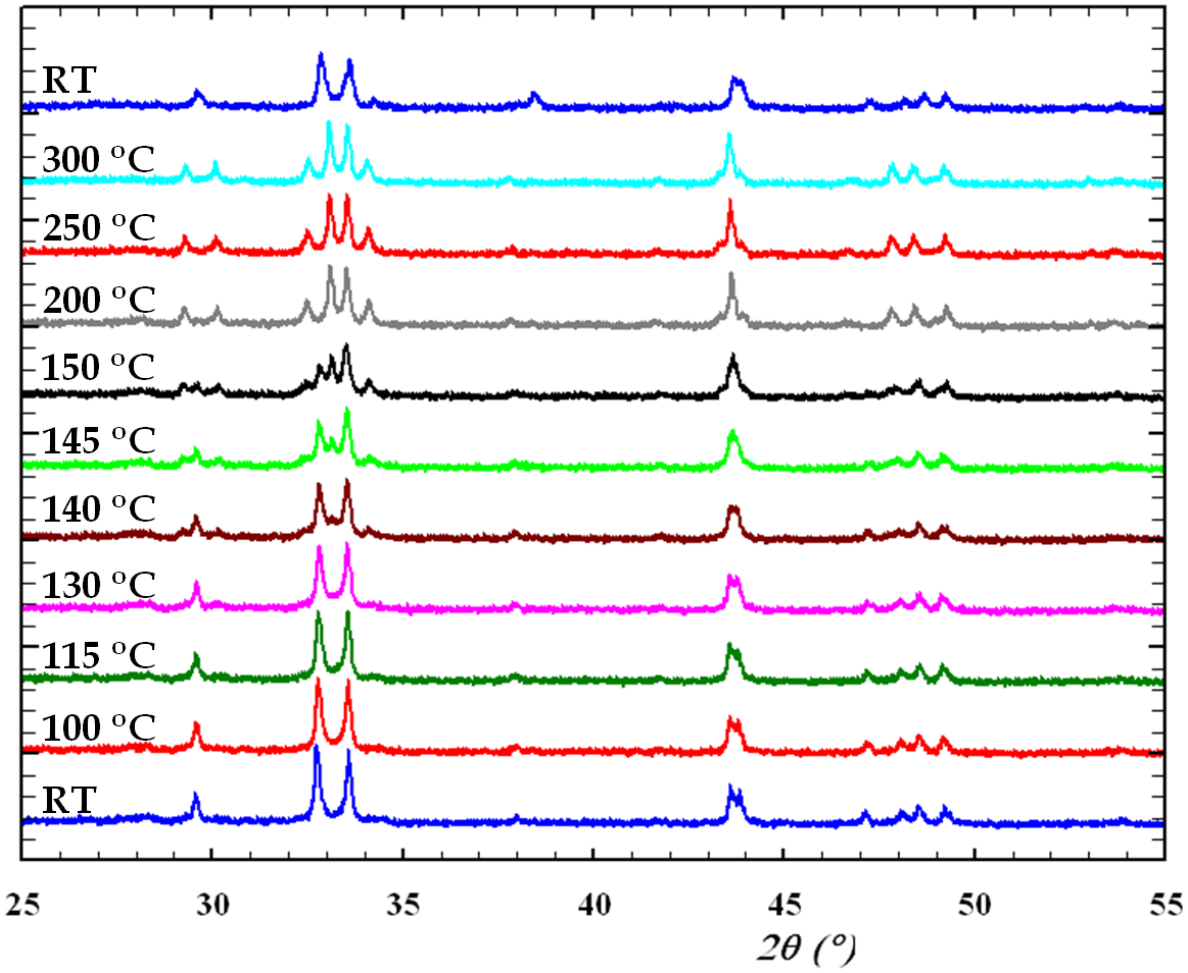

Figure 5.6. X-ray thermodiffraction patterns of 5 minutes single-mode microwave synthesized $Ba_{1.2}Mn_8O_{16}$.

Figure 5.7 shows the Rietveld refinements at room temperature and at 300 °C of the 5 minutes single-mode microwave sample. The same symmetry *I2/m* (#12) was used for both refinements.

Figure 5.8 evidences the existence of a transition to a different monoclinic structure occurring at ≈ 140 °C. At this temperature, there is a discontinuity in all lattice parameters, indicating a reversible first-order monoclinic-monoclinic transition. This unusual behaviour is similar as described by T. Kuwabara *et al*. for the $K_xMn_8O_{16}$ hollandite phase.[10]

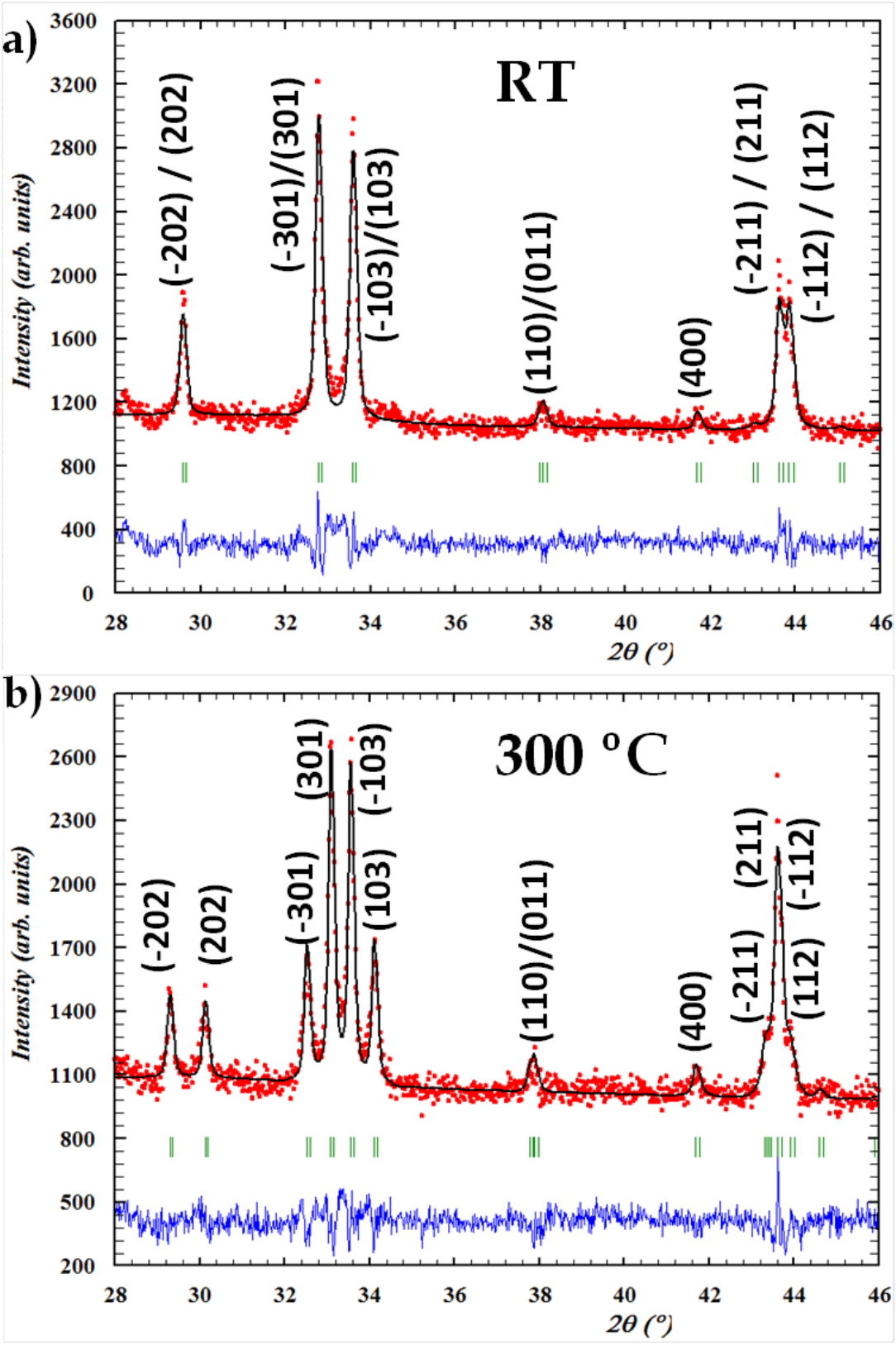

Figure 5.7. Rietveld refinement of powder X-ray diffraction patterns of 5 minutes single-mode microwave irradiation $Ba_{1.2}Mn_8O_{16}$ sample: a) at room temperature (RT) and b) at 300 °C.

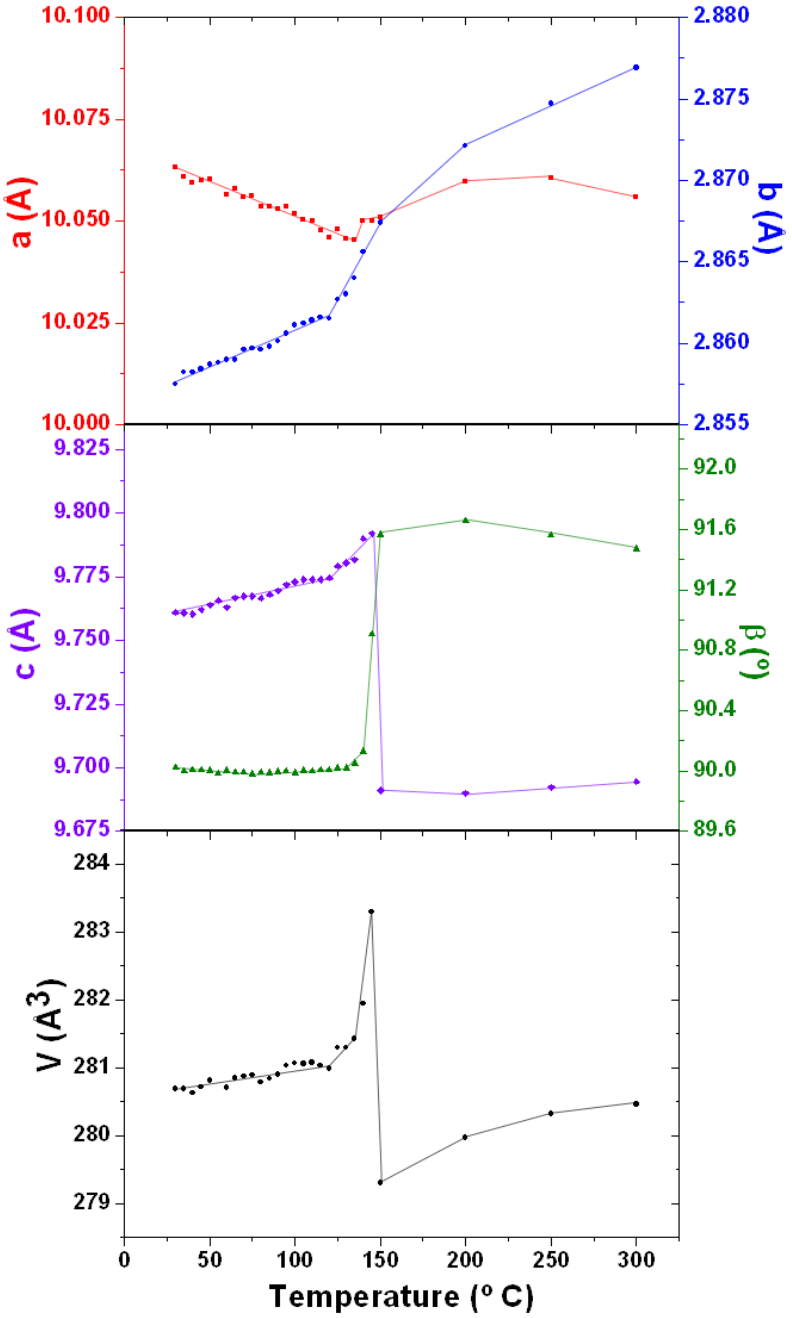

Figure 5.8. Temperature dependence of lattice parameters and unit cell volume. All the values were obtained from Rietveld refinement data. Solid lines are guide to the eyes.

Table 5.3. summarizes Mn-O distances and Mn-O-Mn bond angles for the microwave sample (structure in Figure 5.9) both at room temperature and 300 °C. It is clear that in both cases the MnO_6 octahedra are distorted. The differences between the structure at room temperature and at 300 °C, may be

related to the Mn2 bond angles, which in turn could be related to the existence of different kinds of oxidation states for Mn ions in the double chains.

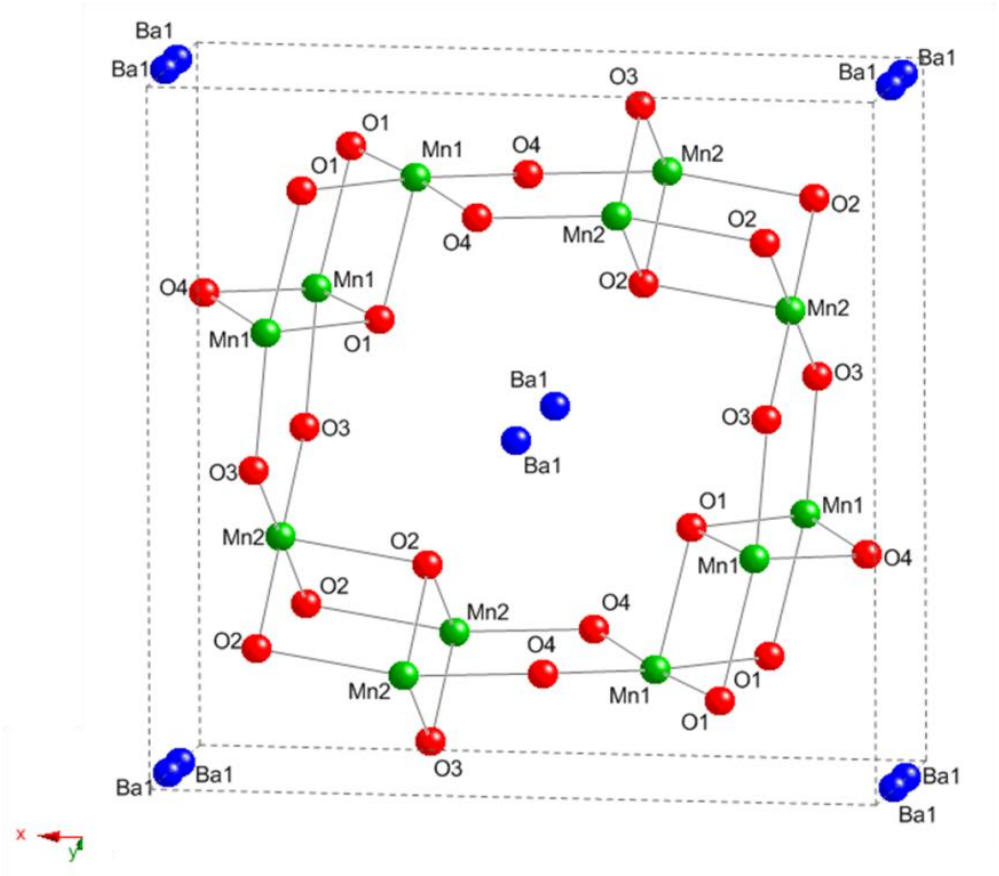

Figure 5.9. Crystal structure of $Ba_xMn_8O_{16}$

Table 5.3. Selected Mn-O-Mn bond angles and Mn-O bond lengths for 5 minutes single-mode MW $Ba_{1.2}Mn_8O_{16}$ sample at room temperature (RT) and 300 ºC, and the differences between both values.

Bond angle (º)				**Bond length (Å)**			
	RT	**300 ºC**	**Δ**		**RT**	**300 ºC**	**Δ**
Mn1-O1-Mn1	98.88	97.05	1.83	Mn1-O1	2.02	1.89	0.13
Mn1-O1'-Mn1	82.73	82.95	-0.22	Mn1-O1'	2.05	2.04	0.01
Mn1-O4-Mn1	99.01	99.15	-0.14	Mn1-O3	1.69	1.93	-0.24
Mn2-O2-Mn2	99.09	98.75	0.34	Mn1-O4	1.88	1.89	-0.01
Mn2-O2'-Mn2	80.34	84.67	-4.33	Mn2-O2	1.88	1.89	-0.01
Mn2-O3-Mn2	91.43	99.69	-8.26	Mn2-O2'	1.91	2.06	-0.15
Mn1-O3-Mn2	134.16	129.93	4.23	Mn2-O3	1.99	1.88	0.11
Mn1-O4-Mn2	124.48	129.19	-4.71	Mn2-O4	2.03	1.93	0.1

5.2.3. Microstructural characterization.

SEM

Figure 5.10 shows SEM images in backscattered electron (BSE) modes collected on $Ba_{1.2}Mn_8O_{16}$ powders. A rod morphology is obvious with a width of the particles on the submicron scale. EDS analysis was performed in different areas of some rods and the atomic composition resulted in good agreement with the nominal composition of $Ba_{1.2}Mn_8O_x$.

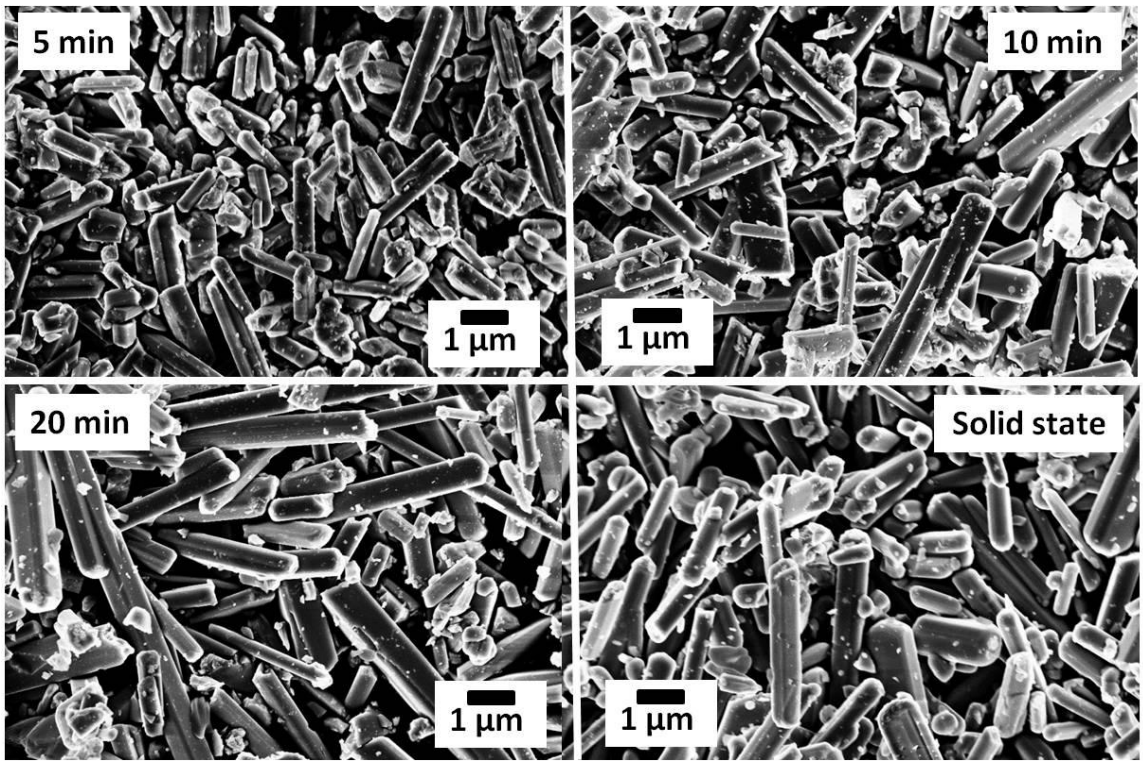

Figure 5.10. SEM micrograph of $Ba_{1.2}Mn_8O_{16}$ rods obtained by: a) 5 minutes , b) 10 minutes, c) 20 minutes microwave synthesis and d) ceramic route.

Average grain sizes were determined by averaging the size of some randomly selected grains. This analysis yielded a moderate grain growth with increasing microwave irradiation time. Figure 5.11 illustrates this behaviour: (a) width and (b) length increase of the particles when increasing microwave irradiation time. The average grain size trend is approximately linear (Figure 5.11c).

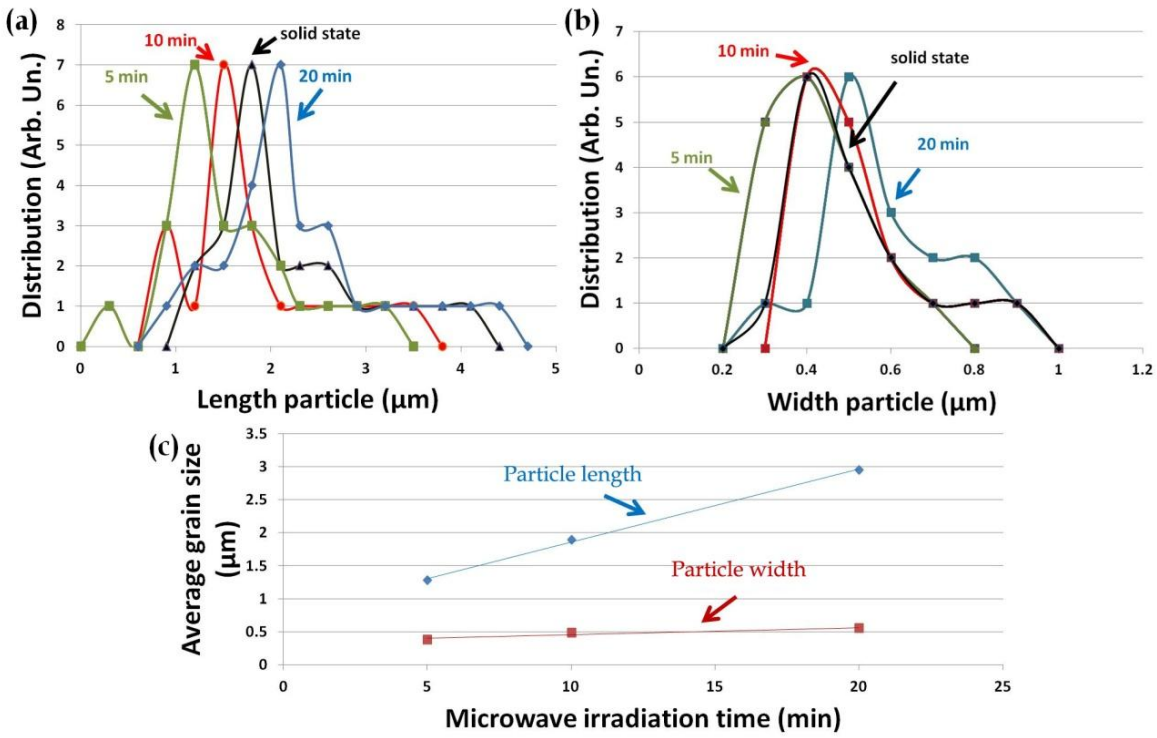

Figure 5.11. Grain size distribution for $Ba_{1.2}Mn_8O_{16}$ powder obtained at different microwave irradiation times. a) Width particle distribution, b) Length particle distribution, c) Average grain size vs microwave irradiation time.

SAED

Electron diffraction patterns along the [001] zone axe are shown in Figure 5.12 for the 5 minutes microwave - sample a) at Room Temperature and b) at 573 K. The reciprocal lattice presented is consistent with the monoclinic body-centered lattice found by XRD.

Diffuse lines are present perpendicular to the ***a**** direction, which correspond to an interatomic separation of 2 *b*. These lines are more evident at high temperature than at room temperature, indicating diffuse scattering, directly related to the state of order of the different sublattices,[13, 16] and probably due to the disorder configuration of the Ba ions along the channels.

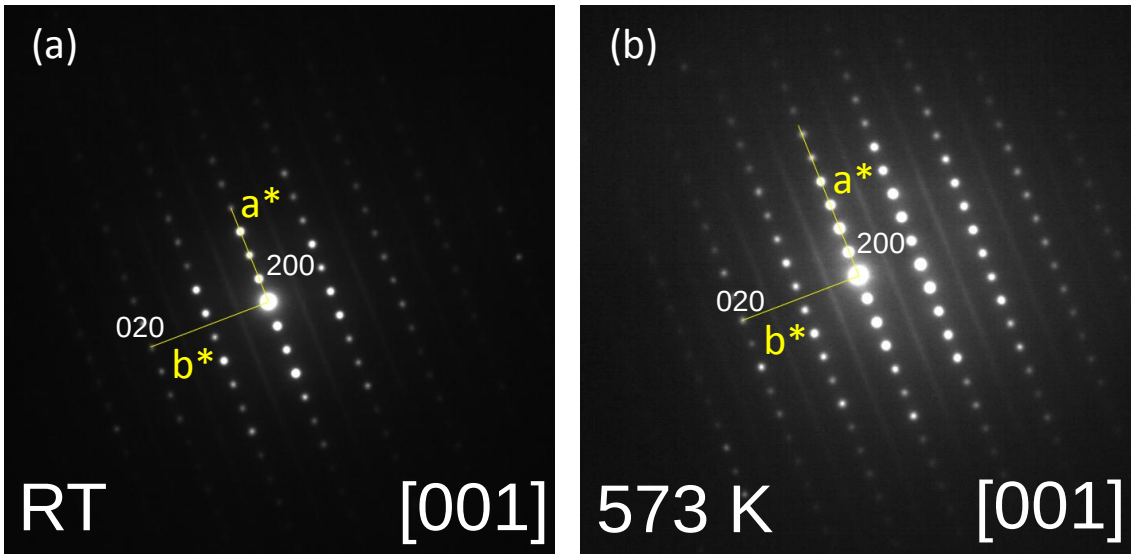

Figure 5.12. SAED micrographs of the [001] zone axis taken at different temperatures for a 5 minutes single-mode microwave sample: a) room temperature, b) 573 K.

5.2.4. Magnetic properties

Figure 5.13 shows the temperature dependence of the magnetic susceptibility curves for the $Ba_{1.2}Mn_8O_{16}$ powder obtained by 5 minutes microwave synthesis and the control sample from the conventional ceramic route, in zero-field-cooled (ZFC) and field-cooled (FC) modes with an applied field of 1 kOe. The sharp change in the ZFC and FC magnetizations observed in both samples a) microwave: T ≈ 42 K and b) solid state: T ≈ 45 K, can be attributed to the canted antiferromagnetic state in $Ba_{1.2}Mn_8O_{16}$ reported for bulk ($T_N \approx 40$ K).[15]

The susceptibility values for the microwave sample are much higher than those for the conventional sample as is shown in Figure 5.13. However, the susceptibility signal for the microwave sample observed here is quite similar to the susceptibility reported by Yu *et al.*[28] for a molten-salt method synthesized sample. Yu *et al.*[28] found that the coexistence of a weak ferromagnetic phase may be responsible for the high magnetic susceptibility. Nevertheless, it seems possible that small amounts of Mn_3O_4 secondary phase in the 5 minutes microwave sample, not detected by X-ray diffraction, could be responsible for these magnetic differences, taking into account that bulk Mn_3O_4 present a

ferromagnetic transition at 42 K that is similar to the temperature transition in $Ba_{1.2}Mn_8O_{16}$. The upper inset in Figure 5.13 shows the temperature dependence of the inverse of susceptibility ($1/\chi$) of the conventionally synthesized sample. The $1/\chi$ versus T curve in the paramagnetic state follows the Curie-Weiss law: $\chi = C/(T-\theta)$. Linear fitting was carried out, which is indicated by a solid line in the Figure inset. The fitting procedure yielded the following values: C = 19.33 emu K/mol and θ = - 461K. The estimated effective moment per Mn mol is 4.3 μ_B, close to the expected 4.2 μ_B, taking into account the high spin state for Mn^{3+} and Mn^{4+} with an average valence state of +3.7.

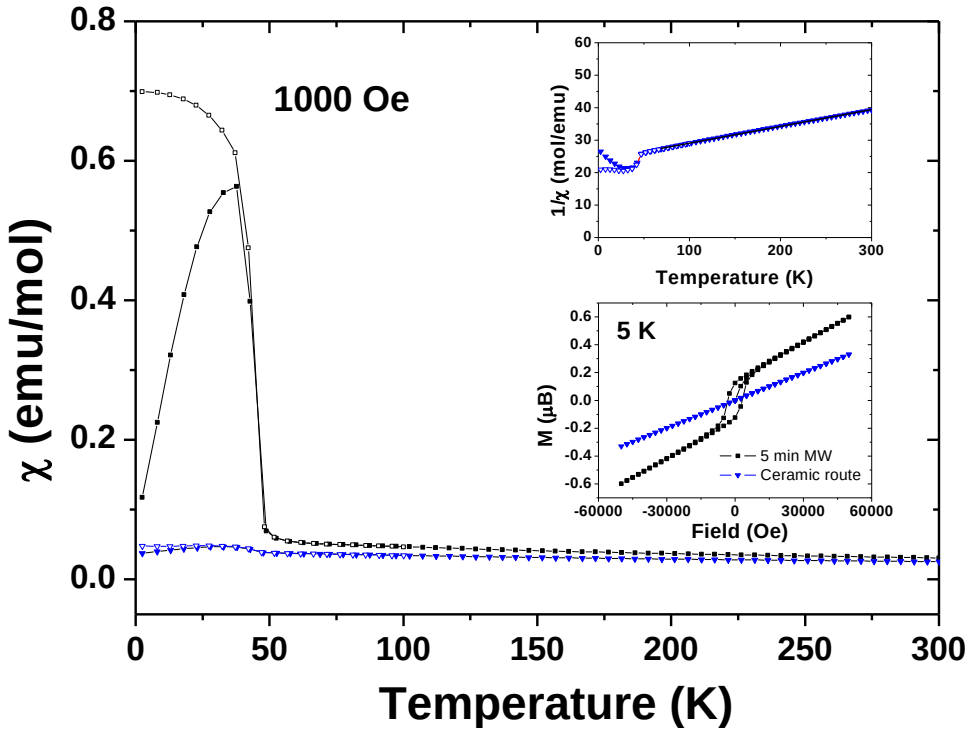

Figure 5.13. Temperature dependence of the magnetic susceptibilities of $Ba_{1.2}Mn_8O_{16}$ a) 5 minutes microwave (blue) and b) ceramic synthesis (black), at 1000 Oe. ZFC and FC curves are indicated by solid markers and hollow markers respectively. Upper-Inset: Inverse susceptibility $1/\chi$ for a sample prepared by the ceramic route. The black solid line represents the fit of the data to the Curie-Weiss law. Bottom-inset: Magnetization vs applied magnetic field hysteresis loop of samples at 5 K for both commented samples.

Strong antiferromagnetic interactions are indicated by the large negative Weiss constant. Furthermore, the canted antiferromagnetic transition temperature at $T_N \approx 40$ - 45 K is much lower than the absolute value of the Weiss temperature (461 K). The rather low T_N compared to the Weiss

temperature could be attributed to the geometrical frustration of the hollandite (see structure in Fig. 5.1), since the Mn–Mn network forms a triangular lattice (zigzag chains in the hollandite structure)[10] that, supposing all interactions are antiferromagnetic, should suppress the ordering.[15]

The bottom inset shows the hysteresis loops of both samples. In the microwave sample there is a small ferromagnetic component that is less evident in the sample prepared by the conventional route.

5.2.5. Charge transport properties

For the manganese cations a Mn^{4+}/Mn^{3+} mixed-valance is expected, giving rise to high electrical conductivity. The temperature dependence of the electrical dc resistivity of the hollandite sintered pellets is shown in Fig. 5.14. The electrical resistivity decreases when increasing temperature in all samples. At room temperature, the resistivity value is roughly 3 $\Omega \cdot$ cm, and corresponds to a semiconductor-type behaviour. However, it is evident (see logarithmic plot of resistivity vs the inverse of temperature in Figure 5.14) that there is a transition temperature at ≈ 400 K, consistent with the first-order structural temperature transition mention before, which was ascribed previously to a one-dimensional variable range hopping (VRH) conduction mechanism.[15, 29] Ishiwata *et al*.[15] have attributed the one-dimensional electronic character to a short - ranged incommensurate ordering of Ba ions since such incommensurate structures are often found in hollandite oxides.[30] Above the transition temperature, the sample no longer obeys the VRH law, but shows good linearity on Arrhenius axes. This could be attributed to a breach of the short ranged incommensurate ordering of Ba ions along the tunnels of $Ba_{1.2}Mn_8O_{16}$.

The activation energy (E_a) of each sample above the observed transition temperature is obtained from the Arrhenius plot. Activation energy values in meV are presented in Table 5.4.

Table 5.4. Activation energy (E_a) of the differently prepared samples from the linear fits of the data in Figure 5.14., above the structural and charge transport transition temperature (linear Arrhenius regime).

	Activation energy (Ea)
5 minutes MW	143 meV
10 minutes MW	158 meV
20 minutes MW	150 meV
Ceramic route	155 meV

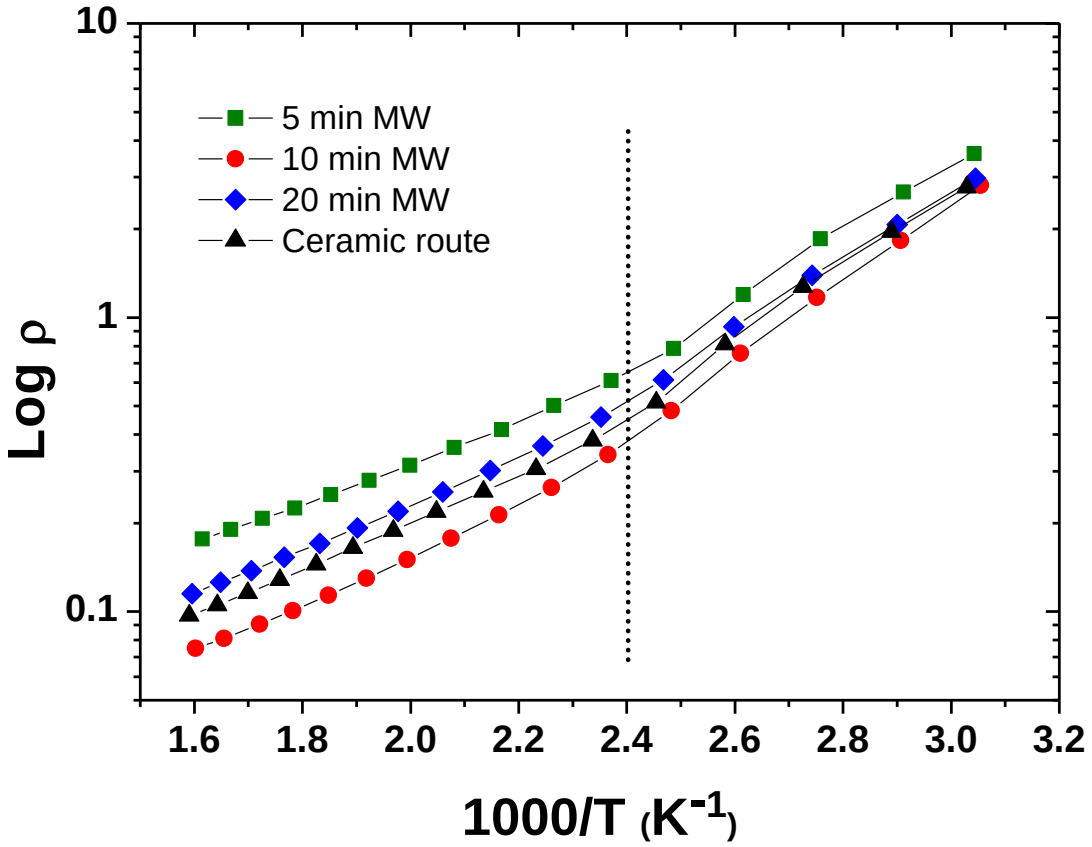

Figure 5.14. Resistivity (Ω·cm) Vs 1/Temperature (K^{-1}) behaviour of the different samples.

The temperature dependence of the Seebeck coefficients for each sample are presented in Figure 5.15. All Seebeck coefficients are negative, indicative of p-type hole conduction.

The Seebeck value is ≈ -90 μV/K at 650 K and the temperature dependence is almost flat down to 400 K. The curve drops sharply below 400 K, showing a minimum at ≈ -160 μV/K at 225 K.

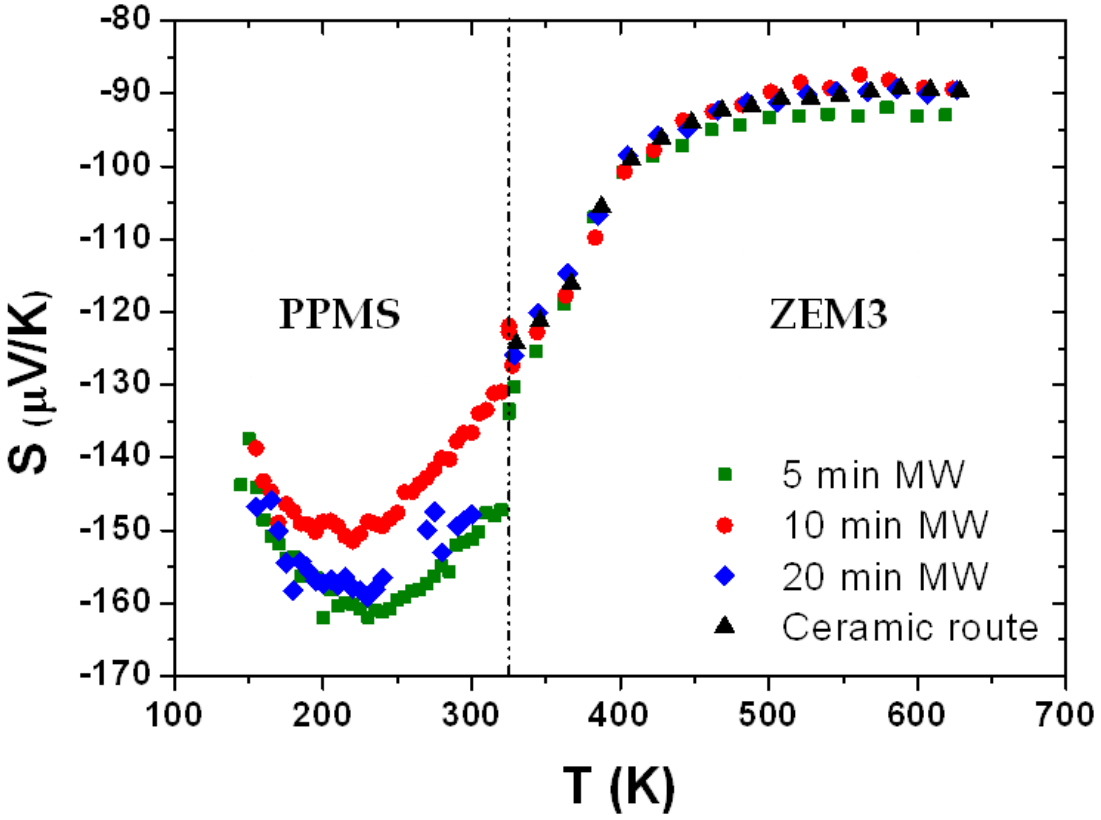

Figure 5.15. Temperature dependence of Seebeck coefficient S for different $Ba_{1.2}Mn_8O_{16}$ samples.

Considering the flat temperature dependence of Seebeck coefficient at the higher temperature range, the extended Heikes formula (equation 5.1) can be used.[31]

$$S(T) = -\frac{K_B}{e}\ln\left[\frac{g_A}{g_B}\cdot\frac{p}{1-p}\right] \qquad [5.1]$$

Where g_A *and* g_B are the degeneracy of the electron configuration on the A and B ions, and p the concentration of the B ion.

According to equation 5.1, it is possible to calculate a theoretical value S for Mn^{3+} : Mn^{4+} = 3:7 (p = 0.7). The Mn^{3+} and Mn^{4+} ions are in the high-spin state, where Mn^{3+} has an electron configuration of $(t_{2g})^3(e_g)^1$ (Figure 5.16). In this model, the Jahn-Teller distortion of the high spin state is important, because it causes a split of the e_g orbital and changes the electronic degeneracy g (Mn^{3+}) from 10 to 5 (see Table 5.5). Since the spin degeneracy g of the Mn^{4+} ions in the $(t_{2g})^3$ levels has no orbital degeneracy, g (Mn^{4+}) is equal to 4 owing to the spin S = 3/2.[32]

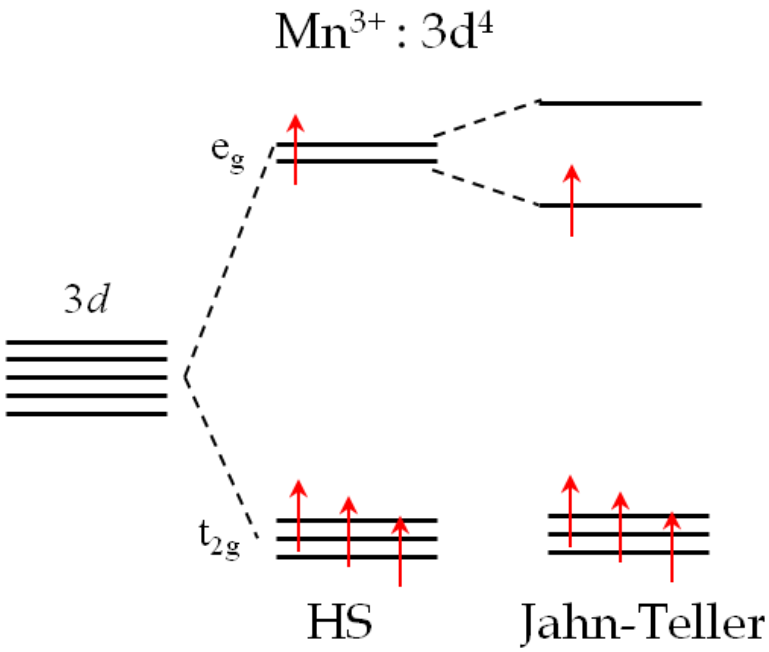

Figure 5.16. Electron energy levels of the high spin Mn^{3+} with $3d^4$ electron configuration, taking into account the Jahn-Teller distortion.

Table 5.5. Electronic (g), spin (g_{spin}) and orbital ($g_{orbital}$) degeneracy for high spin Mn^{n+} (n = 2 ,3, 4) cations in tetrahedral (T) octahedral (O) and Jahn – Teller distorted octahedral (DO) crystal fields (CF).[32]

Cation	d^n	CF	g_{spin}	$g_{orbital}$	g
Mn^{2+}	d^5	T	6	1	6
		O	6	3	18
Mn^{3+}	d^4	T	5	3	15
		O	5	2	10
		DO	5	1	5
Mn^{4+}	d^3	T	4	3	12
		O	4	1	4

Spin degeneracy g can be calculated with the commonly used formula $g_{spin} = 2S + 1$. The total orbital degeneracies for each orbital type is calculated from eq. 5.2:

$$g_{orbital} = \prod [(n_{orbital})!/(n_{orbital} - n_e)!\, n_e!] \qquad [5.2]$$

where $n_{orbital}$ is the number of orbitals of one type and ne denotes the number of unpaired electrons in this specific orbital type.[32]

The theoretical Seebeck coefficient values can be evaluated for structures without Jahn-Teller distortions and with Jahn-Teller distortions, using eq. 5.1.

$$S(T) = -\frac{K_B}{e}\ln\left[\frac{g_{Mn^{3+}}}{g_{Mn^{4+}}}\cdot\frac{0.7}{0.3}\right]$$

No Jahn-Teller distortion: $S(T) = -\frac{K_B}{e}\ln\left[\frac{10}{4}\cdot\frac{0.7}{0.3}\right] = -170\ \mu V/K$

Jahn-Teller distortion: $S(T) = -\frac{K_B}{e}\ln\left[\frac{5}{4}\cdot\frac{0.7}{0.3}\right] = -90\ \mu V/K$

The experimental Seebeck value of ≈ -90 μV/K from 650 to 400 K can account for the Jahn-Teller distortion of Mn^{3+}, indicating that the e_g orbitals are split at this temperature range. However, at lower temperatures this distortion is not significant, because the number of carriers is no longer constant, and decreases due to electron localization below 400 K. This electron localization may relate to the charge and/or orbital ordering of Mn^{3+} and Mn^{4+} ions.

Thermal conductivity and specific heat of the 5 minutes microwave sample are shown in Figure 5.17. In this case, a peak at the transition temperature in the thermal conductivity (λ) and in the specific heat (Cp) are observed.

The value of the thermal conductivity (λ) reaches a maximum of 1.3 W/m·K at 400 K. Specific heat ranges from ≈ 450 J/mol·K in the flat zone to 760 J/mol·K at the maximum at the transition temperature.

Therefore, it seems clear that close relationship between the transport properties and the first order structural transition observed by X-ray diffraction exists.

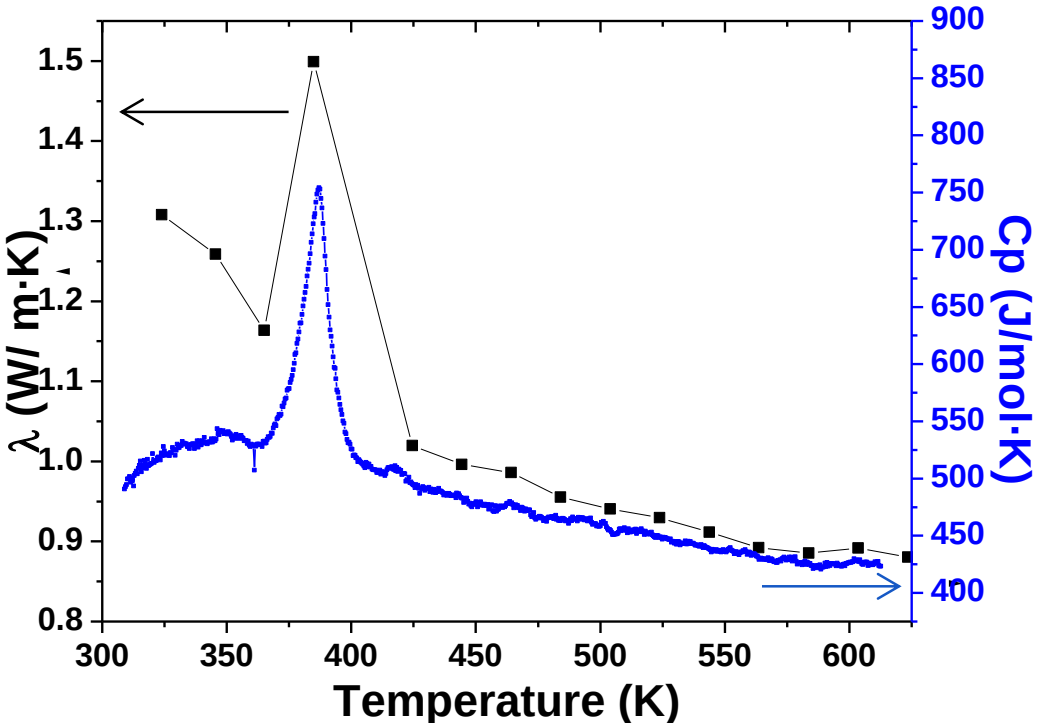

Figure 5.17. Temperature dependence of thermal conductivity λ and specific heat (Cp) of the 5 minutes single-mode microwave sample.

5.3. Conclusions

Pollycrystalline $Ba_{1.2}Mn_8O_{16}$ hollandite rods have been synthesized through the new, time and energy efficient single-mode microwave route. This is the first time that microwave synthesis has been employed for preparing a hollandite phase. For the single-mode microwave synthesis, the use of KCl as a flux is crucial and helps the hollandite phase to form.

Structure, magnetism and transport properties have been studied. All of the diffraction peaks can be indexed to the monoclinic phase $BaMn_8O_{16}$ *I2/m*. X-ray thermodiffraction shows a reversible first order monoclinic – monoclinic transition at ≈ 400 K. Magnetic susceptibility measurements indicate a canted antiferromagnetic state below 42 K. In the microwave sample there is a small ferromagnetic component which is less evident in the ceramic route sample.

The $Ba_{1.2}Mn_8O_{16}$ hollandite exhibits a semiconducting behaviour, consistent with one-dimensional variable range hopping up to ≈ 400 K. Above

this temperature, samples undergo a structural transition and the carriers follow a linear Arrhenius law. The Seebeck coefficient is negative and has a plateau above the transition temperature.

5.4. References

1. Barbato, S.; Gautier, J. L., Hollandite cathodes for lithium ion batteries. 2. Thermodynamic and kinetics studies of lithium insertion into $BaMMn_7O_{16}$ (M=Mg, Mn, Fe, Ni). *Electrochimica Acta* **2001,** 46, (18), 2767-2776.

2. Zhu, S.; Marschilok, A. C.; Lee, C.-Y.; Takeuchi, E. S.; Takeuchi, K. J., Synthesis and Electrochemistry of Silver Hollandite. *Electrochemical and Solid-State Letters* **2010,** 13, (8), A98-A100.

3. Noailles, L. D.; Johnson, C. S.; Vaughey, J. T.; Thackeray, M. M., Lithium insertion into hollandite-type TiO_2. *Journal of Power Sources* **1999,** 81-82, 259-263.

4. Feng, Q.; Kanoh, H.; Miyai, Y.; Ooi, K., Alkali Metal Ions Insertion/Extraction Reactions with Hollandite-Type Manganese Oxide in the Aqueous Phase. *Chemistry of Materials* **1995,** 7, (1), 148-153.

5. Wang, Z. M.; Tezuka, S.; Kanoh, H., Characterization of the Structural and Surface Properties of a Synthesized Hydrous Hollandite by Gaseous Molecular Adsorption. *Chemistry of Materials* **2001,** 13, (2), 530-537.

6. Zhou, H.; Wang, J. Y.; Chen, X.; O'Young, C.-L.; Suib, S. L., Studies of oxidative dehydrogenation of ethanol over manganese oxide octahedral molecular sieve catalysts. *Microporous and Mesoporous Materials* **1998,** 21, (4-6), 315-324.

7. Chen, J.; Tang, X.; Liu, J.; Zhan, E.; Li, J.; Huang, X.; Shen, W., Synthesis and Characterization of Ag Hollandite Nanofibers and Its Catalytic Application in Ethanol Oxidation. *Chemistry of Materials* **2007,** 19, (17), 4292-4299.

8. Bystrom, A.; Bystrom, A. M., The crystal structure of hollandite, the related manganese oxide minerals, and α-MnO_2. *Acta Crystallographica* **1950,** 3, (2), 146-154.

9. Miura, H., The crystal structure of hollandite. *Mineralogical Journal* **1986,** 13, (3), 119-129.

10. Kuwabara, T.; Isobe, M.; Gotou, H.; Yagi, T.; Nishio-Hamane, D.; Ueda, Y., Synthesis, Structure, and Electromagnetic Properties of Manganese Hollandite, $K_xMn_8O_{16}$. *Journal of the Physical Society of Japan* **2012,** 81, 104701

11. Ching, S.; Driscoll, P. F.; Kieltyka, K. S.; Marvel, M. R.; Suib, S. L., Synthesis of a new hollandite-type manganese oxide with framework and interstitial Cr(III). *Chemical Communications* **2001**, (23), 2486-2487.

12. Barbato, S.; Restovic, A.; Gautier, J. L., Hollandite cathodes for lithium ion batteries: 1. Synthesis and characterization of the $MM'Mn_7O_{16}$ compounds (M= K, Ba; M' = Mg, Mn, Fe, Ni). *Boletín de la Sociedad Chilena de Química* **2001,** 46, 165-173.

13. Nistor, L. C.; Van Tendeloo, G.; Amelinckx, S., Defects and Phase Transition in Monoclinic Natural Hollandite: $Ba_xMn_8O_{16}$. *Journal of Solid State Chemistry* **1994,** 109, (1), 152-165.

14. Bursill, L. A., Structural relationships between b-Gallia, rutile, hollandite, pslomelane, ramsdellite and gallium titanate type structures. *Acta Crystallogr.* **1979,** B35, 530-538.

15. Ishiwata, S.; Bos, J. W. G.; Huang, Q.; Cava, R. J., Structure and magnetic properties of hollandite $Ba_{1.2}Mn_8O_{16}$. *Journal of Physics: Condensed Matter* **2006,** 18, (15), 3745.

16. Lan, C.; Gong, J.; Liu, S.; Yang, S., Synthesis and magnetic properties of single-crystalline $Na_{2-x}Mn_8O_{16}$ nanorods. *Nano Express* **2011,** 6, 133.

17. Sato, H.; Enoki, T.; Yamaura, J.-I.; Yamamoto, N., Charge localization and successive magnetic phase transitions of mixed-valence manganese oxides $K_{1.5}(H_3O)_xMn_8O_{16}$ ($0<x<0.5$). *Physical Review B* **1999,** 59, (20), 12836-12841.

18. Pirrotta, I.; Fernandez-Sanjulian, J.; Moran, E.; Alario-Franco, M. A.; Gonzalo, E.; Kuhn, A.; Garcia-Alvarado, F., Driving Curie temperature towards room temperature in the half-metallic ferromagnet $K_2Cr_8O_{16}$ by soft redox chemistry. *Dalton Transactions* **2012,** 41, (6), 1840-1847.

19. Terasaki, I.; Sasago, Y.; Uchinokura, K., Large thermoelectric power in $NaCo_2O_4$ single crystals. *Physical Review B* **1997,** 56, (20), R12685-R12687.

20. Lee, M.; Viciu, L.; Li, L.; Wang, Y.; Foo, M. L.; Watauchi, S.; Pascal Jr, R. A.; Cava, R. J.; Ong, N. P., Large enhancement of the thermopower in Na_xCoO_2 at high Na doping. *Nature Materials* **2006,** 5, (7), 537-540.

21. Hébert, S.; Maignan, A., Thermoelectric Oxides. In *Functional Oxides*, Bruce, D. W.; O'Hare, D.; Walton, R. I., Eds. John Wiley & Sons, Ltd: 2010; pp 203-255.

22. Brock, S. L.; Duan, N.; Tian, Z. R.; Giraldo, O.; Zhou, H.; Suib, S. L., A Review of Porous Manganese Oxide Materials. *Chemistry of Materials* **1998,** 10, (10), 2619-2628.

23. Singh, R. N.; Shivakumara, C.; Vasanthacharya, N. Y.; Subramanian, S.; Hegde, M. S.; Rajagopal, H.; Sequeira, A., Synthesis, Structure, and Properties of Sodium or Potassium-Doped Lanthanum Orthomanganites from NaCl or KCl Flux. *Journal of Solid State Chemistry* **1998,** 137, (1), 19-27.

24. Manako, T.; Kubo, Y.; Shimakawa, Y., Transport and structural study of $Tl_2Ba_2CuO_{6+\delta}$ single crystals prepared by the KCl flux method. *Physical Review B* **1992,** 46, (17), 11019-11024.

25. Thirumal, M.; Jain, P.; Ganguli, A. K., Molten salt synthesis of complex perovskite-related dielectric oxides. *Materials Chemistry and Physics* **2001,** 70, (1), 7-11.

26. Post, J. E.; Von Dreele, R. B.; Buseck, P. R., Symmetry and cation displacements in hollandites: structure refinements of hollandite, cryptomelane and priderite. *Acta Crystallographica Section B* **1982,** 38, (4), 1056-1065.

27. Abriel, W.; Rau, F.; Range, K. J., New compounds $A_{2-x}V_8O_{16}$ (A = K,Tl) with hollandite type structure. *Materials Research Bulletin* **1979,** 14, (11), 1463-1468.

28. Yu, J.; Tang, S.; Wang, L.; Du, Y., Spin-glass-like behavior in hollandite $Ba_{1+\delta}Mn_8O_{16}$ nanoribbons synthesized by molten-salt method. *Chemical Physics Letters* **2010,** 496, 117-121.

29. Mott, N. F., Conduction in non-crystalline materials. *Philosophical Magazine* **1969,** 19, (160), 835-852.

30. Carter, M. L.; Withers, R. L., A universally applicable composite modulated structure approach to ordered $Ba_xM_yTi_{8-y}O_{16}$ hollandite-type solid solutions. *Journal of Solid State Chemistry* **2005,** 178, (6), 1903-1914.

31. Koshibae, W.; Tsutsui, K.; Maekawa, S., Thermopower in cobalt oxides. *Physical Review B* **2000,** 62, (11), 6869-6872.

32. Sparks, T. D.; Gurlo, A.; Clarke, D. R., Enhanced n-type thermopower in distortion-free $LiMn_2O_4$. *Journal of Materials Chemistry* **2012,** 22, (11), 4631-4636.

6. MICROWAVE -ASSISTED HYDROTHERMAL SYNTHESIS

6.1. Introduction

Hydrothermal synthesis is an important branch of inorganic synthesis. The use of microwaves combined with the efficiency of the hydrothermal method has facilitated the preparation of a wide variety of technological important materials, as it was previously described in *Chapter 2.6.3*. Synthesis and characterization of nano-sized rare earth doped ceria with fluorite structure for SOFC electrolyte applications, $BiFeO_3$ perovskite with multiferroic properties and $H_2V_3O_8$ with one-dimensional (1D) nanostructure for lithium battery technology are presented in this chapter.

Fluorite and perovskite structures were briefly described in *Chapter 4.1* (Figures 4.1 and 4.2). The structure of $H_2V_3O_8$ is evaluated in this chapter (*section 6.4.2*) according to the structural resolution by synchrotron X-ray diffraction analysis.

6.2. Rare Earth Doped Ceria

Ceria-based solid solutions have been regarded promising candidates to serve as electrolytes in IT - SOFCs since their oxygen ion conductivities are higher than that of yttria stabilized zirconia YSZ in the intermediate temperature range (500 – 800 ^oC).[1, 2] Gadolinium and samarium-doped ceria have been extensively studied due to their high ionic oxygen conductivity.[3, 4] This increased ionic conductivity is a direct result of chemically doping the parent compound $Ce^{4+}O_2$ with the trivalent RE cations Gd^{3+} and Sm^{3+}. The

charge compensation mechanism for such alio-valent doping is by formation of oxygen vacancies ($Ce^{4+}_{1-x}RE^{3+}_{x}O_{2-x/2}$), which leads to strongly increased ionic oxygen vacancy conduction.

One major problem for the application of polycrystalline oxygen ionic conductors as SOFC electrolytes is the ceramic grain boundary (GB) resistance, which is usually larger than or in the same range as the bulk resistance although GB areas are expected to be thin. This implies that GBs constitute barriers for ionic charge transport and they indeed often act as Schottky barriers.[5-7] Therefore, the reduction of the barrier height, i.e. the reduction of the GB resistance, is of uppermost importance to facilitate application of polycrystalline electrolytes. In two recent publications[8,9] it had been demonstrated that the optimum ionic conductivity may be encountered in lightly Ca doped $Ce_{0.78}Ca_{0.02}Sm_{0.2}O_{1.88}$ and $Ce_{0.8}Sm_{0.18}Ca_{0.02}O_{1.9-\delta}$ ceramics. Furthermore, several attempts have been made to increase the sinter activity of as-prepared ceria powders by decreasing the grain size to the nanometer range, and the ionic conductivity has been reported to be significantly enhanced in ceramics made from such powders with increased sinter activity, as compared to powders made from conventional methods.[10, 11] Accordingly, preparation of ultrafine ceria powders has been intensively investigated. Several techniques that include hydrothermal synthesis,[12-14] urea-based homogeneous precipitation,[15] co-precipitation,[16] the flux method[17] and mechanical mixing[18] have been developed for the synthesis of cation-doped and undoped ceria nano-sized particles.

Nanosized ceria powders have been prepared before under microwave – hydrothermal conditions in a two-step process: (1) MW irradiation of the precursor solution forming $Ce(OH)CO_3$, and (2) crystallization of the fluorite structure by heat treatment.[18] An improvement of such synthesis technique using a one-step microwave-hydrothermal synthesis has been demonstrated on rare-earth Pr doped ceria,[19] but the method has not been developed successfully

to Sm and Gd doped ceria before. Furthermore, there are no previous studies of microwave sintering of these materials.

In this chapter section one-step microwave-hydrothermal synthesis of $Ce_{0.85}RE_{0.15}O_{1.925}$ (RE = Gd, Sm), $Ce_{0.8}(Gd_{0.1}Sm_{0.1})O_{1.9}$, $Ce_{0.8}Sm_{0.18}Ca_{0.02}O_{1.9-\delta}$ and $CeO_{2-\delta}$ nano-powders is presented. The structural and microstructural characterization of each material and a comprehensive study of the ionic conductivities in sintered ceramics are discussed.

6.2.1. Synthetic aspects

Nano-sized particle powders can be synthesized by microwave-assisted hydrothermal synthesis at low reaction temperature (200 ^{o}C), where particle growth is minimized. The main process parameters to be controlled are the chemical reaction of the precursor solution, the pH of the solution, reaction temperature and pressure. Such parameters determine the particle nucleation mechanism and growth kinetics, ideally leading to the desired morphology of the crystallites.[20,21] Cerium (III) nitrate hexahydrate $Ce(NO_3)_3{\cdot}6H_2O$, ≥ 99% (Sigma-Aldrich), Samarium (III) nitrate hexahydrate $Sm(NO_3)_3{\cdot}6H_2O$, 99.9% (Sigma-Aldrich), Gadolinium (III) nitrate hexahydrate $Gd(NO_3)_3{\cdot}6H_2O$, 99.9% (Sigma-Aldrich), Calcium (II) nitrate tetrahydrate $Ca(NO_3)_2{\cdot}4H_2O$, ≥ 99% (Sigma-Aldrich) and Potassium hydroxide KOH flakes, 90% (Sigma-Aldrich) were used as starting chemicals (the hydrate grade of the nitrates was determined by TGA). The aqueous solutions of each composition were prepared by dissolving the nitrate salt to the desired concentrations in distilled water and dilution in 1.2 M KOH under constant stirring. The solution was ultrasonically dispersed for 2 min and the reactions were carried out in double-walled vessels consisting of an inner Teflon sealed autoclave and an outer shell high strength polymer. The double-walled vessels were placed in a commercial Milestone ETHOS 1 microwave system, which was operated at 2.45 GHz. The heating ramp up to 200 °C was set to ≈ 12 ^{o}C/min, the holding time at 200 °C was 30 min, which was followed by switching off the microwave power to furnace cool to room temperature at ≈ 5 ^{o}C/min. The reaction vessels were

connected to a pressure transducer in order to monitor the autogenous pressure, which was found to amount to ≈ 16 bars during the 30 minutes holding time at 200 °C. The crystallized powders obtained were decanted 3 times, rinsed with distilled water to eliminate the remaining impurities and dried at 80 °C.

Two different sintering procedures have been employed. In both cases synthesized powders were compacted into pellets in a uni-axial 2 ton die press for 5 min.

(1) In the first case densification sintering was carried out at 1450 °C in a conventional furnace for 4 - 8 hours followed by slow cooling at 1.5 °C/min.

(2) The pellet was introduced into a SiC crucible. This material absorbs microwaves strongly and works as secondary heater –hybrid. Different times of sintering were performed from 5 to 20 minutes in a single-mode microwave applicator working at 2.45 GHz (SAIREM Company). The radiation was guided along a commercial TE_{10p} waveguide equipped with two circulators that absorb the reflected power and therefore protect the generator. The length of the microwave cavity was tuned to excite the magnetic TE_{102} mode. The temperature was measured using a pyrometer (modline 5 from IRCON – from 350 °C to 2000 °C) focused on the sample surface. The thermal cycle systematically included a ramp at ≈ 300 °C/min and a dwell at 1450 °C in adjusting both 3 stub tuners and the incident power. The incident power required to achieve ≈ 1450 °C was roughly 300 W. After a specified amount of time spent at high temperature (from 5 minutes to 1 hour at 1450°C), the power was switched off and the sample was cooled down to room temperature.

In both sintering procedures (1) & (2), the density of the obtained pellets was found to be ≈ 95%.

6.2.2. Structural characterization

Phase purity and the fluorite CeO_2 crystal structure of each sample were confirmed from the powder XRD pattern shown in Fig.6.1. The nanometric size of the synthesized powders was evident by perceptible diffraction line broadening. The average crystallite sizes were calculated from the full width half maximum of the (220) reflection line by using the Debye - Scherrer formula. The particle sizes obtained are 9 nm for $CeO_{2-\delta}$, 10 nm for $Ce_{0.8}Gd_{0.1}Sm_{0.1}O_{1.9}$, 12 nm for $Ce_{0.85}Gd_{0.15}O_{1.925}$, 14 nm for $Ce_{0.85}Sm_{0.15}O_{1.925}$ and 15 nm for $Ce_{0.8}Sm_{0.18}Ca_{0.02}O_{1.9-\delta}$.

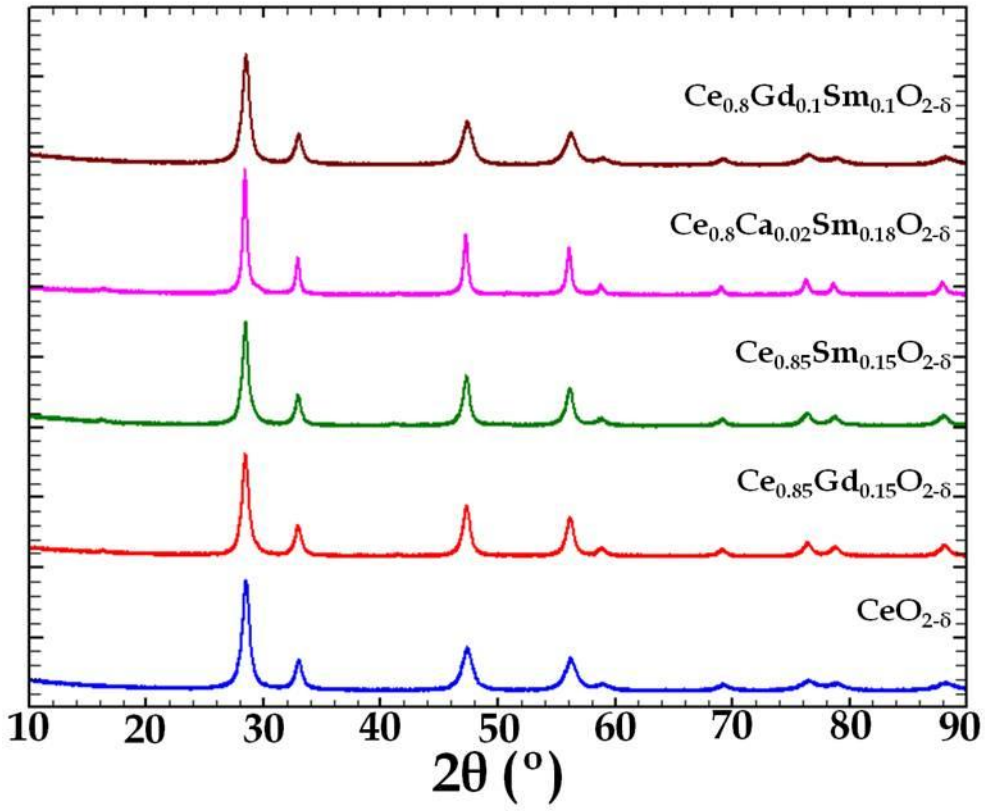

Figure 6.1. X-ray diffraction patterns of ceria and rare earth doped cerias. The high width of the reflexions in the patterns showed that particle size is in the nanometric range.

Structural Rietveld refinements yielded satisfactory fits by using the cubic #225 *Fm-3m* space group (Figure 6.2). Table 6.1 shows the results of the performed structural analysis. Numbers in parentheses represent standard deviations. The lattice parameters obtained after data refinement are in good agreement with data reported in the literature[22, 23]. All atom positions are fixed

by the symmetry of the *Fm-3m* space group and were not refined. Rare earth cations are situated at the 4a site with the atomic coordinate (0, 0, 0) and oxygen is at the 8c site corresponding to the (¼, ¼, ¼) position.

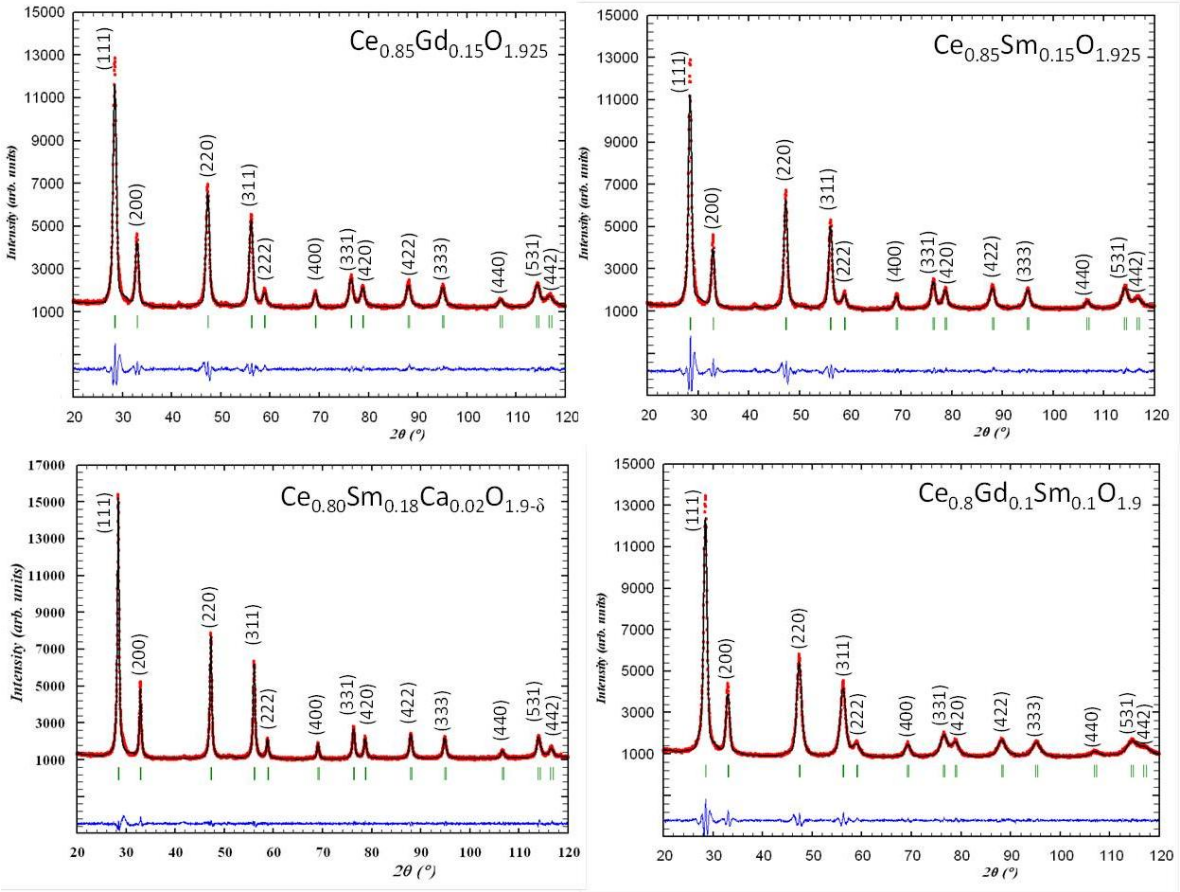

Figure 6.2. Rietveld refinement of XRD patterns: observed (red dotted lines), refined (black solid lines), and their difference (blue bottom line). Green vertical bars indicate the X-ray reflection positions.

Table 6.1. Unit cell parameters and agreement factors, obtained through Rietveld analysis of the Powder X-Ray diffraction patterns.

	Space group: *Fm-3m* (#225)	
	***a* (Å)**	**Agreement factors**
$CeO_{2-\delta}$	5.4211 (1) Å	R_p=3.65 ; R_{wp}=4.87 ; R_{exp}=2.75 ; χ^2=3.14
$Ce_{0.85}Gd_{0.15}O_{1.925}$	5.4297 (1) Å	R_p=3.24 ; R_{wp}=4.51 ; R_{exp}=2.48 ; χ^2=3.31
$Ce_{0.85}Sm_{0.15}O_{1.925}$	5.4345 (1) Å	R_p=3.69 ; R_{wp}=5.30 ; R_{exp}=2.58 ; χ^2= 4.24
$Ce_{0.8}Sm_{0.18}Ca_{0.02}O_{1.9-\delta}$	5.4372(1) Å	R_p=2.38 ; R_{wp}=3.31 ; R_{exp}=2.69 ; χ^2= 1.52
$Ce_{0.8}Gd_{0.1}Sm_{0.1}O_{1.9}$	5.4259 (2) Å	R_p=3.28 ; R_{wp}=4.31 ; R_{exp}=2.72 ; χ^2=2.51

6.2.3. Microstructural characterization

TEM images of the synthesized ceria powders show agglomerated particles (Figure 6.3) with nanometric size. The corresponding SAED patterns (insets of Figure 6.3) show the diffraction rings commonly observed in polycrystalline materials. The mean particle sizes determined from TEM images are consistent with the XRD particle size calculation using the Debye-Scherrer formula as described before. The radii of the rings are inversely proportional to the interplanar spacings d_{hkl} of lattice planes of crystals.

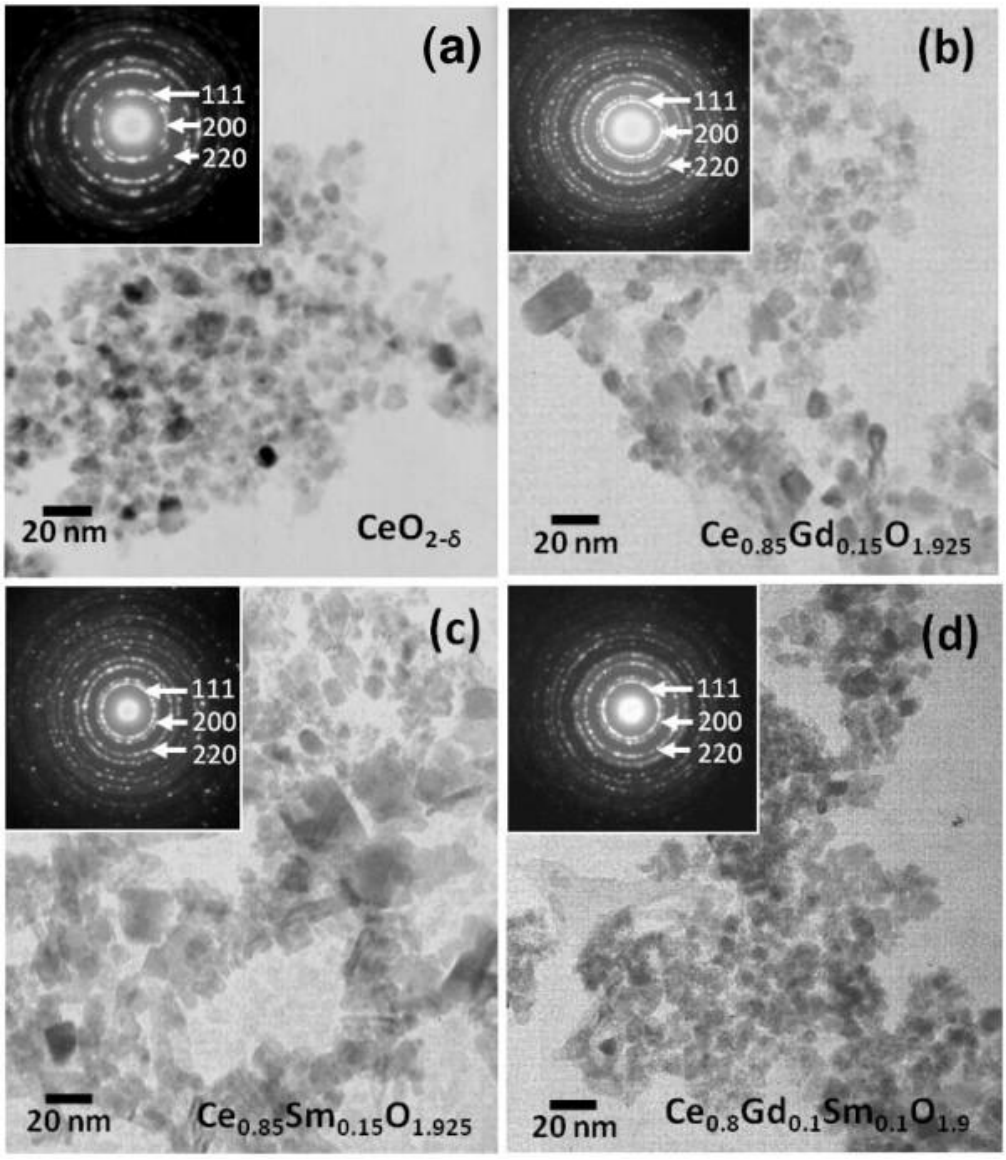

Figure 6.3. TEM micrographs of rare earth doped cerias and in the top corners the SAED patterns.

Figure 6.4 shows a higher magnification micrograph of $Ce_{0.8}Sm_{0.18}Ca_{0.02}O_{1.9-\delta}$ powder, where it is clear that the particles are less agglomerated than those in the samples presented in Figure 6.3.

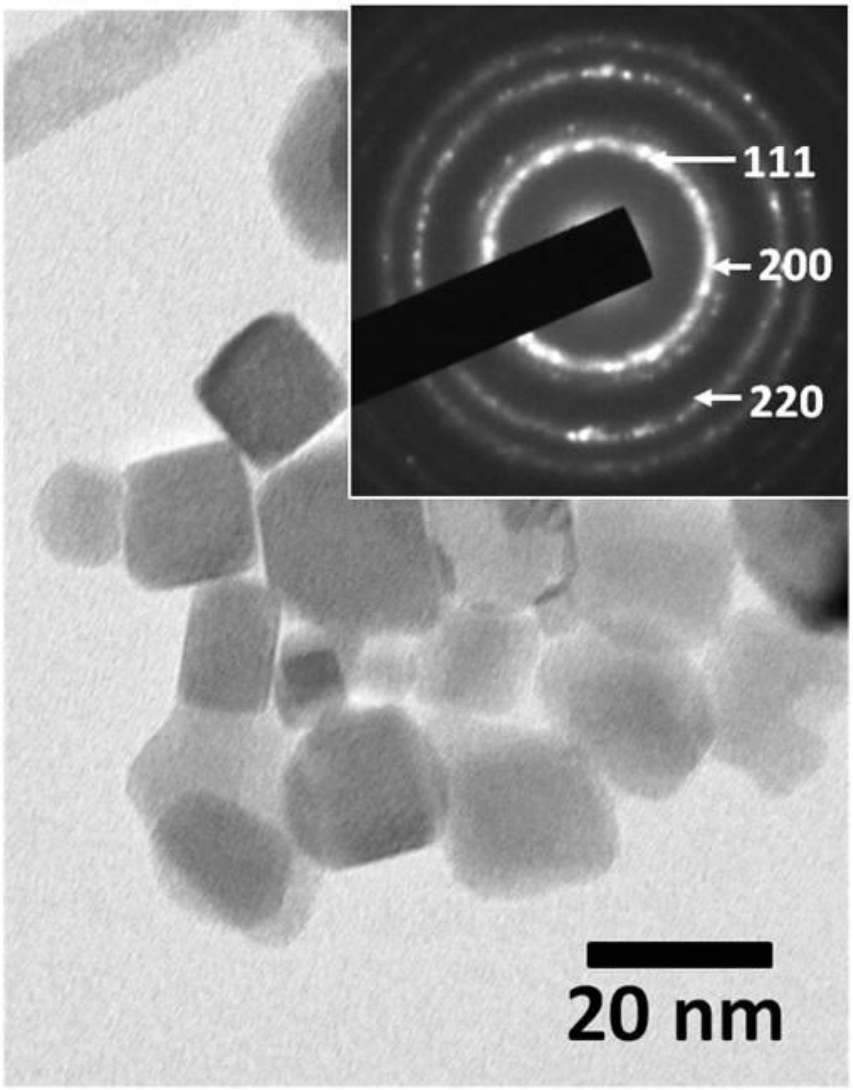

Figure 6.4. TEM micrograph of $Ce_{0.8}Sm_{0.18}Ca_{0.02}O_{1.9-\delta}$ and in the top corners the SAED patterns.

In Figure 6.5 SEM micrographs of undoped and doped ceria sintered pellets, 4 h at 1450 ^{o}C in air in a conventional furnace, indicate uniform particle size and a dense microstructure. As a result of the densification sintering, perceptible grain growth was detected by increased grain sizes as compared to those from the synthesized powders. The rather efficient grain growth mechanism may be associated with the high sinter activity of nano-powders.

In the case of $Ce_{0.8}Sm_{0.18}Ca_{0.02}O_{1.9-\delta}$ ceramics, different times of sintering in the conventional furnace (4 – 8 h at 1450 ^{o}C) were employed in order to improve the pellet density. Furthermore, single mode microwave sintered pellets were prepared at different microwave irradiation time in order to establish a relationship between grain size, density and microwave irradiation time.

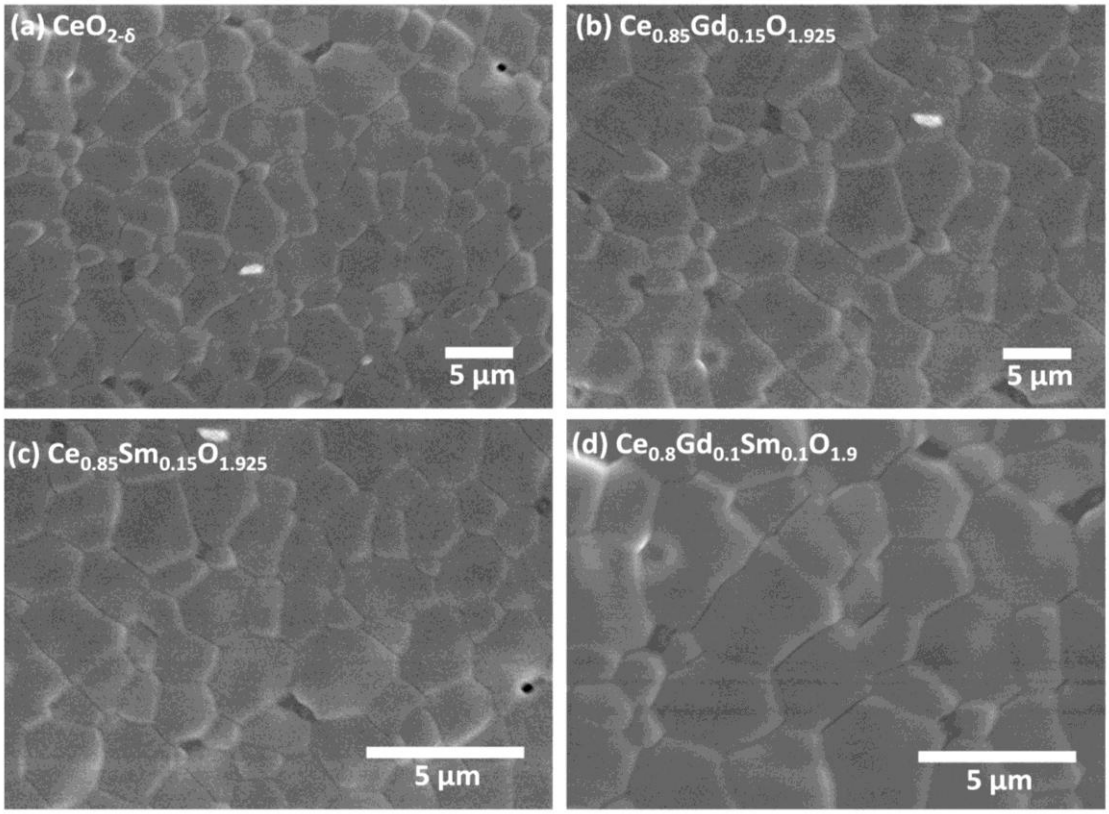

Figure 6.5. SEM micrographs of sintered pellets at 1450 ^{o}C for 4 h.

Figure 6.6 shows the micrographs of sintered $Ce_{0.8}Sm_{0.18}Ca_{0.02}O_{1.9-\delta}$ using different sintering conditions (conventional sintering, microwave sintering and different heating times).

In all cases the pellets are well sintered. Continuous grain growth by increased grain sizes was detected when increasing microwave irradiation time as indicated in Figure 6.6.

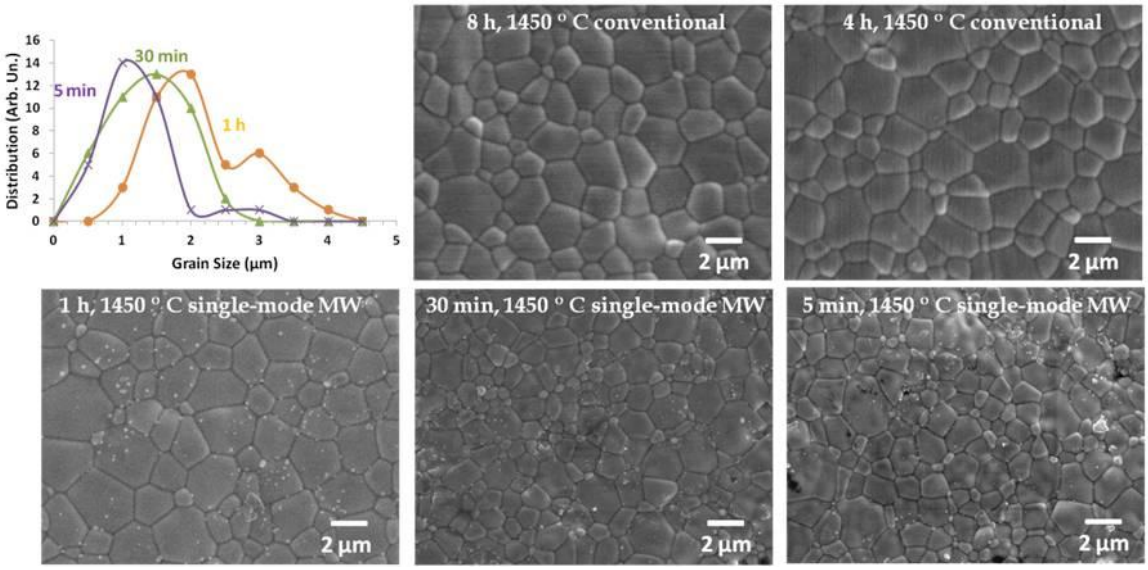

Figure 6.6. SEM micrographs of sintered $Ce_{0.8}Sm_{0.18}Ca_{0.02}O_{1.9-\delta}$ pellets and grain size distribution for microwave sintered samples.

6.2.4. BET surface area analysis

N_2 adsorption–desorption isotherms of powders are presented in Figure 6.7. The plots show the amount of gas adsorbed (cm^3/g) versus the relative pressure (P/Po), where P is the equilibrium pressure of the adsorbed vapor and Po is the saturated vapor pressure at the temperature of the experiment (77 K). These isotherms exhibit a hysteresis loop, where the lower branch represents measurements obtained by progressive addition of gas to the adsorbent, and the upper branch by progressive withdrawal. Such hysteresis is usually associated with the filling and emptying of meso-pores by capillary condensation.[24, 25] The lower limit of hysteresis is thus dependent on the adsorptive and the operational temperature. The lower hysteresis closure point is found at a relative pressure P/Po of ≈ 0.4, which is within the expected range according to the literature.[36]

The surface area determination using the BET technique yielded values of 57.4(1) m^2/g for $Ce_{0.8}Sm_{0.18}Ca_{0.02}O_{1.9-\delta}$, 62.2(4) m^2/g for $CeO_{2-\delta}$, 86.6(2) m^2/g for $Ce_{0.85}Sm_{0.15}O_{1.925}$, 89.2(4) m^2/g for $Ce_{0.85}Gd_{0.15}O_{1.925}$ and 97.6(5) m^2/g for $Ce_{0.8}Gd_{0.1}Sm_{0.1}O_{1.9}$.

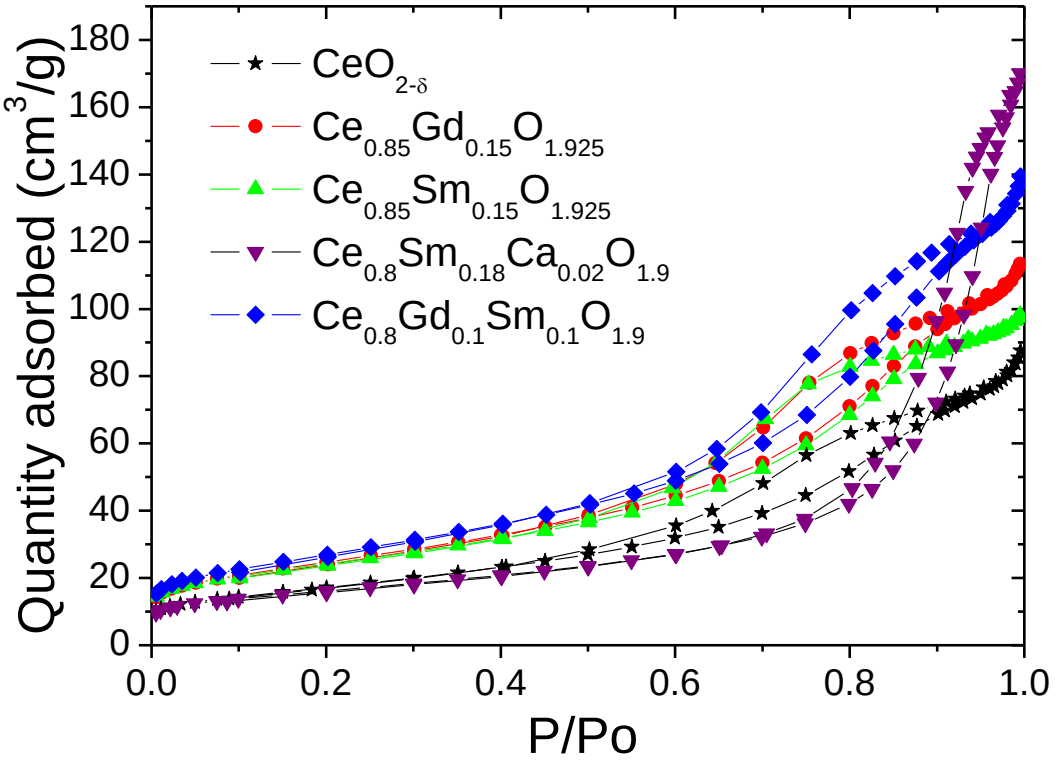

Figure 6.7. BET N_2 adsorption–desorption isotherms at 77 K for the $CeO_{2-\delta}$ and doped-ceria powder samples synthesized by the microwave-hydrothermal method. The amount of gas adsorbed and desorbed (cm^3/g) is plotted vs the relative pressure (P/Po).

Apparently, alio-valent chemical doping increases the ceria surface area. This trend is somewhat different to the crystallite sizes determined by XRD and TEM, which may be explained by differences in the particle agglomeration behaviour. Generally, the surface area values obtained for the system were rather high considering the fact that the synthetic route is template free. Previous reports all suggested lower surface area values for materials synthesized by the hydrothermal method (37-80 m^2/g),[26] sol-gel (73 m^2/g)[27] or a surfactant-free emulsion methods (43 m^2/g).[28] It is clear that the microwave-hydrothermal method is an effective route for the synthesis of materials with relatively large surface areas.

6.2.5. Ionic conductivity measurements by impedance spectroscopy

Various data representations and equivalent circuit fitting

Impedance Spectroscopy (IS) data collected for the 8 h conventionally sintered $Ce_{0.8}Sm_{0.18}Ca_{0.02}O_{1.9-\delta}$ sample at 480 K is shown in Fig. 6.8 in terms of

the complex impedance plane plot of $-Z''$ vs. Z'. Two regular semicircles are displayed, which are consistent with a series connection of two conventional dielectric relaxation processes and can, therefore, be modelled by a series of two parallel resistor-capacitor (RC) elements.[29] The high frequency semicircle can be ascribed to an intrinsic bulk contribution, whereas the intermediate frequency semi-circle is interpreted as a GB response.[27, 30] It should be noted though that the semi-circles in Fig. 6.8 are slightly suppressed in a way such that the semicircle centre seems to be slightly suppressed below the Z' x-axis. This indicates a certain degree of non-ideality of the relaxation process, which can be accounted for by replacing the ideal capacitor in the RC element with a constant phase element (CPE).[31] Fig. 6.8 shows an equivalent circuit consisting of a series of such two non-ideal R-CPE elements and an almost ideal fit was obtained at intermediate and high frequencies. The CPE behaviour is usually explained in the framework of a jump-relaxation model,[32] or in simpler terms by a broadening of the distribution of relaxation times τ across the macroscopic sample,[33] where $\tau = RC$, with R being the resistance and C the capacitance of an ideal RC element.

At the low frequency end the data points in $-Z''$ vs. Z' (Fig. 6.8) align linearly in a "pike"-like fashion, which is inconsistent with the conventional RC element model and is commonly interpreted as a blocking effect of the electrode sample interface. This is typical for ionic charge transport,[34] where the blocking effect of the interface occurs as a result of the different types of dominating charge carriers in the Au electrodes (electrons) and in the ceramics (oxygen vacancies). Therefore, ionic conductivity in the $Ce_{0.8}Sm_{0.18}Ca_{0.02}O_{1.9-\delta}$ sample is evident, electronic contributions may be small, a potential mixed valence Ce^{3+}/Ce^{4+} electronic hopping conduction is not visible and, consequently, the $Ce_{0.8}{}^{4+}Sm_{0.18}{}^{3+}Ca_{0.02}{}^{2+}O_{1.9}{}^{2-}$ sample may be close to the ideal stoichiometry. The charge transport across blocking electrode interfaces is usually by diffusion, which was not accounted for in the equivalent circuit model here, because rather complex circuit components such as Warburg elements are needed to describe diffusion processes, as it was comment in *section 4.4.5.* for $Gd_2Ti_2O_7$.[28]

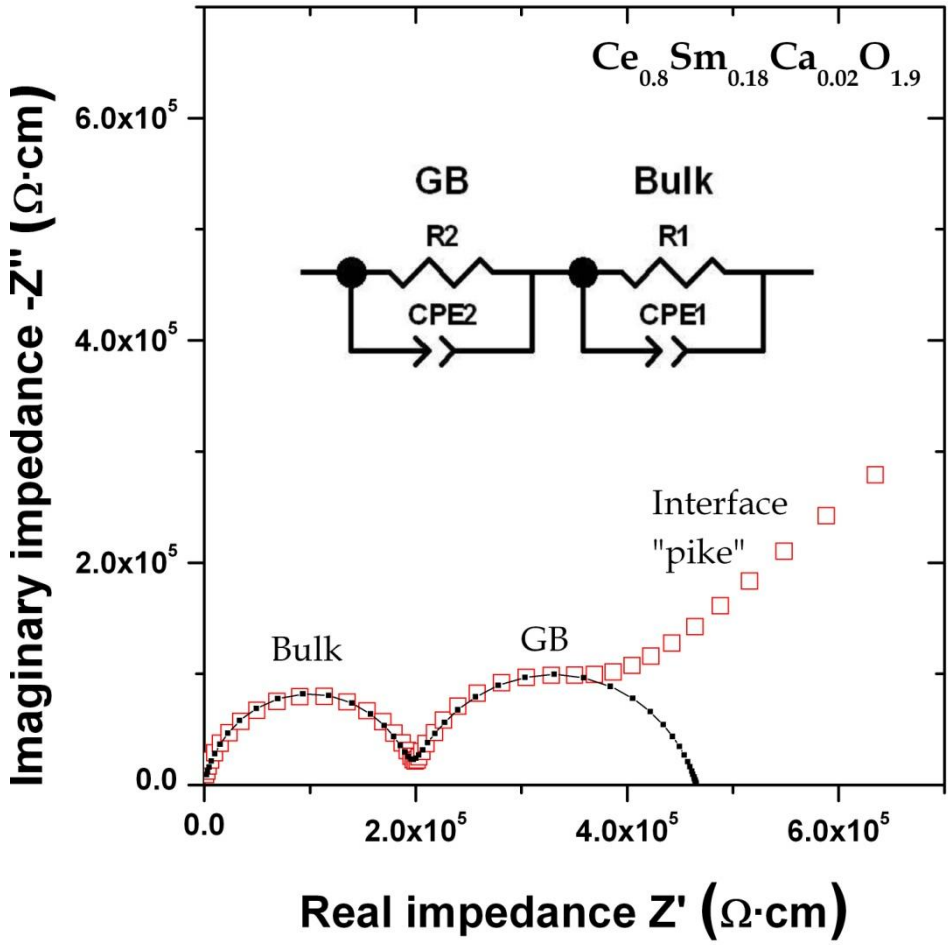

Figure 6.8. Complex impedance plot of $-Z''$ vs. Z' for $Ce_{0.8}Sm_{0.18}Ca_{0.02}O_{1.9-\delta}$ (8 h. sintered sample) at 480 K, demonstrating bulk, GB and interface relaxations. Open symbols (◊) represent measured data, squares (■) and solid lines represent equivalent circuit fits at intermediate/high frequency using the model presented in the figure.

Fig. 6.9 displays plots of only the imaginary parts of the impedance $-Z''$ vs. frequency f for the $Ce_{0.8}Sm_{0.18}Ca_{0.02}O_{1.9-\delta}$ sample on double-logarithmic axes in order to display the curves for all measured temperatures as indicated. Two dielectric relaxation peaks for the bulk and GB contribution are evident, consistent with the two bulk and GB semi-circles in Fig. 6.8. The low frequency interface relaxation shows clearly different trends with f, again inconsistent with the standard RC element model and confirming the above interpretation of an electrode blocking effect. The height of the bulk and GB relaxation peaks are proportional to the resistance of the respective contribution and the thermal activation of GB and bulk ionic charge transport is indicated by solid lines in

Fig. 6.9. The fits using the model in Fig. 6.8 are also shown at lower frequencies but for demonstration purposes only. The actual fitting procedure itself was restricted to intermediate and high frequencies where the GB and bulk relaxations would be dominant (see also Fig. 6.8).

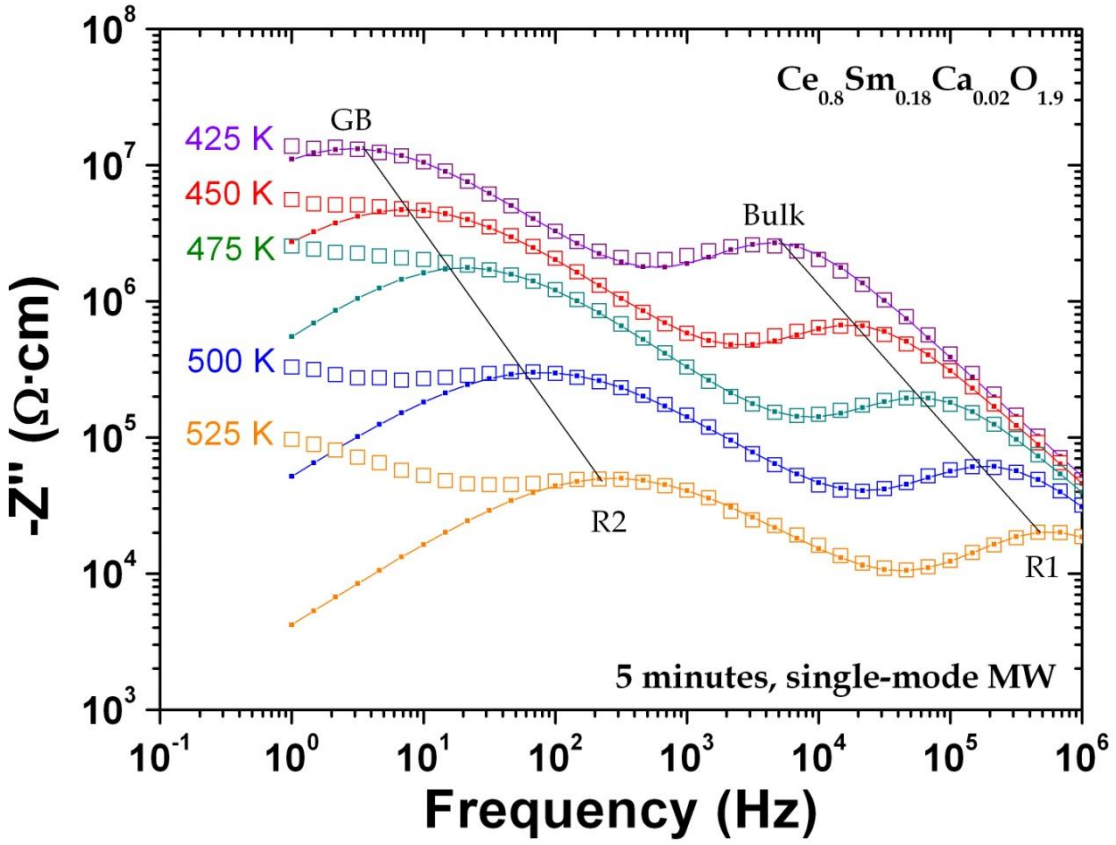

Figure 6.9. Imaginary part of the impedance (-*Z*'') plotted vs frequency for $Ce_{0.8}Sm_{0.18}Ca_{0.02}O_{1.9-\delta}$. Two relaxation peaks are displayed, for the GB and bulk contributions. Both peaks exhibit thermal activation of the ionic charge transport (indicated by solid lines). Open symbols (◊) represent measured data, squares (■) and solid lines represent equivalent circuit fits using the model presented in Figure 6.8.

The impedance data was additionally converted into the real part of dielectric permittivity ε' in order to obtain further confirmation of the electrode blocking effect and the ionic charge transport (Fig. 6.10): the ε' vs. f spectra for the $Ce_{0.8}Sm_{0.18}Ca_{0.02}O_{1.9-\delta}$ sample show 3 distinct regimes, where the bulk and GB contributions are manifested by approximately frequency independent ε' plateaus each (as indicated in the graph), whereas the electrode interface contribution shows a uniform and linear increase of ε' with decreasing f. The

bulk and GB plateaus are consistent with standard dielectric theory, whereas the interface again shows the typical signs for an electrode blocking effect.

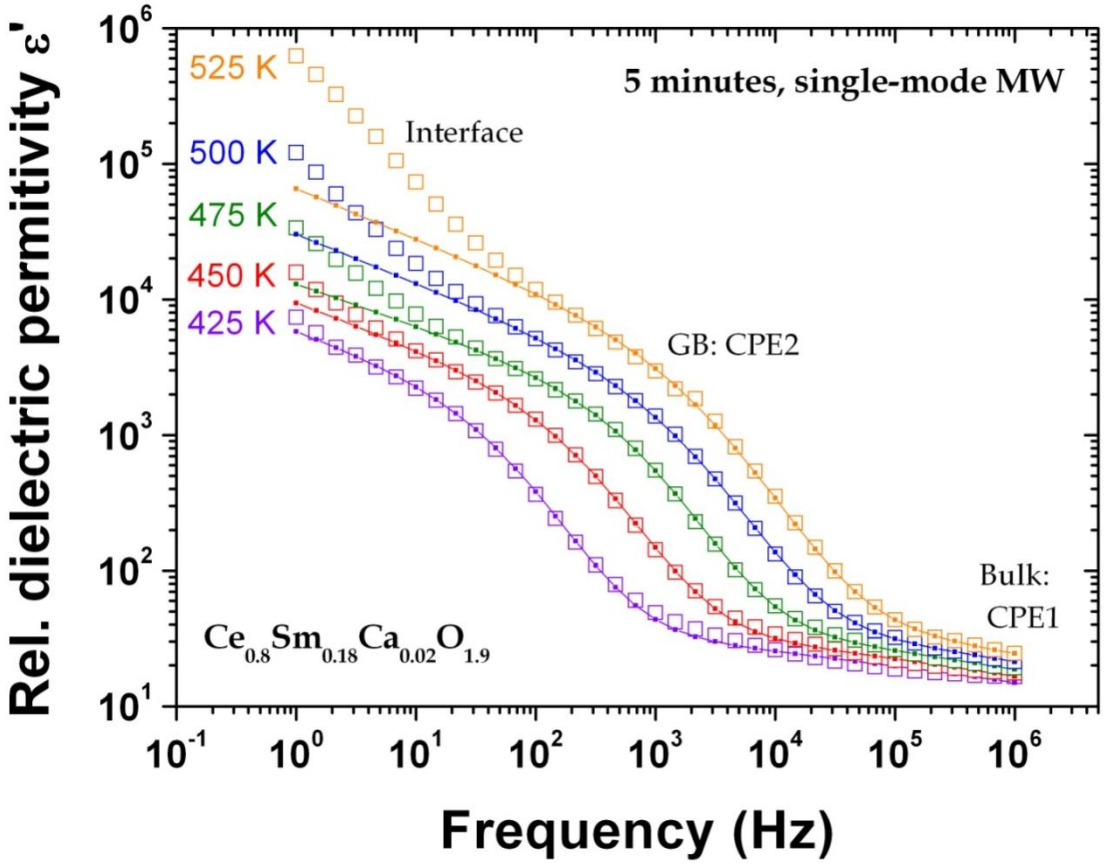

Figure 6.10. Relative dielectric permittivity ε' vs f for $Ce_{0.8}Sm_{0.18}Ca_{0.02}O_{1.9-\delta}$. The dielectric response at intermediate and high temperature is well represented by a series connection of two non-ideal RC elements, one for GB and one for the bulk dielectric relaxations.

The trends of $-Z''$ vs. Z', $-Z''$ vs. f and ε' vs. f shown in Fig. 6.8, Fig. 6.9 and Fig. 6.10 were equivalent for the $Ce_{0.85}Gd_{0.15}O_{1.925}$, $Ce_{0.85}Sm_{0.15}O_{1.925}$ and $Ce_{0.8}Sm_{0.1}Gd_{0.1}O_{1.9}$ samples, all of them sintered during 4 h at 1450 ºC using a conventional furnace, and for $Ce_{0.8}Sm_{0.18}Ca_{0.02}O_{1.9-\delta}$ samples sintered using conventional heating and microwave sintering. Ionic conductivity was indicated consistently.

Resistivity vs. temperature trends

The GB and bulk resistivity values ρ obtained from data fitting were plotted on a logarithmic scale vs. reciprocal temperature $1/T$ in Fig. 6.11 and

Fig. 6.12, including the activation energies (E_A) determined from the slopes of the corresponding Arrhenius plots of ln(ρ) vs. 1/T. Fig. 6.11 shows that all GB activation energies were in the range of 1 eV, typical for ionic charge transport. The GB resistivity values were considerably higher than all bulk values and confirm the notion that GBs constitute barriers for the ionic charge transport. The lowest GB resistivity was found for the $Ce_{0.8}Sm_{0.18}Ca_{0.02}O_{1.9-\delta}$ sample, which may, therefore, be regarded preferential for IT-SOFC applications. Such preferential GB resistivity cannot be associated with the relatively small variations in grain size and may well be an inherent property of the ionic dopant. In fact, the average grain size in the Sm doped sample is the lowest, emphasizing further the low GB resistivity. Such findings are confirmed by the bulk resistivity, showing optimum ionic conductivity for the Sm – Ca doped sample (Fig. 6.12). The ionic charge transport is known to be determined by the defect association energy and the local defect structure,[35, 36] which appear to be optimal in Sm – Ca doped ceria.

The GB activation energy for the preferential $Ce_{0.8}Sm_{0.18}Ca_{0.02}O_{1.9-\delta}$ sample was 1.02 eV, which is a slightly higher value from that obtained for $Ce_{0.8}Sm_{0.2}O_{2-\delta}$ (0.96 eV). Both values are comparable with previous work on $Ce_{0.8}Sm_{0.2}O_{2-\delta}$ samples synthesized by the sol–gel method (0.97 eV).[37] The overall GB resistivity at 500 K is decreased though in the work presented here by a factor of ≈ 100 as compared to such sol–gel samples[35] and by a factor of ≈ 400 as compared to more recent $Ce_{0.8}Sm_{0.2}O_{1.9}$ sol–gel samples.[8] Microwave - assisted hydrothermal synthesis appears to be an effective way of synthesizing highly ionically conducting ceria ceramics.

Recently, Moure *et al.*[9] have claimed though that the GB resistivity encountered here can be further decreased by another factor of 8 using mechanosynthesis of ceria powders. Such samples had composition of $Ce_{0.8}Sm_{0.2}O_{1.9}$. The origin of this factor 8 may partially be debited to the higher ac amplitude of the impedance measurement signal of 500 mV used by Moure and co-workers, as compared to the 100 mV amplitude applied here. The GB

resistivity in ionic conductors is commonly influenced by the ac amplitude, because GBs act as Schottky barriers resulting in a non-ohmic (non-linear) GB resistance.[5] In fact, the intrinsic bulk ionic resistivity in the work by Moure *et al.*[9] was lower than in the sample presented here by a factor of only 2, which is a realistic decrease as a result of the higher Sm doping level. Bulk ionic charge transport is usually ohmic (linear)[5] and, therefore, the ac test signal amplitude is irrelevant and the bulk resistivity values can be compared unambiguously.

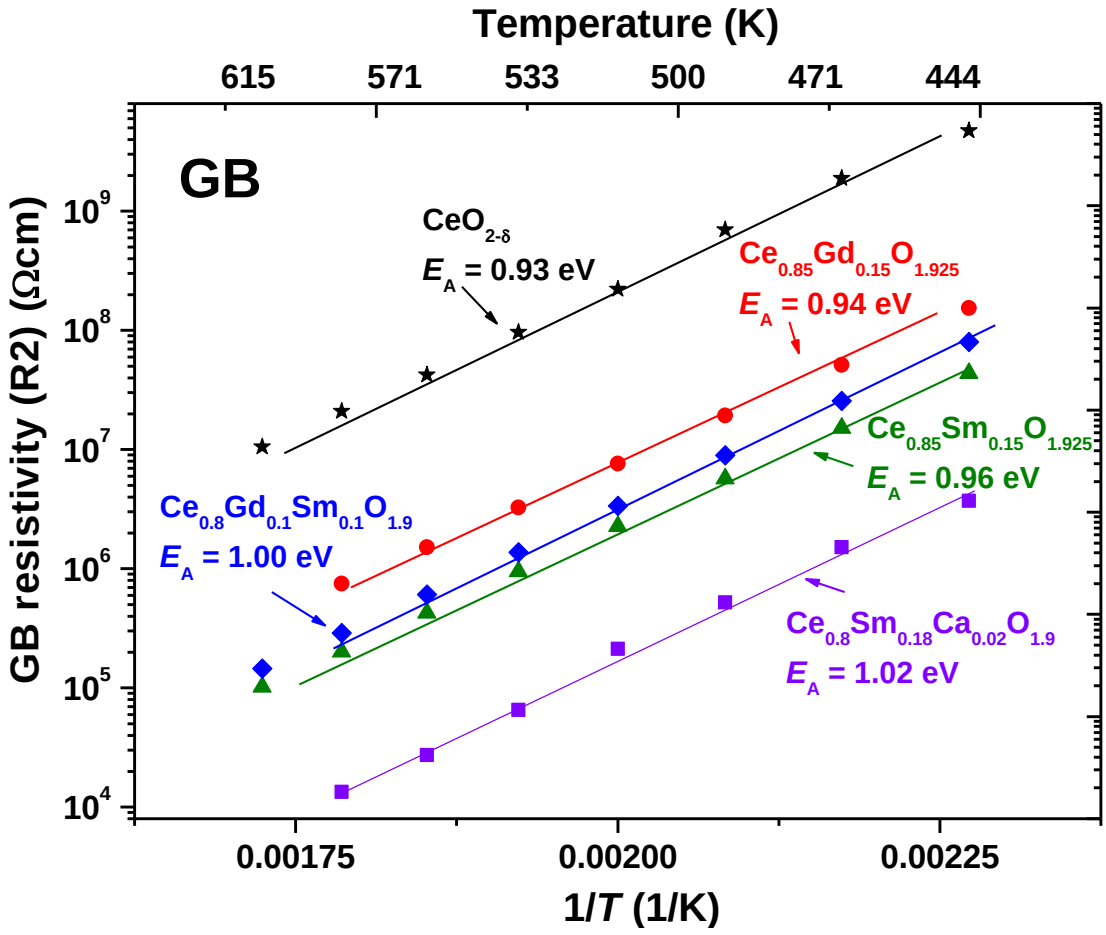

Figure 6.11. Fitted GB resistivity (ρ) values obtained from the resistor R2 in the equivalent circuit plotted vs. reciprocal temperature $1/T$. The GB activation energies (E_A) are given in electron volts (eV) obtained from the respective $\ln(\rho)$ vs. $1/T$ plots.

The bulk E_A values here were all in the range of 0.85 eV as shown in Fig. 6.12, except for the $CeO_{2-\delta}$ curve where both the bulk ρ and E_A values are rather low for ionic charge transport.

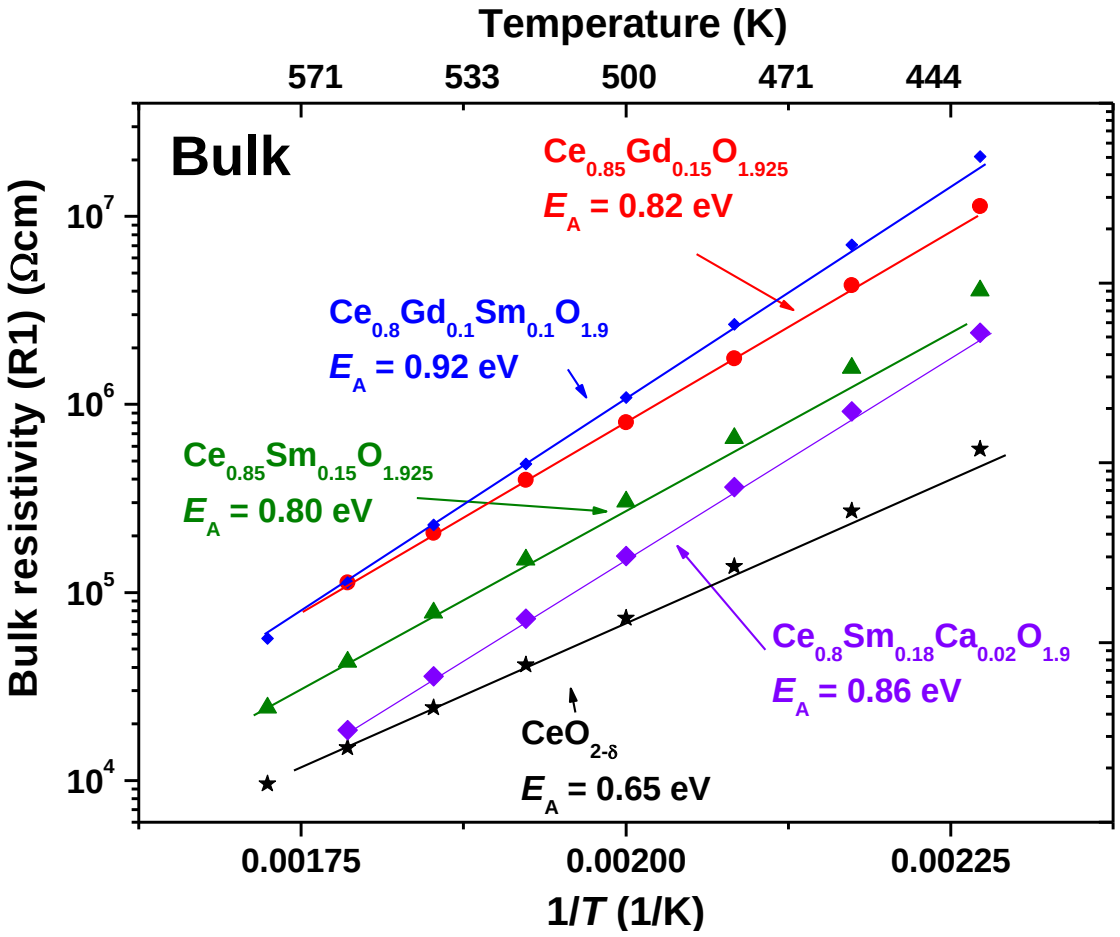

Figure 6.12. Fitted bulk resistivity (ρ) values obtained from the resistor R1 in the equivalent circuit plotted vs. reciprocal temperature $1/T$. The GB activation energies (E_A) are given in electron volts (eV) obtained from the respective $\ln(\rho)$ vs. $1/T$ plots.

Dielectric properties of single – mode microwave sintered samples

The trends of the temperature dependence of GB and bulk resistivity at different sintering conditions are presented in Figure 6.13a and Figure 6.13b, respectively. It is shown that there are no remarkable differences between using conventional sintering and single – mode microwave sintering.

The strongly improved sintering activity of nano-sized powders is shown to lead to exceptionally high ionic conductivities in $Ce_{0.8}Sm_{0.18}Ca_{0.02}O_{1.9-\delta}$ ceramics.

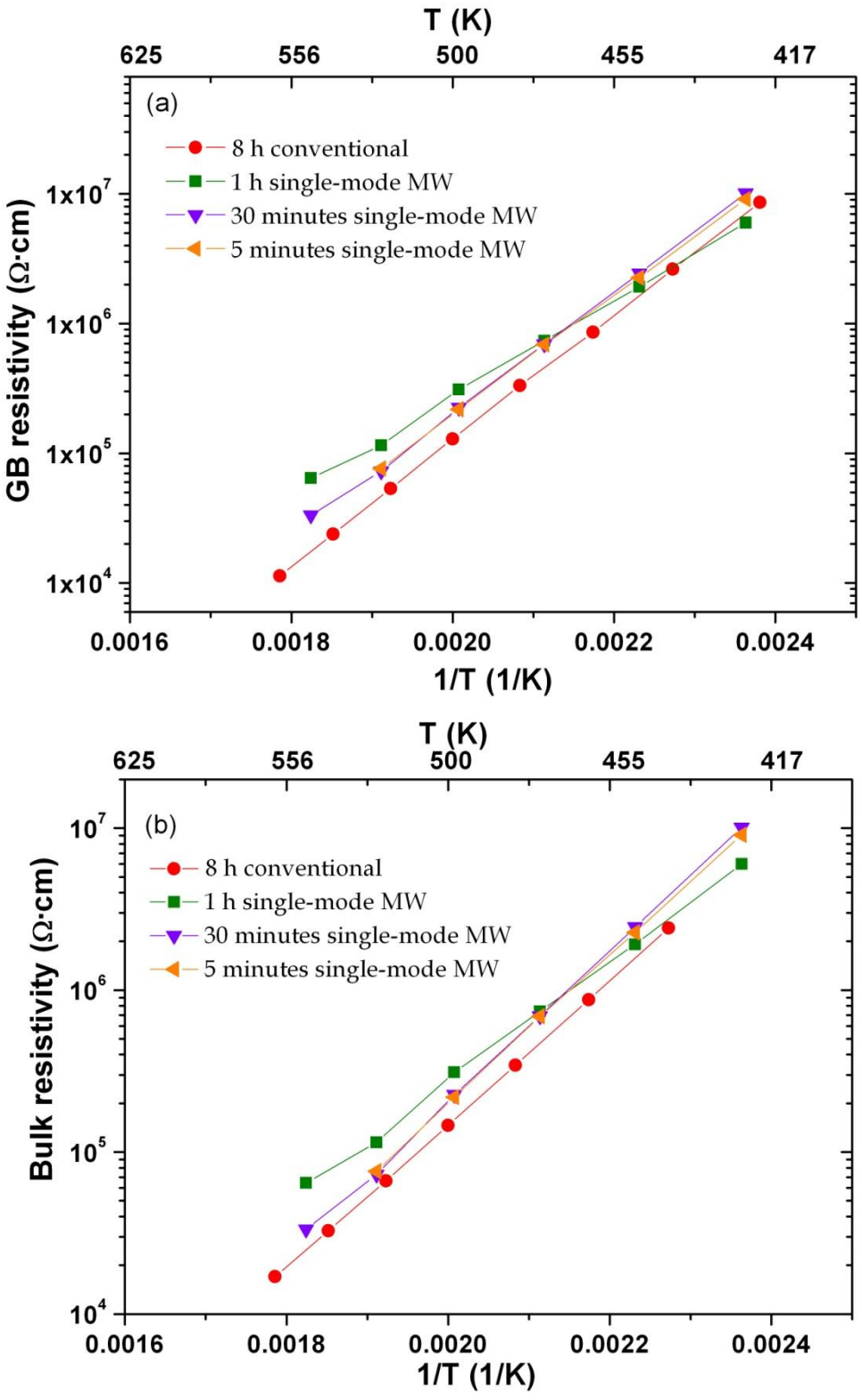

Figure 6.13. a) Fitted GB resistivity (ρ) values obtained from the resistor R2 in the equivalent circuit plotted vs. reciprocal temperature $1/T$ b) Fitted bulk resistivity (ρ) values obtained from the resistor R1 in the equivalent circuit plotted vs. reciprocal temperature $1/T$. In both cases the data are from samples sintered by conventional route and by single – mode microwave using different irradiation times.

DC bias IS measurements in 5 minutes single-mode microwave sintered pellets

The impedance spectroscopy spectra for a 5 minutes microwave sintered ceramic with a super-imposed dc bias of 0 - 20 V are shown in Fig. 6.14. The GB resistance decreases with the increase of the dc bias voltage, while the grain resistance is almost constant. This behaviour is common for ionic conductors and the GB Schottky blocking behaviour can be confirmed by using a Mott–Schottky plot, which is shown in the inset of Figure 6.14. In this plot $1/C^2$ is represented as a function of the DC voltage, V, where C is the capacitance. A linear tendency is evident and the obtained value found at the intersection of the $1/C^2$ line with the horizontal axis corresponds to - 1.61 V. This value is an estimate for the potential that each oxygen vacancy charge carrier needs to overcome in order to move across a GB from one grain to the next.

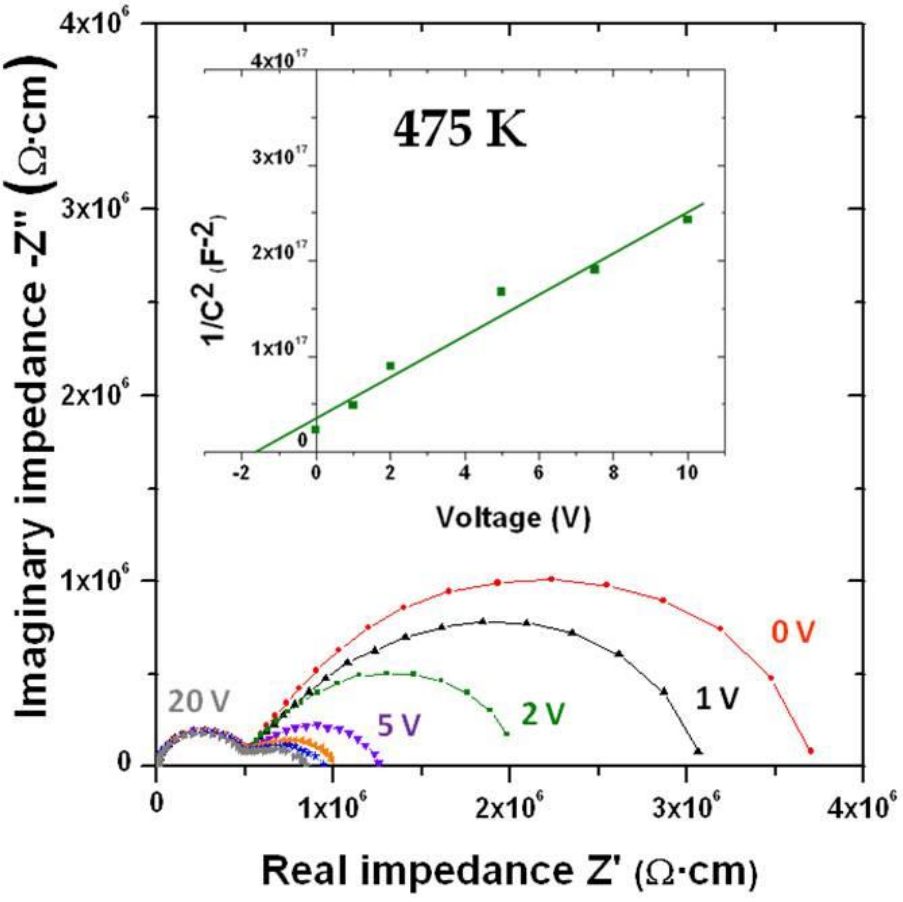

Figure 6.14. Complex impedance plot of $-Z''$ vs. Z' for $Ce_{0.8}Sm_{0.18}Ca_{0.02}O_{1.9-\delta}$ at 475 K, using different dc voltages from 0 to 20 V. Inset: Plot of $1/C^2$ where C is the capacitance as a function of applied DC bias.

Undoped $CeO_{2-\delta}$

The charge transport properties in $CeO_{2-\delta}$ show the signs of a significant electronic contribution, as is evident from the ε' vs. f curve for $CeO_{2-\delta}$ shown in Fig. 6.15. The curve does not show the typical behaviour of ionic conductors at low f mentioned above (Fig. 6.10). Fig. 6.15 shows that the interface dielectric permittivity approaches another ε' plateau at the low frequency end, consistent with the behaviour of a conventional dielectric relaxation as described by an RC element.

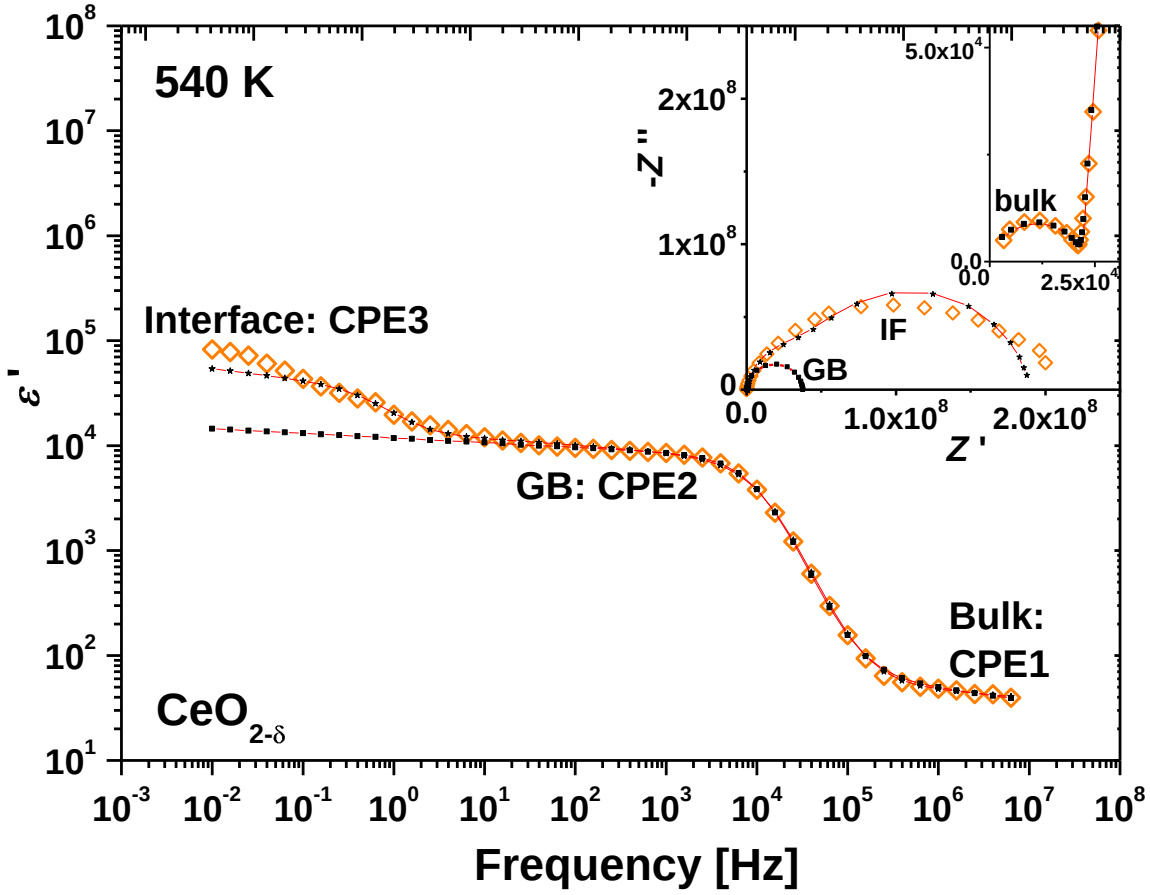

Figure 6.15. Relative dielectric permittivity ε' vs. f for $CeO_{2-\delta}$. Open symbols (◊) represent measured data, squares (■) and solid lines represent equivalent circuit fits using the model presented in Fig. 6.8, (*) represent fits to the model in Fig. 6.16. ***Insets:*** complex impedance plots of $-Z''$ vs. Z' on different resistivity scales exhibiting interface (low f), GB (intermediate f) and bulk (high f) semicircles.

The first figure inset demonstrates that the GB semicircle in $-Z''$ vs. Z' plots is overlaid by a conventional interface (IF) semicircle. Such semicircle overlap occurs, because the IF and GB time constants τ are similar. In the ε' vs. f

notation the IF and GB relaxations are clearly separated though, and two equivalent circuit fits were performed: one with a circuit containing a series of 2 R-CPE elements for the bulk and GB relaxations at high/intermediate *f* (■), and another fit with 3 series R-CPE elements for the bulk, GB and interface (IF) relaxations over the full frequency range. Without an interface "pike" structure in the $-Z''$ vs. Z' plot and the interface response being consistent with a conventional RC element, the signs of a blocking electrode are missing in $CeO_{2-\delta}$. Ionic charge transport is not indicated and an electronic contribution appears to be dominant.

The second Fig. 6.15 inset shows the same data as in the first inset but is magnified at the high frequency end. The $CeO_{2-\delta}$ bulk semicircle can be seen clearly, whereas the GB semicircle appears to be much larger in size, which indicates a large difference between bulk and GB resistivity. This confirms the findings of Fig. 6.11 and Fig. 6.12 and is illustrated in plots of $-Z''$ vs. *f* depicted in Fig. 6.16: two peaks can be seen, which are largely separated in magnitude on both the $-Z''$ *y*-axis and the frequency *x*-axis. It has to be noted though that the high resistivity peak at low frequency is in fact a double peak, consisting of the GB and IF contributions (as indicated).

The low $CeO_{2-\delta}$ bulk resistivity is believed to be a result of incomplete oxygenation and the formation of oxygen vacancies (δ). Such vacancies would be compensated by partial reduction of Ce^{4+} to Ce^{3+}, leading to electronic hopping conductivity.[38] Fully oxygenated CeO_2 is expected to be insulating, and the formation of oxygen vacancies may be the only plausible mechanism to induce perceptible conductivity into undoped cerium oxide.

The high GB resistivity in $CeO_{2-\delta}$ (Fig. 6.11) suggests that the GB areas showed significantly higher levels of oxygenation as the bulk, which is a common feature in electroceramic materials. Generally, the MW synthesized $CeO_{2-\delta}$ sample seems little suitable for ionic conductor applications in contrast to the rare-earth doped specimen. The equivalent circuit for $CeO_{2-\delta}$ with a series

of 3 R-CPEs is shown in Fig. 6.16, giving an imperfect match between data and model at low frequencies due to the strong overlap of GB and IF relaxations (see also Fig. 6.15).

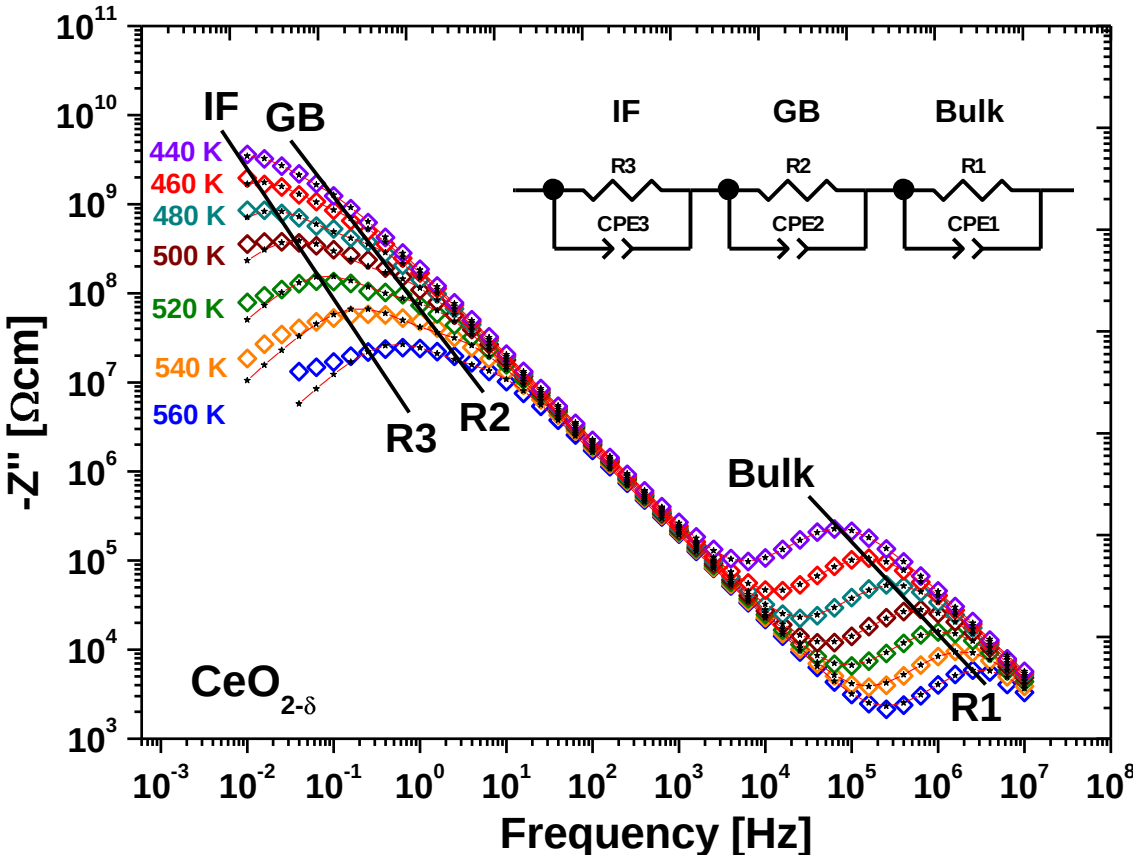

Figure 6.16. Imaginary part of the impedance (−*Z*″) plotted vs. frequency for $CeO_{2-\delta}$. Two relaxation peaks are displayed, one double peak structure for the GB and the interface (IF) and one for the bulk dielectric relaxation. Open symbols (◇) represent measured data, stars (*) and solid lines represent equivalent circuit fits using the model presented in the figure.

6.3. $BiFeO_3$

$BiFeO_3$ is one of the most intensively studied multiferroic materials, because its ferroelectric and antiferromagnetic ordering occurs concurrently at room temperature.[39] $BiFeO_3$ is a rhombohedrally distorted ferroelectric perovskite (Tc ≈ 1100 K) with G-type canted antiferromagnetism up to 643 K (T_N), where all neighboring magnetic spins are oriented antiparallel to each other.[40] This antiferromagnetism is caused by superexchange interaction via the

oxygen atoms connecting Fe^{3+} cations. The antiparallel alignment of the Fe spins is not perfect because the Dzyaloshinskii-Moriya interaction produces a slight canting of the magnetic moments and thus, weak ferromagnetism appears.[41] The average-bulk magnetism tends to zero because their resultant magnetic moments generate an incommensurable cycloid with a zero net magnetization. Ferroelectricity in $BiFeO_3$ is well established to be driven by the Bi^{3+} lone pair electrons (Figure 6.17).[42-45]

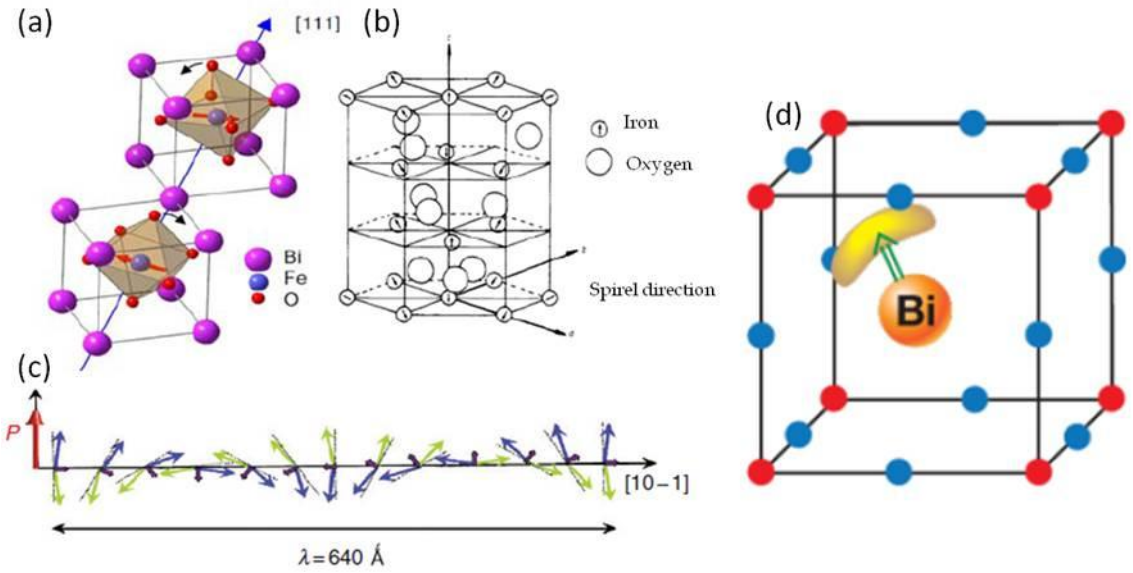

Figure 6.17. a) Crystal structure of bulk $BiFeO_3$.[41] b) The part of the $BiFeO_3$ lattice with only iron and oxygen ions is shown. The arrows indicate the direction of the Fe^{3+} magnetic moment.[44] c) Incommensurate cycloidal distribution of resultant magnetic dipoles.[45] d) In $BiFeO_3$ the ordering of lone pairs (yellow part) of Bi^{3+} cations, contributes to the polarization (green arrow).[43]

$BiFeO_3$ synthesis is often performed by the high temperature ceramic method which has several drawbacks. For synthesizing $BiFeO_3$, the kinetics of phase formation in the Bi_2O_3-Fe_2O_3 system can easily lead to the appearance of secondary phases such as Bi_2O_3, mullite-type $Bi_2Fe_4O_9$, and sillenite-type $Bi_{25}FeO_{39}$.[46, 47] Furthermore, the high volatility of Bi makes high temperature processing troublesome.

Besides the solid state route, several alternative techniques have been used to prepare this material: wet chemical routes, rapid sintering process,

hydrothermal methods.[48-55] In order to obtain a pure phase, the temperature and time of the heat treatment are critical. For instance, more than one hour treatment at 600 °C induces decomposition of the compound. $BiFeO_3$ is a metastable phase at this temperature and decomposes according to the reaction:

$$49\ BiFeO_3 \rightarrow 12\ Bi_2Fe_4O_9 + Bi_{25}FeO_{39},$$

So one must take care to avoid long heat treatments.[56] According to all versions of published binary phase diagrams (Figure 6.18),[57, 58] these phases are not thermodynamically compatible.

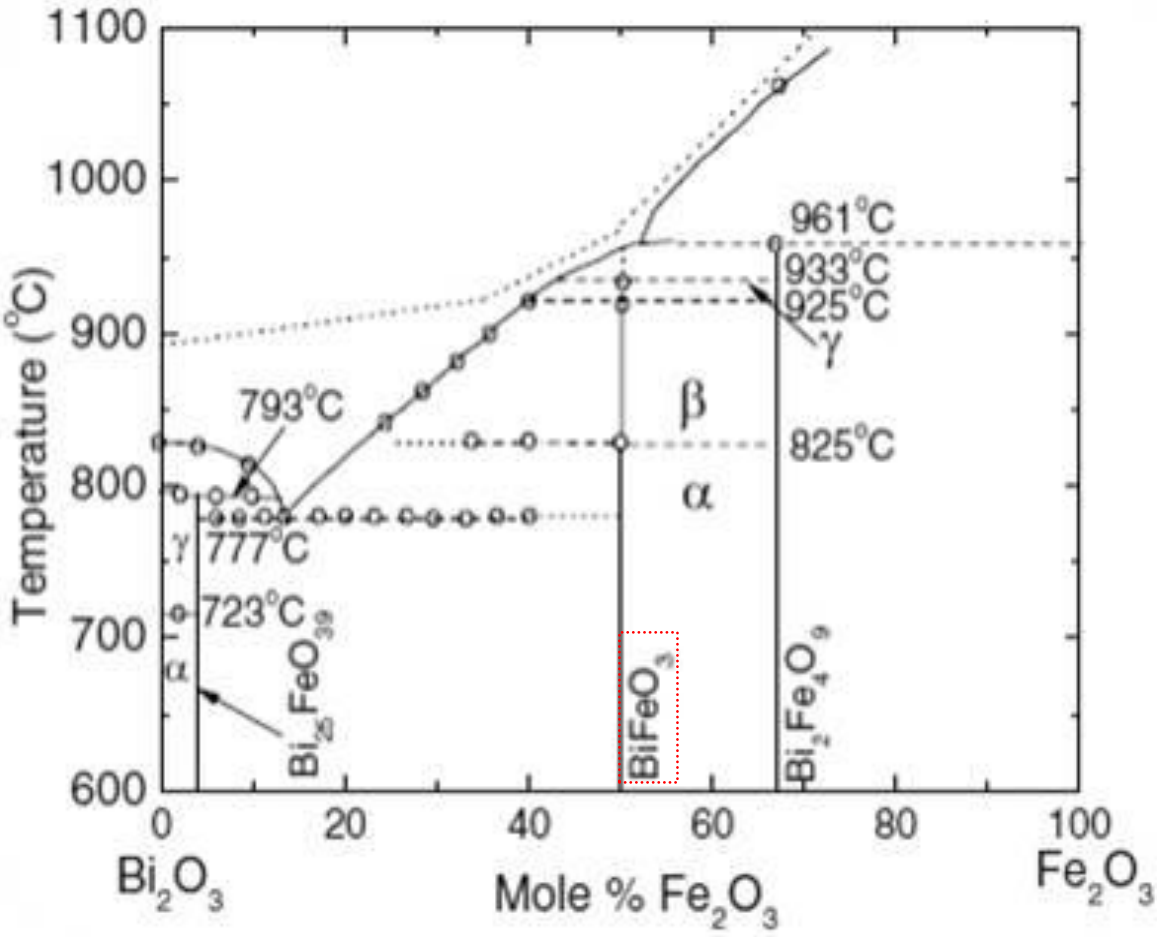

Figure 6.18. Phase diagram of the Bi_2O_3-Fe_2O_3 system. The α, β and γ phases are rhombohedral, orthorhombic and cubic, respectively. Reproduced from Palai *et al*.[58]

Moreover, at higher temperatures phase transitions take place: a transition to a $GdFeO_3$-type orthorhombic phase (β-polymorph) has been

reported to occur above 825 ^{o}C (close to, or associated to the ferroelectric transition) and a third cubic polymorph ("γ-phase") has been claimed.[59] Taking all of this into account it is clear that a low temperature synthesis method for $BiFeO_3$ is more convenient.

Further problems in $BiFeO_3$ high temperature synthesis are related to ionic valences and oxygen stoichiometry because Fe^{2+} can be easily formed if accompanied by oxygen vacancies to keep the charge balance, with a concomitant change of the magnetic and electric properties.[60]

The $BiFeO_3$ crystal lattice is generally accepted to possess a trigonal symmetry, with space group *R3c* (# 161),[61] but a distorted tetragonal phase (*P4mm*) has been identified also in thin films under strain.[62] Besides, chemical doping of $BiFeO_3$ can stabilize more structure types. For example, it has been recently reported that the solid solution $0.8BiFeO_3$-$0.2BaTiO_3$ processed by high energy ball milling yields a monoclinic phase *Cm* (# 8).[63]

Furthermore, the sintering is another critical problem: with increasing temperature, Bi^{3+} tends to evaporate, causing stoichiometric variations as mentioned above.[64] For the study of electric properties and actual applications of $BiFeO_3$ ceramics, it is necessary to synthesize high resistivity samples, achieving sintered densities above 90% of the theoretical density, which is a difficult task using the conventional sintering procedures. In this work single-mode microwave sintering is demonstrated to yield high density pellets using moderate temperatures.

Thus, the aim of this section is to ascertain the space group and analyse the microstructure of $BiFeO_3$ powder prepared as a single phase by a new, low temperature and fully reproducible method. Furthermore magnetic and dielectric properties have been investigated.

6.3.1. Synthetic aspects

Initial reactants were 10% excess $Bi(NO_3)_3 \cdot 5H_2O$ (Merck, 98%) and $Fe(NO_3)_3 \cdot 9H_2O$ (Merck, 98%) in different KOH concentrations (2 M, 4 M, 8 M). The heating ramp up to 200 °C was set to ≈ 12 °C/min, and the reaction was carried out at 200 °C in a teflon vessel during 15 min and 30 min under 13 bar pressure and with power limited to 500 W in the Milestone Ethos One microwave. Finally, the products were decanted and leached with HNO_3 2 M, water rinsed to eliminate remaining impurities, and dried at 80 °C in a conventional oven. To complete oxidation of the iron atoms from Fe^{2+} to Fe^{3+}, the sample was heat treated at 300 °C during 3 hours in flowing oxygen.

A possible multistep formation mechanism is suggested as follows. First, $BiONO_3$ is formed by hydrolyzation of $Bi(NO_3)_3 \cdot 5H_2O$. Next, $Fe(OH)_3$ may form from the reaction between $Fe(NO_3)_3 \cdot 9H_2O$ and KOH. Subquently, they nucleate to form $BiFeO_3$ and Bi_2O_3 because of the excess of $Bi(NO_3)_3 \cdot 5H_2O$. HNO_3 2 M eliminates this secondary phase (Figure 6.19).

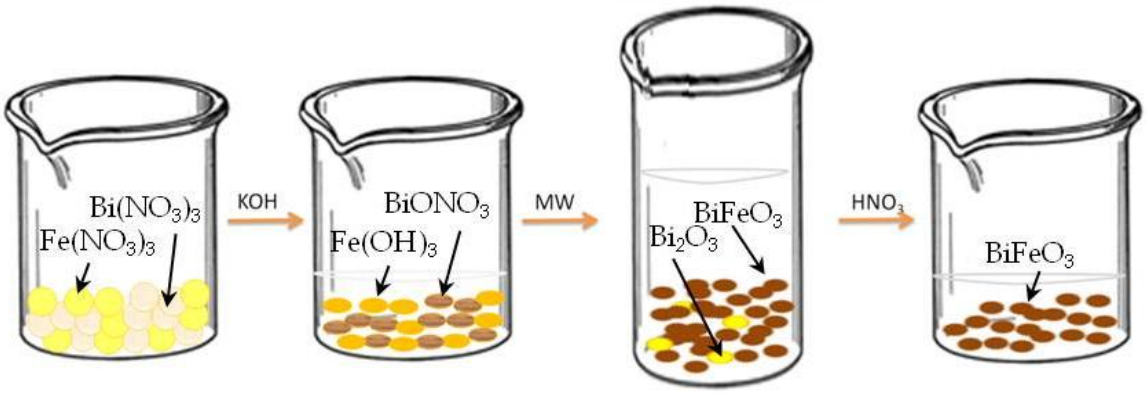

Figure 6.19. Sequence picture of the $BiFeO_3$ synthesis

The reactions involved during this process are as follows[65]:

$$BiONO_3 + H_2O \leftrightarrow Bi^{3+}_{aq} + 2OH^- + NO_3^-$$

$$Fe^{3+} + 3OH^- \rightarrow Fe(OH)_3 \leftrightarrow FeO_3^{3-}{}_{aq} + 3H^+$$

$$Bi^{3+}_{aq} + FeO_3^{3-}{}_{aq} \rightarrow BiFeO_3$$

Furthermore, the concentration of KOH is essential for the morphology of the sample, as explained in *section 6.3.3. Microstructural characterization*.

Single-mode microwave sintering has been employed after the synthesized powders were compacted into pellets in a uni-axial 2 ton die press for 5 min. The sintering procedure is similar to that previously described for $Ce_{0.8}Sm_{0.18}Ca_{0.02}O_{1.9-\delta}$. The pellet was introduced into a SiC crucible and 5 minutes of single – mode microwave irradiation proved to be sufficient to obtain a high density pellet (93 %) in the TE_{102} mode. The temperature measured by the pyrometer focused on the sample surface was 750 ^{o}C and power was limited to 120 W.

6.3.2. Structural characterization

The generally accepted trigonal space group *R3c* (# 161),[40, 61, 66] as well as the recently suggested monoclinic symmetry [*Cm* (# 8) and *Cc* (#9)],[62] were tested in the search for the best Rietveld refinement fit in the $BiFeO_3$ powder sample, prepared using KOH 4M during 30 minutes microwave irradiation.

The best fit was obtained with the trigonal *R3c* model (see Fig. 6.20a). Table 6.2 shows the results of the performed structural analysis. The coordinates of bismuth atoms, which are located at high-symmetry sites, were taken as a reference. The oxygen temperature factor did not show stability and it was fixed during the refinement. The final reliability factors were: R_p = 4.62, R_{wp} = 6.26, R_{exp} = 3.52 and χ^2 = 3.16. Refinement results using a monoclinic *Cc* model led to similar reliability factors, specifically R_p = 4.34, R_{wp} = 6.09, R_{exp} = 3.12 and χ^2 = 3.81 so the difference is not large enough to fully discriminate any symmetry by this method (Figure 6.20b).

Correction of intensities to counterbalance the influence of possible preferred crystallize orientation is necessary. Preferred orientations can be easily recognized by powder diffraction using the (012) reflection for *R3c* or the (200) for *Cc* (Figure 6.20a and 6.20b). Electron microscopy has been used, as described in *section 6.3.3*, as a powerful and complementary structural tool to unambiguously determine the symmetry. There is no evidence of texture in the oxygenated sample (Figure 6.21).

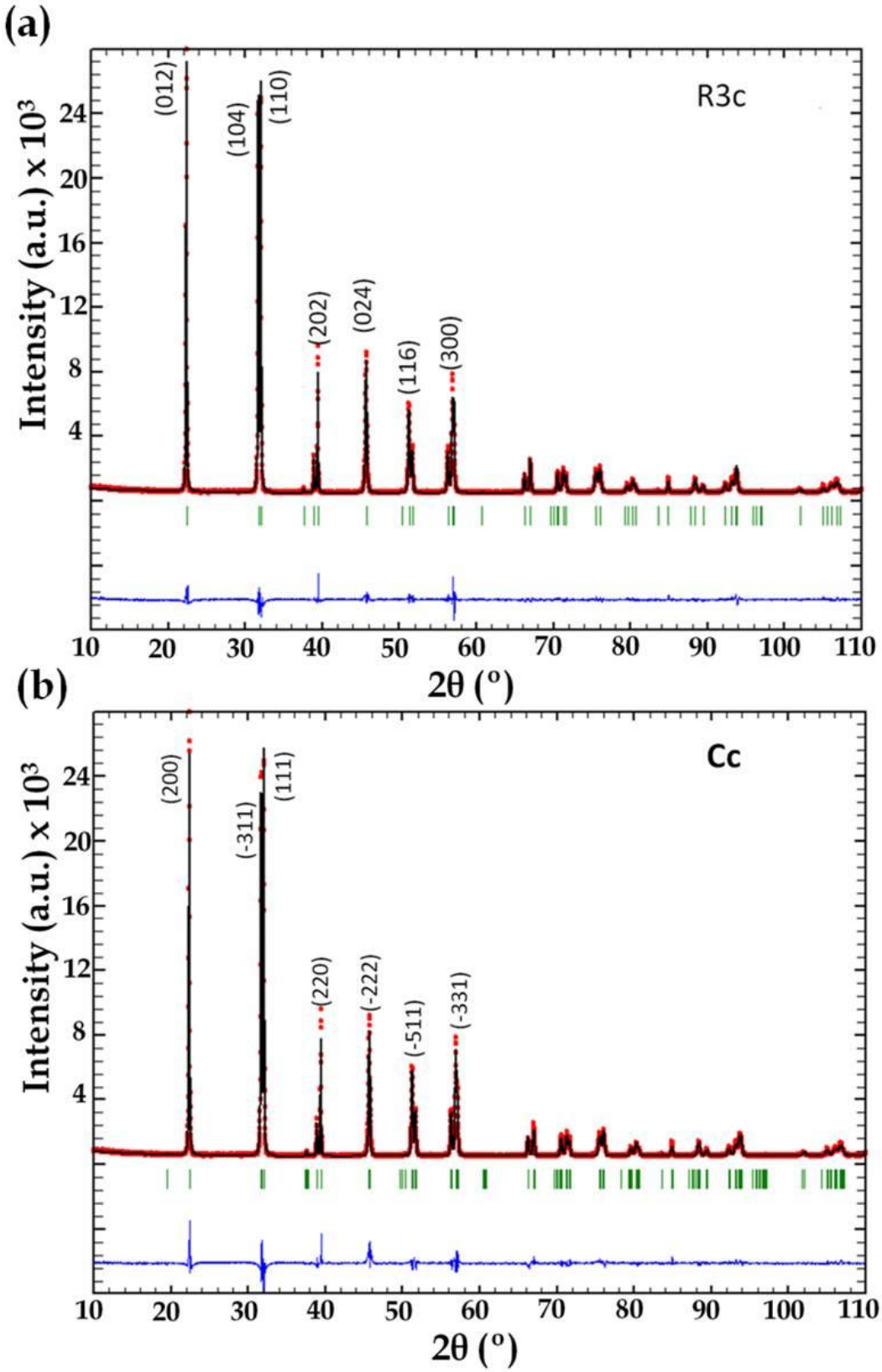

Figure 6.20. Rietveld refinement: Observed and calculated diffraction patterns of $BiFeO_3$ prepared by microwave hydrothermal method during 30 minutes using KOH 4M a) *R3c* space group b) *Cc* space group.

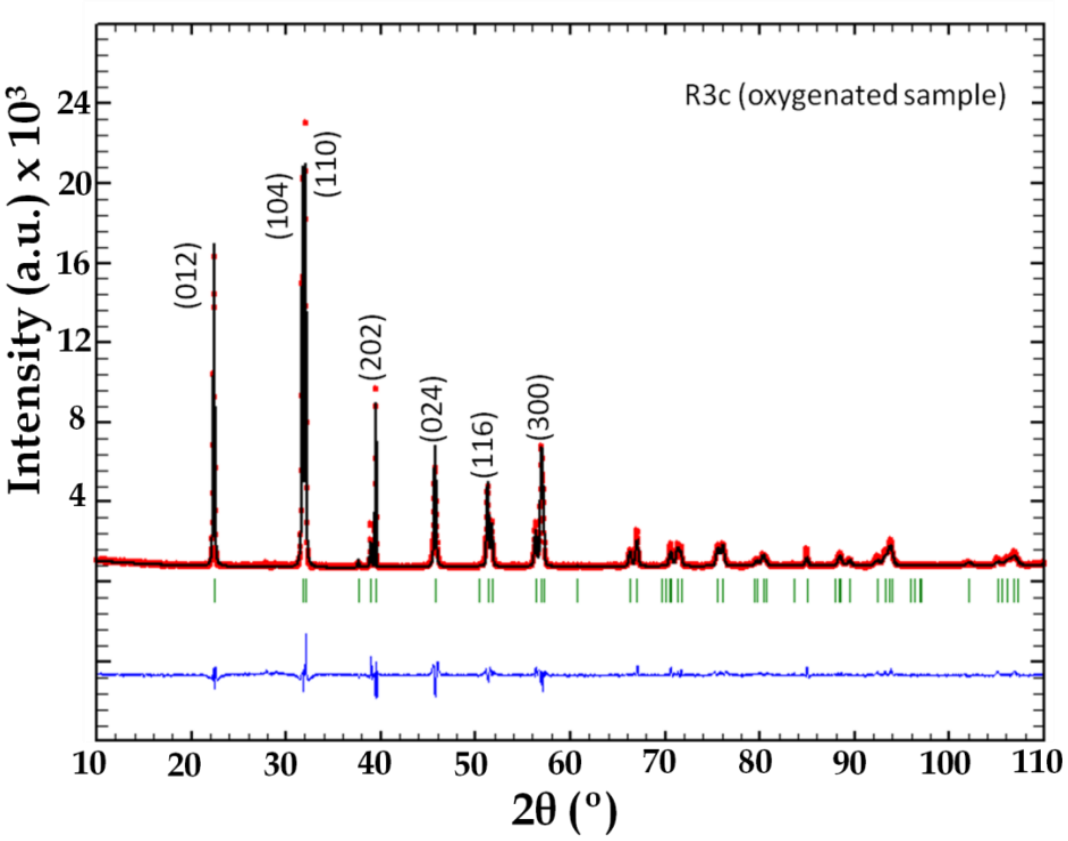

Figure 6.21. Rietveld refinement: Observed and calculated diffraction patterns of oxygenated $BiFeO_3$ prepared by microwave hydrothermal method during 30 minutes using KOH 4M using *R3c* space group. (R_p = 4.51, R_{wp} = 6.60, R_{exp} = 3.12 and χ^2 =4.47)

Table 6.2. Cell and atomic parameters of $BiFeO_3$ prepared by the microwave hydrothermal method during 30 minutes using KOH 4M obtained from Rietveld refinement.

	$BiFeO_3$	$BiFeO_3$ (oxygenated)
$a = b$ (Å)	5.58068(5)	5.5790(1)
c (Å)	13.8725(1)	13.8674(3)
Bi position	6a	
U*100 (Å^2)	0.48(1)	0.97(2)
Fe position	6b	
z	0.7210(1)	0.7212(3)
U*100 (Å^2)	0.77(7)	0.70(1)
O position	18b	
x	0.909(1)	0.9191(2)
y	0.204(1)	0.224(2)
z	0.6204(4)	0.6595(8)
U*100 (Å^2)	0.20	0.20

6.3.3. Microstructural characterization

Due to the ambiguity of the X-ray diffraction patterns to distinguish between both crystal systems, a transmission electron microscopy study has been performed. The SAED (Selected Area Electron Diffraction) study of the reciprocal space (Figure 6.22) shows that the reflection conditions are consistent either with trigonal space group *R3c* (hexagonal unit cell $a_o = b_o = 5.58$ Å and $c_o = 13.87$ Å) or with monoclinic *Cc* (a =9.80 Å b = 5.57 Å, c = 5.62 Å and $\beta = 125^o$). The semi-quantitative EDS analysis of the metal composition over 10 crystals yields an average composition of $Bi_{0.98(4)}Fe_{0.99(3)}$, in good agreement with the nominal one.

Choosing between a trigonal cell and a monoclinic one is actually just a convention, because both cells are equivalent. *R3c* is a minimal non isomorphic supergroup of index 3 of the *Cc* space group[67] and SAED cannot distinguish between both cases, because the same reflections would be present, with the same spacing, changing only the nomenclature of the *hkl* indices, e.g., the 001 monoclinic cell reflection would be equivalent to the -1102 trigonal cell reflection (see Figure 6.22)

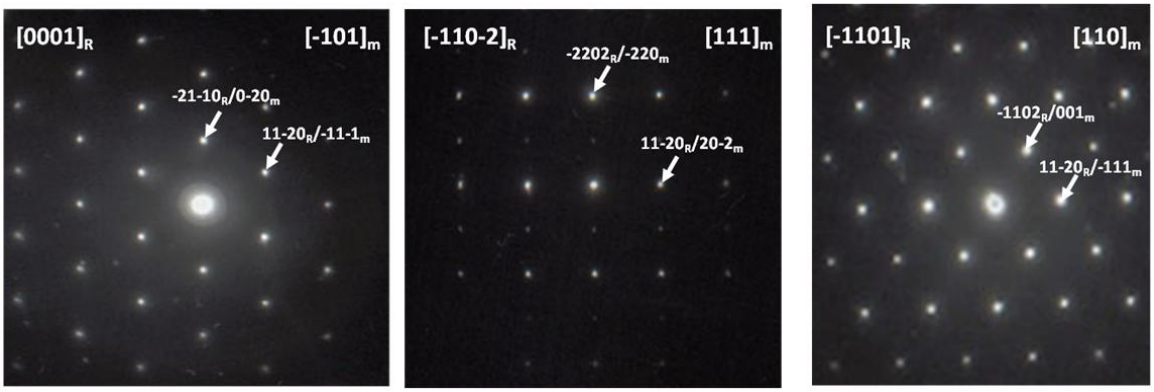

Figure 6.22. SAED patterns along the zone axes $[0001]_R/[-101]_m$, $[-110-2]_R/[111]_m$, $[-1101]_R/[110]_m$ of 30 minutes microwave irradiated $BiFeO_3$ sample. The subscripts R and m define trigonal and monoclinic symmetry respectively.

In order to distinguish *R3c* and *Cc* a micro-diffraction analysis is required. Micro-diffraction patterns allow obtaining the crystal symmetry by

employing the "net" symmetry, which is that of a lattice created from the reflections in the pattern. Since the "net" symmetry of the reciprocal lattice depends on the crystal system, the "net" symmetries of the micro-diffraction patterns are directly connected with the crystal system.[68]

In Figure 6.23, the micro-diffraction pattern from the $[0001]_R$ or $[-101]_m$ is displayed. The zero order Laue zone (ZOLZ) net symmetry for a trigonal *R3c* system along [0001] is 6mm whereas it must be 2mm along [u0w] in the monoclinic *Cc* case (see Table 6.3). The ZOLZ symmetry observed in the experimental pattern is 6mm indicating that the true crystal symmetry is trigonal in the *R3c* space group.

Table 6.3. Relations between the "net" symmetry and the crystal systems.[68]

Space Group	**Net Symmetry in ZOLZ**	
	[0001]	[-101]
R3c	(6mm)	
Cc		(2mm)

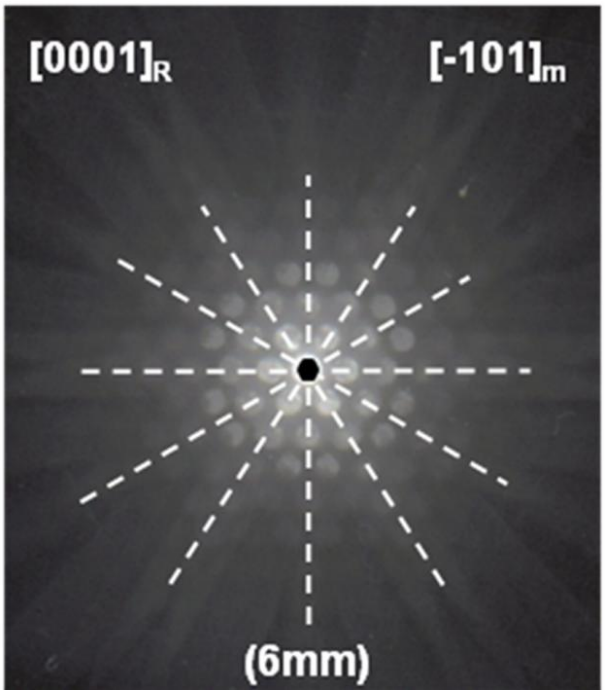

Figure 6.23. Microdiffraction pattern along $[0001]_R/[-101]_m$ zone axis showing net symmetry (6mm) in the ZOLZ.

The absence of extra reflections or streaking in SAED patterns indicates a well-ordered structure. In order to confirm the degree of ordering of this material, an HREM study was carried out.

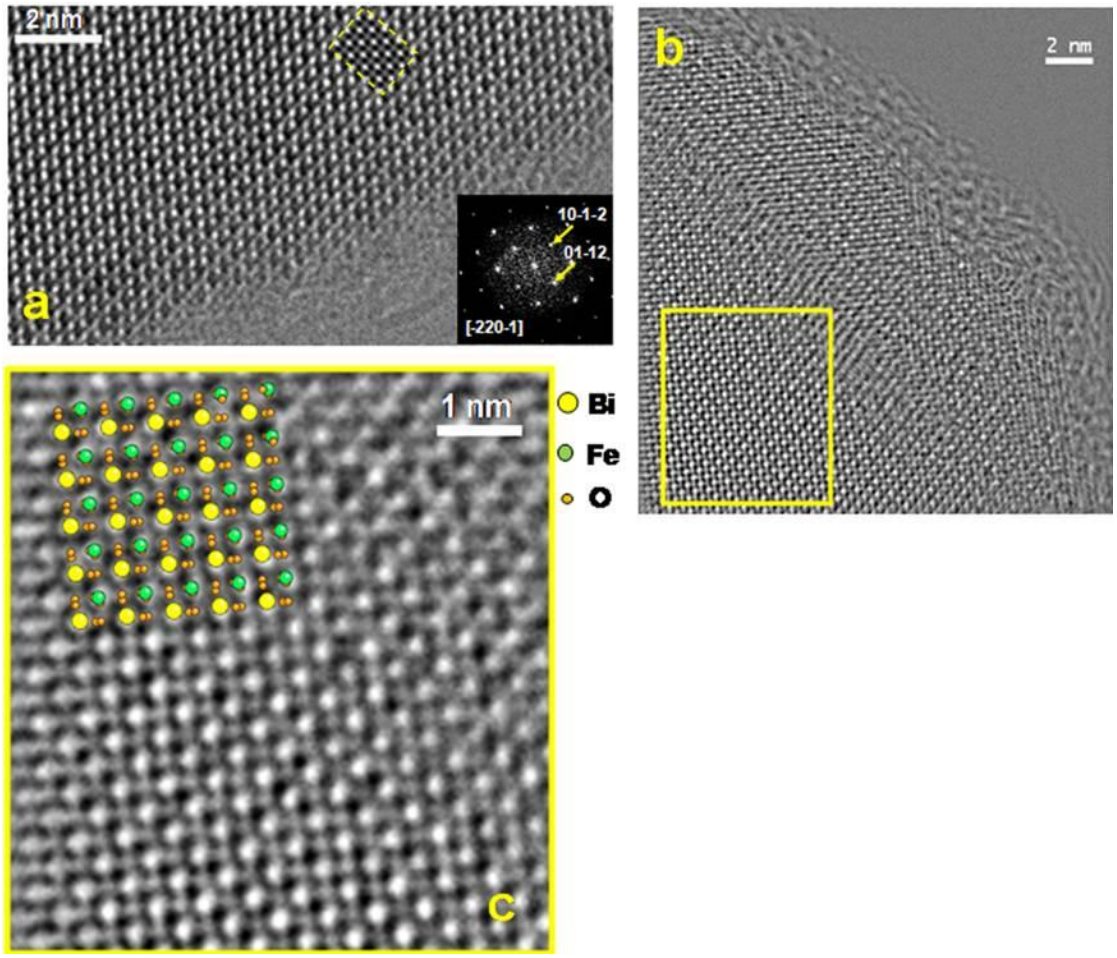

Figure 6.24. a) Conventional HRTEM image from a thin crystal of $BiFeO_3$ along [-220-1] showing the cation arrangement, and the good agreement with the calculated cell (see the inset within the yellow markers). b) Phase of the reconstructed exit wave function from a focal series of a different area of the same specimen with all the cations and anions resolved. c) Enlargement of the squared yellow area of b) with the projected atomic model overlapped.

A conventional HRTEM image along the [-220-1] zone axis with the restored exit wave phase along the same zone axis is presented in Fig. 6.24a. It is remarkable that in the HRTEM image taken near the Scherzer defocus (notice the good matching of the calculated image, squared in yellow, for a defocus value Δf =−400 Å and a thickness t = 30 Å) only the heavy Bi and Fe atoms are visible as dark blobs, however the phase image shows an improvement in resolution details and both cations and the light oxygen anions are clearly

imaged with the contrast inverted. Figure 6.24c shows further detail extracted from an enlarged area of Figure 6.24b, together with the projected structural model. This structural image confirms the absence of any distortion yielding the trigonal symmetry as it has been observed in thin films.[62]

All the TEM characterization has been carried out for 30 minutes microwave irradiated samples which have been synthesized with KOH 4M. Furthermore, the influence of the KOH concentration was studied by SEM. It was found that the shape of the particles is strongly influenced by KOH. When the KOH concentration is in the range of 2 – 4 M polyhedral particles are evident, some of them present hexagonal faces and sizes up to 2 μm. When the KOH concentration is increased to 8 M, microcubes are gradually formed (Figure 6.25).

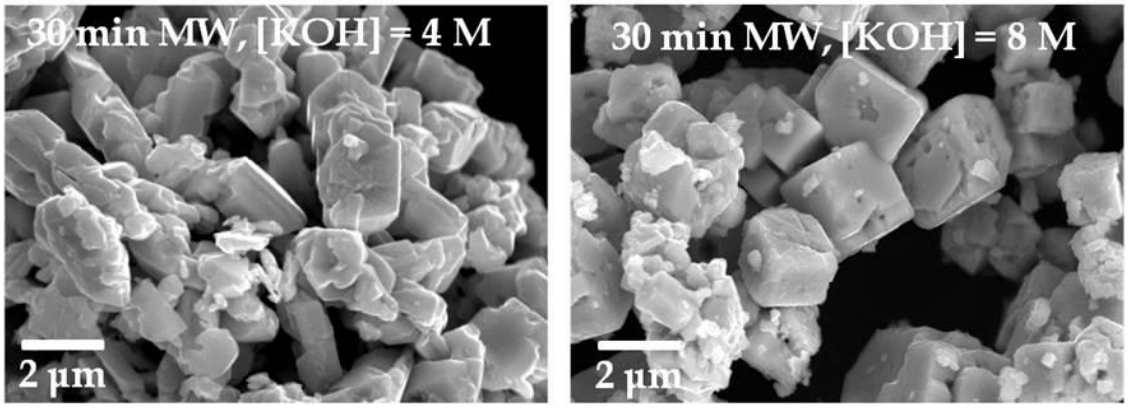

Figure 6.25. SEM micrograph of the $BiFeO_3$ samples after 30 minutes MW irradiation using different concentration of KOH a) 4 M b) 8 M.

It is interesting to remark that it is possible to obtain pure and crystalline $BiFeO_3$ just programming a heating ramp, without maintaining the solution for minutes at the maximum temperature, in the microwave-hydrothermal apparatus. Figure 6.26 shows the sequence of SEM pictures obtained by using different microwave irradiation time using KOH 8 M. It is possible to observe that in all the cases microcubes are present and the rough surface of the cubes could be associated with the effect of KOH.

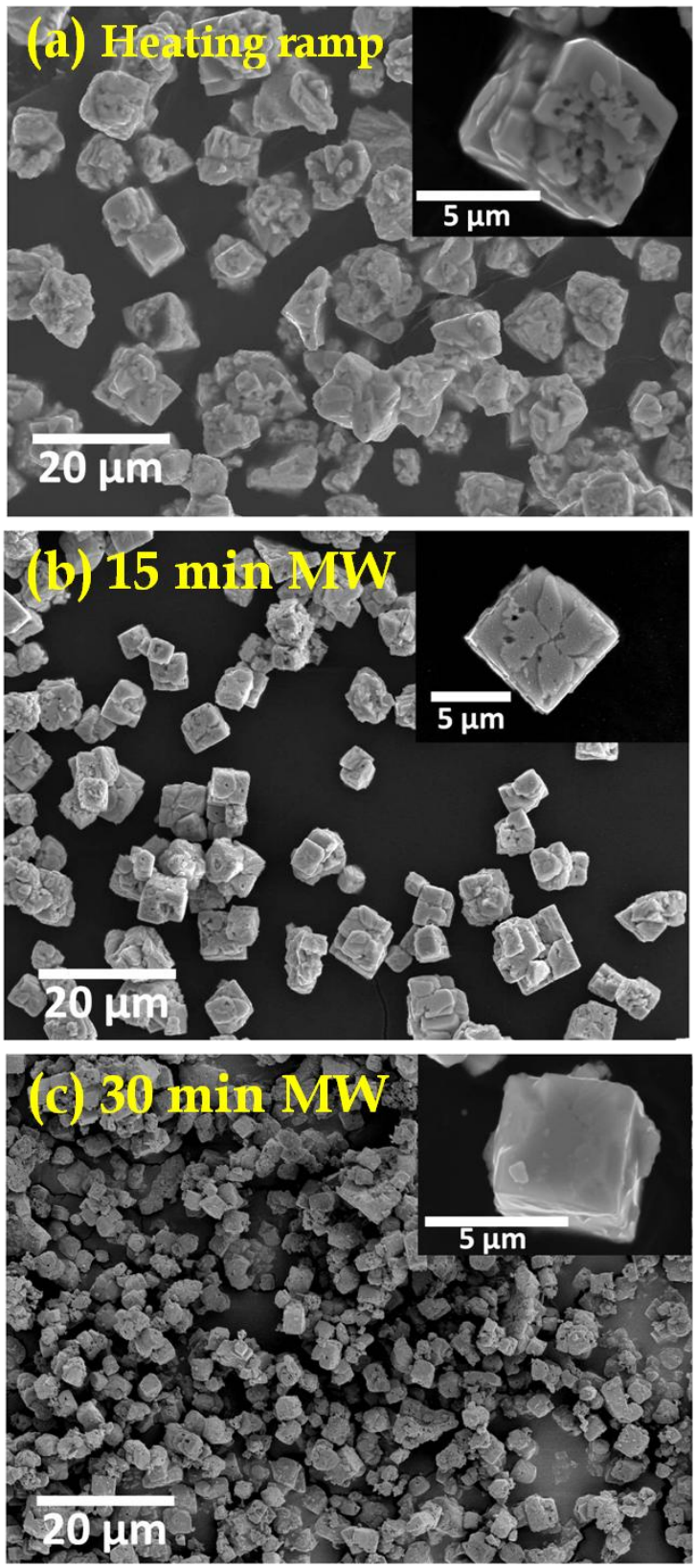

Figure 6.26. SEM micrograph of the $BiFeO_3$ samples using KOH 8 M at different microwave irradiation times. (a) Just the 15 min heating ramp, without maintaining the solution at the maximum temperature. After the heating ramp, the program was dwell for (b) 15 minutes and (c) 30 minutes.

6.3.4. DTA analysis

Figure 6.27 shows the DTA curve for $BiFeO_3$ (30 min MW – KOH 4 M, pristine sample) in the 400 °C to 1000 °C interval, where three endothermic peaks are observed. The first peak appears at 821 °C and has been reported as the ferroelectric phase transition. The peak at 915 °C may correspond to the incongruent melting temperature of $BiFeO_3$, and the endothermic peak at 957 °C corresponds to the incongruent melting point of $Bi_2Fe_4O_9$, which is formed at high temperature. Nevertheless, the reported antiferromagnetic - paramagnetic transition at ≈ 370 °C does not appear in this plot, probably due to the small amount of energy involved. The electric transitions are in good agreement with reported data.[69]

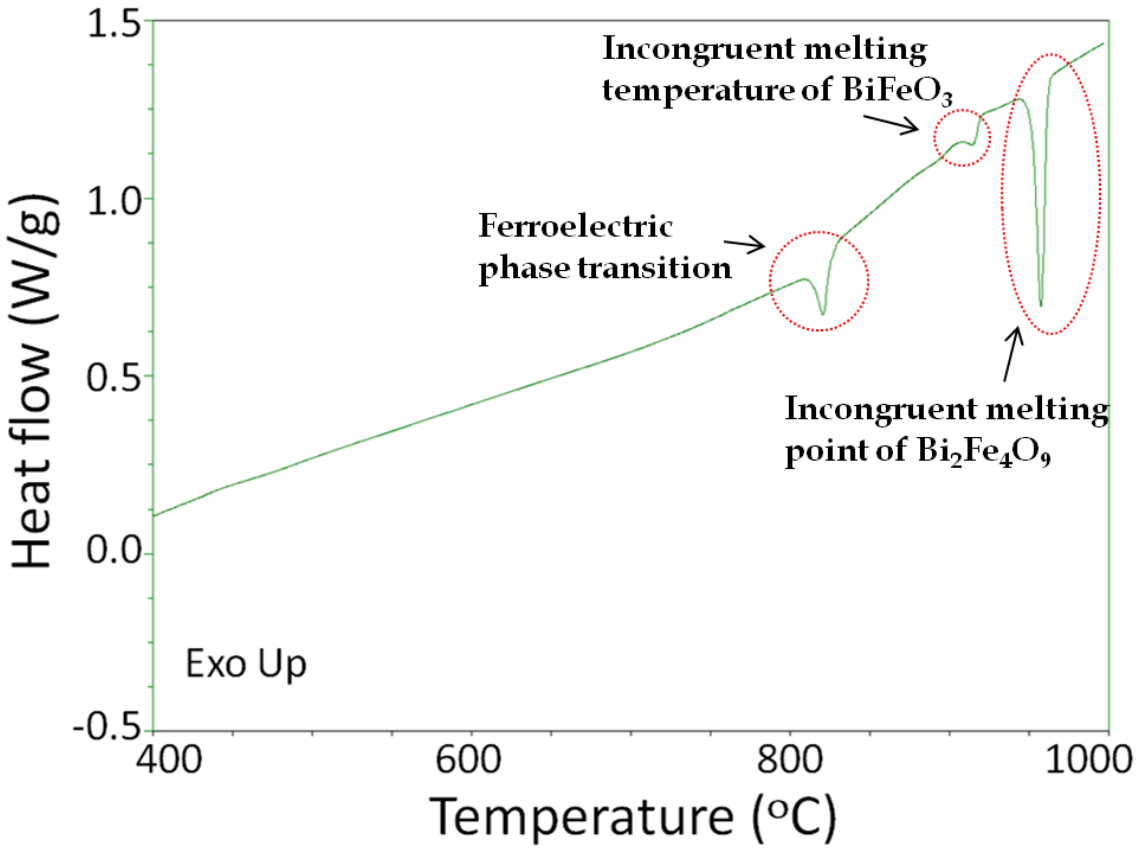

Figure 6.27. DTA curve for $BiFeO_3$ measured from 400 – 1000 °C

6.3.5. Magnetic properties

The observed magnetic behaviour for the as prepared microwave-hydrothermal $BiFeO_3$ (30 min MW, KOH 4M) (Fig. 6.28) is similar to that reported by S. Basu *et al.*[70] for samples synthesized with the standard hydrothermal method without microwaves. The inset in Fig.6.28 shows the temperature dependence of the inverse of susceptibility ($1/\chi$). The $1/\chi$ versus T curve in the paramagnetic state follows the Curie–Weiss law.

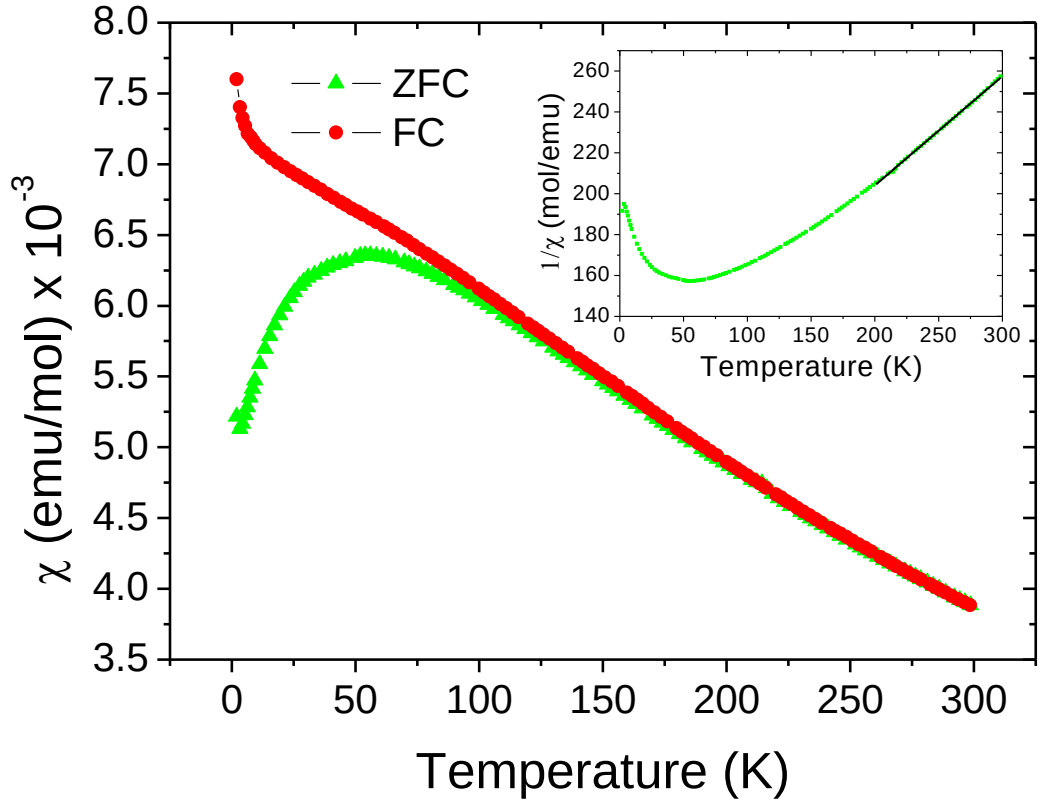

Figure 6.28. Temperature dependence of the magnetic susceptibility (χ) of $BiFeO_3$ at 1000 Oe. ZFC and FC curves are indicated by green triangles and red circles respectively. Inset: Inverse susceptibility $1/\chi$. The black solid line represents the fit of the data to the Curie–Weiss law.

Data fitting was carried out, as is indicated by a solid line in the inset of Fig. 6.28. The fitting procedure yielded: $C = 1.9$ and $\theta = -181$ K corresponding to a magnetic moment of 3.9 μ_B.

Plots of magnetization vs applied field collected at different temperatures confirm that these samples show a spontaneous magnetization which does not reach saturation indicating a small ferromagnetic moment.[71, 72] Weak ferromagnetism due to possible antiferromagnetism spin - canting has been suggested by earlier magnetic measurements.[73-75]

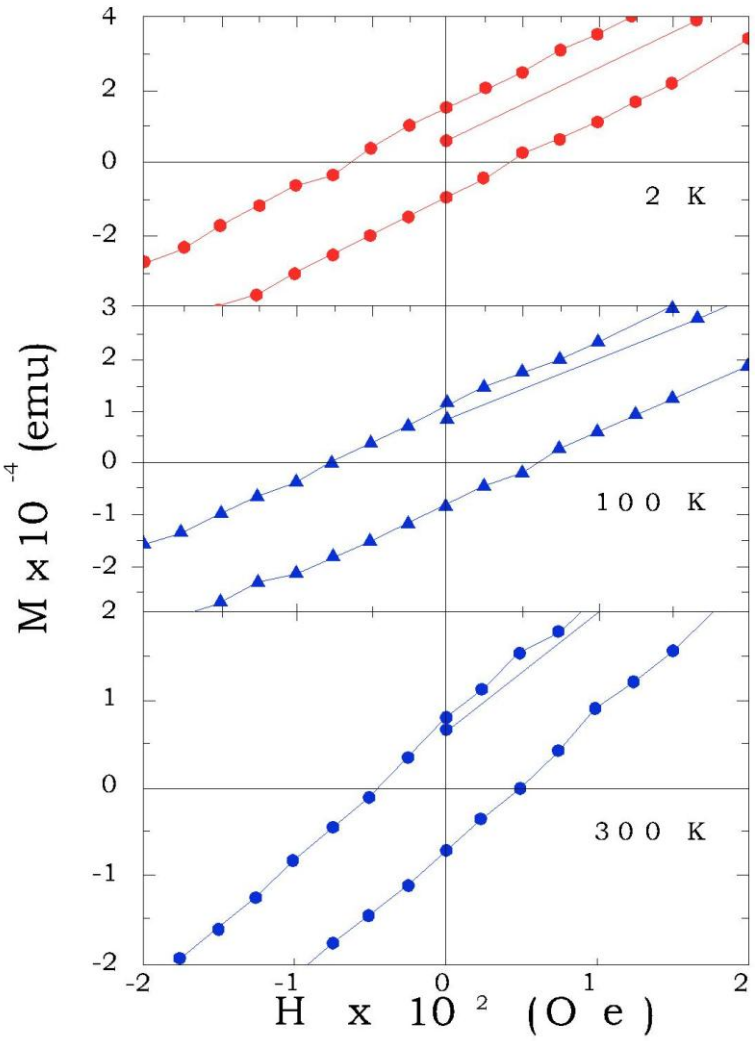

Figure 6.29. Isothermal magnetic measurements performed at three temperatures; 2, 100, and 300 K. Note the hysteresis, indicative of coercive field and characteristic of a ferromagnetic ordering.

In order to see if additional magnetic effects exist as competing processes in the surface and bulk, the coercive field is plotted as a function of temperature

in Fig. 6.30, from 2 to 300 K. Clearly, a small but distinct exchange bias is observed. This behaviour illustrates that two different magnetic orders exist in the sample: ferromagnetism and antiferromagnetism.

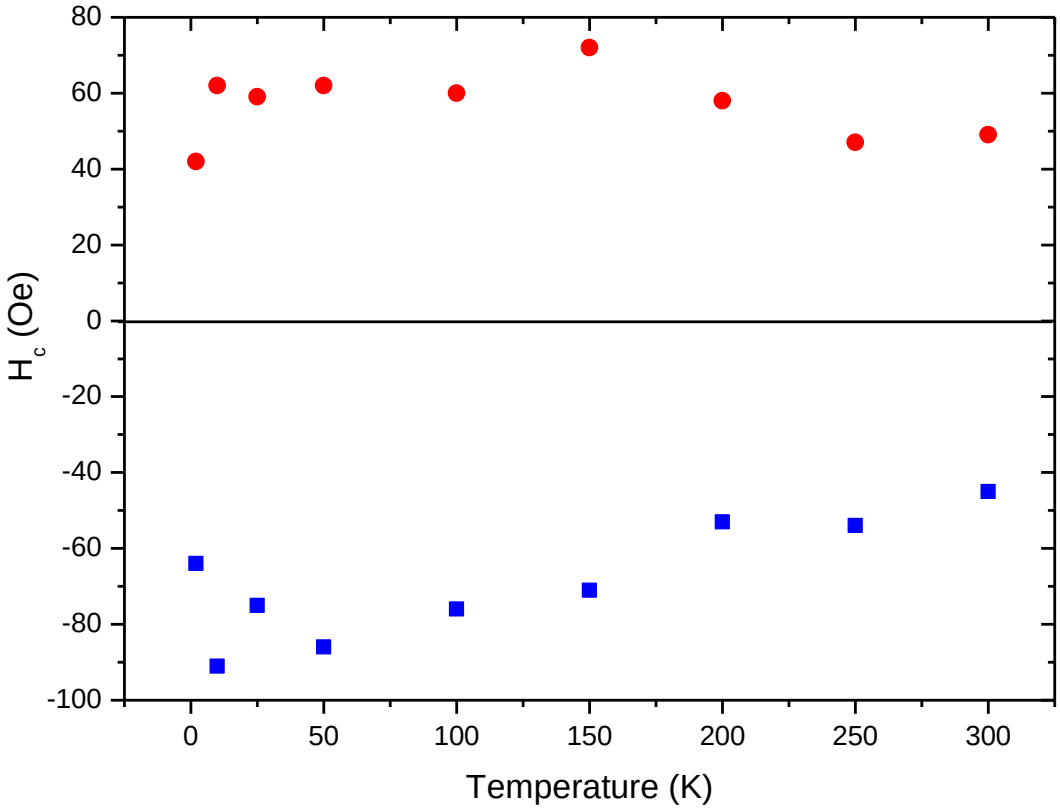

Figure 6.30. Coercive field, H_C, as function of temperature, both panels show the positive (red) and negative parts (blue). It is important to note the small but distinctive size in both the positive and negative parts. This is a clear indicating that a small exchange bias exists, probably due to ferromagnetic and antiferromagnetic orders.

6.3.6. Impedance spectroscopy

Figure 6.31 shows complex plane plots of Z'' vs. Z' at 530 K. Three different semicircles are displayed, which implies that the equivalent circuit displayed in the inset of Figure 6.31 would contain three RC elements in series to describe three series dielectric relaxations (bulk, GB and interface electrode). An unconventional ideal RC element with a CPE in parallel has been proposed to adequately fit the bulk relaxation. Such non - ideal, non-Debye-like behaviour of bulk electroceramics is well-documented and can often be

successfully modelled using a parallel combination of *R*, *C* and CPE components.[76]

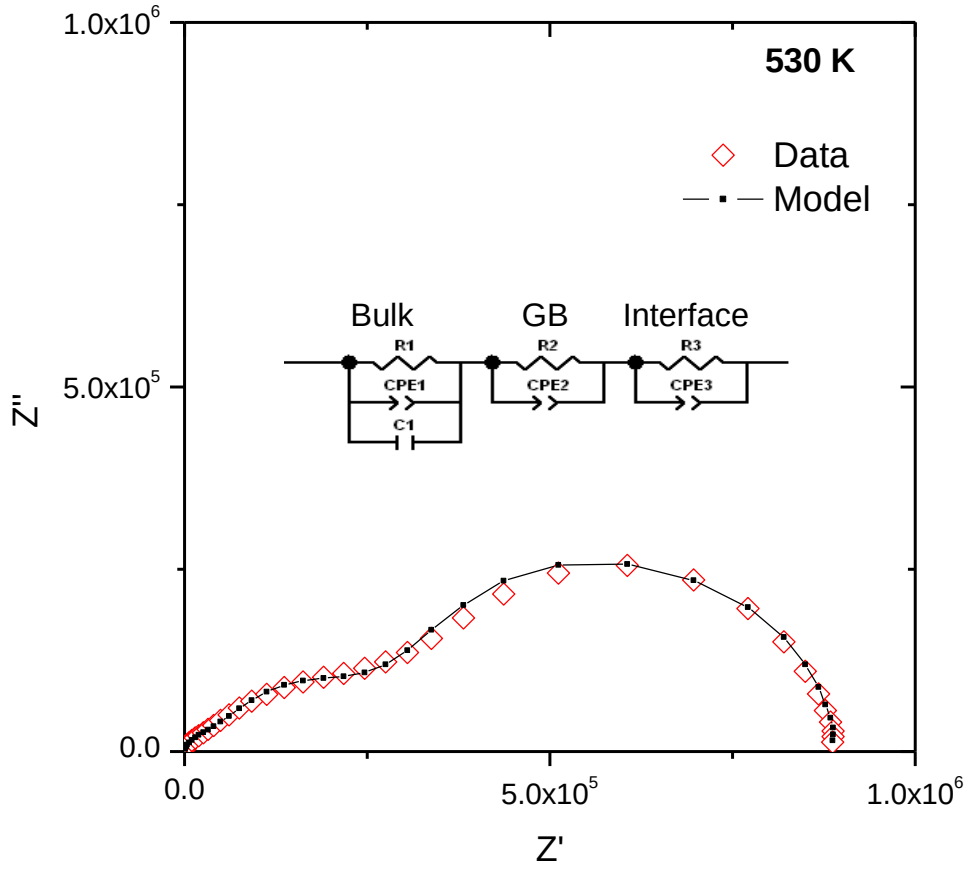

Figure 6.31. Plots of the imaginary vs real part of the impedance (-Z'' vs Z') at 530 K for $BiFeO_3$ sample (30 minutes MW, KOH 4 M). The equivalent circuit used for the fitting is depicted in the figure inset.

Resistivity values extracted from the data fits are illustrated in Fig. 6.32 on plots of logarithmic resistivity vs reciprocal temperature. The bulk resistance of the sample is relatively high confirming the insulating nature of the material. This suggests that the Fe cation is predominantly Fe^{3+} and there is no perceptible electronic conductivity due to the presence of Fe^{2+}. As it is shown in Figure 6.32 the activation energy (Ea) values of the sample, calculated using the Arrhenius relation, are high. These relatively high values of activation energy as compared with the literature value (0.65 – 0.86),[33, 77] indicate a more pronounced insulating behaviour of this sample.

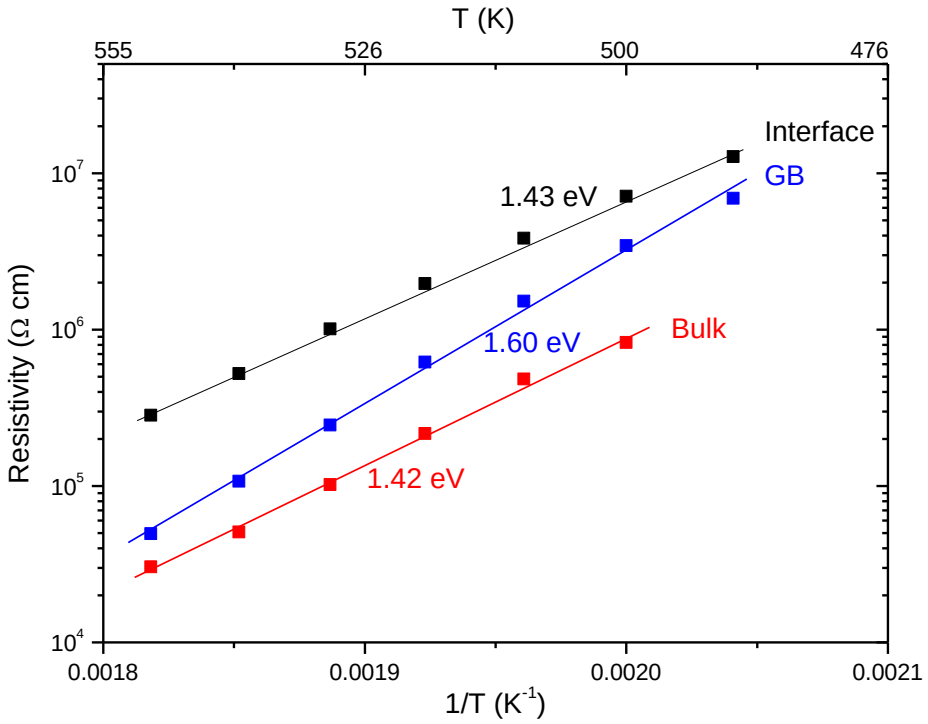

Figure 6.32. Resistivity plotted vs reciprocal temperature 1/T for $BiFeO_3$ sample (30 minutes MW, KOH 4 M) for the different relaxations. Solid lines are guides to the eyes, indicating good linearity and Arrhenius behaviour.

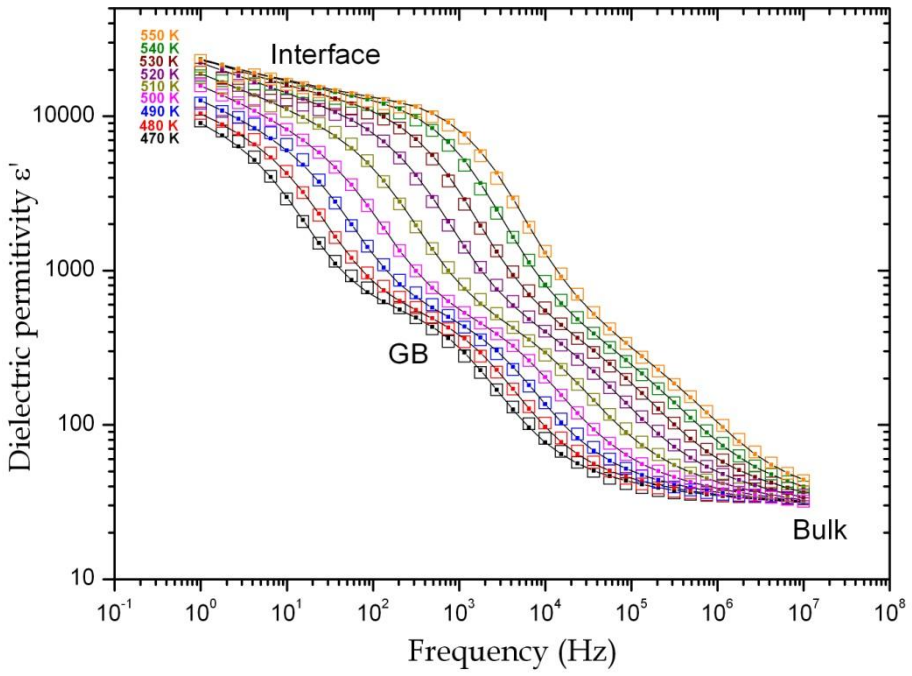

Figure 6.33. Relative dielectric permittivity ε' vs f for $BiFeO_3$ sample (30 minutes MW, KOH 4 M). The dielectric response is well represented by the equivalent circuit presented in Figure 6.31. Open symbols (◊) represent measured data, squares (■) and solid lines represent equivalent circuit fits using the model.

The impedance was also converted into the real parts of dielectric permittivity ε' (Fig. 6.33): the ε' vs. f spectra for the sample show 3 distinct regimes, where the bulk, GB and interface contributions are manifested by approximately frequency independent ε' plateaus each (as indicated in the graph). The dielectric response is well represented by the proposed equivalent circuit (Figure 6.31).

Figure 6.34 shows the temperature dependence of the dielectric permittivity at selected frequencies. An unexpected transition about 430 K appears. The magnetic properties at this temperature should be studied in future work to check if there is any relationship between the magnetism and the dielectric behaviour.

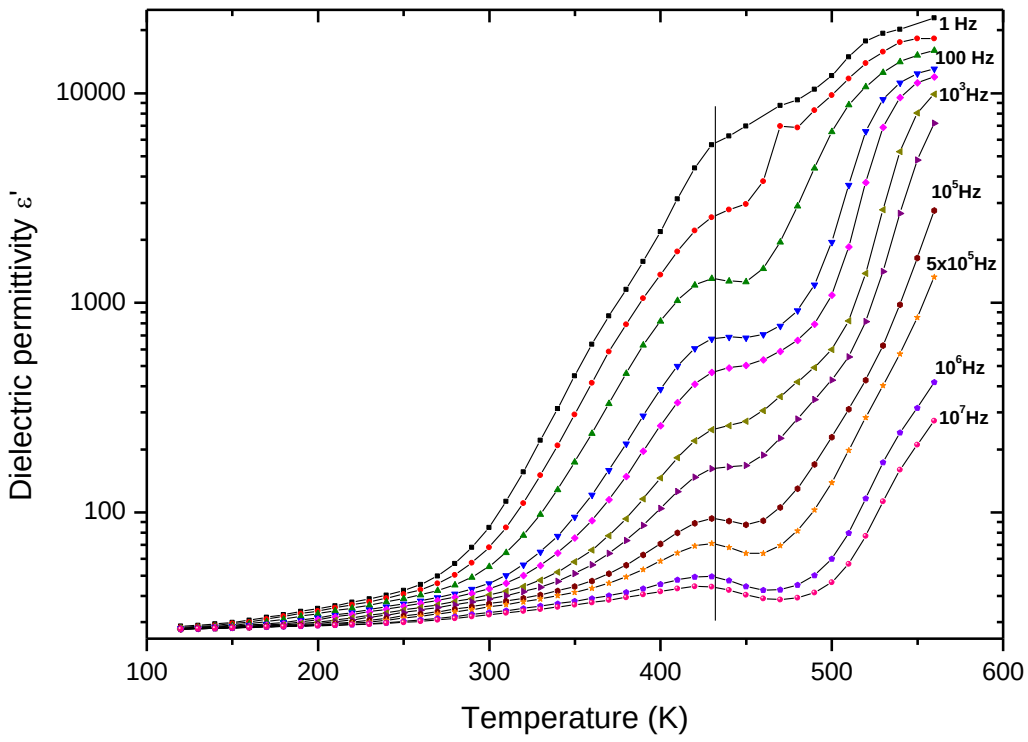

Figure 6.34. Relative dielectric permittivity ε' vs Temperature for $BiFeO_3$ sample (30 minutes MW, KOH 4 M).

6.4. $H_2V_3O_8$

Vanadium oxides, oxyhydroxides and hydrated oxides with one-dimensional (1D) nanostructures, such as nanobelts, nanoribbons or nanorods, have attracted great attention due to their diverse physiochemical properties. These oxides present a large number of different structures and exist in a range of single and mixed metal oxidation states (from +2 to +5).[78] They are excellent electrode materials for rechargeable lithium batteries due to their large specific capacity, good cyclability and low cost.

Controlling the growth, size and shape of nanosized objects are important research areas in materials science. In fact, the physical properties depend not only on the composition but also on the particle size and shape. The electrochemical behaviour of these materials strongly depends on these factors and usually, the smaller the particle size is, the lower the cell polarization and the higher the cell capacity become.[79-81]

$H_2V_3O_8$ is one of the most attractive vanadium oxide hydrates due to its interesting electrochemical properties. Early works reported the insertion of up to 2.5 Li per formula unit (Li/f.u. hereafter) in the 4 - 1.5 V range corresponding to a specific capacity of 240 mAh g^{-1}.[78, 82] Interestingly, simultaneous oxidation and partial exchange of H by alkali metals produce superior performances. For example, $Na_{0.9}H_{0.1}V_3O_8$ allows inserting 2.9 Li/f.u and shows 260 mAh g^{-1} specific capacity, due to the larger extent of the proton exchange and the better order within the structure.[82, 83]

The synthesis of $H_2V_3O_8$ was first reported by Théobald and Cabala using a hydrothermal treatment.[84] The crystal structure presents orthorhombic symmetry *Pnam* (#62). The structure was first described as a nearly layered arrangement of V_3O_8,[85] where two different VO_x polyhedra are present: VO_6 octahedra and VO_5 trigonal bipyramids with vanadium oxidation states of +4, +5 in the former and +5 in the latter.

The more common hydrothermal treatment implies the use of sealed Pyrex ampoules containing aqueous $VOSO_4$ or solutions with different reduced vanadium compounds, which are heated at 180 - 220 ^oC for several hours up to several days.[79, 82, 85, 86] Alternatively, $H_2V_3O_8$ can be prepared from V_2O_5 xerogel to avoid using a precursor containing V^{4+}.[87] However, this route is energy costly because the xerogel has to be prepared previously at high temperatures of up to 800 ^oC.

Due to the technological interest of $H_2V_3O_8$, a big effort is being made in order to improve its synthesis and electrochemical performance connected to low production costs. Therefore, recent reports on the synthesis of $H_2V_3O_8$ describe the preparation from the cheapest and more available vanadium oxide, V_2O_5.[88] Regarding electrochemical performances, the highest specific capacity reported up to now is 409 mAh g^{-1} corresponding to the insertion of 4.32 Li/f.u in the 4 - 1.5 V voltage range.[86] The material was prepared before in the form of crystal nanobelts through a hydrothermal route at 180 ^oC for 7 days from a mixture of V_2O_3 and V_2O_5.

In this section it is shown that $H_2V_3O_8$ nanobelts can be produced by microwave - hydrothermal synthesis. The characterisation of the prepared materials, as well as their intercalation chemistry, is presented. The study includes the evolution of the vanadium oxidation state from mixed 2 V^{5+} + 1 V^{4+} to 3 V^{3+}.

High capacities, even at high current densities, have been found in this study showing that microwave-hydrothermal synthesis is a promising synthetic procedure to prepare electrode materials in a fast and environmental friendly way. Interestingly, a preprint has been made recently available describing the application of a similar procedure to the preparation of compounds of general formula $VO_x \cdot nH_2O$ with application in aqueous-based Li-ion supercapacitors.[89] Due to the lack of structural characterisation the true nature of those $VO_x \cdot nH_2O$ was not unveiled though.

6.4.1. Synthetic aspects

The reaction was carried out in a quartz pressure vessel (45 ml with 40 bars and 250 °C as maximum pressure and temperature values, respectively for this kind of vessel) instead of the Teflon autoclaves used in the other procedures described in this Chapter. The convenience of using a quartz vessel is due to high melting point of quartz material which will not being damaged by localized superheating of any material inside the vessel. In the case of $H_2V_3O_8$ and vanadium oxides, the possible formation of conducting phases can produce "hot spots" easily around the walls and the effect with Teflon vessel would be catastrophic (see Figure 6.35).

Figure 6.35. Catastrophic failure of a teflon vessel due to an uncontrolled formation of hot spots in the vessel walls during the synthesis of $H_2V_3O_8$

The reactants V_2O_5 (0.5 mmol, Aldrich, 98%) and ethanol (5 ml, Scharlau, synthesis grade) are mixed in 20 ml distilled water as solvent and placed and stirred in the vessel. The following optimized heating program was used: a heating ramp of 12 °/min up to 200 °C, then 2 h holding time at 200 °C followed by switching off the microwave. The microwave power was limited to 500 W. The product obtained was washed with distilled water and dried at 80 °C. This product can be observed by eye to form an entangled green sheet (Figure 6.36).

Figure 6.36. Entangled green sheet of $H_2V_3O_8$ obtained after 2 hours microwave irradiation.

6.4.2. Structural characterization

The synchrotron XRD pattern of the green powder obtained by microwave-hydrothermal treatment is shown in Figure 6.37. Diffraction peaks can be indexed, using Rietveld refinement, to the *Pnam* (#62) orthorhombic system with lattice constants which are similar to the values previously reported in the literature for $H_2V_3O_8$ (ICDD 04-011-3466).[84] The refined parameters are summarized in Table 6.5.

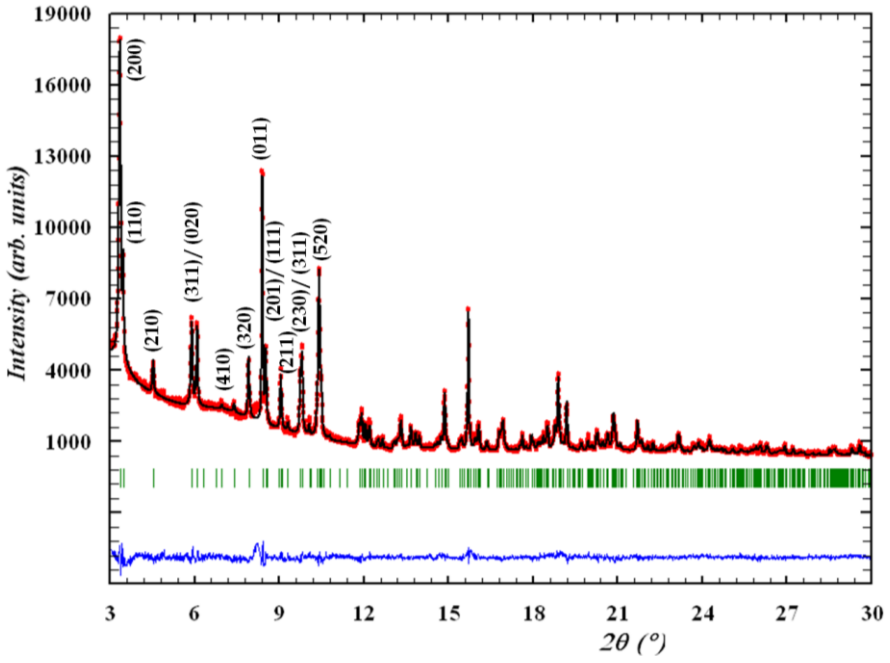

Figure 6.37. Rietveld refinement of $H_2V_3O_8$ synchrotron XRD pattern: observed (red dotted lines), refined (black solid lines), and their difference (blue bottom line). Green vertical bars indicate the X-ray reflection positions.

Table 6.5. Structural parameters for orthorhombic *Pnam* $H_2V_3O_8$ obtained by microwave – hydrothermal synthesis.

$H_2V_3O_8$			
***a* (Å)**	16.8600(4)	**O(3) position 4c**	
***b* (Å)**	9.3325(2)	*x*	0.1310 (1)
***c* (Å)**	3.63388(8)	*y*	0.1311(9)
		U*100 (Å²)	0.20(9)
V(1) position 4c		**O(4) position 4c**	
x	0.0458(3)	*x*	0.9384(9)
y	0.1231(4)	*y*	0.217(1)
U*100 (Å²)	0.73(4)	**U*100 (Å²)**	0.20(9)
V(2) position 4c		**O(5) position 4c**	
x	0.8509(3)	*x*	0.7798(7)
y	0.0765(5)	*y*	0.187(1)
U*100 (Å²)	0.73(4)	**U*100 (Å²)**	0.20(9)
V(3) position 4c		**O(6) position 4c**	
x	0.4474(2)	*x*	0.7789(7)
y	0.0905(4)	*y*	0.898(1)
U*100 (Å²)	0.73(4)	**U*100 (Å²)**	0.20(9)
O(1) position 4c		**O(7) position 4c**	
x	0.9594(9)	*x*	0.5164(7)
y	0.931(1)	*y*	0.927(1)
U*100 (Å²)	0.20(9)	**U*100 (Å²)**	0.20(9)
O(2) position 4c		**O(8) position 4c**	
x	0.0955(8)	*x*	0.355(1)
y	0.277(1)	*y*	0.035(1)
U*100 (Å²)	0.20(9)	**U*100 (Å²)**	0.20(9)
χ^2	5.29		
R_{wp} / R_{exp} (%/ %)	4.45 / 2.57		
R_{Bragg}	5.67		
Space Group	*Pnam* (#62) : 4*c* (*x* y ¼)		

After the refinement, a Bond-Valence Sum (BVS) model calculation [90, 91] was performed in order to assign the oxidation state of the 3 different vanadium cations. The values obtained are: V(1) = 4.74, V(2) = 4.29, V(3) =4.82.

These numbers are close to those reported in the literature 2 V^{5+} + 1 V^{4+}.[84, 85]

Taking into account all the structural information, the $H_2V_3O_8$ structure was drawn in Figure 6.38.

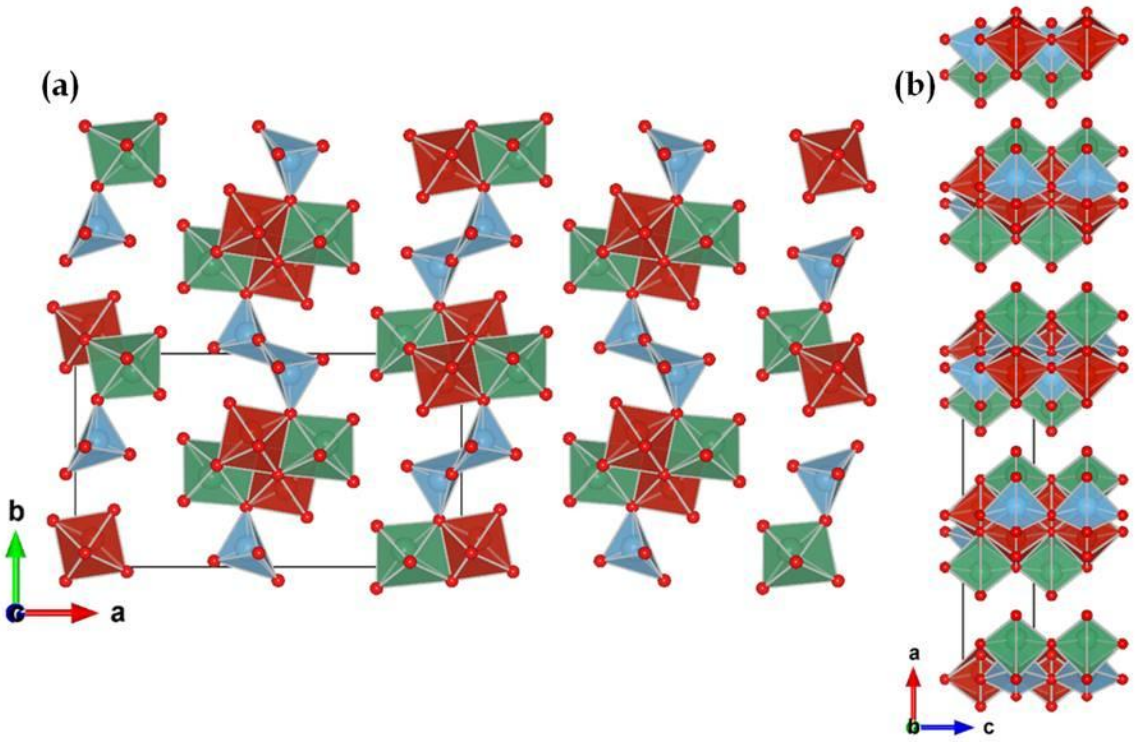

Figure 6.38. Crystal structure of $H_2V_3O_8$ viewed along the (a) c-axis, (b) b-axis. V(1) in green, V(2) in dark red and V(3) in blue.

The structure is characterized as a nearly two-dimensional framework (V_3O_8 layers) comprised of 3 kinds of polyhedra: 2 VO_6 octahedra and a VO_5 distorted square based pyramid. This description is different to Oka *et al,*[85] who claim that VO_5 contains a trigonal bypiramid. As shown in Figure 6.39 this is not totally correct, a trigonal bipyramid is a polyhedron formed by joining a trigonal pyramid and its mirror image base to base and in this case the presence of two inverted and distorted square based pyramids sharing an edge is clear.

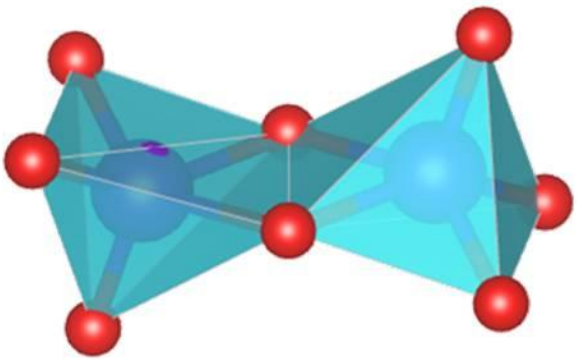

Figure 6.39. Framework of V_2O_5 polyhedra in the structure of $H_2V_3O_8$.

The stoichiometry of the $H_2V_3O_8$ sample was confirmed by ICP - OES. This analysis reveals a vanadium content of 51(2) %, in reasonable agreement with the theoretical value (54%).

The structure was confirmed at the local level by IR spectroscopy. Figure 6.40 shows the IR spectrum of a sample heated at 80 °C in order to remove absorbed water. The spectral features could be assigned to the previously reported values for $H_2V_3O_8$ with good agreement.[88, 92]

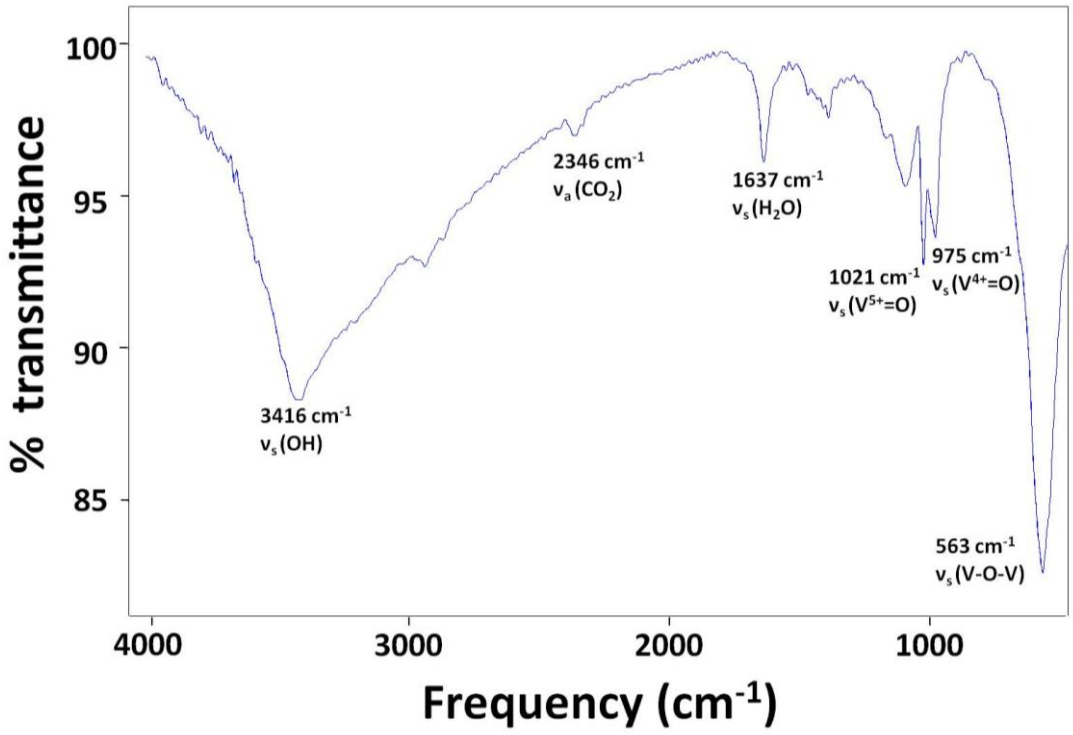

Figure 6.40. FTIR spectrum of $H_2V_3O_8$ prepared by microwave-hydrothermal route.

The broad band at 3416 cm^{-1} originates from the OH group vibrations, whereas a narrow band at 1637 cm^{-1} is ascribed to the H_2O bending mode. Both vibrations indicate the presence of coordinated water in agreement with the structure proposed by Oka *et al.*[85]. The bands at 1021 cm^{-1} and 975 cm^{-1} correspond to the symmetric stretching of the (V^{5+}= O) and (V^{4+}= O) bonds, respectively, showing the presence of mixed valence state for vanadium.

6.4.3. Microstructural characterization

SEM

The SEM image displayed in Figure 6.41 shows the morphology of $H_2V_3O_8$ nanobelts obtained using the microwave-hydrothermal route. They exhibit a width close to 100 nm and a length of several tens of micrometres.

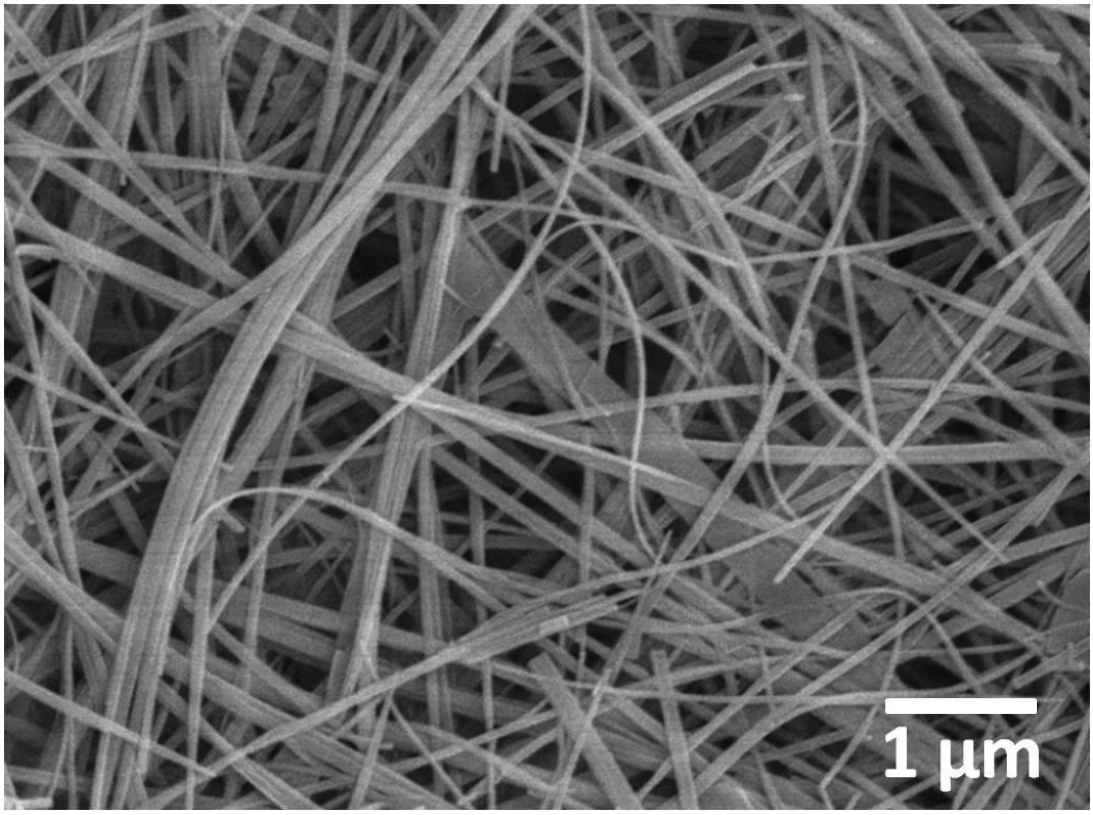

Figure 6.41. Nanobelt morphology typical of $H_2V_3O_8$ prepared by 2 h microwave - hydrothermal route.

HRTEM

A structural HRTEM image along the [100] zone axis (see Fig. 6.42a) shows a regular stacking with periodicity of 0.36 and 0.93 nm, which corresponds to the ***c*** and ***b*** cell parameters, respectively. The simulated image, using the structural model described above, a defocus value of *f* = - 30 nm and a thickness of t = 5 nm was found to be in good agreement with the experimental image, which is demonstrated in the inset of the right part of Figure 6.42a (delimited with yellow asterisks). At this optimum defocus, the vanadium positions correspond to the dark dots and in the magnified area of the image displayed in Figure 6.42b, the arrangement of the vanadium network perfectly fits with the dark dots.

A similar situation is found in the HRTEM image recorded along the [010] zone axis (see Figure 6.42c). In this case, due to the presence of amorphous material in the surface of the nanobelts, a part of the image was filtered yielding a complex arrangement of dots, where a periodicity in the image contrast with values of 0.36 and 1.69 nm can be detected, which corresponds to the lattice parameters ***a*** and ***c*** of the orthorhombic unit cell (Figure 6.42d).

Note again the excellent matching between the calculated image delimited by yellow asterisks (defocus value of *f* = -40 nm and a thickness of t = 6 nm) and the experimental one (Figure 6.42d). The dark dots of the image represent the arrangement in layers of the vanadium atoms along the ***a*** direction (see the projected model inserted in the image).

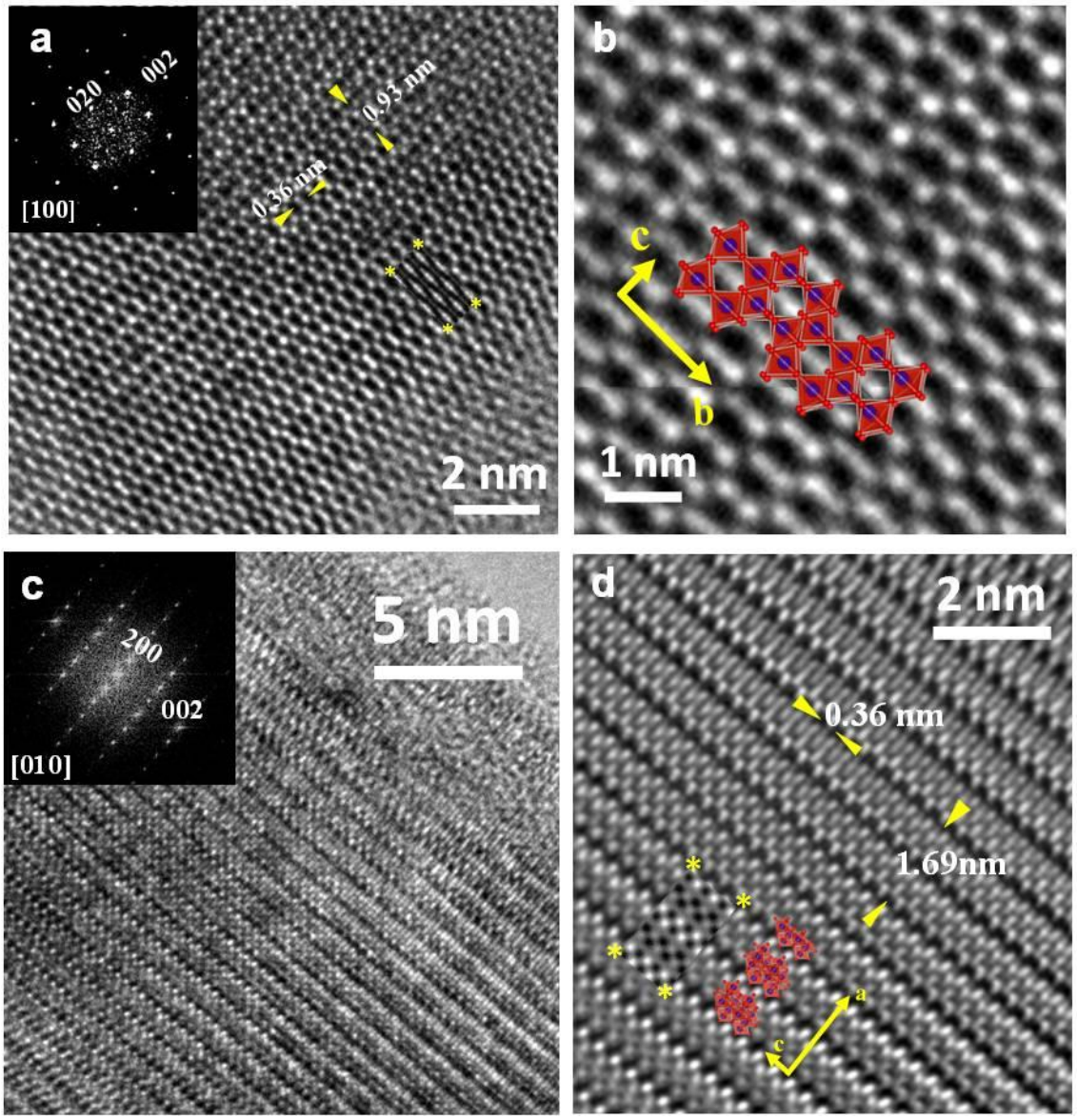

Figure 6.42. a) HRTEM image of a $H_2V_3O_8$ crystal along the [100] zone axis and its corresponding optical diffraction pattern; the calculated image is delimited by yellow asterisks; b) High magnification of (a) where the dark dots are clearly identified with the vanadium cations of the projected crystal structure; c) HRTEM image of the nanobelts along the [010] zone axis and d) the corresponding filtered image showing the arrangement of the vanadium sheets (see the projected structure inserted) along the ***a*** axis and the excellent agreement with the calculated image delimited by yellow asterisks.

6.4.4. TGA analysis

$H_2V_3O_8$ powder was analysed using TGA in a H_2/He atmosphere in order to determine if hydration water is present in the as-prepared sample (Figure 6.43). A small weight loss (≈ 0.5%) below 100 °C is observed and attributed to adsorbed species on the surface of the sample, such as ethanol

and water, and an evident plateau appears corresponding to the stability range of pure $H_2V_3O_8$ sample. A second weight loss of 6.5% occurs around 200 ^oC and is ascribed to the loss of water yielding V_3O_7. Finally, as temperature increases under the reducing conditions another weight loss (13.6%) is observed around 500 ^oC accounting for the reduction to V_2O_3. The total weight loss between 75 and 500 ^oC is 20.1%. This is the expected weight loss for the overall reaction:

$$2\ H_2V_3O_8 + 5\ H_2 \rightarrow 3\ V_2O_3 + 7\ H_2O$$

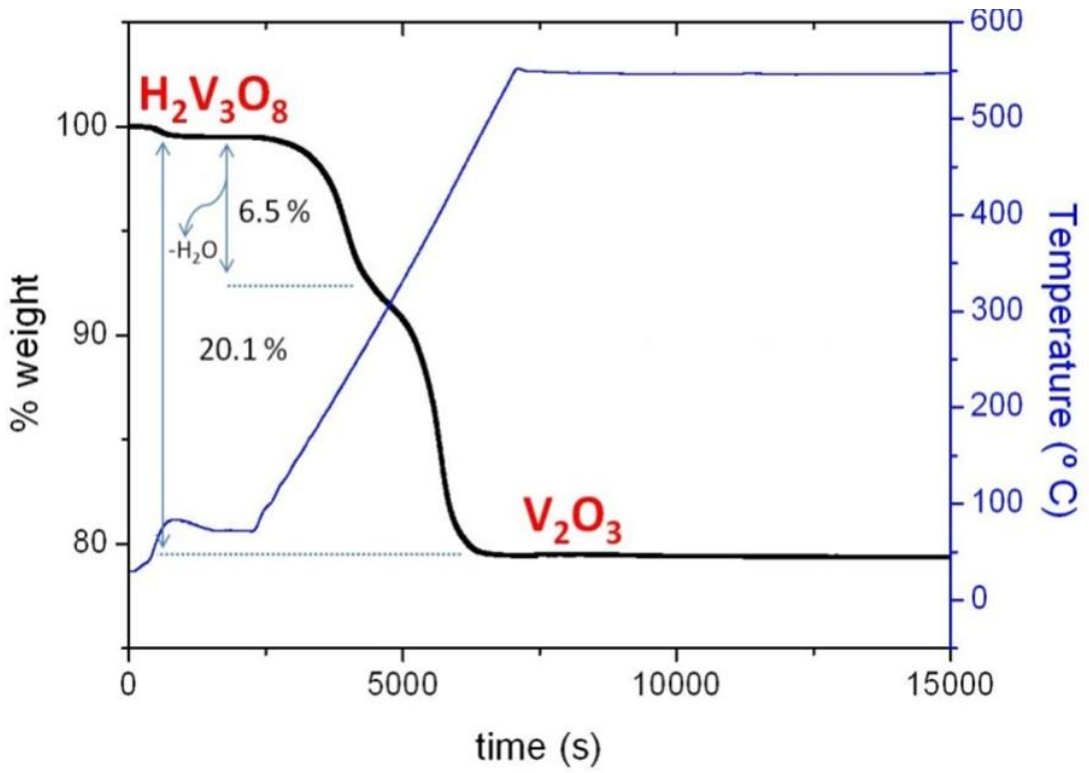

Fig. 6.43. Weight loss and temperature of a $H_2V_3O_8$ sample as a function of time under an atmosphere of H_2 (200 mbar)/He (400 mbar). Heating rate: 5 $^oC\ min^{-1}$.

The XRD analysis of the product obtained after heating at 500 ^oC confirms the formation of V_2O_3, in accordance with the above proposed equation. Taking these results into account, the presence of a significant amount of intercalated water or ethanol is discarded. Nevertheless, prior to the electrochemical characterisation, the as-prepared $H_2V_3O_8$ has been dried at T ≈ 80 ^oC to avoid the presence of small amounts of absorbed substances.

6.4.5. BET surface area analysis

Electrochemical properties of $H_2V_3O_8$ have been found to be highly dependent on the preparation method, because different capacities have been reported. The early report by Legagneur *et al.*[82] described the electrochemical behaviour of samples with low specific surface area (2 - 3 m^2g^{-1}) that develop a capacity of 240 mAh g^{-1} in the 4 - 1.5 V voltage range. Their $H_2V_3O_8$ sample showed an increase of capacity upon cycling that was interpreted as a result of decreasing particle size by electrochemical grinding. Higher capacities ranging from 300 to 400 mAh g^{-1} and above have been achieved in $H_2V_3O_8$ nanobelts with lengths larger than 10 mm and widths of several tens of nanometres.[86, 87, 92, 93] Unfortunately, these reports do not give information on the specific surface area. Based on the results of Chine *et al.*,[88] who prepared nanobelts of similar size and reported a specific surface area of 13 m^2 g^{-1}, it was assumed that a specific surface area of that order of magnitude is needed to enhance lithium insertion thus yielding high performances.

Specific surface area (SSA) of the sample here was measured by physiosorption of nitrogen using the Brunauer, Emmett and Teller (BET) method.[94] The N_2 adsorption - desorption isotherm of $H_2V_3O_8$ powder is presented in Figure 6.44. This isotherm exhibits a hysteresis loop, similar to that described in *section 6.2.4* for rare earth doped ceria. The isotherm is again identified as type IV, typical for mesoporous materials.[25] The surface area determination using the BET technique yields a value of 11.92(2) m^2 g^{-1} for this material. A Barrett –Joyner - Halenda (BJH) type pore size distribution is shown in the inset of Figure 6.44. From the distribution curve it is suggested that a wide distribution of pores with small pore volume (≈ 10^{-4} cm^3 g^{-1} nm^{-1}) and diameters mainly in the mesopore range (2 - 50 nm) occurs. It is possible to observe two peaks, the first narrow one corresponds to 2.6 nm pores, while the second peak shows a broad contribution with a maximum at about 24 nm pore size, probably due to the packing of the nanobelts.

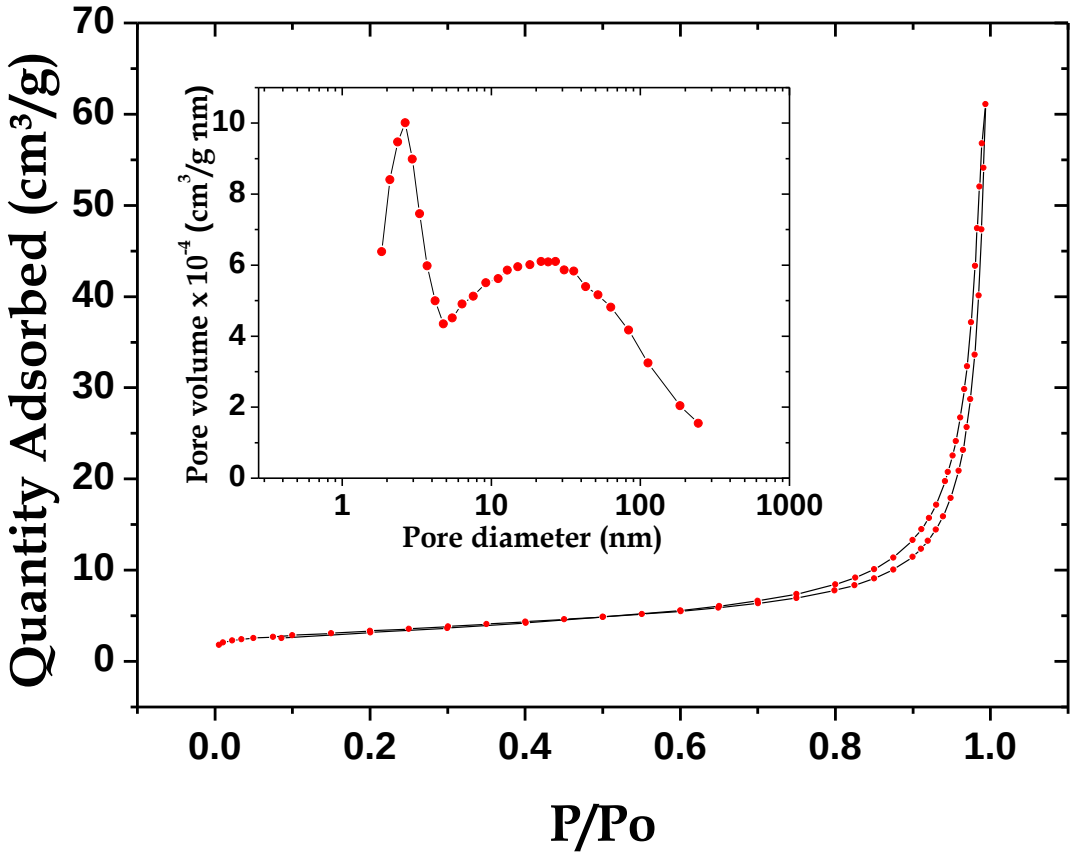

Fig. 6.44. N_2 adsorption–desorption isotherm of $H_2V_3O_8$ nanobelts showing the amount of gas adsorbed versus the relative pressure. Inset: BJH pore size distribution derived from the adsorption branch of the isotherm

6.4.6. Electrochemical properties

Figure 6.45 shows the electrochemical behaviour of $H_2V_3O_8$ nanobelts produced by the microwave – hydrothermal method at C/20 rate, which means that 20 h are necessary to insert 1 Li/f.u. The lower cut off voltage is set to 1.5 V. This is the common value used in recent studies reporting electro-chemical performances of $H_2V_3O_8$ nanobelts produced by hydrothermal synthesis.[78, 82] A high capacity of 400 mAh g^{-1} is achieved. Hydrogen evolution due to H^+ reduction upon lithium reaction, does not seem to take place in this case since discharge and charge curves have the same voltage profile even for deep discharges as is shown below (see Figure 6.47a). This behaviour of $H_2V_3O_8$ is remarkable, because protonated systems tend to be unstable as it was observed recently for $H_2Ti_6O_{13}$.[95] The absence of hydrogen displacement during lithium

insertion in $H_2V_3O_8$ indicates that not all protonated systems must be discarded as prospective electrode materials.

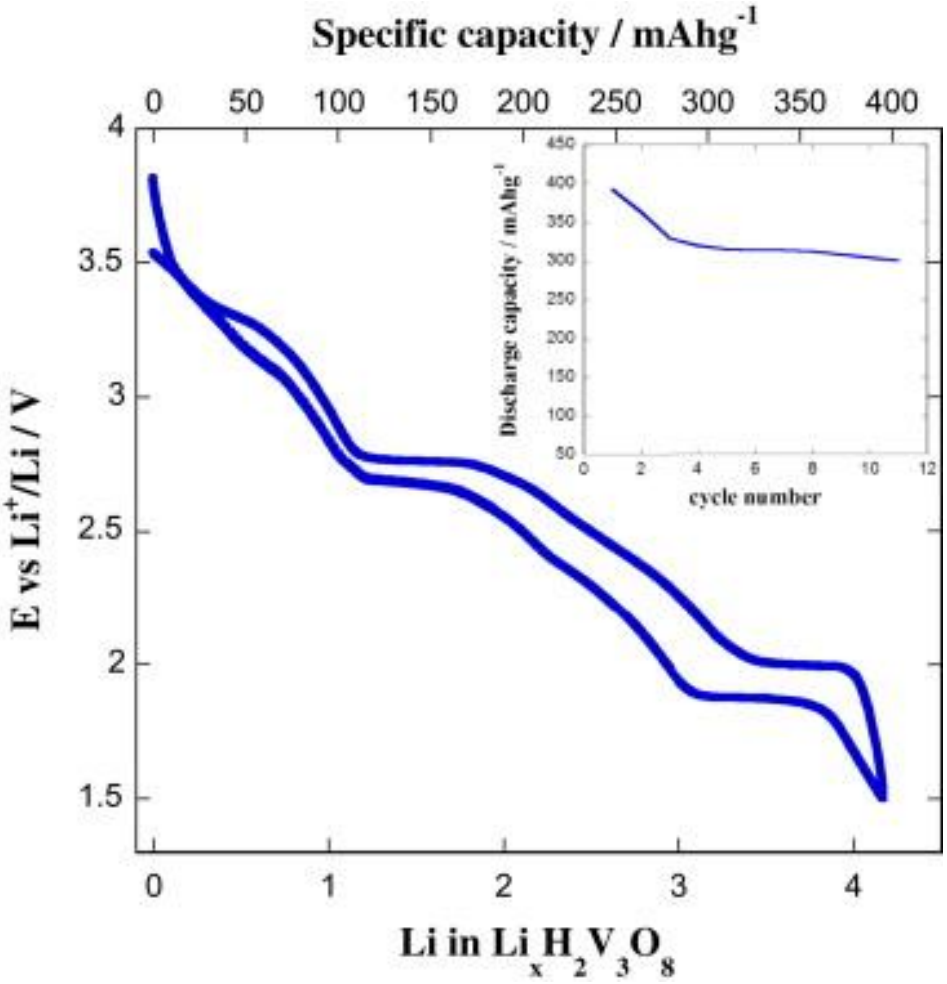

Fig. 6.45. Variation of voltage versus composition and corresponding specific capacity of $H_2V_3O_8$ discharged down to 1.5 V at a *C*/20 discharge rate. The inset shows the discharge capacity of the cell upon cycling.

On the other hand, the cycling behaviour, shown in the inset of 6.45, reveals that a significant drop of capacity is observed after the first cycle, although still a high capacity (≈300 mAh g^{-1}) is kept afterwards. Note that the loss of capacity after the first cycle seems to be a characteristic of $H_2V_3O_8$ nanobelts when cycled in the 4 - 1.5 V range as deduced from previously reported data.[86, 87, 93] In order to shed some light on this capacity loss, the solubility of $H_2V_3O_8$ in the electrolyte (1M $LiPF_6$ solution in EC:DMC (1:1), more details in *Chapter 3.15*) and the structural stability of $H_2V_3O_8$ were investigated.

The vanadium content of the electrolyte was analysed by ICP in both cells cycled 5 times and in the solution obtained after stirring $H_2V_3O_8$ with the electrolyte for 24 h. In both cases only small amounts (1.6 ± 0.2 ppm and 10.4 ± 0.5 ppm, respectively) of vanadium were detected. The X-ray diffraction pattern of the electrode after a discharge down to 1.5 V show that the main reflections of $H_2V_3O_8$ were maintained as expected for a topotactic reaction. However, some intensity changes and peak shifts were detected. A more detailed study of X-ray diffraction using synchrotron radiation to determine the structure of lithiated phases is shown below (*section 6.4.8*). Therefore, it is conclude that the capacity loss after the first cycle is more likely to be related to processing or morphology issues of the electrode rather than to the reversibility of the insertion reaction or dissolution of the active material.

The discharge behaviour of $H_2V_3O_8$ at different current rates varying from C/20 to 1C and down to 1 V is shown in Figure 6.46. The horizontal line indicates the lower cut off voltage that has been normally used when researching this material (1.5 V). Up to date, the highest capacity reported for $H_2V_3O_8$, 409 mAh g^{-1}, corresponds to the insertion of 4.32 Li/f.u. at a current rate of 20 mA g^{-1}.[86] Although a simple comparison with the data depicted in Figure 6.46 is difficult due to differences in electrode processing and fabrication (type of current collector, electrode surface, nature and quantity of carbon black, binder, etc.), it can be seen that capacity data in the 3.75 - 1.5 V range (limited by the horizontal dashed line in Figure 6.46) vary from 4.48 Li/f.u. (425 mAh g^{-1}) for C/20 (4.7 mA g^{-1}) to 3.2 Li/f.u (300 mAh g^{-1}) for 1C (87 mA g^{-1}). Therefore, it can be concluded that good electrochemical performances are reached for the $H_2V_3O_8$ samples prepared following the proposed fast, cost-effective and green chemistry procedure and being comparable to those prepared by other means.[92] Figure 6.46 also shows that the polarisation increase at high current rate seems to become more significant beyond intercalation of 2 Li/f.u. (see shaded areas in Fig. 6.46), likely due to a slower Li diffusion and more severe structural stress.

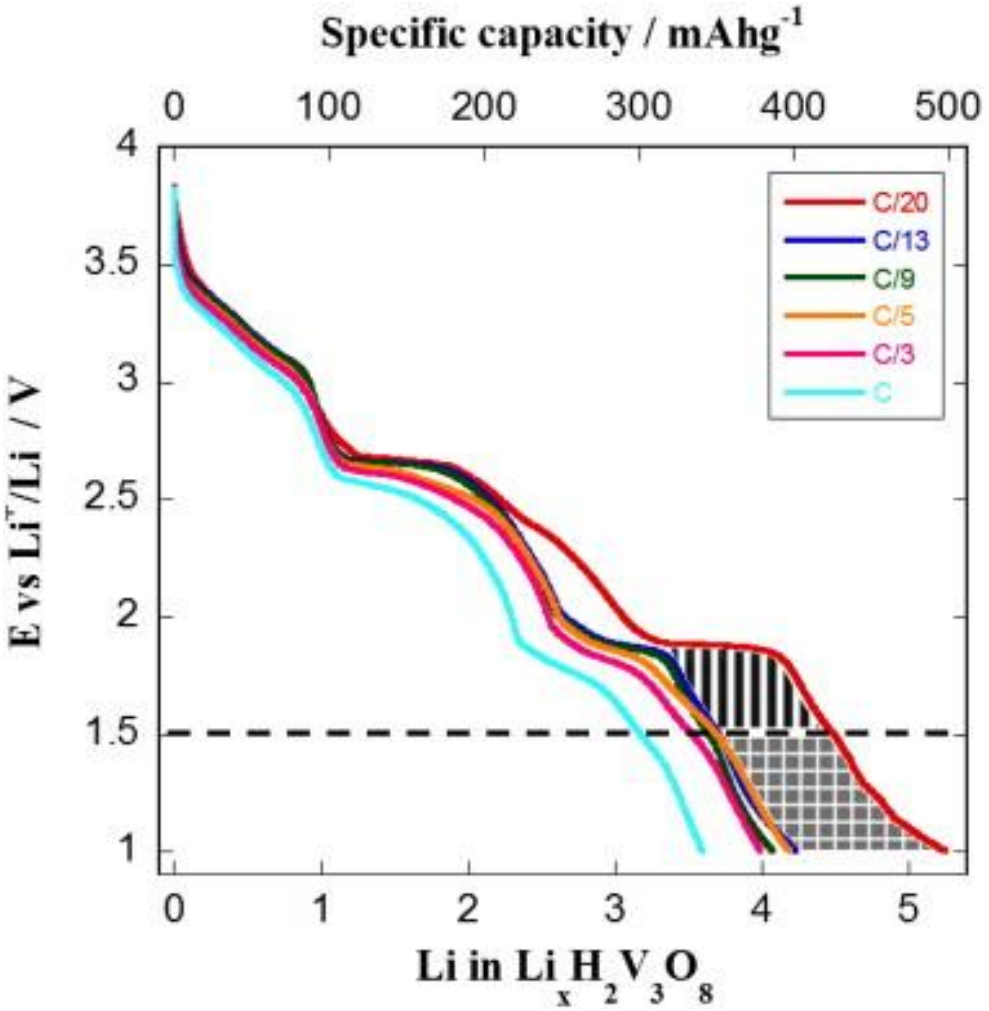

Fig. 6.46. Voltage variation versus composition and corresponding specific capacity of $H_2V_3O_8$ at different current rates (C/n). Note that n stands for the hours needed to insert 1 Li/f.u.

As it was shown in Figure 6.45, the discharge down to 1.5 V corresponds to the insertion of ≈ 4.2 Li/f.u. Thus at this voltage a mixed $V^{4+/3+}$ state is expected. In order to test if $H_2V_3O_8$ inserts more lithium in a reversible way, some cells were discharged to a lower voltage and charged back to 3.75 V. A full discharge - charge cycle in the 3.75 - 1.0 V voltage range of a lithium cell bearing the $H_2V_3O_8$ material as the positive electrode material is presented in Figure 6.47a. The cycling experiment in the 3.75 - 1.0 V range shows a reversible insertion of a lithium quantity that corresponds to the complete reduction of 2 V^{5+} and 1 V^{4+} to 3 V^{3+}, this is 5 Li/f.u. Therefore, the reversible insertion of 5 Li/f.u. unveils that this material develops a large reversible capacity of ≈ 498 mAh g^{-1} which is much higher than previously reported values,[86, 87, 92, 93]

because it allows a deeper discharge. However, from data shown in Figure 6.46 note that the extra capacity obtained at low voltage (below 1.8 V) is very sensitive to the current rate, since from the moment when the current rate increases from C/20 to C/13 a large drop of energy occurs involving mainly the energy developed at low voltage, below 1.8 V (see shaded area below 1.5 V in Figure 6.46). For practical uses only the capacity obtained down to 1.5 V, in the order of 400 mAh g^{-1} may be relevant.

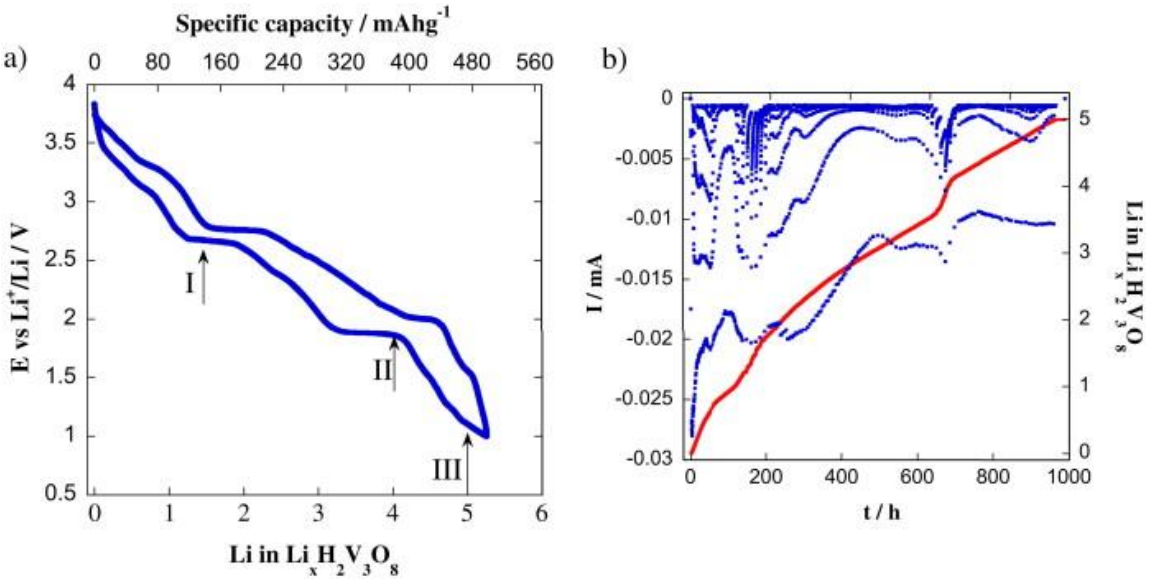

Fig. 6.47. a) Variation of voltage versus composition and corresponding specific capacity of $H_2V_3O_8$ discharged down to 1 V at a *C*/20 discharge rate and b) PITT quasi-equilibrium measurement on a Li/$H_2V_3O_8$ cell at ±10 mV for 12 h down to 1.0 V.

Several features of the voltage-composition profile are clearly seen in Figure 6.47a allowing the identification of the solid solution and two-phase regions (continuous variation and plateaus of voltage, respectively). The nature of the mentioned regions is more clearly seen in Figure 6.47b, where the relaxation of current with time during a potentiostatic discharge is shown in the whole intercalation range. Thus it can be seen that for reaction time $t \approx 175$ h and 675 h, current relaxation follows an anomalous behaviour far from a $t^{-1/2}$ law indicating that lithium diffusion is not ruling the intercalation reaction. Those two regions are then assigned to biphasic regions. In all other regions the expected relaxation trend indicates that a single phase of variable composition

is being formed. However, in spite of the long time the system was allowed to relax, limited kinetics are observed throughout the whole intercalation regions, and the current does not relax to zero. As expected, the effect of limited kinetics is more evident in the two-phase regions, where lithium diffusion through the interphase shows a delayed reaction.

6.4.7. EELS spectroscopy

In order to determine the changes in vanadium oxidation states, several samples in the $0 \leq x \leq 5$ compositional range were isolated by discharging different cells down to 2.65, 1.85 and 1.0 V. The corresponding compositions $Li_xH_2V_3O_8$ (x = 1.5, 4.0 and 5.0), located on the discharge - charge curve shown in Figure 6.47a as I, II and III, were further characterised by EELS. Of particular interest is the last one, since it represents the maximum lithium quantity that $H_2V_3O_8$ can incorporate reversibly.

It is well known that the white lines (L_2 and L_3 absorption edges) in the 3*d* transition metals are sensitive to valence changes and the position and total intensity or L_3/L_2 ratio of these lines can be used to extract this information.[96] Another method that was shown to give good results is to measure the difference in energy onset between the oxygen K edge and the transition metal L_{23} edge.[97] Here, in this case the V L_{23} edge and the O K edge overlap, and therefore a modification of the last method and in the approximation the shift of the V L_{23} for different reference compounds is compared, the pristine $H_2V_3O_8$ nanobelts and the Li intercalated materials with respect to the C K edge used as reference for energy calibration. Note that the latter materials are mixed with carbon black due to the preparation route (see details in the experimental techniques *section 3.15*). According to this, V_2O_3 (V^{3+}), VO_2 (V^{4+}), $H_2V_3O_8$ ($V^{4.67+}$) and V_2O_5 (V^{5+}) samples mixed with carbon were used as valence standard. Linear fitting of the vanadium L_3 energy maximum (E_{L3}) and the vanadium oxidation state (V_V) shows a relation following $E_{L3} = a + b \cdot V_V$ with a = 514.05(27) and b = 1.27(6) (Figure 6.48a).

If the V L_{23} edge of $Li_xH_2V_3O_8$ with x = 0, 1.5, 4.0 and 5.0 is represented together with the reference compounds (Figure 6.48b), it can be observed that for low lithium content the V L_3 edge is close to those of V_2O_5 and VO_2. However, it shifts towards VO_2 and V_2O_3 for higher lithium content and finally is similar to that of V_2O_3 for x = 5.0. The average oxidation state of vanadium for $Li_xH_2V_3O_8$ with x = 1.5, 4.0 and 5.0 can be estimated from the linear relationship plotted in Figure 6.48a to be +4.1(1), +3.8(1) and +3.1(1). These results fairly agree with the expected variation of average oxidation states (+4.2, +3.4, +3.0) accordingly to their composition. Interestingly, full reduction to V^{3+} is confirmed for the first time in this electrode material.

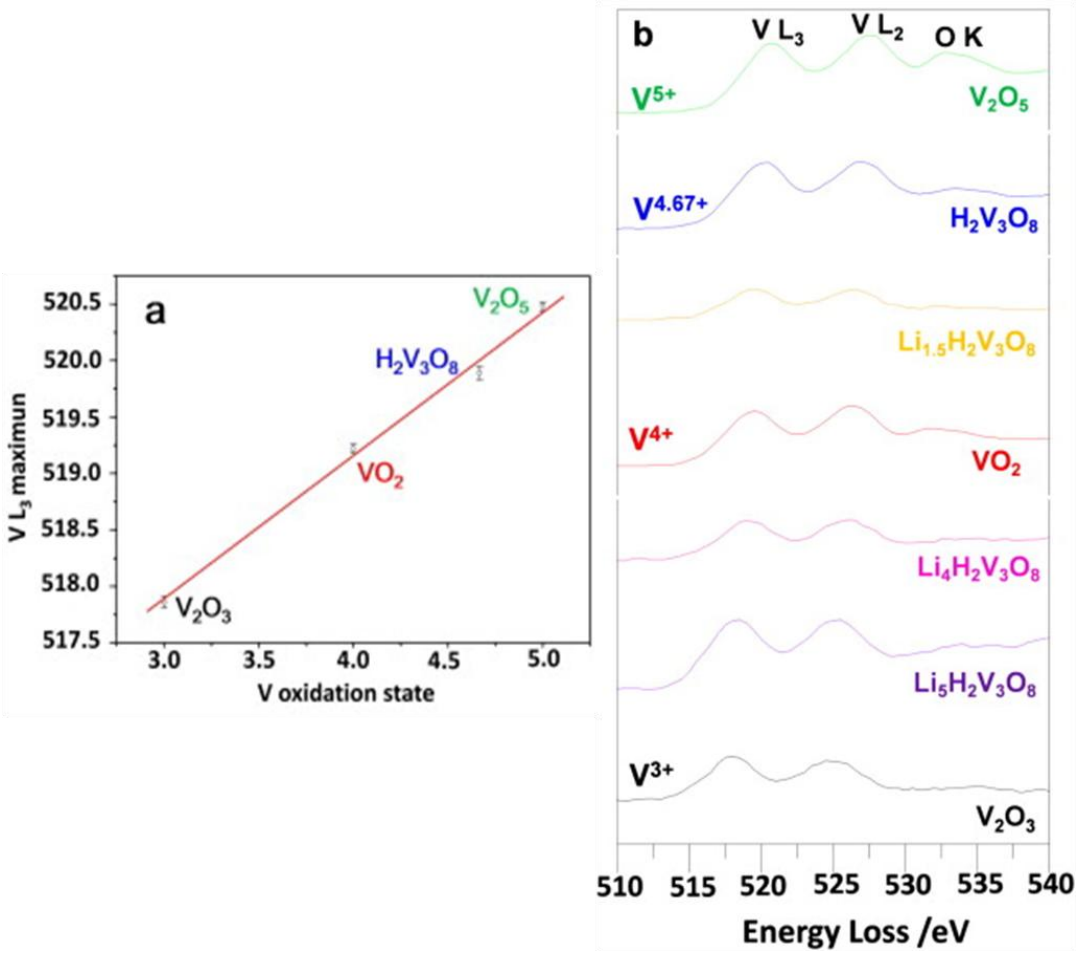

Fig. 6.48. a) Graph showing the linear increase of the V L_3 maximum position with vanadium oxidation state (R factor of 0.993); b) ELNES of vanadium L_{23} edges from the oxides used in the calibration and the lithiated materials $Li_xH_2V_3O_8$ with x = 1.5, 4.0 and 5.0, sorted by their oxidation state.

6.4.8. Synchrotron X-ray diffraction of $Li_xH_2V_3O_8$

Chemical lithiation of $H_2V_3O_8$ was done with n-butyl lithium 1.6 M in hexane (Aldrich, d = 0.68 g/mL) in order to study if there is any structural change between the samples with lithium and the initial $H_2V_3O_8$. Three different stoichiometric ratios were used to obtain three lithiated compounds, nominally $Li_xH_2V_3O_8$, x = 0.94, 2.85, 4.5.

The diffraction patterns of preliminary synchrotron X-ray diffraction analysis of $Li_xH_2V_3O_8$, x = 0, 0.94, 2.85, 4.5 are depicted in Fig. 6.49. $Li_xH_2V_3O_8$, x = 0.94, 2.85, 4.5 crystallize in the orthorhombic system with space group *Pnam* (#*62*), as is the case for $H_2V_3O_8$ (see *section 6.4.3*).

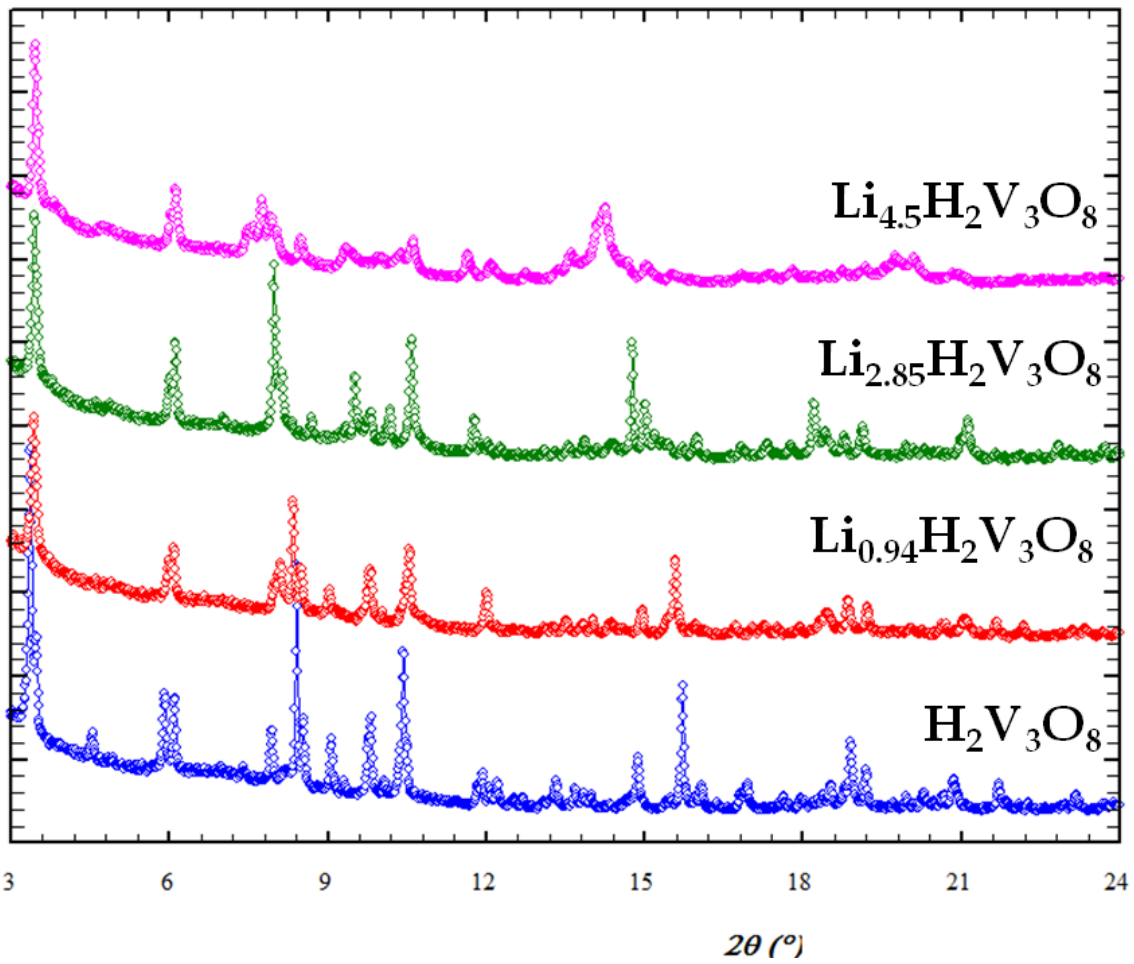

Fig. 6.49. Synchrotron X-ray diffraction patterns of $Li_xH_2V_3O_8$, x = 0, 0.94, 2.85, 4.5

Rietveld refinements of X-ray synchrotron data of all the prepared samples $Li_xH_2V_3O_8$, x = 0, 0.94, 2.85, 4.5 were performed (Figure 6.50). Table 6.6 summarized all the structural information obtained from the Rietveld refinement of each sample. It is important to comment that the lithium cation positions were not refined due to the scarce information about the crystallographic position of lithium in these phases. For future work it is suggested to carry out additional neutron experiments in order to localize the lithium. However, vanadium is a strong scatterer of X-rays, but its nucleus hardly scatters any neutrons, which is a problem for characterizing the samples by neutron diffraction.

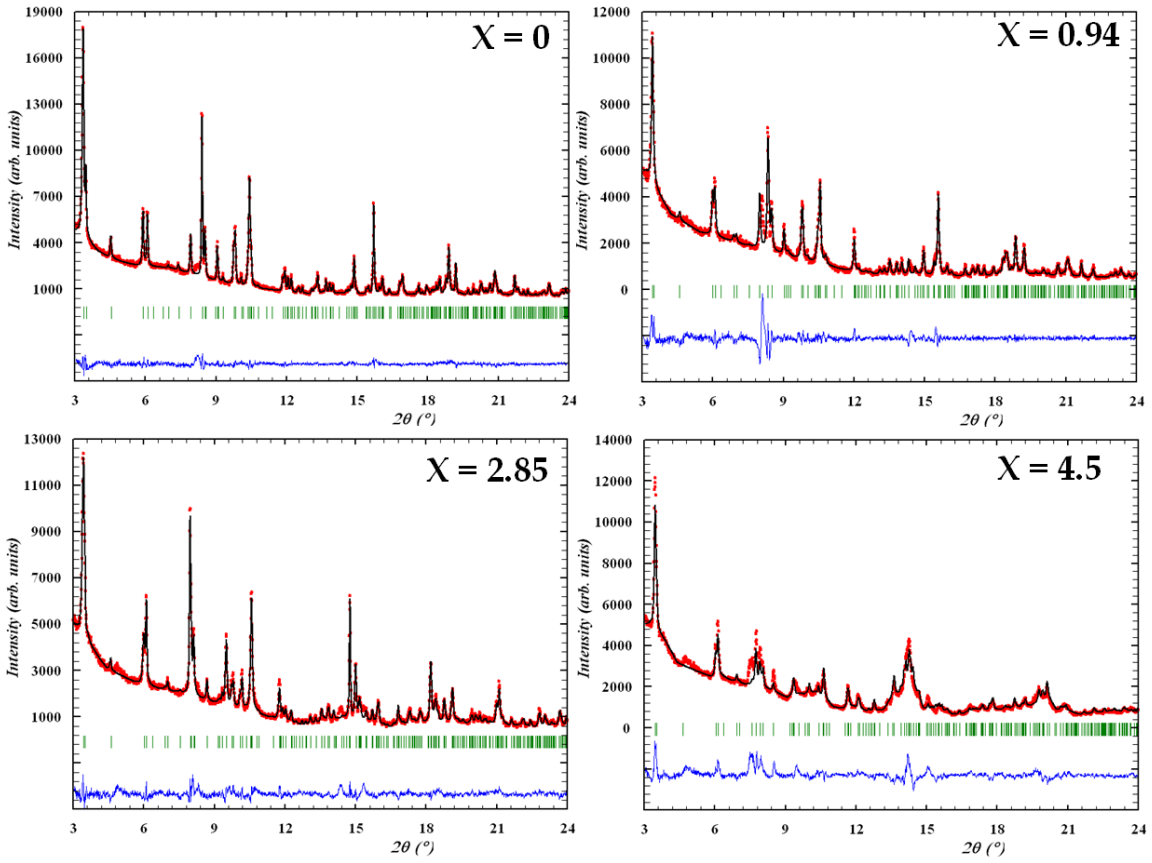

Figure 6.50. Rietveld refinement of synchrotron XRD patterns of $Li_xH_2V_3O_8$ (x = 0, 0.94, 2.85, 4.5): observed (red dotted lines), refined (black solid lines), and their difference (blue bottom line). Green vertical bars indicate the X-ray reflection positions.

Table 6.6a Structural parameters for orthorhombic *Pnam* $Li_{0.94}H_2V_3O_8$

$Li_{0.94}H_2V_3O_8$			
***a* (Å)**	16.552(1)	**O(3) position 4c**	
***b* (Å)**	9.3469(9)	*x*	0.148(2)
***c* (Å)**	3.6684(3)	*y*	0.986(3)
		U*100 (Å²)	0.22(7)
V(1) position 4c		**O(4) position 4c**	
x	0.0424(6)	*x*	0.922(1)
y	0.124(1)	*y*	0.218(4)
U*100 (Å²)	0.73(3)	**U*100 (Å²)**	0.22(7)
V(2) position 4c		**O(5) position 4c**	
x	0.8526(7)	*x*	0.756(2)
y	0.066(1)	*y*	0.167(3)
U*100 (Å²)	0.73(3)	**U*100 (Å²)**	0.22(7)
V(3) position 4c		**O(6) position 4c**	
x	0.4400(6)	*x*	0.774(2)
y	0.089(1)	*y*	0.893(3)
U*100 (Å²)	0.73(3)	**U*100 (Å²)**	0.22(7)
O(1) position 4c		**O(7) position 4c**	
x	0.961(2)	*x*	0.510(2)
y	0.933(3)	*y*	0.936(4)
U*100 (Å²)	0.22(7)	**U*100 (Å²)**	0.22(7)
O(2) position 4c		**O(8) position 4c**	
x	0.108(2)	*x*	0.361(3)
y	0.263(1)	*y*	0.014(3)
U*100 (Å²)	0.22(7)	**U*100 (Å²)**	0.22(7)
χ^2	13.8		
R_{wp}/R_{exp} (%/%)	9.48 / 2.55		
R_{Bragg}	9.07		
Space Group	*Pnam* (#62) : 4*c* (*x* y ¼)		

Table 6.6b Structural parameters for orthorhombic *Pnam* $Li_{2.85}H_2V_3O_8$

$Li_{2.85}H_2V_3O_8$			
***a* (Å)**	16.5002(9)	**O(3) position 4c**	
***b* (Å)**	9.3060(5)	*x*	0.134(1)
***c* (Å)**	3.8674(1)	*y*	0.967(2)
		U*100 (Å²)	0.48(3)
V(1) position 4c		**O(4) position 4c**	
x	0.0477(5)	*x*	0.922(1)
y	0.1115(7)	*y*	0.228(2)
U*100 (Å²)	0.27(5)	**U*100 (Å²)**	0.48(3)
V(2) position 4c		**O(5) position 4c**	
x	0.8477(5)	*x*	0.770(1)
y	0.0726(7)	*y*	0.191(2)
U*100 (Å²)	0.27(5)	**U*100 (Å²)**	0.48(3)
V(3) position 4c		**O(6) position 4c**	
x	0.4406(4)	*x*	0.783(1)
y	0.0752(7)	*y*	0.889(2)
U*100 (Å²)	0.27(5)	**U*100 (Å²)**	0.48(3)
O(1) position 4c		**O(7) position 4c**	
x	0.956(1)	*x*	0.531(1)
y	0.932(2)	*y*	0.919(2)
U*100 (Å²)	0.48(3)	**U*100 (Å²)**	0.48(3)
O(2) position 4c		**O(8) position 4c**	
x	0.102(1)	*x*	0.347(3)
y	0.246(2)	*y*	0.005(2)
U*100 (Å²)	0.48(3)	**U*100 (Å²)**	0.48(3)
χ^2	8.16		
R_{wp} / R_{exp} (% / %)	6.86 / 2.40		
R_{Bragg}	6.58		
Space Group	*Pnam* (#62) : 4*c* (*x* y ¼)		

Table 6.6c Structural parameters for orthorhombic *Pnam* $Li_{4.5}H_2V_3O_8$

$Li_{4.5}H_2V_3O_8$			
***a* (Å)**	16.424(1)	**O(3) position 4c**	
***b* (Å)**	9.278(1)	*x*	0.164(2)
***c* (Å)**	4.0034(3)	*y*	0.031(1)
		U*100 (Å²)	0.49(4)
V(1) position 4c		**O(4) position 4c**	
x	0.0241(8)	*x*	0.933(2)
y	0.080(1)	*y*	0.250(1)
U*100 (Å²)	0.26(6)	**U*100 (Å²)**	0.49(4)
V(2) position 4c		**O(5) position 4c**	
x	0.856(7)	*x*	0.754(1)
y	0.033(1)	*y*	0.120(3)
U*100 (Å²)	0.26(6)	**U*100 (Å²)**	0.49(4)
V(3) position 4c		**O(6) position 4c**	
x	0.4650(9)	*x*	0.759(2)
y	0.119(1)	*y*	0.940(2)
U*100 (Å²)	0.26(6)	**U*100 (Å²)**	0.49(4)
O(1) position 4c		**O(7) position 4c**	
x	0.961(2)	*x*	0.513(3)
y	0.853(1)	*y*	0.903(2)
U*100 (Å²)	0.49(4)	**U*100 (Å²)**	0.49(4)
O(2) position 4c		**O(8) position 4c**	
x	0.135(2)	*x*	0.358(3)
y	0.260(1)	*y*	0.021(4)
U*100 (Å²)	0.49(4)	**U*100 (Å²)**	0.49(4)
χ^2	17.5		
R_{wp}/R_{exp} (%/%)	10.0 / 2.41		
R_{Bragg}	20.07		
Space Group	*Pnam* (#62) : 4*c* (*x* y ¼)		

The cell parameters show certain variations as is shown in Figure 6.51. The ***a*** parameter decreases (≈- 2.6 % from x = 0 to x = 4.5), ***b*** slightly decreases (≈- 0.6 % from x = 0 to x = 4.5) and ***c*** increases (≈ 9.3 % from x = 0 to x = 4.5). The total unit cell volume clearly increases along with lithium content (≈ 6.3 % from x = 0 to x = 4.5). These changes could give a rough idea of the lithium position. The considerable increase of ***c*** could be a signal of lithium entering into the structure along the ***c*** direction. During the initial stage of the electrochemical

reduction of $H_2V_3O_8$, lithium diffusion into the interior of $H_2V_3O_8$ occurs. It was shown by EELS (*section 6.4.7*) that reduction of V^{5+} to V^{3+} occurs. It is well known that the ionic radius (IOR) of V^{3+} decreases with oxidation state up to V^{5+} which may explain the decrease of ***a*** and ***b*** parameters. Furthermore, the attractive electrostatic forces between the bound anions (possible existence of OH^-) and the lithium could make the ***a*** and ***b*** parameters to decrease (see structure in Figure 6.32).

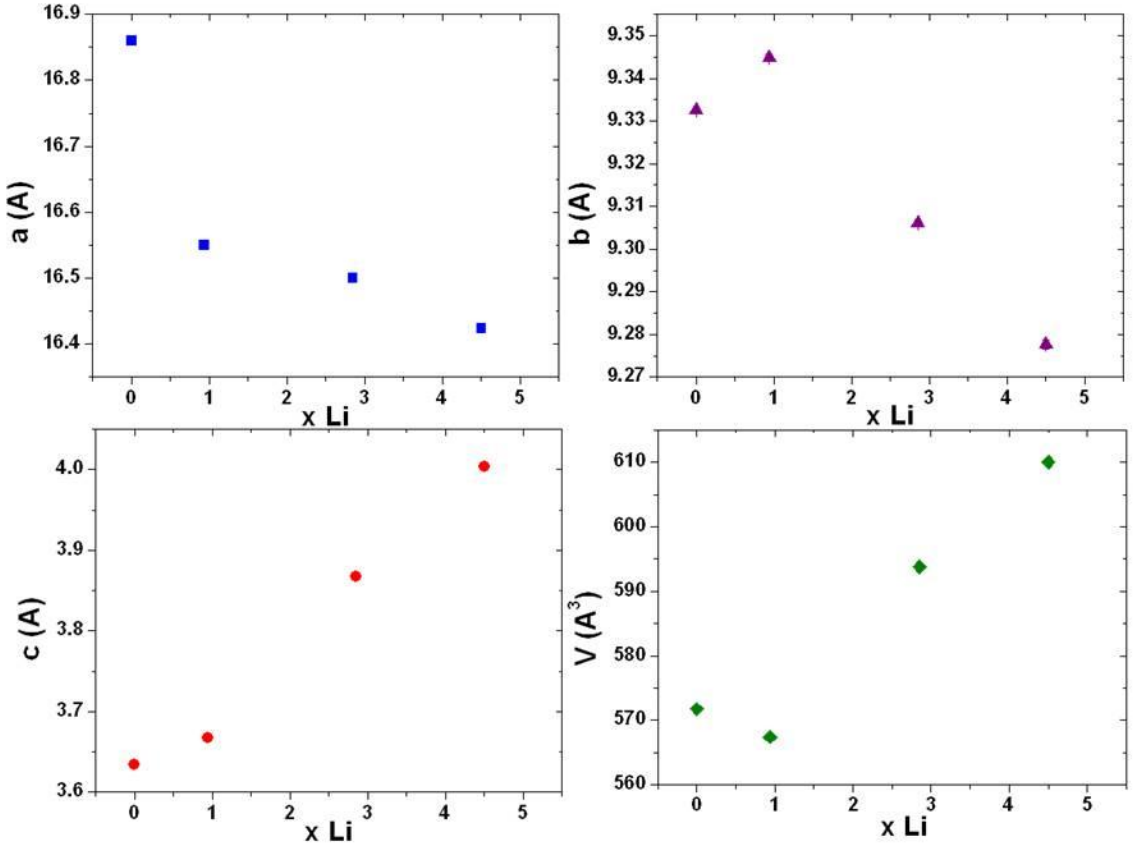

Figure 6.51. Evolution of the unit cell parameters and total volume as a function of *x* in $Li_xH_2V_3O_8$.

A similar behaviour for $Li_xV_2O_5$ was reported in the literature,[98-100] where an increased packing of the layers is revealed by the decrease in the ***a*** parameter (***a*** = 11.51 Å for V_2O_5 to ***a*** = 11.40 Å for $Li_{0.6}V_2O_5$). However, ***b*** is almost constant (***b*** = 3.56 Å). The increase of the number of inserted lithium ions between the layers is responsible for the increase in the ***c*** parameter (***c*** = 4.37 Å for V_2O_5 to ***c*** = 4.53 Å for $Li_{0.6}V_2O_5$).[98]

6.5. Conclusions

Microwave – hydrothermal synthesis can be carried out for a wide variety of combinations of aqueous systems. The coupling efficiency of the solvent with the microwave is crucial for the outcome of the reaction.

This simple method yields pure materials, where in most of the cases the particles are nano-sized, and it is possible to obtain metastable phases. Compared to hydrothermal procedures, the method is faster, less expensive and more environmentally friendly. The synthesis and characterization of nano-sized rare earth doped ceria with fluorite structure, $BiFeO_3$ perovskite and $H_2V_3O_8$ oxide with one-dimensional (1D) nanostructure has been presented in this chapter.

- Concerning **rare-earth (RE) doped ceria ($Ce_{1-x}RE_xO_{2-\delta}$)**, samarium and calcium doped ($Ce_{0.8}Sm_{0.18}Ca_{0.02}O_{1.9-\delta}$) and undoped ceria, the structural and microstructural characterization of a pure samples were presented. Impedance spectroscopy measurements confirmed ionic conductivity in all the doped materials, whereas the undoped $CeO_{2-\delta}$ parent compound exhibited signs of electronic conduction, most likely due to mixed valent Ce^{3+}/Ce^{4+} electron hopping. Deconvolution of GB and intrinsic bulk ionic conductivity revealed that GBs constitute barriers for ionic charge transport, with the Sm - Ca doped ceria $Ce_{0.8}Sm_{0.18}Ca_{0.02}O_{1.9-\delta}$ exhibiting the highest GB ionic conductivity. The highest intrinsic bulk ionic conductivity was detected for the $Ce_{0.8}Sm_{0.18}Ca_{0.02}O_{1.9-\delta}$ ceramic as well.

Single mode microwave sintering was performed for $Ce_{0.8}Sm_{0.18}Ca_{0.02}O_{1.9-\delta}$ and the obtained ionic conductivities for samples sintered after 5 minutes reveals similar values as these of conventionally sintered samples (4 – 8 h).

- The structural and microstructural characterization of a pure sample of **$BiFeO_3$** was presented. The X-ray data can be refined in two symmetries (*R3c* or *Cc*) with similar reliability factors. TEM and associated techniques have been

employed as fundamental tools to corroborate that the *R3c* space group is superior. The microstructure of the material has been studied by HRTEM showing a well ordered material free of extended defects. This order is also detected in the oxygen sub-lattice imaged in the phase of the reconstructed exit wave. Magnetic properties of the sample are similar to those reported in literature for samples obtained by conventional methods. Weak ferromagnetism has been suggested. Impedance spectroscopy shows the that bulk resistance of the sample is high, thus confirming the insulating nature of the material.

- Concercing cathode materials for lithium rechargeable batteries, **$H_2V_3O_8$** nanobelts of about 100 nm width and several micrometres length have been obtained. Synchrotron X-ray diffraction was performed in order to determine the structure of the $H_2V_3O_8$ phase. The structure is characterized as a framework of V_3O_8 layers comprised of 3 kinds of polyhedra: 2 VO_6 octahedra and a VO_5 distorted square - based pyramid. Only V_2O_5, water and ethanol are used to prepare the electrode material in just 2 h. The electrochemical characterisation performed confirmed the production of $H_2V_3O_8$ with the adequate morphology to exhibit high electrochemical performances. At C/20 an initial capacity of ≈ 400 mAh g^{-1} is observed in the 3.75 - 1.5 V range. After a significant capacity loss in the first cycle, a capacity of ≈ 300 mAh g^{-1} is maintained upon cycling. Full reduction to V^{3+} was detected by discharging Li cells with $H_2V_3O_8$ as a cathode material down to 1 V; a significant increase of reversible capacity to 498 mAh g^{-1} is thereby obtained. However, this extra capacity is more readily lost at high current rate than capacity developed above 2 V. For practical use only the capacity obtained down to 1.5 V may be relevant.

Furthermore, the similarity of discharge and charge curves points to the absence of hydrogen displacement during lithium insertion in $H_2V_3O_8$. Not all protonated systems must be necessarily discarded as prospective electrode materials.

6.6. References

1. Brett, D. J. L.; Atkinson, A.; Brandon, N. P.; Skinner, S. J., Intermediate temperature solid oxide fuel cells. *Chemical Society Reviews* **2008,** 37, (8), 1568-1578.

2. Garcia-Barriocanal, J.; Rivera-Calzada, A.; Varela, M.; Sefrioui, Z.; Iborra, E.; Leon, C.; Pennycook, S. J.; Santamaria, J., Colossal Ionic Conductivity at Interfaces of Epitaxial ZrO_2:Y_2O_3/$SrTiO_3$ Heterostructures. *Science* **2008,** 321, (5889), 676-680.

3. Zha, S.; Xia, C.; Meng, G., Effect of Gd (Sm) doping on properties of ceria electrolyte for solid oxide fuel cells. *Journal of Power Sources* **2003,** 115, (1), 44-48.

4. Steele, B. C. H., Materials for IT-SOFC stacks: 35 years R&D: the inevitability of gradualness? *Solid State Ionics* **2000,** 134, (1-2), 3-20.

5. Guo, X.; Waser, R., Electrical properties of the grain boundaries of oxygen ion conductors: Acceptor-doped zirconia and ceria. *Progress in Materials Science* **2006,** 51, (2), 151-210.

6. Guo, X.; Sigle, W.; Maier, J., Blocking Grain Boundaries in Yttria-Doped and Undoped Ceria Ceramics of High Purity. *Journal of the American Ceramic Society* **2003,** 86, (1), 77-87.

7. Mahato, N.; Gupta, A.; Balani, K., Doped zirconia and ceria-based electrolytes for solid oxide fuel cells: a review. *Nanomaterials and Energy* **2012,** 1, (1), 27-45.

8. Ramesh, S.; Kumar, V. P.; Kistaiah, P.; Reddy, C. V., Preparation, characterization and thermo electrical properties of co-doped $Ce_{0.8-x}Sm_{0.2}Ca_xO_2$ materials. *Solid State Ionics* **2010,** 1-2, (86-91).

9. Moure, A.; Moure, C.; Tartaj, J., A significant improvement of the processing and electric properties of CeO_2 co-doped with Ca and Sm by mechanosynthesis. *Journal of Power Sources* **2011,** 196, (24), 10543-10549.

10. Tuller, H. L., Ionic conduction in nanocrystalline materials. *Solid State Ionics* **2000,** 131, (1-2), 143-157.

11. Trovarelli, A., Catalytic Properties of Ceria and CeO_2-Containing Materials. *Catalysis Reviews* **1996,** 38, (4), 439-520.

12. Wu, N.-C.; Shi, E.-W.; Zheng, Y.-Q.; Li, W.-J., Effect of pH of Medium on Hydrothermal Synthesis of Nanocrystalline Cerium(IV) Oxide Powders. *Journal of the American Ceramic Society* **2002,** 85, (10), 2462-2468.

13. Shuk, P.; Greenblatt, M., Hydrothermal synthesis and properties of mixed conductors based on $Ce_{1-x}Pr_xO_{2-\delta}$ solid solutions. *Solid State Ionics* **1999,** 116, (3-4), 217-223.

14. Walton, R. I., Solvothermal synthesis of cerium oxides. *Progress in Crystal Growth and Characterization of Materials* **2011,** 57, (4), 93-108.

15. Chu, X.; Chung, W.-i.; Schmidt, L. D., Sintering of Sol—Gel-Prepared Submicrometer Particles Studied by Transmission Electron Microscopy. *Journal of the American Ceramic Society* **1993,** 76, (8), 2115-2118.

16. Kirk, T. J.; Winnick, J., A Hydrogen Sulfide Solid Oxide Fuel Cell Using Ceria Based Electrolytes. *Journal of The Electrochemical Society* **1993,** 140, (12), 3494-3496.

17. Bondioli, F.; Corradi, A. B.; Manfredini, T.; Leonelli, C.; Bertoncello, R., Nonconventional Synthesis of Praseodymium-Doped Ceria by Flux Method. *Chemistry of Materials* **1999,** 12, (2), 324-330.

18. Upadhyaya, D. D.; Bhat, R.; Ramanathan, S.; Roy, S. K.; Schubert, H.; Petzow, G., Solute effect on grain growth in ceria ceramics. *Journal of the European Ceramic Society* **1994,** 14, (4), 337-341.

19. Bondioli, F.; Ferrari, A. M.; Lusvarghi, L.; Manfredini, T.; Nannarone, S.; Pasquali, L.; Selvaggi, G., Synthesis and characterization of praseodymium-doped ceria powders by a microwave-assisted hydrothermal (MH) route. *Journal of Materials Chemistry* **2005,** 15, (10), 1061-1066.

20. Bonamartini Corradi, A.; Bondioli, F.; Ferrari, A. M.; Manfredini, T., Synthesis and characterization of nanosized ceria powders by microwave-hydrothermal method. *Materials Research Bulletin* **2006,** 41, (1), 38-44.

21. Tompsett, G. A.; Conner, W. C.; Yngvesson, K. S., Microwave Synthesis of Nanoporous Materials. *ChemPhysChem* **2006,** 7, (2), 296-319.

22. Whitfield, H. J.; Roman, D.; Palmer, A. R., X-ray study of the system ThO_2 - CeO_2 - Ce_2O_3. *Journal of Inorganic and Nuclear Chemistry* **1966,** 28, (12), 2817-2825.

23. Brauer, G.; Gradinger, H., Über heterotype Mischphasen bei Seltenerdoxyden. I. *Zeitschrift für anorganische und allgemeine Chemie* **1954,** 276, (5-6), 209-226.

24. Schull, C. G., The Determination of Pore Size Distribution from Gas Adsorption Data. *Journal of the American Chemical Society* **1948,** 70, (4), 1405-1410.

25. Rouquerol, J.; Rouquerol, F.; Sing, K. S. W., *Adsorption by Powders and Porous Solids*. Elsevier Science: 1998; p 467.

26. Pan, C.; Zhang, D.; Shi, L., CTAB assisted hydrothermal synthesis, controlled conversion and CO oxidation properties of CeO_2 nanoplates, nanotubes, and nanorods. *Journal of Solid State Chemistry* **2008,** 181, (6), 1298-1306.

27. Pavasupree, S.; Suzuki, Y.; Pivsa-Art, S.; Yoshikawa, S., Preparation and characterization of mesoporous MO_2 (M =Ti, Ce, Zr, and Hf) nanopowders by a modified sol-gel method. *Ceramics International* **2005,** 31, (7), 959-963.

28. He, Y., A novel emulsion route to sub-micrometer polyaniline/nano-ZnO composite fibers. *Applied Surface Science* **2005,** 249, (1-4), 1-6.

29. Irvine, J. T. S.; Sinclair, D. C.; West, A. R., Electroceramics: Characterization by Impedance Spectroscopy. *Advanced Materials* **1990,** 2, (3), 132-138.

30. Barsoukov, E.; Macdonald, J. R., *Impedance Spectroscopy: Theory, Experiment, and Applications*. 2005; p 608.

31. Díez, A.; Schmidt, R.; Sagua, A. E.; Frechero, M. A.; Matesanz, E.; Leon, C.; Morán, E., Structure and physical properties of nickel manganite $NiMn_2O_4$ obtained from nickel permanganate precursor. *Journal of European Ceramic Society* **2010,** 30, 2617-2624.

32. Funke, K.; Hoppe, R., Jump-relaxation model yields Kohlrausch-Williams-Watts behaviour. *Solid State Ionics* **1990,** 40 - 41, Part 1, (0), 200-204.

33. Schmidt, R.; Eerenstein, W.; Winiecki, T.; Morrison, F. D.; Midgley, P. A., Impedance spectroscopy of epitaxial multiferroic thin films. *Physical Review B* **2007,** 75, (24), 245111.

34. Rivera-Calzada, A.; Diaz-Guillen, M. R.; Dura, O. J.; Sanchez-Santolino, G.; Pennycook, T. J.; Schmidt, R.; Bruno, F. Y.; Garcia-Barriocanal, J.; Sefrioui, Z.; Nemes, N. M.; Garcia-Hernandez, M.; Varela, M.; Leon, C.; Pantelides, S. T.; Pennycook, S. J.; Santamaria, J., Tailoring Interface Structure in Highly Strained YSZ/STO Heterostructures. *Advanced Materials* 23, (44), 5268-5274.

35. Kilner, J. A., Fast oxygen transport in acceptor doped oxides. *Solid State Ionics* **2000,** 129, (1 - 4), 13-23.

36. Yoshida, H.; Inagaki, T.; Miura, K.; Inaba, M.; Ogumi, Z., Density functional theory calculation on the effect of local structure of doped ceria on ionic conductivity. *Solid State Ionics* **2003,** 160, (1-2), 109-116.

37. Sánchez Bautista, C.; Dos Santos García, A. J.; Peña Martínez, J.; Canales-Vázquez, J., Processing of samarium doped ceria for IT-SOFC. Grain boundary effect on the electrical conductivity. *Boletín de la Sociedad Española de Cerámica y Vidrio* **2010,** 49, (1), 7-14.

38. Tuller, H. L.; Nowick, A. S., Small polaron electron transport in reduced CeO_2 single crystals. *Journal of Physics and Chemistry of Solids* **1977,** 38, (8), 859-867.

39. Eerenstein, W.; Mathur, N. D.; Scott, J. F., Multiferroic and magnetoelectric materials. *Nature* **2006,** 442, (7104), 759-765.

40. Michel, C.; Moreau, J.-M.; Achenbach, G. D.; Gerson, R.; James, W. J., The atomic structure of $BiFeO_3$. *Solid State Communications* **1969,** 7, (9), 701-704.

41. Lubk, A.; Gemming, S.; Spaldin, N. A., First-principles study of ferroelectric domain walls in multiferroic bismuth ferrite. *Physical Review B* **2009,** 80, (10), 104110.

42. Zhao, T.; Scholl, A.; Zavaliche, F.; Lee, K.; Barry, M.; Doran, A.; Cruz, M. P.; Chu, Y. H.; Ederer, C.; Spaldin, N. A.; Das, R. R.; Kim, D. M.; Baek, S. H.; Eom, C. B.; Ramesh, R., Electrical control of antiferromagnetic domains in multiferroic $BiFeO_3$ films at room temperature. *Nat Mater* **2006,** 5, (10), 823-829.

43. Khomskii, D., Trend: Classifying multiferroics: Mechanisms and effects. *Physics* **2009,** 2, (20).

44. Sosnowska, I.; Neumaier, T. P.; Steichele, E., Spiral magnetic ordering in bismuth ferrite. *Journal of Physics C: Solid State Physics* **1982,** 15, (23), 4835.

45. Fuentes-Cobas, L. E.; Matutes-Aquino, J. A.; Fuentes-Montero, M. E.; Buschow, K. H. J., Magnetoelectricity. In *Handbook of Magnetic Materials*, Elsevier: 2011; Vol. 19, pp 129-229.

46. Bernardo, M. S.; Jardiel, T.; Peiteado, M.; Caballero, A. C.; Villegas, M., Reaction pathways in the solid state synthesis of multiferroic $BiFeO_3$. *Journal of the European Ceramic Society* **2011,** 31, (16), 3047-3053.

47. Mostafavi, E.; Ataie, A.; Ahmadzadeh, M., Characterization of Nano-Structured Multiferroic Bismuth Ferrite Produced via Solid State Reaction Route. *Advanced Materials Research* **2014,** 829, 683-687.

48. Jiang, J.; Zou, J.; Anjum, M. N.; Yan, J.; Huang, L.; Zhang, Y.; Chen, J., Synthesis and characterization of wafer-like $BiFeO_3$ with efficient catalytic activity. *Solid State Sciences* **2011,** 13, (9), 1779-1785.

49. Kim, J. K.; Kim, S. S.; Kim, W.-J., Sol-gel synthesis and properties of multiferroic $BiFeO_3$. *Materials Letters* **2005,** 59, (29-30), 4006-4009.

50. Mazumder, R.; Chakravarty, D.; Bhattacharya, D.; Sen, A., Spark plasma sintering of $BiFeO_3$. *Materials Research Bulletin* **2009,** 44, (3), 555-559.

51. Fischer, P.; Polomska, M.; Sosnowska, I.; Szymanski, M., Temperature dependence of the crystal and magnetic structures of $BiFeO_3$. *Journal of Physics C: Solid State Physics* **1980,** 13, (10), 1931.

52. Fang, T.-T.; Ting, C.-C.; Miao, J. H., A Template-Free Synthesis of the One-Dimensional Nanostructure of Multiferroic $BiFeO_3$. *Journal of the American Ceramic Society* **2009,** 92, (12), 3065-3069.

53. Chen, Z.; Wu, Y.; Hu, J., Ethanol-Assisted Hydrothermal Synthesis and Characterization of $BiFeO_3$ Nanopowders. *Journal of the American Ceramic Society* **2013,** 96, (5), 1345-1348.

54. Liu, B.; Hu, B.; Du, Z., Hydrothermal synthesis and magnetic properties of single-crystalline $BiFeO_3$ nanowires. *Chemical Communications* **2011,** 47, (28), 8166-8168.

55. Miao, H.; Zhang, Q.; Tan, G.; Zhu, G., Co-precipitation/hydrothermal synthesis of $BiFeO_3$ powder. *Journal of Wuhan University of Technology-Mater. Sci. Ed.* **2008,** 23, (4), 507-509.

56. Yu, J.; Koshikawa, N.; Arai, Y.; Yoda, S.; Saitou, H., Containerless solidification of oxide material using an electrostatic levitation furnace in microgravity. *Journal of Crystal Growth* **2001,** 231, (4), 568-576.

57. Sosnowska, I.; Schäfer, W.; Kockelmann, W.; Andersen, K. H.; Troyanchuk, I. O., Crystal structure and spiral magnetic ordering of $BiFeO_3$ doped with manganese. *Applied Physics A* **2002,** 74, (1), s1040-s1042.

58. Palai, R.; Katiyar, R. S.; Schmid, H.; Tissot, P.; Clark, S. J.; Robertson, J.; Redfern, S. A. T.; Catalan, G.; Scott, J. F., β phase and γ–β metal-insulator transition in multiferroic $BiFeO_3$. *Physical Review B* **2008,** 77, (1), 014110.

59. Arnold, D. C.; Knight, K. S.; Morrison, F. D.; Lightfoot, P., Ferroelectric-Paraelectric Transition in $BiFeO_3$: Crystal Structure of the Orthorhombic β Phase. *Physical Review Letters* **2009,** 102, (2), 027602.

60. Valant, M.; Axelsson, A.-K.; Alford, N., Peculiarities of a Solid-State Synthesis of Multiferroic Polycrystalline $BiFeO_3$. *Chemistry of Materials* **2007,** 19, (22), 5431-5436.

61. Reyes, A.; de la Vega, C.; Fuentes, M. E.; Fuentes, L., $BiFeO_3$: Synchrotron radiation structure refinement and magnetoelectric geometry. *Journal of the European Ceramic Society* **2007,** 27, (13-15), 3709-3711.

62. Zeches, R. J.; Rossell, M. D.; Zhang, J. X.; Hatt, A. J.; He, Q.; Yang, C.-H.; Kumar, A.; Wang, C. H.; Melville, A.; Adamo, C.; Sheng, G.; Chu, Y.-H.; Ihlefeld, J. F.; Erni, R.; Ederer, C.; Gopalan, V.; Chen, L. Q.; Schlom, D. G.; Spaldin, N. A.; Martin, L. W.; Ramesh, R., A Strain-Driven Morphotropic Phase Boundary in $BiFeO_3$. *Science* **2009,** 326, (5955), 977-980.

63. Gotardo, R. A. M.; Santos, I. A.; Cótica, L. F.; Botero, É. R.; Garcia, D.; Eiras, J. A., Improved ferroelectric and magnetic properties of monoclinic structured $0.8BiFeO_3$-$0.2BaTiO_3$ magnetoelectric ceramics. *Scripta Materialia* **2009,** 61, (5), 508-511.

64. Wang, Y. P.; Zhou, L.; Zhang, M. F.; Chen, X. Y.; Liu, J.-M.; Liu, Z. G., Room-temperature saturated ferroelectric polarization in $BiFeO_3$ ceramics synthesized by rapid liquid phase sintering. *Applied Physics Letters* **2004,** 84, (10), 1731-1733.

65. Fei, L.; Yuan, J.; Hu, Y.; Wu, C.; Wang, J.; Wang, Y., Visible Light Responsive Perovskite $BiFeO_3$ Pills and Rods with Dominant $\{111\}_c$ Facets. *Crystal Growth & Design* **2011,** 11, (4), 1049-1053.

66. Palewicz, A.; Przenioslo, R.; Sosnowska, I.; Hewat, A. W., Atomic displacements in $BiFeO_3$ as a function of temperature: neutron diffraction study. *Acta Crystallographica Section B* **2007,** 63, (4), 537-544.

67. Hahn, T., *International Tables of Crystallography* 5th ed.; Kluwer Academic Publishers: Boston, 2002; Vol. A.

68. Morniroli, J. P.; Steeds, J. W., Microdiffraction as a tool for crystal structure identification and determination. *Ultramicroscopy* **1992,** 45, (2), 219-239.

69. Zalessky, A. V.; Frolov, A. A.; Khimich, T. A.; Bush, A. A.; Pokatilov, V. S.; Zvezdin, A. K., ^{57}Fe NMR study of spin-modulated magnetic structure in $BiFeO_3$. *EPL (Europhysics Letters)* **2000,** 50, (4), 547.

70. Basu, S.; Pal, M.; Chakravorty, D., Magnetic properties of hydrothermally synthesized $BiFeO_3$ nanoparticles. *Journal of Magnetism and Magnetic Materials* **2008,** 320, (24), 3361-3365.

71. Fruth, V.; Mitoseriu, L.; Berger, D.; Ianculescu, A.; Matei, C.; Preda, S.; Zaharescu, M., Preparation and characterization of $BiFeO_3$ ceramic. *Progress in Solid State Chemistry* **2007,** 35, (2 - 4), 193-202.

72. Azough, F.; Freer, R.; Thrall, M.; Cernik, R.; Tuna, F.; Collison, D., Microstructure and properties of Co-, Ni-, Zn-, Nb- and W-modified multiferroic $BiFeO_3$ ceramics. *Journal of the European Ceramic Society* 30, (3), 727-736.

73. Moreau, J. M.; Michel, C.; Gerson, R.; James, W. J., Ferroelectric $BiFeO_3$ X-ray and neutron diffraction study. *Journal of Physics and Chemistry of Solids* **1971,** 32, (6), 1315-1320.

74. Troyanchuk, I. O.; Bushinsky, M. V.; Chobot, A. N.; Mantytskaya, O. S.; Tereshko, N. V., Weak ferromagnetism in $BiFeO_3$-based multiferroics. *JETP Letters* **2009,** 89, (4), 180-184.

75. Han, S.; Sung Kim, C., Weak ferromagnetic behavior of $BiFeO_3$ at low temperature. *Journal of Applied Physics* **2013,** 113, (17), 17D921.

76. Abram, E. J.; Sinclair, D. C.; West, A. R., A Strategy for Analysis and Modelling of Impedance Spectroscopy Data of Electroceramics: Doped Lanthanum Gallate. *Journal of Electroceramics* **2003,** 10, (3), 165-177.

77. Masó, N.; West, A. R., Electrical Properties of Ca-Doped $BiFeO_3$ Ceramics: From p-Type Semiconduction to Oxide-Ion Conduction. *Chemistry of Materials* **2012,** 24, (11), 2127-2132.

78. Chirayil, T.; Zavalij, P. Y.; Whittingham, M. S., Hydrothermal Synthesis of Vanadium Oxides. *Chemistry of Materials* **1998,** 10, (10), 2629-2640.

79. Chang, K.-H.; Hu, C.-C., $H_2V_3O_8$ single-crystal nanobelts: Hydrothermal preparation and formation mechanism. *Acta Materialia* **2007,** 55, (18), 6192-6197.

80. Niederberger, M.; Muhr, H.-J.; Krumeich, F.; Bieri, F.; Günther, D.; Nesper, R., Low-Cost Synthesis of Vanadium Oxide Nanotubes via Two Novel Non-Alkoxide Routes. *Chemistry of Materials* **2000,** 12, (7), 1995-2000.

81. Luca, V.; Hook, J. M., Study of the Structure and Mechanism of Formation through Self-Assembly of Mesostructured Vanadium Oxide. *Chemistry of Materials* **1997,** 9, (12), 2731-2744.

82. Legagneur, V.; Le Gal La Salle, A.; Verbaere, A.; Piffard, Y.; Guyomard, D., Lithium insertion/deinsertion properties of new layered vanadium oxides obtained by oxidation of the precursor $H_2V_3O_8$. *Electrochimica Acta* **2002,** 47, (7), 1153-1161.

83. Legagneur, V.; Le Gal La Salle, A.; Verbaere, A.; Piffard, Y.; Guyomard, D., New layered vanadium oxides $M_yH_{1-y}V_3O_8 \cdot nH_2O$ (M = Li, Na, K) obtained by oxidation of the precursor $H_2V_3O_8$. *Journal of Materials Chemistry* **2000,** 10, (12), 2805-2810.

84. Theobald, F.; Cabala, R., L'hydrate V_3O_7, H_2O. *Comptes Rendus Hebdomadaires Des Seances De L Academie Des Sciences, Serie C* **1970,** 270, 2138.

85. Oka, Y.; Yao, T.; Yamamoto, N., Structure determination of $H_2V_3O_8$ by powder X-ray diffraction. *Journal of Solid State Chemistry* **1990,** 89, (2), 372-377.

86. Gao, S.; Chen, Z.; Wei, M.; Wei, K.; Zhou, H., Single crystal nanobelts of $V_3O_7 \cdot H_2O$: A lithium intercalation host with a large capacity. *Electrochimica Acta* **2009,** 54, (3), 1115-1118.

87. Mho, S.-I.; Reddy, C. V.; Kim, Y.; Yeo, I.-H.; Park, S.-M., Hydrothermal Synthesis of $H_2V_3O_8$ Nanobelts from V_2O_5 Xerogels for Lithium Battery Applications. *Journal of Korean Physical Society* **2009,** 54, (6), 2420-2424.

88. Chine, M. K.; Sediri, F.; Gharbi, N., Hydrothermal Synthesis of $V_3O_7 \cdot H_2O$ Nanobelts and Study of Their Electrochemical Properties *Materials Sciences and Application* **2011,** 2, 964-970.

89. Li, J.-M.; Chang, K.-H.; Wu, T.-H.; Hu, C.-C., Microwave-assisted hydrothermal synthesis of vanadium oxides for Li-ion supercapacitors: The influences of Li-ion doping and crystallinity on the capacitive performances. *Journal of Power Sources* **2013,** 224, (0), 59-65.

90. Brown, I. D.; Altermatt, D., Bond-valence parameters obtained from a systematic analysis of the Inorganic Crystal Structure Database. *Acta Crystallographica Section B* **1985,** 41, (4), 244-247.

91. Naskar, J. P.; Hati, S.; Datta, D., New Bond-Valence Sum Model. *Acta Crystallographica Section B* **1997,** 53, (6), 885-894.

92. Li, H.; Zhai, T.; He, P.; Wang, Y.; Hosono, E.; Zhou, H., Single-crystal $H_2V_3O_8$ nanowires: a competitive anode with large capacity for aqueous lithium-ion batteries. *Journal of Materials Chemistry* **2011,** 21, (6), 1780-1787.

93. Zhang, Y.; Liu, X.; Xie, G.; Yu, L.; Yi, S.; Hu, M.; Huang, C., Hydrothermal synthesis, characterization, formation mechanism and electrochemical property of $V_3O_7 \cdot H_2O$ single-crystal nanobelts. *Materials Science and Engineering: B* **2010,** 175, (2), 164-171.

94. Brunauer, S.; Emmett, P. H.; Teller, E., Adsorption of Gases in Multimolecular Layers. *Journal of the American Chemical Society* **1938,** 60, (2), 309-319.

95. Perez-Flores, J. C.; Baehtz, C.; Hoelzel, M.; Kuhn, A.; Garcia-Alvarado, F., $H_2Ti_6O_{13}$, a new protonated titanate prepared by Li^+/H^+ ion exchange: synthesis, crystal structure and electrochemical Li insertion properties. *RSC Advances* **2012,** 2, (8), 3530-3540.

96. Schmid, H. K.; Mader, W., Oxidation states of Mn and Fe in various compound oxide systems. *Micron* **2006,** 37, (5), 426-432.

97. Bach, D.; Störmer, H.; Schneider, R.; Gerthsen, D.; Verbeeck, J., EELS Investigations of Different Niobium Oxide Phases. *Microscopy and Microanalysis* **2006,** 12, (05), 416-423.

98. Baddour-Hadjean, R.; Marzouk, A.; Pereira-Ramos, J. P., Structural modifications of $Li_xV_2O_5$ in a composite cathode ($0 \leq x < 2$) investigated by Raman microspectrometry. *Journal of Raman Spectroscopy* **2011,** 43, (1), 153 -160.

99. Cocciantelli, J. M.; Doumerc, J. P.; Pouchard, M.; Broussely, M.; Labat, J., Crystal chemistry of electrochemically inserted $Li_xV_2O_5$. *Journal of Power Sources* **1991,** 34, (2), 103-111.

100. Sato, Y.; Asada, T.; Tokugawa, H.; Kobayakawa, K., Observation of structure change due to discharge/charge process of V_2O_5 prepared by ozone oxidation method, using in situ X-ray diffraction technique. *Journal of Power Sources* **1997,** 68, (2), 674-679.

7. CONCLUSIONS

The main purpose of the present work was to show that the use of microwave irradiation is a promising alternative heat source for the synthesis of inorganic materials. It has been demonstrated that the method offers massive energy and time savings as compared to the traditional ceramic method.

The basic principles of the microwave heating mechanism based on interactions between dipoles in the material and the electromagnetic microwave radiation have been reviewed. It is clear that both the magnetic and the electric part of the microwave are important for the heating mechanism, not only the electric part as previously described in the literature.

The preparation of inorganic materials by using different microwave techniques was shown to be fruitful from the compositional, structural, properties and applications points of view:

- A wide range of different structure-types have been prepared: perovskite, pyrochlore, hollandite, fluorite and one-dimensional structures.

- The prepared materials show a wide range of functional properties: ferromagnetism, ferroelectricity, multiferroicity, thermoelectricity, lithium and oxygen ion conductivity.

- The materials synthesized may have application in a wide range of different technologies: information technology, telecommunication, thermoelectric applications, solid oxide fuel cells and batteries.

The broad variety of different microwave or microwave-assisted synthesis techniques opens up opportunities for the preparation of inorganic nanoparticles and nanostructures. This allows the possibility to tune the morphology, and the physical and chemical properties of nanoscale materials.

Various microwave synthesis techniques have been employed: solid-state microwaves, single-mode microwaves using a TE_{10p} cavity and microwave-assisted hydrothermal synthesis.

At the end of each experimental chapter in this thesis some conclusions had been drawn already, which are again summarized here:

Chapter 4: Solid – State Microwave Synthesis

Synthesis was performed by using a domestic microwave. The efficiency of the procedure using this fast and cheap apparatus is remarkable. The main problem of this method is the lack of temperature control.

- The **$LaMO_3$ and $La_{1-x}A'_xMO_3$ (A' = Sr, M = Al, Cr, Mn, Fe, Co)**, family was synthesized successfully, whereby different synthesis routes had to be established for different species.

- $LaCoO_3$ ceramics showed a different level of oxygen vacancy defects when synthesized with microwaves as compared to conventional synthesis. This allows studying the influence of defects on the physical and magnetic properties of $LaCoO_3$.

- A comprehensive characterization in terms of the structural and physical properties was performed for the microwave synthesized perovskite **$(RE)CrO_3$** series. No clear correlations of the magnetic and dielectric properties were found in these materials, and major magneto-electric coupling effects could not be detected. No indications for a non-centrosymmetric space-group and associated ferroelectricity were detected from XRD pattern, Raman spectroscopy and temperature dependent dielectric permittivity data.

Microwave synthesized (RE)CrO_3 chromites may therefore not be classified as magneto-electric or multiferroic materials.

- Synchrotron X-ray diffraction experiments in **$(RE)_2Ti_2O_7$ (RE = Gd, Ho)** showed an antisite defect concentration of 3.6 % for $Gd_2Ti_2O_7$ and 2.4 % for $Ho_2Ti_2O_7$ at 1100 ^oC. A reduction of antisite defect concentration with the increasing temperature treatment was observed using synchrotron X-ray radiation. In both studied samples a weak ferromagnetic component was observed at 1.7 K. Impedance spectroscopy reveals that $Gd_2Ti_2O_7$ shows considerably higher ionic oxygen vacancy conductivity as compared to $Ho_2Ti_2O_7$.

Chapter 5: Single – Mode Microwave Synthesis

By using a TE_{10p} cavity the electromagnetic field is well defined in space and the material can be heated in different resonant modes using either the electric or magnetic component of the microwave. The synthesis temperature was monitored easily using a pyrometer.

Structure, magnetism and transport properties have been studied for single-mode microwave prepared hollandite structure $Ba_{1.2}Mn_8O_{16}$. A reversible first order monoclinic – monoclinic transition was found at ≈ 400 K. Magnetic susceptibility measurements indicate a canted antiferromagnetic state at 42 K. The $Ba_{1.2}Mn_8O_{16}$ hollandite exhibits semiconducting electronic conduction, consistent with one-dimensional variable range hopping up to ≈ 400 K. Above this temperature, samples undergo a structural transition and the the charge transport mechanism is modified. The Seebeck coefficient is negative and has a plateau above the transition temperature.

Chapter 6: Microwave - Hydrothermal Synthesis

The combination of two rapid and "green chemistry" synthesis techniques, hydrothermal synthesis and microwave synthesis, is promising to minimize heat exposure and reaction times for chemical synthesis. The particle sizes and shapes of the product can be tuned by the synthesis parameters.

- Concerning **rare-earth (RE) doped ceria ($Ce_{1-x}RE_xO_{2-\delta}$)**, samarium and calcium doped ($Ce_{0.8}Sm_{0.18}Ca_{0.02}O_{1.9-\delta}$) and undoped ceria, impedance spectroscopy measurements confirmed ionic conductivity in all doped materials, whereas the undoped $CeO_{2-\delta}$ parent compound exhibited signs of electronic conduction. Deconvolution of GB and intrinsic bulk ionic conductivity revealed that GBs constitute barriers for ionic charge transport, with the Sm - Ca doped ceria $Ce_{0.8}Sm_{0.18}Ca_{0.02}O_{1.9-\delta}$ exhibiting the highest GB ionic conductivity. The highest intrinsic bulk ionic conductivity was detected for the $Ce_{0.8}Sm_{0.18}Ca_{0.02}O_{1.9-\delta}$ ceramic as well.

The GB resistance of microwave – hydrothermal synthesized rare-earth (RE) doped ceria is lower than previously described in the literature for samples prepared by other synthetic methods. The nano-sized particles and the high sintering activity of the samples help to obtain highly compacted pellets, which is ideal for applications and here in this study for reliable impedance spectroscopy measurements.

Single mode microwave sintering was performed for microwave – hydrothermal synthesized $Ce_{0.8}Sm_{0.18}Ca_{0.02}O_{1.9-\delta}$ nanopowder in just 5 minutes. The ionic conductivity obtained reveals comparable values as the conventionally sintered ceramics (4 – 8 h).

- The structural and microstructural characterization of a phase pure **$BiFeO_3$** sample was presented. The *R3c* space group has been confirmed and the material was shown to be highly insulating using impedance spectroscopy. Large Bi-loss does not seem to be a problem using the microwave-hydrothermal synthesis technique. The magnetic properties are similar to the ones reported in

the literature for **$BiFeO_3$** obtained by conventional methods. Weak ferromagnetism was indicated.

- **$H_2V_3O_8$** nanobelts with approximately 100 nm wide and several micrometres long particles have been obtained. The structure of the phase was revealed by synchrotron X-ray diffraction experiments and HRTEM, and can be characterized as a nearly two-dimensional framework (V_3O_8 layers) comprised of 3 kinds of polyhedra: 2 VO_6 octahedra and a VO_5 distorted square based pyramid. The characterization performed confirmed the production of $H_2V_3O_8$ nanobelts with the adequate morphology to exhibit high electrochemical performances. At C/20 rate an initial capacity of ≈ 400 mAh g^{-1} is developed in the 3.75 - 1.5 V range. After a significant capacity loss in the first cycle, a capacity of ca. 300 mAh g^{-1} is maintained upon cycling. Full reduction to V^{3+} has been observed for the first time by discharging Li cells down to 1 V using $H_2V_3O_8$ as a cathode material. A large reversible capacity of 498 mAh g^{-1} was obtained. Furthermore, the similarity of discharge and charge curves point towards the absence of hydrogen displacement during lithium insertion in $H_2V_3O_8$. This in turn suggests that not all protonated systems must be necessarily discarded as prospective electrode materials.

Final remark

During this thesis a huge number of different technologically important materials have been prepared by using microwaves. It is clear that changing the conventional methodologies of inorganic synthesis to more environmental-friendly and cost effective methods, may help the development of a sustainable chemistry contributing to the preservation of the natural environment. The development of microwave synthesis for inorganic materials on a small scale in the laboratory has been demonstrated, but such techniques should also be further extended to industrial large scale production processes.

Annex 1.

Publications and conferences contributions

Publications (articles & book chapter)

From this work

1. Prado-Gonjal, J.; Schmidt, R.; Romero, J.-J.; Ávila, D.; Amador, U.; Morán, E., Microwave-Assisted Synthesis, Microstructure, and Physical Properties of Rare-Earth Chromites. *Inorganic Chemistry* **2013,** 52, (1), 313-320.

2. Prado-Gonjal, J.; Molero-Sánchez, B.; Ávila-Brande, D.; Morán, E.; Pérez-Flores, J. C.; Kuhn, A.; García-Alvarado, F., The intercalation chemistry of $H_2V_3O_8$ nanobelts synthesised by a green, fast and cost-effective procedure. *Journal of Power Sources* **2013,** 232, 173-180.

3. Prado-Gonjal, J.; Schmidt, R.; Morán, E., Microwave-Assisted Synthesis and Characterization of Perovskite Oxides In *Perovskite: Crystallography, Chemistry and Catalytic Performance*, Zhang, J.; Li, H., Eds. Nova Science Pub Incorporated: 2012; pp 117-140

4. Prado-Gonjal, J.; Schmidt, R.; Espíndola-Canuto, J.; Ramos-Alvarez, P.; Morán, E., Increased ionic conductivity in microwave hydrothermally synthesized rare-earth doped ceria $Ce_{1-x}RE_xO_{2-(x/2)}$. *Journal of Power Sources* **2012,** 209, 163-171.

5. Prado-Gonjal, J.; Schmidt, R.; Ávila, D.; Amador, U.; Morán, E., Structural and physical properties of microwave synthesized orthorhombic perovskite erbium chromite $ErCrO_3$. *Journal of the European Ceramic Society* **2012,** 32, (3), 611-618.

6. Prado-Gonjal, J.; Morán, E., Síntesis asistida por microondas de sólidos inorgánicos *Anales de Química* **2011**, (2), 129-136.

7. Prado-Gonjal, J.; Ávila, D.; Villafuerte-Castrejón, M. E.; González-García, F.; Fuentes, L.; Gómez, R. W.; Pérez-Mazariego, J. L.; Marquina, V.; Morán, E., Structural, microstructural and Mössbauer study of $BiFeO_3$ synthesized at low temperature by a microwave-hydrothermal method. *Solid State Sciences* **2011,** 13, (11), 2030-2036.

8. Prado-Gonjal, J.; Arévalo-López, A. M.; Morán, E., Microwave-assisted synthesis: A fast and efficient route to produce $LaMO_3$ (M=Al, Cr, Mn, Fe, Co) perovskite materials. *Materials Research Bulletin* **2011,** 46, (2), 222-230.

Before the PhD studies:

9. Prado-Gonjal, J.; Villafuerte-Castrejón, M. E.; Fuentes, L.; Morán, E., Microwave-hydrothermal synthesis of the multiferroic $BiFeO_3$. *Materials Research Bulletin* **2009,** 44, (8), 1734-1737. In Most Cited Materials Research Bulletin Articles list

Collaborations

10. Schmidt, R.; Stennett, M. C.; Hyatt, N. C.; Pokorny, J.; Prado-Gonjal, J.; Li, M.; Sinclair, D. C., Effects of sintering temperature on the internal barrier layer capacitor (IBLC) structure in $CaCu_3Ti_4O_{12}$ (CCTO) ceramics. *Journal of the European Ceramic Society* **2012,** 32, (12), 3313-3323.

11. Villafuerte-Castrejón, M. E.; García-Guaderrama, M.; Fuentes, L.; Prado-Gonjal, J.; González, A. M.; de la Rubia, M. Á.; García-Hernádez, M.; Morán, E., New Fe^{3+}/ Cr^{3+} Perovskites with Anomalous Transport Properties: The Solid Solution $La_xBi_{1-x}Fe_{0.5}Cr_{0.5}O_3$ ($0.4 < x < 1$). *Inorganic Chemistry* **2011,** 50, (17), 8340-8347.

Conference contributions

1. Prado-Gonjal, J.; Schmidt, R.; Gómez Pérez, A.; Herrero Ansorregui, I.; Gutierrez Seijas, J.; Morán, E., *Síntesis asistida por microondas de sólidos inorgánicos*. In *XXXIV Reunión Bienal de la Real Sociedad Española de Química*, Santander (Spain), 2013, 15th -18th September (Oral communication)

2. Gutierrez Seijas, J.; Prado-Gonjal, J.; Schmidt, R.; Ávila, D.; Morán, E., *Síntesis directa asistida por microondas y caracterización de cobaltitas de tierras raras $LnCoO_3$ (Ln = La-Dy)*. In *XXXIV Reunión Bienal de la Real Sociedad Española de Química*, Santander (Spain), 2013, 15th -18th September (Oral communication).

3. Prado-Gonjal, J.; Gutiérrez Seijas, J.; Schmidt, R.; Ávila, D.; Morán, E., *Propiedades magnéticas y eléctricas de cobaltitas de tierras raras ($TRCoO_3$, TR= La-Dy) sintetizadas por microondas*. In *XI Reunión de Electrocerámica*, Zaragoza (Spain), 2013, 19th - 21st June (Poster communication).

4. Prado-Gonjal, J.; Schmidt, R.; Morán, E., *Cerias dopadas con tierras raras: síntesis hidrotermal asistida por microondas y conductividad iónica*. In *XI Reunión de Electrocerámica*, Zaragoza (Spain), 2013, 19th -21st June (Oral communication).

5. Prado-Gonjal, J.; Schmidt, R.; Heuguet, R.; Savary, E.; Marinel, S.; Morán, E., *Síntesis de sólidos inorgánicos empleando un microondas monomodal*. In *XI Reunión de Electrocerámica*, Zaragoza (Spain), 2013, 19th -21st June (Oral communication)

6. Morán, E.; Prado-Gonjal, J.; Molero-Sánchez, B.; Avila-Brande, D.; Pérez-Flores, J. C.; Kunh, A.; García Alvarado, F., *Microwave-hydrothermally synthesized $H_2V_3O_8$ nanobelts as cathodes for lithium batteries*. In *MRS 2013 Spring Meeting*, San Francisco (USA), 2013, 1st -5th April (Oral communication).

7. Morán, E.; Prado-Gonjal, J.; Schmidt, R.; Herrero Ansorregui, I., *Microwave-assisted synthesis and characterization of perovskite oxides*. In *MRS 2013 Spring Meeting* San Francisco (USA), 2013, 1st -5th April (Poster communication).

8. Prado-Gonjal, J.; Morán, E.; Hébert, S.; Pelloquin, D.; Marinel, S., *Single-mode microwave synthesis and physical properties of $Ba_{1.2}Mn_8O_{16}$ hollandite*. In *MRS 2013 Spring Meeting*, San Francisco (USA), 2013, 1st -5th April (Oral communication).

9. Prado Gonjal, J.; Avila-Brande, D.; Morán, E., *EELS Study of $H_2V_3O_8$ and their Li-intercalated materials*. In *VII Encuentro Franco-Español de Química y Física del Estado Sólido*, Paris (France), 2012, 13th -17th June (Oral communication).

10. Prado-Gonjal, J.; Schmidt, R.; Espíndola-Canuto, J.; Ramos-Alvarez, P.; Morán, E., *Síntesis hidrotermal asistida por microondas de $Ce_{1-x}TR_xO_{2-(x/2)}$ (TR = Tierra rara) Mejorando la conductividad iónica de electrolitos para pilas SOFC*. In *QIES12*, Gerona (Spain), 2012, 1st -4th July (Poster communication)

11. Prado Gonjal, J.; Molero-Sánchez, B.; Avila-Brande, D.; Morán, E.; Pérez-Flores, J. C.; Kuhn, A.; García-Alvarado, F., $H_2V_3O_8$ nanowires Microwave-assisted synthesis, characterization and Li-electrochemistry. In *Power Our Future*, Vitoria (Spain), 2012, 20th - 21st March (Poster communication)

12. Gómez-Pérez, A.; Prado-Gonjal, J.; Morán, E., *Microwave synthesis and characterization of $RE_2Ti_2O_7$ (RE = Y, Eu, Tb, Ho,Er, Yb) pyrochlores.* In *Zing Conferences - Solid State*, Lanzarote (Spain), 2012, 24th -27th February (Poster communication).

13. Prado-Gonjal, J.; Schmidt, R.; Ávila, D.; Amador, U.; Morán, E.; , *Microwave assisted synthesis and physical properties of rare-earth chromites*. In *Zing Conferences -Solid State*, Lanzarote (Spain), 2012, 24th -27th February (Poster communication).

14. Prado-Gonjal, J.; Schmidt, R.; Espíndola-Canuto, J.; Ramos-Alvarez, P.; Morán, E., *Increased ionic conductivity in microwave hydrothermally synthesized rare earth (RE) doped ceria $Ce_{1-x}RE_xO_{2-(x/2)}$* . In *Zing Conferences -Solid State*, Lanzarote (Spain), 2012, 24th - 27th February (Poster communication) Best poster award

15. Morán, E.; Prado-Gonjal, J., *Microwave-assisted synthesis of perovskite materials*. In *Zing Conferences -Solid State*, Lanzarote (Spain), 2012, 24th -27th February (Oral communication).

16. Morán, E.; Prado-Gonjal, J., *Microwave-assisted synthesis of Rare Earth Chromites*. In *ISRS17 Reactivity of Solids*, Bourdeaux (France), 2011, 27th June - 1st July (Poster communication).

17. Morán, E.; Prado-Gonjal, J., *Microwave-assisted synthesis A "Fast Chemistry" route to produce inorganic materials*. In *ISRS17 Reactivity of Solids*, Bourdeaux (France), 2011, 27th June - 1st July (Oral communication)

18. Prado-Gonjal, J.; Ávila, D.; Schmidt, R.; Amador, U.; Morán, E., *Cromitas de tierras raras nuevos materiales multiferroicos sintetizados por microondas*. In *X Reunión Nacional de Electrocerámica*, Madrid (Spain), 2011, 13th -15th June (Poster communication) Young Researcher Award

19. Villafuerte-Castrejón, M. E.; Prado-Gonjal, J.; Molero-Sánchez, B.; Ávila, D.; Fuentes, L.; González García, F.; Morán, E., *Propiedades dieléctricas de $BiFeO_3$ sintetizado por vía hidrotermal asistida por microondas*. In *X Reunión Nacional de Electrocerámica*, Madrid (Spain), 2011, 13th -15th June (Oral communication)

20. Prado Gonjal, J.; Schmidt, R.; Morán, E.; Terry, I., *Physical properties of microwave synthesized $LaCoO_3$*. In *X Reunión Nacional de Electrocerámica*, Madrid (Spain), 2011, 13th - 15th June (Oral communication).

21. Conde Román, J. L.; Prado-Gonjal, J.; Morán, E., *Síntesis asistida por microondas y caracterización de óxidos y oxi-hidróxidos de aluminio*. In *XIV Reunión Bienal del grupo especializado de Química Inorgánica y VIII del Grupo Especializado de Química de Estado Sólido*, Cartagena (Spain) 2010, 12th -15th September (Poster communication).

22. Prado-Gonjal, J.; Morán, E., Síntesis asistida por microondas de cromitas de tierras raras. In *XIV Reunión Bienal del grupo especializado de Química Inorgánica y VIII del Grupo Especializado de Química de Estado Sólido*, Cartagena (Spain) 2010, 12th -15th September (Poster communication).

23. Morán, E.; Prado-Gonjal, J.; Prado-Escudero, J.; Blanco-Carazo, M.; Conde-Román, J. L., *Microwave assisted synthesis of inorganic materials* In *Seventh International Conference on Inorganic Materials*, Biarritz (France) 2010, 12th -14th September (Poster communication).

24. Prado-Gonjal, J.; Morán, E.; Ávila, D.; Fuentes, L.; Escudero, R.; González García, F.; Marquina, V.; Villafuerte-Castrejón, M. E., *Characterization and Mösbauer study of the multerroic $BiFeO_3$ synthesized by a microwave hydrothermal method.* In *XIX International Materials Research 2010* Cancun (Mexico) 2010, 15th -19th August (Poster communication).

25. Prado-Gonjal, J.; Morán, E.; Villafuerte-Castrejón, M. E.; Fuentes, L., *Characterization and properties of $BiFeO_3$ synthesized by a microwave-assisted hydrothermal method*. In *VI Encuentro Franco-Español de Química y Física del Estado Sólido*, Tarragona (Spain) 2010, 17th -19th March (Oral communication).

26. Prado-Gonjal, J.; Arévalo-López, Á. M.; Canales-Vázquez, J.; Morán, E., *Microwave synthesis of materials for SOFC's components* In *I Workshop on Solid Oxide Fuel Cells Materials and Technology* Albacete (Spain) 2009, 18th -20th November (Poster communication)

27. Prado-Gonjal, J.; Arévalo-López, Á. M.; Morán, E., *Síntesis -asistida por microondas- y caracterización de perovskitas $LaMO_3$ (M= Al, Mn, Fe, Co)* In *XXXII Reunión Bienal de la Real Sociedad Española de Química* Oviedo (Spain) 2009, 13th -18th September (Oral communication).

28. Morán, E.; Prado-Gonjal, J.; Arévalo-López, Á. M.; Villafuerte, M. E.; García-Guaderrama, M., *"Fast Chemistry" synthetic methods applied to perovskites* In *XVIII International Materials Research 2009* Cancun (Mexico) 2009, 16th -21st August (Oral communication)

29. Prado-Gonjal, J.; Arévalo-López, Á. M.; Morán, E., *Microwave synthesis and characterization of perovskites $LaMO_3$ (M = Al, Co, Fe, Mn)* In *XVIII International Materials Research 2009* Cancun (Mexico) 2009, 16th -21st August (Poster communication).

Fragmento del **Concierto de Aranjuez** (1939), para guitarra y orquesta, *Adagio*.

Maestro Joaquín Rodrigo (1901 – 1999)